CONSOLIDATION OF Al-TiO_2 AND Ti_3Al-Al_2O_3 COMPOSITE POWDERS

A thesis submitted in partial fulfilment
of the requirements for the degree of
Ph.D.
in Materials and Process Engineering
at
The University of Waikato
by
CHING ZEN HAN

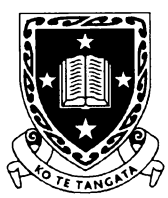

THE UNIVERSITY OF
WAIKATO
Te Whare Wānanga o Waikato

Hamilton, New Zealand
2005

To Tak Sam and my family

for their love and support

Abstract

Pressureless sintering, hot pressing and sinter-HIP of Ti_3Al-Al_2O_3 and Al-TiO_2 composite powders have been carried out under inert atmospheres. The Al-TiO_2 composite powders were produced by discus milling Al/TiO_2 powder mixtures followed by ball milling. The Ti_3Al-Al_2O_3 composite powders were produced by heating Al/TiO_2 powder mixtures. Densification, sintering behaviour, microstructural development and mechanical properties of the composites were investigated for the variables of pressure and temperature at different powder particle sizes. It was shown that higher bulk density and lower porosity were obtained by hot pressing compared to pressureless sintering. A temperature of 1600°C is required to achieve >95% theoretical density of the composites when fabricated by pressureless sintering Ti_3Al-Al_2O_3 composite powder. However, fully densified composites could be fabricated by hot pressing 1.2μm Ti_3Al-Al_2O_3 composite powder at 1474°C under vacuum for a one hour holding period. The growth of Al_2O_3 particle size and the development of microcracks at the Ti_3Al-TiO-Al_2O_3 interfaces were evident with the increasing temperature above 1500°C for the composites produced by pressureless sintering and hot pressing.

Near fully densified Ti_3Al-TiO-Al_2O_3 and Ti_3Al-Al_2O_3 composites (96% of theoretical density) with ≤4μm Al_2O_3 particle size in the composites could be achieved by pressureless sintering Al-TiO_2 composite powder at 1480°C in argon for 4-5 hours of holding period. Fully dense Ti_3Al-Al_2O_3 composite microstructures could be achieved by hot pressing four hours discus milled composite powder subjected to 24 hours of ball milling giving a starting median particle diameter of 7μm, at 1387°C under vacuum. The XRD traces show that the Ti_3Al phase in the Ti_3Al-Al_2O_3 composites is maintained above 50% XRD peak intensity up to 1500°C. The composite microstructure demonstrates that both the Al_2O_3 and Ti_3Al phases are continuous and exhibit an interpenetrating network.

Near fully densified Ti_3Al-TiO-Al_2O_3 composites (≤98% of theoretical density) were fabricated by sinter-HIP of Al-TiO_2 composite powders with a starting median particle diameter of 7.7μm. The coarsening of the Al_2O_3 particles was suppressed after hot isostatic pressing at 1350°C in argon for two hours at 200MPa for the Ti_3Al-TiO-Al_2O_3 composites prepared by pressureless sintering Al-TiO_2 composite powder at 1480°C.

Vickers hardness of the composites increased with increasing densification and increased Al_2O_3 ceramic phase content. Vickers hardness of ≤17.5GPa was achieved for the fully densified Ti_3Al-TiO-Al_2O_3 composite whereas Vickers hardness of ≤15GPa was achieved for the fully densified Ti_3Al-Al_2O_3 composites with Al_2O_3 particle size of ≤4μm. In the sinter-HIP experiments, the Vickers hardness increased by up to 2GPa due to the decreased total porosity after hot isostatic pressing of the pre-sintered Ti_3Al-TiO-Al_2O_3 composites with 96% theoretical density. Biaxial strength of ≤350MPa and ≤278MPa were achieved for Ti_3Al-TiO-Al_2O_3 and Ti_3Al-Al_2O_3 composites, respectively. In this study, fracture toughness as high as 7.5±0.8MPa.$m^{1/2}$ was obtained when the phase structure exhibited fine (≤4μm) and homogeneous microstructure with 50% XRD peak intensity of Ti_3Al ductile phase in the matrix.

Acknowledgements

First of all I would like to thank my supervisor, Associate Professor Deliang Zhang for giving me this opportunity to embark on this project as part of my PhD study. Exceptional gratitude to my co-supervisor, Dr Ian Brown who took me under his wing for three years at Industrial Research Limited (IRL), Lower Hutt.

Thanks to Glen Barris, Neville Baxter, Mark Bowden, Conrad Lendrum, Bill Owers, Carolyn Sheppard, and Vaughan White for their invaluable discussions and suggestions. Many thanks to Martin Ryan for XRD analyses and Kay Card for SEM/EDS analyses, which formed a big part of this thesis. Also thanks to Mary Dalbert, Paul Ewart, Stiliana Raynova, Yuanji Zhang from the University of Waikato and Darien Scott from IRL for their technical support throughout the duration of my PhD study.

Thanks to Jeremie Barrel, Shen Chong, Marc Daglish, Catherine Dickson, Chris Dixson, Ross Fletcher, Graeme Gainsford, David Grant-Taylor, Camila Hosie, Tim Kemmitt, Frederic Lecarpentier and Eugene Stytsenko who made my stay at IRL more enjoyable.

I would like to thank The Foundation for Research, Science and Technology for funding this project through a New Economy Research Fund (NERF contract no: UOWX9909).

Last but not least, special thanks to Tak Sam Lee and my family for their constant support in every aspect. I would not have endured all the predicaments of getting this PhD thesis finalised without their support and understanding.

Table of Contents

pg

List of Figures

pg

List of Tables

pg

Abbreviations

3A	Alumina-aluminide alloys
AUX	Back scattered electron
CIP	Cold isostatic pressing
CTE	Coefficient of thermal expansion
DTA	Differential thermal analysis
EDS	Energy dispersive spectroscopy
EVA	XRD evaluation software
HIP	Hot isostatic pressing
K_{IC}	Fracture toughness
PS	Pressureless sintering
SE	Secondary electron
SEM	Scanning electron microscopy
SHS	Self-propagating high temperature synthesis
SPS	Spark plasma sintering
XRD	X-ray diffraction

CHAPTER ONE:

Introduction

And

Literature Review

1.1 Introduction

The drive to develop and improve processing technologies based on advanced materials is focussed towards producing near net-shape components with favourable microstructures and properties, while minimising expensive materials waste and reducing the cost of machining. Functional and structural ceramics are characterised by their excellent wear resistance and hardness as well as high thermal and chemical stability. However, such advanced ceramic materials exhibit very low fracture toughness, which limits their technical utilisation. This has lead to the development of a novel powder metallurgy technique for the low-cost manufacturing of alumina-aluminide alloys (3A). The process involves the reaction sintering of intensively milled powder mixtures consisting of inexpensive raw materials such as aluminium, metal oxides and/or elemental metals, heat-treated in a non-oxidising atmosphere. The outcome is the production of alumina-aluminide composites whose interpenetrating networks offer the possibility of greatly enhanced mechanical properties and engineering performance.

Intermetallic compounds in the system Ti-Al, namely Ti_3Al and TiAl, are considered to be important future structural materials because of their favourable high temperature properties such as creep resistance and stability of microstructure. This thesis presents results for pressureless sintering, hot pressing and hot isostatic pressing of a 3A system developed from TiO_2 and Al produced by high-energy mechanical milling with or without heat treatment in an inert (Ar or vacuum) atmosphere. Previous research indicates that the resulting composites should exhibit the typical thermomechanical properties of Al_2O_3 ceramics such as high resistance to wear and oxidation and high temperature strength, along with enhanced fracture toughness due to the interpenetrating ceramic/intermetallic network.

The high energy milling device used in this project is the New Zealand developed *Rocklabs* "Split Discus" mill located at the University of Waikato, Hamilton. High energy mechanical milling is a versatile and promising solid state materials processing technique of significant technological advantage. Although the solid-state reactions of the 3A process[2-4] have been known for some time, successful pressureless densification of bodies with homogeneous microstructure has not

previously been achieved. The lack of success to date results from differences in the molar volumes of the reactants and products, porosity of the green compact, and/or the evolution of gases adsorbed on the reactant powders. Although the 3A reactions typically commence at approximately 400°C, the exothermic nature of these reactions necessitates careful process control. For 3A systems with low reaction enthalpies, such as the TiO_2/Al system (ΔH = -258.6kJ/mol), the reaction can be controlled by utilising slow heating rates. The complex relationships between the process conditions, microstructural development and mechanical properties are studied to better understand and ultimately control the properties and performance of composites within this system.

Part of the work carried out by Ying[5] at the University of Waikato in his PhD research, involved the examination of the effects of high energy milling on the phase formation and reaction kinetics in the Al-TiO_2 system. Ying reported that the first phase formed by the interfacial reaction was Al_3Ti irrespective of the initial composition of the powder mixture. The formation of Ti-rich phases proceeded much more slowly than that of Al_3Ti and required higher temperature and longer time. The formation of α-Al_2O_3 could not be observed immediately during the reaction between Al and TiO_2. However, Ying observed that high energy mechanical milling accelerated the reaction kinetics of the α-Al_2O_3 formation, resulting in its formation at lower temperature and shorter time.

This work was continued by Cai[6] in his PhD research, synthesizing Ti_xAl_y/Al_2O_3 metal-ceramic composites (Ti_xAl_y includes α-Ti(Al,O), Ti_3Al or TiAl) with different volume fractions of ceramic reinforcement phases using a complex combination of high energy mechanical milling, thermal treatment and powder consolidation process. The research was concentrated on the definition of the processing/microstructure/property relationships of titanium alloy based composites produced using Al and TiO_2.

The research described in this thesis aims to achieve a comprehensive understanding of the processes for consolidating discus milled Al-TiO_2 and Ti_3Al-Al_2O_3 composite powders by pressureless sintering, hot pressing and hot isostatic pressing techniques. The primary research objectives are:

- To define the effect of powder characteristics and process conditions on the sintering behaviour of alumina-aluminide composites produced by pressureless sintering
- To study the microstructure development and mechanical properties of dense alumina-aluminide composites fabricated by hot pressing of Al-TiO_2 powder blends.
- To establish the relationship between process conditions and microstructure during hot isostatic pressing

This thesis has seven chapters and an appendix. The first chapter covers this introduction and a literature review on the formation of alumina-aluminide alloys, the production, processing and consolidation of metal-ceramic *in-situ* composites and mechanical properties of metal-ceramic *in-situ* composites. Chapter Two describes the experimental methods used in this project. Chapters Three to Six are devoted to presenting and discussing the results. Chapter Three presents the findings of pressureless sintering and hot pressing of the Ti_3Al-Al_2O_3 composite powders produced by heat treating the Al-TiO_2 composite powders. Chapter Four demonstrates and discusses the results of a study on pressureless sintering of discus milled Al-TiO_2 composite powders. Chapter Five displays and examines the results of a study on hot pressing and sinter-HIP of Al and TiO_2 composite powders. Chapter Six presents and discusses the results of a study on the mechanical properties of the composites produced in this research. Finally, Chapter Seven summarises the conclusions and recommendations for future work. Appendix A contains XRD peak intensity measurements of the composites and method of obtaining the particle size of Al_2O_3 in the composites.

1.2 Solid State Reaction of Al and TiO_2

The solid state reactions between Al and TiO_2 have been studied widely over the past ten years. The reaction consists of the reduction of TiO_2 by Al in an inert atmosphere to form dense, interpenetrating composite of *metal* matrix and Al_2O_3. The *metal* phase can be a single phase metal matrix or an alloyed Al phase or an intermetallic phase based on Al. Aluminium cannot reduce TiO_2 to pure Ti[6, 7]. Rather, the formation of different titanium alloy or titanium aluminides-Al_2O_3

composites is possible through the use of different initial Al-TiO_2 mole ratios. Titanium aluminide phases such as $TiAl_3$, TiAl or Ti_3Al are formed. Further, Ying et al reported additional phases such as α-Ti(Al,O), $Ti_3Al(O)$ and/or TiAl(O) in which a solid solution of oxygen and aluminium in a Ti matrix is formed[7].

Factors such as starting compositions and particle sizes affect the reaction temperatures and final product phase structure and microstructure. The reaction between Al and TiO_2 can be enhanced by reducing the starting powder particle size or the microstructure scale of the Al-TiO_2 composite powder by milling techniques such as ball milling and discus milling, which increase the Al-TiO_2 interfacial area. Welham et al. described that by heating a powder mixture that had been ball milled for 100 hours under vacuum, $TiAl_3$ and Al_2O_3 phases were formed at a lower temperature compared to the unmilled powder mixture[8].

On the other hand, by adjusting the starting powder composition, it is possible to vary the final composition of 3A materials over a wide compositional and ceramic volume fraction range. At ceramic volume fractions of more than 20%, both phases are continuous and hence exhibit an interpenetrating network[9, 10].

Thermodynamically, Al will react with TiO_2 as follows[2, 11, 3]:

$$\mathbf{13Al + 3TiO_2 \rightarrow 3TiAl_3 + 2Al_2O_3} \qquad \textbf{Equation 1.1}$$

$$\mathbf{7Al + 3TiO_2 \rightarrow 3TiAl + 2Al_2O_3} \qquad \textbf{Equation 1.2}$$

$$\mathbf{5Al + 3TiO_2 \rightarrow Ti_3Al + 2Al_2O_3} \qquad \textbf{Equation 1.3}$$

It has been found that Al and TiO_2 react in the temperature range from 500-800°C to form $TiAl_3$. Al_2O_3 does not form below 772°C. A potential reason for the temperature/time gap between the formation of $TiAl_3$ and Al_2O_3 is that nucleation of Al_2O_3 is difficult because of the high melting point of Al_2O_3 (>2300°C) while nucleation of $TiAl_3$ is easier because of its relative low melting point (~1220°C)[12]. Regardless of the initial composition, $TiAl_3$ is the first intermetallic phase formed. A summary of the major phases formed at different temperature reported by different authors is presented in Table 1.1.

Table 1.1: Major phases formed from the reactions between Al and TiO_2 at different temperatures

Temperature (°C)	Phase/Reaction	Reference
500	*No reaction*	[8, 3, 7, 13]
660	*Al melting*	[11, 8]
500-650	*Formation of $TiAl_3$*	[3]
500-700	"	[13]
600	"	[14] [10] (milled powder)
650	"	[13]
700	"	[7]
750	"	[11]
~772	"	[2]
800	"	[11] [8] (unmilled powder)
700-1000	*Formation of Ti_3Al, TiAl*	[3] (high Al)
1000	*Formation of Ti_3Al*	[13]
650-700	*Formation of TiAl*	[3] (low Al)
~588		[2]
600-700	*Formation of γ-Al_2O_3*	[13]
750		[11]
1000		[3] (low Al)
~772		[2]
800		[11] [8] (unmilled & milled powder)
900	*Formation of α-Al_2O_3*	[7]
700-1000		[3] (high Al)
1000		[7]
1000-1500		[3] (low Al)

In a DTA curve obtained by thermal analysis of the Al-TiO_2 composite powder, an endothermic peak is expected at about 660°C due to Al melting. Exothermic peaks are seen at temperatures in the range of 500-1500°C, reflecting the formation of $TiAl_3$, TiAl, Ti_3Al, γ-Al_2O_3 and/or α-Al_2O_3 according to the following sets of equations:

SET 1:	$2Al + 3TiO_2 \rightarrow 3TiO + \gamma\text{-}Al_2O_3$	**Equation 1.4**
	$2Al + 3TiO \rightarrow 3Ti + \alpha\text{-}Al_2O_3$	**Equation 1.5**
	$3Al + Ti \rightarrow TiAl_3$	**Equation 1.6**
SET 2:	$4Al + 3TiO_2 \rightarrow 3Ti + 2\alpha\text{-}Al_2O_3$	**Equation 1.7**
	$3Al + Ti \rightarrow TiAl_3$	**Equation 1.8**
SET 3:	$2Al + 3TiO_2 \rightarrow \gamma\text{-}Al_2O_3 + 3TiO$	**Equation 1.9**
	$11Al + 3TiO \rightarrow 3Al_3Ti + \alpha\text{-}Al_2O_3$	**Equation 1.10**

It is assumed that the reduction of TiO_2 according to Equation 1.5 or Equation 1.7 is a necessary prerequisite for aluminide formation. TiO is a transitional phase which does not exist after heating at 800°C. γ-Al_2O_3 is not stable when heated. Hence, only α-Al_2O_3 is detected in heated composite powders.

1.3 Production of Metal-Ceramic Composites

Advanced ceramic materials have attracted considerable attention in modern industrial technologies because of their outstanding physical and mechanical properties. Alumina is one of the most widely used ceramic materials because of its excellent physical and thermomechanical properties. Like most other ceramics, the applications of advanced ceramics have been limited due to manufacturing complexities, poor machinability, low fracture toughness and poor response to thermal and mechanical shock.

On the other hand titanium metal and titanium alloys are attractive materials of choice in applications requiring corrosion resistance, a high strength to weight ratio, a low rate of thermal expansion and good elevated temperature properties. There are, however, drawbacks with the final stage of manufacturing. Machining of wrought, rolled or forged titanium bars and billets remains the major method of fabrication of custom components, leading to high machining costs and expensive materials waste.

The drivers to develop net shape technologies include (1) cost-effective production of high performance parts while yielding an enhanced mechanical

property characteristics and (2) minimisation of waste, which reduces or eliminates the cost of machining. High wear resistance is achieved from metal-ceramic composites microstructures because of the high hardness and high wear resistance of the ceramic component of the composite whereas the metallic portion increases the fracture toughness through crack bridging, which improves its strength and resistance to thermal shock and impact damage.

There are a number of processing routes for metal-ceramic composites. Some are important at a laboratory scale while others, such as the production of powder metallurgy parts, are widely used in a variety of industries including computers, automobile, household appliances and the aerospace industry. The remainder of this section is devoted to a review of powder processing methods and design restrictions.

Although the solid-state reactions of the 3A process have been known for some time, successful pressureless densification of homogeneous microstructures has not previously been achieved. The lack of success is the result of differences in the molar volumes of the reactants and reaction products, porosity of the green compact, and/or evolution of gases adsorbed on the reactant powders. In the 3A process, however, the intense mechanical milling of powders and high powder compaction pressures allow complete and homogeneous densification of a number of materials over a wide range of ceramic volume fractions from 20% to more than 90%[15, 10]. The advantage of this wide range is that the properties of the composites can be tailored to suit the desired application. For 3A systems with low reaction enthalpies, such as the Al-TiO_2 system (ΔH = -258.6kJ/mol)[16], the exothermic nature of these reactions can be controlled by utilising slow heating rates between 400 to 700°C. However, for 3A systems with high reaction enthalpies, the reaction cannot be controlled by adjustment of the heating rate alone. For such systems, it is usually necessary to reduce the concentration of one of the reactants by diluting the starting powder mixture with a product phase (e.g. Al_2O_3), which can act as thermal ballast. Controlling the reaction rate is also believed to help in controlling the microstructure and properties of the final products[16].

Metal/intermetallic-containing Al_2O_3 composites with interpenetrating networks have been fabricated by various techniques such as pressureless sintering[9, 17, 10, 16, 13, 18, 14], reaction squeeze-casting[11, 19], pressure assisted thermal explosion[20, 21], reactive infiltration[22-27], pressure infiltration[28, 29], hot pressing[30, 31] and directed metal oxidation[32, 33].

Other ceramic-metal/intermetallic composite processing systems have been widely studied, some using similar techniques such as pressureless sintering[34], reactive infiltration[35, 26] and hot pressing[36, 34]. Others have used techniques such as spark plasma sintering[37], gas pressure isostatic pressing[38] and a mechanical alloying-thermohydrogen processing approach[39]. The composites fabricated include Ni_3Al and FeAl with WC, TiC and TiB_2; nanocrystalline TiAl reinforced with nanometer size particles of Ti_5Si_3; sintered AlN infiltrated with Al metal; TiC-Ni_3Al cermets with Ni_3Al binder; ZrO_2-W composites and TiAl/Ti_2AlC composites.

The development and improvement of these processing techniques is focussed towards the production of near net-shape components with favourable microstructures and properties while minimising expensive materials waste and reducing or eliminating the cost of machining.

1.3.1 Reaction Squeeze Casting

Squeeze casting, also know as liquid metal forging, is a combination of casting and forging processes. In the squeeze casting process, molten metal is poured into the bottom half of a pre-heated die. As the metal starts to solidify, the upper half closes the die and applies pressure during the solidification process. The pressure applied is significantly less than that used in conventional forging and parts of great detail can be produced. The porosity is low and the mechanical properties are improved. One example is the reaction squeeze casting of aluminium into particulate TiO_2 preforms to form composites of TiAl intermetallic reinforced with alumina[11].

Squeeze casting is suitable for high strength, high ductility, and light weight structural aluminium casting needed for advanced components. A major market is the automotive market, which is increasingly demanding lightweight components

to improve fuel efficiency. Squeeze casting is a relatively new and developing casting process; therefore much work needs to be done to better understand its fundamentals of the process. In particular, the relationships between the design, the processing parameters and the integrity of the squeeze cast parts are not well understood. In the absence of well established guidelines, the industrial uptake of this process has been slow.

1.3.2 Infiltration

In the melt infiltration process, a liquid is infiltrated into a porous ceramic body. The melt infiltration technique can be divided into reactive, non-reactive, pressure and pressureless processes.

In reactive infiltration process, the molten metal fills the open spaces in the ceramic preform and reaction takes place between the preform and the molten metal. Composites with interconnected Al_2O_3 and $TiAl_3$ networks have been fabricated by reactive infiltration of Al into porous Al_2O_3/TiO_2[22]

Pressure infiltration is a process where gas pressure forces a metallic melt to penetrate into a porous preform while it is immersed in a molten metal bath. The bond between the components is created by controlled chemical reactions at the component interfaces. A number of composites have been fabricated by gas pressure infiltration including Al_2O_3-Al and Al_2O_3-Ni_3Al composites with interpenetrating networks. These have been formed to near net shape by gas pressure infiltration of Al_2O_3 bodies by molten Al or Ni_3Al[28, 29].

In non-reactive infiltration, the liquid phase simply fills the open spaces in the ceramic preform. The composite material can be made with desired dimensions, shapes and density. The amount of molten metal required can be determined from the volume of the open spaces in the ceramic preform. Near net shape components can be produced using this technique[6].

Metal-ceramic composites in the systems SiC/Al-bronze, AlN/Al-bronze, and AlN/cast iron have been prepared by a pressureless melt infiltration process[40]. Mechanical properties were determined and correlate well with the microstructure of the composites.

1.3.3 Combustion Synthesis

Combustion synthesis has received considerable attention in the last twenty years as an innovative method for the synthesis of advanced ceramic materials. Combustion synthesis, also known as Self-propagating high temperature synthesis[21] (SHS) or thermal explosion[20], offers a unique combination of technologically relevant characteristics. The method makes possible the rapid synthesis of several highly refractory materials, thus avoiding the prolonged high temperature treatment usually required by conventional processes. The reactants in the form of fine powders capable of undergoing highly exothermic reactions are usually dry mixed and cold pressed in order to obtain cylindrical pellets. These pellets are then placed in a controlled atmosphere and ignited through an electrical heated coil, a laser beam or an electric discharge. Due to the low energy requirement, short production cycle and simple production equipment, a significant cost reduction may be achieved. Dense Al_2O_3-TiAl-Ti_3Al composites have been fabricated by pressure assisted thermal explosion of Al and TiO_2 powder blends[20, 21]

1.3.4 Directed Metal Oxidation

Directed metal oxidation has been used to produce metal-ceramic composites. For example, Al_2O_3-Al composites have been formed by the directed metal oxidation of Al-Mg-Si and Al-Mg alloys[33]. The process can produce particulate and fibre reinforced composites with a wide range of compositions and microstructures. The directed metal oxidation involves oxidising a bulk molten metal with a gas to produce a solid ceramic body. Oxide growth is maintained by transporting additional metal through the reaction product. The composite composition is determined by the parent metal and the oxidising atmosphere chosen. The volume fractions of the ceramic phase, the microstructure, porosity level and the degree of interconnectivity of the metallic phase in the product can be controlled by varying processing temperature, atmosphere and time.

1.3.5 Spark Plasma Sintering

Spark Plasma Sintering (SPS) is a newly developed process which makes it possible to sinter some materials to full density in very short times. This is achieved by simultaneously hot pressing the sample while applying a pulsed DC

field and using a very fast heating rate (typically 200°C/min). The outcome can be a greatly enhanced consolidation rate achieved at a temperature several hundred degrees below conventional sintering temperatures. TiAl/Ti_2AlC composites have been produced by spark plasma sintering technology from mixed powders of Ti, Al and TiC[37].

1.4 High Energy Mechanical Milling

High energy mechanical milling is used in the production of metals and alloys, which is usually carried out in a dry condition under an inert atmosphere to prevent oxidation of powders. Process control agents are used to prevent excessive welding of powder particles to the discus or balls and the inner wall of the milling bowl and to achieve proper balance between cold welding and fracture in the case of milling ductile materials. High energy mechanical milling is characterised by repeated cold welding and fracturing of the powder. The extent of cold welding and fracturing is determined by the deformation behaviour of the powder and the temperature of milling. Thus the nature of the phase transitions during milling is a function of the temperature of milling. The milling effect depends largely on the energy transferred to the powder from the moving media during milling. The energy transfer is governed by many parameters such as the milling speed, type of material and size of milling balls or discus, milling medium/powder weight ratio and temperature of milling.

The most commonly used high energy mills[5] include attritor mills, tumbler mills, vibratory mills, planetary mills and discus mills. The energy transfer to the powder particles in these mills takes place by impacts between fast moving media such as balls, discus or rods or between the moving media and container wall. A number of methods have been used to mechanically mill powders having a range of compositions such as Al and TiO_2[8, 41]; Ti_3Al, TiAl and $TiAl_3$[42]; Ti, Al and SiC[43]; Ti, Al and Nb[44]; TiH_2, Al and Si[39]; CuO, Al, Ti and Fe[45]; Ti and Al[46]; CuO and Fe[47] or Al-Ti binary systems with Ti of 25at% or less[48]; prealloyed TiAl and NiAl[49] and PbO, La_2O_3, ZrO_2 and TiO_2[50].

The high energy milling device used in this project is the New Zealand developed Rocklabs "Split Discus" mill located at the University of Waikato, Hamilton. The

discus mill is constructed with a pair of hardened steel discus whose diameter can be varied from 100 to 200mm, which are vibrated in a hardened steel bowl causing shearing and impacting. The current model of discus mill has a capacity of handling powder of 100-1000 grams of powder.

The mechanical milling process is characterised by repeated plastic deformation, fracturing and cold welding of powder particles trapped between the colliding balls during milling. The extent of these individual processes depends mainly on the mechanical behaviour of the powders being milled. Hence, the powder components are usually classified as (i) ductile/ductile, (ii) ductile/brittle or (iii) brittle/brittle systems.

(i) The microstructural evolution of ductile powder particles during mechanical milling is schematically shown in Figure 1.1. In the initial stage of mechanical milling, equiaxed ductile particles are flattened and forged resulting in plate-like particles. The second stage is the period of welding predominance. A multilayered composite structure is formed in the coarser particles, while the finer particles remain elemental with flake-like shapes. The third stage is the period of equiaxed particle formation. The particle size decreases because of further fracturing. The fourth stage is characterised by cold welding in random directions leading to formation of a number of lamellar colonies of random orientation within each composite powder particle. In the fifth stage, a balance is achieved between the welding and fracturing of the particles and thus, the average particle size remains constant. However, the composite microstructure becomes finer and finer with extended milling and eventually the lamellae become unresolvable under an optical microscope.

(ii) In the ductile/brittle system, ductile particles such as Ni or Al are flattened and welded to each other during milling, while the brittle phase such as oxide particles is fragmented and embedded in the layers of the ductile phase. As milling proceeds, the layers of the ductile phase come closer and ultimately become unresolvable, while the brittle phase is uniformly distributed as fine particles in the matrix of the ductile phase.

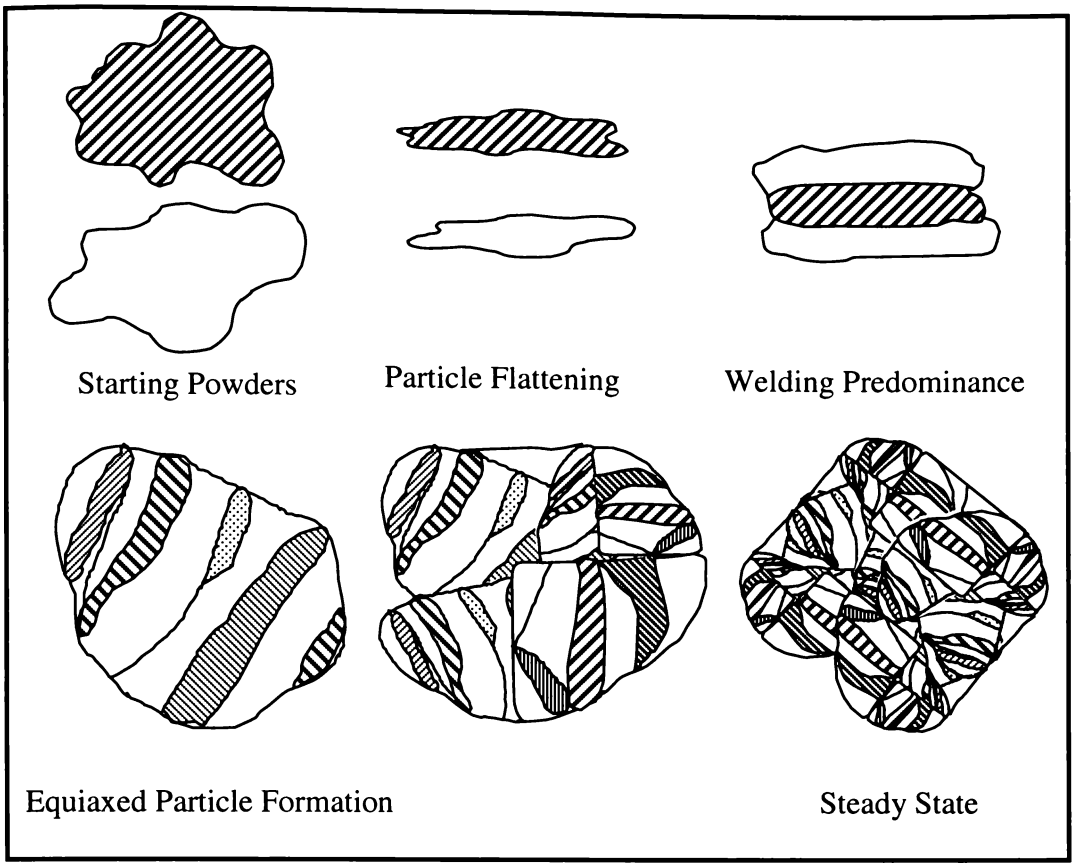

Figure 1.1: Five stages of microstructural evolution [51]

(iii) The microstructural evolution in brittle/brittle system differs markedly from that described previously for ductile systems. In this system, interparticle neckings are observed. The mechanically milled powders do not consist of homogeneous particles but are composed of smaller particles cold welded together[52].

1.5 Consolidation of Metal-Ceramic Composite Powders

The production of ceramic, metal, or metal-ceramic parts is achieved by pressureless sintering[53-66], hot pressing[67-69, 54, 70, 71, 57] or hot isostatic pressing[72, 71, 61, 73] green bodies, which have been previously compacted by die pressing[74, 54, 75], cold isostatic pressing or by a combination of die and cold isostatic pressing[76, 72, 26]. Die pressing contributes to net-shape processing and is a relative fast operation whereas cold isostatic pressing can produce parts with more uniform density distributions[77].

1.5.1 Pressureless Sintering

Some examples of intermetallic-reinforced Al_2O_3 composites have been produced by reaction sintering compacts of intensively milled powder mixtures of Al with TiO_2, Nb_2O_5, ZrO_2 or Fe_2O_3[9, 16, 14]. For the metals route, Al, Ni, Ti, Fe, Nb or Ta powder were blended with Al_2O_3 powder and for the oxides route, Al was blended with the respective transition-metal oxide, which were all subjected to vacuum pressureless sintering to form the intermetallic-Al_2O_3 composites[17, 13, 18].

Most aluminides have the advantage of being in thermodynamic equilibrium with Al_2O_3, leading to thermally stable interfaces even at elevated temperature. Aluminides, especially trialuminides, offer an outstanding oxidation resistance. However, trialuminides possess a relatively low melting point that limits the technical application temperature. In addition, aluminium-rich intermetallics are mostly brittle at room temperature[10].

The principal issue with pressureless sintering is the need to use rather high temperatures to achieve the formation of dense bodies, which inevitably creates other problems such as grain coarsening that lead to poor resulting properties. Up to now there is no complete understanding of the material behaviour and the principles of materials selection for use in different conditions. The lack of design criteria and understanding for the application of metal-ceramic poses a significant barrier to wider application of metal-ceramic composites.

1.5.2 Hot Pressing

Hot pressing is the consolidation of loosely packed powder or a pre-compacted green body by the simultaneous application of heat and pressure. The application of pressure at high temperatures can assist the sintering of ceramic powders to achieve dense compacts. The application of the pressure may allow the sintering temperature to be lowered by up to 500°C[78]. The simplest form of hot pressing consists of a furnace and a uniaxial compression of a piston in a powder-containing die. Graphite dies are usually preferred due to their low cost, ease of machining, low expansion coefficient and excellent creep resistance at high temperatures.

Hot pressing is widely used in practice to produce high quality structural ceramics[67, 68, 70, 79, 80]. It is used when the deformation characteristics of the base powder require high temperatures to achieve plastic flow and adequate consolidation. It allows dense solid ceramic materials to be produced with minimum contamination. The advantage of hot pressing is the improvement in the densification kinetics of the ceramic powder. That is, the densification and operational temperatures are much more desirable than those used for pressureless sintering. In addition, phase transformations can be controlled using hot pressing by controlling grain growth and suppressing pore formation at much lower temperatures[55]. The suppression of grain growth is seen for the development of alumina-metal nanocomposites to improve fracture strength and fracture toughness simultaneously by combining the "nanocomposite effect" with the ductility of the metallic phase[81].

Metal-ceramic composites have been widely fabricated using hot pressing[36, 82-90]. Recent examples of metal/intermetallic-Al_2O_3 composites are powders of NiAl and NiO, which were blended and processed by vacuum hot pressing to form a NiAl- Al_2O_3 composite[30] and Al-based composites reinforced with in situ Al_3Ti plate and Al_2O_3 particle have been prepared by reactive hot pressing method from Al/TiO_2 and Al/TiO_2/B systems[31]

The main disadvantages of graphite are its high reactivity with ceramic powders or compacted bodies and the need to perform pressing operations in a controlled atmosphere. However, the former can be managed by supporting a compacted body in a boron nitride powder bed. The latter is an additional limitation to the disadvantage of these composites produced by complex high cost hot pressing technique, which often cannot be used where near-net shaping is required. Other drawbacks are its limitation of the shape versatility and the die wall friction, which causes non-uniform density distribution in the final product during hot pressing[80]. Also, hot pressing above the melting point of the metal/intermetallic phase should be avoided to reduce the possibility of segregation of the metal/intermetallic phase causing inhomogeneous microstructure. Tiegs reported that hot pressing of Ni_3Al/Al_2O_3 composites above the melting point of Ni_3Al resulted in Ni_3Al being exuded from the composite[36].

1.5.3 Hot Isostatic Pressing (HIP)/Sinter-HIP

Hot isostatic pressing (HIP) is a well established technique for consolidating metal powders to full density[91]. It is a process in which a starting powder or a pre-moulded part is simultaneously subjected to both high temperatures and high isostatic pressures, using an inert gas transfer medium in a specially constructed pressure vessel[92]. The temperature, pressure and process time are all controlled to achieve the optimum material properties. There are two common techniques for producing high density parts using HIP[93]. First technique is the usage of HIP on green bodies of 50-80% theoretical density sealed in a container. For example (i) canning of powder samples in 304 stainless steel tubes under argon atmosphere, which was then sealed by tungsten arc welding[73]; (ii) powders were cold isostatically pressed and introduced inside a silica container and sealed[71] and (iii) near-net-shape integrated turbine wheels were produced using injection moulding and flexible glass powder encapsulation[94]. The second technique is to produce sintered parts of more than 95% theoretical density without open porosity using conventional sintering, followed by HIP, which is known as sinter-HIP. The former technique is costly and the canning process is difficult to manage. The latter technique is preferable, for example, the sinter-HIP of nanoscale pure alumina powders to obtain specimens with sub-micron microstructures has generally improved their mechanical properties and has attracted much attention[95].

The consolidation of powders via HIP in some cases can produce cost-effective, high quality and high performance components[91, 96]. HIP is an enabling technology providing a most efficient method for the densification of ceramic powders and also, allows production of net-shape ceramics with superior and consistent properties. A further variation is solid-solid, solid-powder or powder-powder joining of ceramics to ceramics or metals[97]. Due to its low production rate, high capital cost and unique tool requirements, the HIP process is normally used to produce high value materials such as tool steels, superalloys and titanium equipment[98].

The essential pre-requisite of successful sinter-HIP is ≥95% theoretical density of the pre-sintered composites before hot isostatic pressing[99]. Therefore in order to

achieve ≥95% of pre-sintered composites, the starting powder mixtures should be reactive and fine grained (~1μm)[14], which add to the need for better understanding of the application of sinter-HIP. Although metal-ceramic composites are promising materials for the chemical and process industries, not much work has been done on fabricating these composites using sinter-HIP techniques. The influence of the metal-ceramic interface, the binder volume fraction and temperature cycle on the microstructure and mechanical properties of these composites need to be investigated[100, 101, 99].

1.6 Mechanical Properties of Metal-Ceramic Composites

1.6.1 Deformation Behaviour

When a load is applied to a metal, it deforms elastically and plastically as the load increases. Ceramics deform elastically and then fracture at a limit of their tolerance. Ceramic-metal composites exhibit elastic and plastic deformation because of their metal content. On the other hand, the strength of these composites increases due to the ceramic reinforcement. Typical stress-strain curves of metal, ceramic and ceramic-metal composites are shown in Figure 1.2.

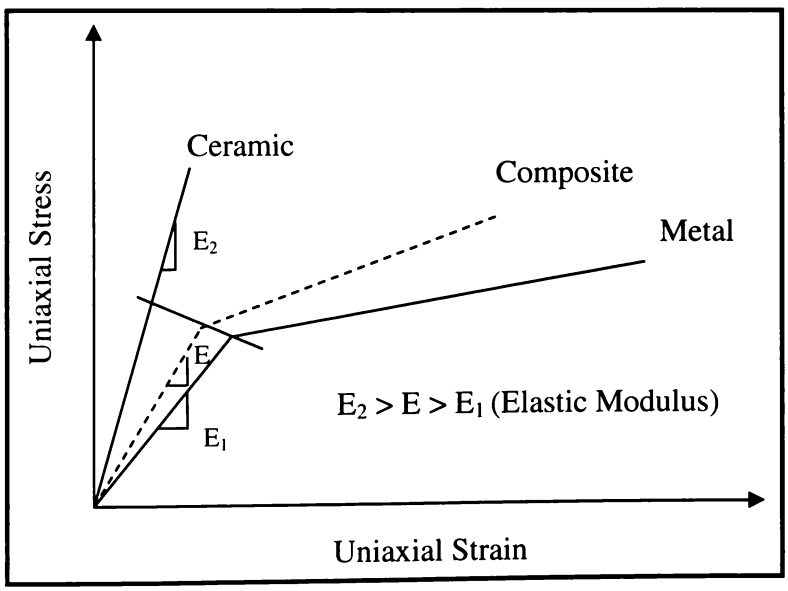

Figure 1.2: Uniaxial stress-strain curve of a ceramic-metal composite[102, 80]

As an example showing the deformation behaviour of metal-ceramic composite, Brown et al.[103] reported that dense bodies of ceramic-metal composites based on

the Fe-TiC system can be synthesised where stress-strain curves obtained by tensile testing of these composites showed ductile behaviour as shown in Figure 1.3. In particular, Brown described that the spheroidal graphite (SG) iron alloy-TiC composite displayed considerable ductility. In comparison, the Ni-hard alloy-TiC composite displayed considerably less ductility. Nevertheless the Ni-hard body does not display completely brittle failure such as might be expected in a ceramic body.

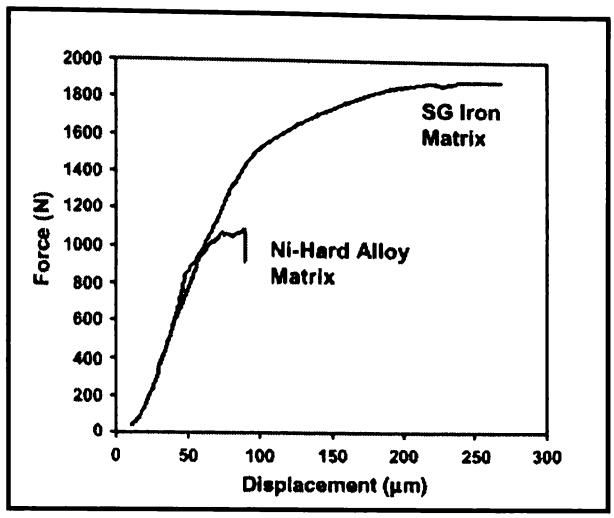

Figure 1.3: Stress-strain curves of Fe-TiC alloy cermets[103]

1.6.2 Fracture Behaviour

The toughening mechanisms in composites can be basically divided into two categories. One is dependent on the crack deflection induced by heterogeneous microstructures including needle-like grains, particles, platelets and whiskers. The other is dependent on the crack shielding effect induced by the crack bridging, phase transformation or microcracking that occurs during fracturing[104-108].

The results presented by Konopka et al.[109] show that the change of fracture toughness of a ceramic-metal composite can be controlled by the volume fraction of metallic phase and size of metal particles. These are supported by the studies reported by (1) Hillig et al.[110], who stated that brittle ceramic matrix composites were toughened by the incorporation of ductile phases, which bridge across a matrix crack in Al-Al_2O_3 systems and by (2) Lu et al.[111], who reported that the

toughening mechanism was closely related to the microstructural refinement of the nano-cermets in Ni-Al_2O_3 systems.

It is also evident that the metal particle distribution in the matrix will influence the crack propagation. Given a defined volume fraction of metal particles in the matrix and the size of these particles, a different level of uniformity of their distribution will result in a different number of metal particles encountered by the propagating crack. Thus, the crack may propagate through areas with no particles as well as zones with high metal particle concentration.

Konopka et al.[109] proposed four possible mechanisms of interactions between the crack and a spherical particle of metal as shown in Figure 1.4. The mechanisms are (note that mechanisms 2 and 3 should produce the same outcome):

(1) The crack passes through the particle, the crack length is a minimum and equal to 2r (Figure 1.4A);
(2) The crack deflects on either side of the particle, the crack length increases by πr (Figure 1.4B);
(3) The crack moves around the metal particle along the particle/matrix interface, the crack length is equal to πr (Figure 1.4C) and
(4) The crack surrounds the metal particle and the crack length is equal to $2\pi r$ (Figure 1.4D)

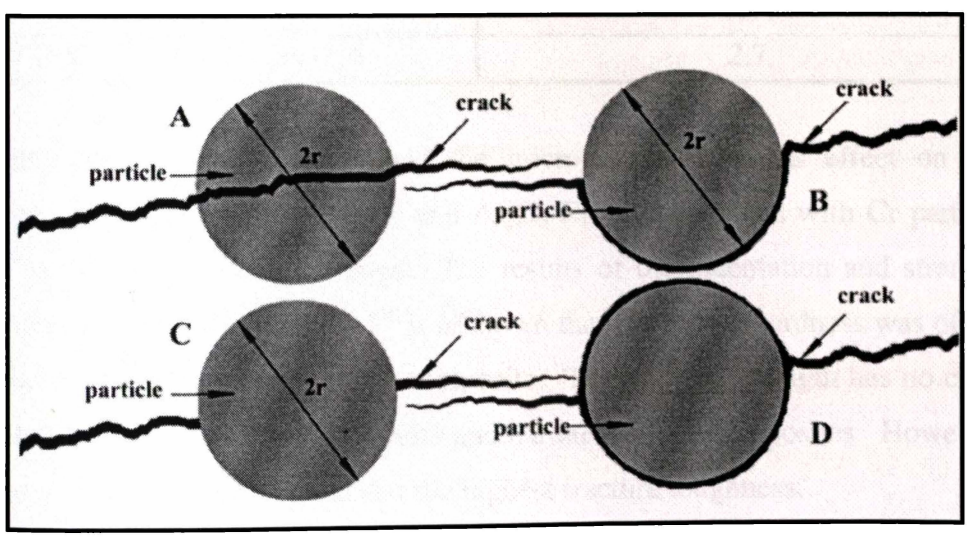

Figure 1.4: Schematic of the mechanisms of interactions between the crack and spherical particle[109]

Agrawal et al.[112] reported that high tensile stresses in the Cu phase and at the Cu-Al_2O_3 interfaces lead to crack propagation through the Cu phase and at the metal-ceramic interface. On the other hand, the crack propagated through the ceramic phase for the Al-Al_2O_3 composite.

For PSZ-inconel alloy composites, Kawasaki et al.[113] reported that the crack propagates through the PSZ matrix or along interfaces between the PSZ matrix and the metal particles. In a finely dispersed microstructure, the fracture toughness increases with increasing the metal phase content because of the high possibility of crack bridging in the metal particles. On the contrary, in bodies having a coarse microstructure, a crack propagates through the PSZ matrix with comparative ease and the connectivity of metal particles is lower, resulting in fewer arresting cracks. In this latter case, there is less improvement in fracture toughness despite the increase in metal phase content. The fracture toughness of the composites densified by hot isostatic pressing (refer Section 1.5.3.1) is displayed in Table 1.2.

Table 1.2: Fracture toughness determined by indentation fracture method at 196N [113]

Materials	$MPa.m^{1/2}$
Monolithic PSZ	5.0
PSZ/25vol.%IN100	5.4
PSZ/50vol.%IN100	11.4
PSZ/50vol.% Inconel718	2.7

A study by Ji et al.[114] examined the microstructure and its effect on the mechanical properties of Al_2O_3-Cr and Al_2O_3-Cr/Ni composites with Cr particle sizes in the micrometer size range. The results of the indentation and strength tests are summarised in Table 1.3. It is shown that the higher hardness was offset by lower fracture toughness of the composite. The bending strength has no clear correlation with the fracture toughness and hardness of the composites. However, the hot pressed composite produced the highest fracture toughness.

The mechanical properties of some conventional cutting tool materials are presented in Table 1.4 to act as a basis reference for comparison with the systems reported and studied in this thesis.

Table 1.3: Mechanical properties of monolithic Al_2O_3 and the composites[114]

Specimen	Relative Density (%)	Hardness (GPa)	Indentation Fracture Toughness ($MPa.m^{1/2}$)	Strength (MPa)
Sintered Al_2O_3	97.5	16.3±0.4	3.2±0.2	320±25
Sintered Al_2O_3-Cr	98.9	13.0±1.1	5.0±0.7	181±8
Sintered Al_2O_3-Cr	94.2	12.7±0.6	6.2±0.8	264±27
HP Al_2O_3	98.2	17.5±0.8	3.4±0.2	476±17
HP Al_2O_3-Cr	98.6	12.0±0.8	7.1±1.1	440±30
HP Al_2O_3-80Cr/20Ni	99.1	12.7±0.4	6.6±0.7	353±38
HP Al_2O_3-20Cr/80Ni	99.1	11.9±0.2	6.8±0.6	418±11

*HP-Hot pressed

Table 1.4: A comparison of mechanical properties of some conventional cutting tool materials[115]

Material	Hardness (GPa)	Fracture Toughness ($MPa.m^{1/2}$)
Microcrystalline		
WC-Co	16-18	14-16
Al_2O_3-TiC	19	4.0
Si_3N_4 (hot pressed)	16-20	5.0
Nanocrystalline		
WC-Co	22-23	-
Al_2O_3-Fe	14.9	6.7
Al_2O_3-diamond	25-30	3.5
Al_2O_3-Nb	20-23	>8

1.6.3 Effect of Ceramic Volume Fraction

The basic strengthening mechanisms of metal-ceramic composites are continuing micromechanism and the movement of dislocations[6]. There are several popular micromechanism models including the rule of mixtures, which considers that the contribution to the overall properties of the composite made by each phase in the composite is proportional to the volume fraction of the corresponding phase. The volume fraction of ductile metal/brittle ceramic in the composites should affect the mechanical properties of the composites such as fracture toughness, Vickers hardness and strength. In particular, ductile metal phases lead to enhanced fracture toughness whereas brittle ceramic phases lead to improved Vickers hardness of the composites.

This is seen in the study by Liu et al. [116] where nano-TiN modified TiC-based cermets with varying metal binder and molybdenum content were fabricated. The microstructures of the carbides and binder phases were shown to be critical to the mechanical behaviour of the nano-TiN modified TiC-based cermets. In addition, the fracture toughness was increased with an increase of the metal binder phase.

In another study by Hussainova[117], WC-, TiC- and Cr_3C_2-based ceramic-metal composites were fabricated through conventional press and sinter powder metallurgy technology. An overview of the composition and mechanical characteristics of the composites is presented in Table 1.5. The fracture toughness of the composites tested had porosity of 0.1-0.2 vol.% with the exception of chromium carbide-based bodies of about 0.5 vol.% porosity. In general, when the composite exhibits a lower Vickers hardness, the composite has a higher fracture toughness or vice versa.

Table 1.5: Composition and mechanical properties of composites tested [117]

Carbide (wt.%)	Composition of the Metal Phase	Vickers Hardness, GPa	Fracture Toughness ($MPa.m^{1/5}$)
92WC	Co	13.2	13.0
80WC	Co	10.1	19.0
80TiC	Austenite steel	14.1	14.0
75TiC	Austenite steel	12.9	15.0
60TiC	Austenite steel	10.4	15.5
60TiC	Martensite steel	12.6	13.2
80TiC	Ni(Mo)	13.5	11.5
60TiC	Ni 8wt.%Mo	9.7	18.5
60TiC	Ni 14wt.%Mo	11.7	18.2
$85Cr_3C_2$	Ni	13.8	9.8
$70Cr_3C_2$	Ni	9.6	18.3
$90Cr_3C_2$	Ni	14.5	9.5

The fracture toughness and microhardness of the composites of ductile Ni_3Al alloys with both non-oxide (WC, TiC) and oxide (Al_2O_3) ceramic powders produced by hot pressing in graphite dies is shown in Table 1.6. Following the data of Tiegs et al[36], the Ni_3Al alloys and the non-oxide ceramic powders form a semi-continuous intergranular phase. Table 1.6 shows the inverse relationship between the microhardness and the fracture toughness for the WC-Ni_3Al system.

It also displays the impact of hard TiC in the Al_2O_3-Ni_3Al system, which raised the microhardness of the overall composites.

Table 1.6: Summary of mechanical properties of Ni_3Al-bonded ceramic composites[36]

Composition (vol.%)	Microhardness (GPa)	Fracture Toughness ($MPa.m^{1/2}$)
WC-17Ni_3Al	14-18	10-19
WC-68Ni_3Al	7	25
TiC-17Ni_3Al	16-20	8-10
Al_2O_3-25TiC-10Ni_3Al	18	7-8
Al_2O_3-10Ni_3Al	14	7-8

1.6.4 Effect of metal-ceramic interface

The use of ceramics in high stress applications requires a substantial increase in their fracture toughness, which may be achieved in the form of metal-ceramic composites as described in more detail in the preceding sections. The mechanical properties of such metal-ceramic microstructures are strongly influenced by the strength of the metal-ceramic interfaces, which is controlled by their structure and chemistry[118-121].

The interfacial reactions is clearly observed in the study of Al_2O_3 and Fe composites reported by Konopka et al.[122] where iron aluminate spinel formation occurs at temperatures above 1000°C. During the formation of spinel, Fe is consumed, which leads to a decrease of the ductile metal phase in the composite. Mechanical properties such as the fracture toughness, which depend on the metal content, inevitably were affected.

In research on functionally gradient materials, the challenge is to control the interfacial bonding between the metal and ceramic. Zhang et al[123] have shown that Ni_3Al has good creep resistance and high strength at elevated temperature and TiC has good bondability and wettability with Ni_3Al.

A study by Hussainova[117] proposed that improvement in wear resistance is mainly due to the increase in interphase bond strength, which acts as a stress concentrator for the propagation of cracks, which might otherwise result in the removal of ceramic particles from the composite matrix. Strong interfacial

bonding between constituent phases will prevent eruption and loss of hard particles during erosion. Multiphase materials analysed in this study were WC-, TiC- and Cr_3C_2 based ceramic-metal composites. Hussainova concluded that (1) High volume fractions of carbides limits the plastic deformation that binder metal can accommodate, which leads to more intensive carbide fracture, matrix-grain debonding and hard grain fragmentation and (2) Intergranular crack propagation indicates relatively weak interphase bonding depends on microstructure and microprocesses such as thermal expansion between the grain and matrix, internal mechanical stresses created during application, the migration of impurities to interfaces and so on.

Saiz et al.[124] reported that the interfacial strength of Al/α-Al_2O_3 increases with increasing sintering temperature. The weak interfacial strength displayed in the lower temperature range can be attributed to the presence of an oxide skin (amorphous alumina) on the aluminium. As the temperature approaches the melting point of aluminium, the oxide skin breaks and aluminium and alumina can form a direct interface with high strength. The highest strength of 400MPa was obtained.

Dense homogeneous mullite/Mo composites have been fabricated at 1650°C in vacuum by Bartolome et al[125]. Good interfacial bonding between the brittle matrix and the ductile phase lead to extensive plastic deformation of the ductile phase and therefore contributed to the toughening of the composites. The bending strengths, fracture toughness and hardness of the composites are shown in Table 1.7.

Sbaizero et al[126] prepared bodies with increasing proportions (10, 15, 20 and 30vol.%) of Mo powder with AlN powder were uniaxially pressed followed by cold isostatic pressing at 100MPa. Hot pressing was then performed in a graphite die at 30MPa and 1700°C. It was found that two stresses affected the composites toughness: (i) compressive residual stresses in the AlN matrix slightly enhanced the crack initiation of the composite, (ii) tensile residual stresses weakened the metal/ceramic interface, leading to an embrittlement of the composite.

Table 1.7: Mechanical properties of mullite/molybdenum composites[125]

Material	Bending Strength (MPa)	Fracture Toughness ($MPa.m^{1/2}$)	Hardness (GPa)
40mullite/60Mo (Mo – 1.4μm) - sintered	440±20	4.3±0.3	7.4
40mullite/60Mo (Mo – 3μm) - sintered	370±15	5±0.4	7.7
40mullite/60Mo (Mo – 3μm) - hot pressed	530±25	6.7±0.5	7.3
Mullite	320±15	1.9±0.2	11

The identity of the ceramic reinforcement influences the interface bond between the metal and the ceramic phase. Wettability between the metal matrix and ceramic reinforcement, and the interface chemical reactions play a key role in the nature of the interface layer. High wettability and reactivity may have a detrimental effect on the interface bond because they may cause the formation of brittle third phases that reduce the mechanical properties[101]. On the other hand, poor wetting behaviour results in weak interfacial bonding with the same outcome. However, ceramic particles with low solubility and reactivity are more suitable for reinforcing metal matrix composites because the possibility of brittle phase formation between matrix and reinforcement is reduced. In addition, any particle coarsening due to diffusion can be avoided. In general, the reactivities of the metal and the ceramic govern the possible reactions between the two phases. For example, for a combination of a very reactive metal, Ti and a relatively stable ceramic, Al_2O_3, previous studies demonstrated that interfacial reactions can yield a variety of products at the interface such as intermetallic compounds, new oxides or solid solutions, depending on the oxygen activity and temperature used in the processing[21, 118, 127, 128]. Formation of titanium oxide(s) is one of the complications due to the presence of oxygen. This reaction has an important bearing on the microstructure, properties and performance of the composite systems described in this thesis. It is generally accepted that the metal-ceramic interface affects the composite properties such as strength and K_{IC}, despite a substantial number of papers where the reaction in the Ti-Al-O system have been

studied[118, 129, 120, 130-133], the issue of chemical stability of Al_2O_3-Ti aluminide interfaces still remains controversial[20].

1.6.5 Effect of Sintering Temperature

The mechanical properties of composites are always enhanced with increasing sintering temperature due to the densification of the composites provided that the undesirable grain growth can be suppressed, for example, with the addition of sintering aids or the use of pressure-assisted sintering. This is seen with the addition of molybdenum that controlled the TiC grain growth and caused a decrease in the fracture toughness of the nano-TiN modified TiC-based cermets[116].

Work by Peng et al[1] has shown that the fracture toughness of Si_3N_4-Al based composites was enhanced with increasing sintering temperature above 1650°C as shown in Figure 1.5.

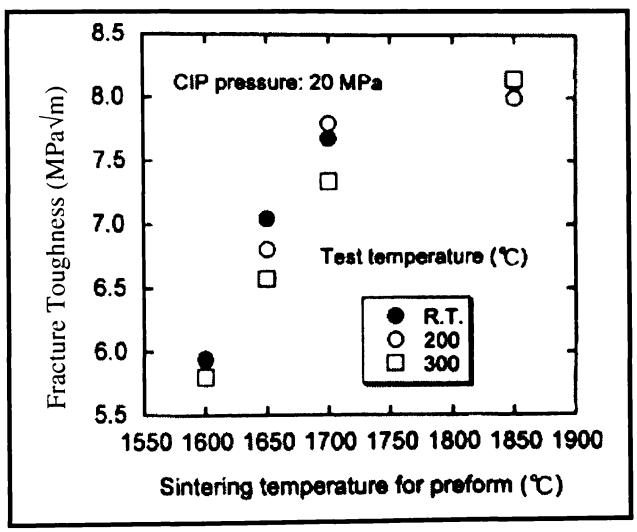

Figure 1.5: Fracture toughness of Si_3N_4-Al-Cu-Si versus sintering temperature[1]

REFERENCES

1. Peng, L.M., J.W. Cao, K. Noda and K.S. Han, *Mechanical properties of ceramic-metal composites by pressure infiltration of metal into porous ceramics.* Materials Science and Engineering A, 2004. **374**: p. 1-9.
2. Feng, C.F. and L. Froyen, *Formation of Al_3Ti and Al_2O_3 from an Al-TiO_2 system for preparing in-situ aluminium matrix composites.* Composite Part A: Applied Science and Manufacturing, 2000. **31**: p. 385-390.
3. Gaus, S.P., M.P. Harmer, H.M. Chan, H.S. Caram and N. Claussen, *Alumina-aluminide alloys (3A) technology: II, Modeling of Ti_xAl_y-Al_2O_3 composite formation.* Journal of the American Ceramic Society, 2000. **83**(7): p. 1606-1612.
4. Gaus, S.P., M.P. Harmer, H.M. Chan, H.S. Caram and N. Claussen, *Alumina-aluminide alloys (3A) technology: I, Model development.* Journal of the American Ceramic Society, 2000. **83**(7): p. 1599-1605.
5. Ying, D.Y., *Effects of high energy mechanical milling on the kinetics of solid state reaction*, PhD Thesis. 2000, The University of Waikato: Hamilton. p. 177.
6. Cai, Z.H., *Processing, microstructure and mechanical properties of Ti_xAl_y/Al_2O_3 and $Al_2Ti_4C_2/Ti_xAl_y/Al_2O_3/TiC$ composites*, PhD Thesis. 2003, The University of Waikato: Hamilton. p. 110.
7. Ying, D.Y., D.L. Zhang and M. Newby, *Solid-state reactions during heating mechanically milled Al/TIO_2 composite powders.* Metallurgical and Materials Transactions A, 2004. **35**(7): p. 2115-2125.
8. Welham, N.J., *Mechanical activation of the solid-state reaction between Al and TiO_2.* Materials science and technology, 1998. **255**: p. 81-89.
9. Bruhn, J., S. Schicker, D.E. Garcia, R. Jansen, F. Wagner and N. Claussen, *Novel reaction-based processing of co-continuous ceramic-metal composites.* Key engineering materials, 1997. **127-131**: p. 73-80.
10. Gunther, R., T. Klassen, B. Dickau, F. Gartner, A. Bartels and R. Bormann, *Advanced alumina composites reinforced with titanium-based alloys.* Journal of American Ceramic Society, 2001. **84**(7): p. 1509-1513.
11. Pan, J., H. Li, H. Fukunage, X.G. Ning, H.Q. Ye, Z.K. Yao and D.M. Yang, *Microstructural study of the interface reaction between titania whiskers and aluminium.* Composites Science and Technology, 1997. **57**: p. 319-325.
12. Zhang, D.L., D.Y. Ying and P. Munroe, *Formation of Al_2O_3 during heating an Al/TiO_2 nanocomposite powder.* Journal of Materials Research, 2005. **20**: p. 307-313.
13. Schicker, S., D.E. Garcia, J. Bruhn, R. Jansen and N. Claussen, *Reaction processing of Al_2O_3 composites containing iron and iron aluminides.* Journal of American Ceramic Society, 1997. **80**(9): p. 2294-2300.
14. Claussen, N., D.E. Garcia and R. Jansen, *Reaction sintering of alumina-aluminide alloys (3A).* Journal of Materials Research, 1996. **11**(11): p. 2884-2888.
15. Klassen, T., R. Gunther, B. Dickau, A. Bartels, R. Bormann and H. Mecking, *Processing and characterisation of novel intermetallic/ceramic composites.* Materials Science Forum, 1998. **269-272**: p. 37-46.

16. Schicker, S., D.E. Garcia, J. Bruhn, R. Jansen and N. Claussen, *Reaction synthesized Al_2O_3-based intermetallic composites.* Acta Materialia, 1998. **46**(7): p. 2485-2492.
17. Garcia, D.E., S. Schicker, J. Bruhn, R. Jansen and N. Claussen, *Processing and mechanical properties of pressureless-sintered niobium-alumina-matrix composites.* Journal of American Ceramic Society, 1998. **81**(2): p. 429-432.
18. Klassen, T., R. Gunther, B. Dickau, F. Gartner, A. Bartels, R. Bormann and H. Mecking, *Processing and properties of intermetallic/ceramic composites with interpenetrating microstructure.* Journal of the American Ceramic Society, 1998. **81**(9): p. 2504-2506.
19. Mattern, A., B. Huchler, D. Staudenecker, R. Oberacker, A. Nagel and M.J. Hoffmann, *Preparation of interpenetrating ceramic-metal composites.* Journal of the European Ceramic Society, 2004. **24**: p. 3399-3408.
20. Travitzky, N., I. Gotman, E.Y. Gutmanas and N. Claussen, *Alumina-Ti aluminide interpenetrating composites: microstructure and mechanical properties.* Materials Letters, 2003. **57**: p. 3422-3426.
21. Horvitz, D., I. Gotman, E.Y. Gutmanas and N. Claussen, *In situ processing of dense Al_2O_3-Ti aluminide interpenetrating phase composites.* Journal of the European Ceramic Society, 2002. **22**: p. 947-954.
22. Wagner, F., D.E. Garcia, A. Krupp and N. Claussen, *Interpenetrating Al_2O_3-$TiAl_3$ alloys produced by reactive infiltration.* Journal of the European Ceramic Society, 1999. **19**: p. 2449-2453.
23. Prielipp, H., M. MKnechtel, N. Claussen, S.K. Streiffer, H. Mullejans, M. Ruhle and J. Rodel, *Strength and fracture toughness of aluminum/alumina composites with interpenetrating networks.* Materials Science and Engineering A, 1995. **197**: p. 19-30.
24. Saiz, E., S. Foppiano, W. MoberlyChan and A.P. Tomsia, *Synthesis and processing of ceramic-metal composites by reactive metal penetration.* Composites: Part A, 1999. **30**: p. 399-403.
25. Loehman, R.E. and K. Ewsuk, *Synthesis of Al_2O_3-Al Composites by Reactive Metal Penetration.* Journal of the American Ceramic Society, 1996. **79**(1): p. 27-32.
26. Tiegs, T.N., P.A. Menchhofer, K.P. Plucknett, P.F. Becher, C.B. Thomas and P.K. Liaw, *Comparison of sintering behaviour and properties of aluminide-bonded ceramics.* Ceramic Engineering and Science Proceedings, 1998. **19**(3): p. 447-455.
27. Raddatz, O., G.A. Schneider and N. Claussen, *Modelling of R-curve behaviour in ceramic/metal composites.* Acta Metallurgica, 1998. **46**(18): p. 6381-6395.
28. Lange, F.F., B.V. Velamakanni and A.G. Evans, *Method for processing metal-reinforced ceramic composites.* Journal of the American Ceramic Society, 1990. **73**(2): p. 388-393.
29. Skirl, S., R. Krause and S.M. Wiederhorn, *Processing and mechanical properties of Al_2O_3/Ni_3Al composites with interpenetrating network microstructure.* Journal of the American Ceramic Society, 2001. **84**(9): p. 2034-2040.

30. Henager, J.C.H. and J.L. Brimhall, *Solid state displacement reaction synthesis of interpenetrating-phase Ni-Al/Al_2O_3 composites.* Scripta Metallurgica, 1993. **29**: p. 1597-1602.
31. Tjong, S.C., K.F. Tam and S.Q. Wu, *Thermal cycling characteristics of in-situ Al-based composites prepared by reactive hot pressing.* Composites Science and Technology, 2003. **63**: p. 89-97.
32. Skirl, S., M. Hoffman, K. Bowman, S. Wiederhorn and J. Rodel, *Thermal expansion behavior and macrostrain of Al_2O_3/Al composites with interpenetrating networks.* Acta Materialia, 1998. **46**(7): p. 2493-2499.
33. Park, H.S. and D.K. Kim, *Effect of silica surface dopants on the formation of alumina/aluminum composites by the directed metal oxidation of an aluminum alloy.* Journal of American Ceramic Society, 2001. **84**(11): p. 2526-2530.
34. Wives, S., C. Guizard, C. Oberlin and L. Cot, *Zirconia-tungsten composites: synthesis and characterisation for different metal volume fractions.* Journal of Materials Science Letters, 2001. **36**: p. 5271-5280.
35. Toy, C. and W.D. Scott, *Ceramic-metal composite produced by melt infiltration.* Journal of the American Ceramics Society, 1990. **73**(1): p. 97-101.
36. Tiegs, T.N., K.B. Alexander, K.P. Plucknett, P.A. Menchhofer, P.F. Becher and S.B. Waters, *Ceramic composites with a ductile Ni_3Al binder phase.* Materials Science and Engineering A, 1996. **209**: p. 243-247.
37. Mei, B. and Y. Miyamoto, *Investigation of TiAl/Ti_2AlC composites prepared by spark plasma sintering.* Materials Chemistry and Physics, 2002. **75**: p. 291-295.
38. Tiegs, T.N., J.L. Schroeder, F.C. Montgomery and D.L. Baker, *Sintering and evolution of microstructure in TiC-Ni_3Al cermets.* The International Journal of Powder Metallurgy, 2000. **36**(4): p. 46-56.
39. Senkov, O.N., F.H. Froes and E.G. Baburaj, *Development of a nanocrystalline titanium aluminide-titanium silicide particulate composite.* Scripta Materialia, 1997. **37**: p. 575-579.
40. KrauB, G., J. Kubler and E. Trentini, *Preparation and properties of pressureless infiltration SiC and AlN particulate reinforced metal ceramic composites based on bronze and iron alloys.* Materials Science and Engineering A, 2002. **337**: p. 315-322.
41. Welham, N.J., *Mechanical activation of the formation of an alumina-titanium trialuminide composite.* Intermetallics, 1998. **6**: p. 363-368.
42. Klassen, T., M. Oehring and R. Bormann, *Microscopic mechanisms of metastable phase formation during ball milling of intermetallic TiAl phase.* Acta Materialia, 1997. **45**(9): p. 3935-3948.
43. Zhang, D.L., J. Liang and J. Wu, *Processing Ti_3Al-SiC nanocomposites using high energy mechanical milling.* Materials Science and Engineering A, 2004. **375-377**: p. 911-916.
44. Suryanarayana, C., G.E. Korth and F.H. Froes, *Compaction and characterization of mechanically alloyed nanocrystalline titanium aluminides.* Metallurgical and Materials Transactions A, 1997. **28**: p. 293-302.
45. Schaffer, G.B. and P.G. McCormick, *Combustion and resultant powder temperatures during mechanical alloying.* Journal of Materials Science Letters, 1990. **9**: p. 1014-1016.

46. Kim, G.H., H.S. Kim and D.W. Kum, *Determination of titanium solubility in alpha-aluminium during high energy milling.* Scripta Materialia, 1996. **34**(3): p. 421-428.
47. Schaffer, G.B. and P.G. McCormick, *On the kinetics of mechanical alloying.* Metallurgical Transaction A, 1992. **23**: p. 1285-1290.
48. Zhu, X., M. Schoenitz and E.L. Dreizin, *Oxidation processes and phase changes in metastable Al-Ti Mechanical alloys.* Materials Research Society Symposium Processing, 2003. **800**: p. 99-104.
49. Mao, S.X., N.A. McMinn and N.Q. Wu, *Processing and mechanical behaviour of TiAl/NiAl intermetallic composites produced by cryogenic mechanical alloying.* Materials Science and Engineering A, 2003. **363**: p. 275-289.
50. Kong, L.B., J. Ma, W. Zhu and O.K. Tan, *Preparation and characterization of PLZT(8/65/35) ceramics via reaction sintering from ball milled powders.* Materials Letters, 2002. **52**: p. 378-387.
51. Benjamin, J.S. and T.E. Volin, *The mechanism of mechanical alloying.* Metallurgical Transaction, 1974. **5**: p. 1929-1933.
52. Davis, R.M. and C.C. Koch, *Mechanical alloying of brittle components: silicon and germanium.* Scripta Metallurgica, 1987. **21**: p. 305-310.
53. Postrach, S. and J. Potschke, *Pressureless sintering of Al_2O_3 containing up to 20 Vol% zirconium diboride (ZrB_2).* Journal of the European Ceramic Society, 2000. **20**: p. 1459-1468.
54. Acchar, W., P. Greil, A.E. Martinelli, C.A.A. Cairo, A.H.A. Bressiani and J.C. Bressiani, *Sintering behaviour of alumina-niobium carbide composites.* Journal of the European Ceramic Society, 2000. **20**: p. 1765-1769.
55. Magnani, G., G. Beltrami, G.L. Minoccari and L. Pilotti, *Pressureless sintering and properties of αSiC-B4C Composite.* Journal of the European Ceramic Society, 2001. **21**: p. 633-638.
56. Sheppard, C.M., K.J.D. Mackenzie and M.J. Ryan, *The physical properties of sintered x-phase sialon prepared by silicothermal reaction bonding.* Journal of the European Ceramic Society, 1998. **18**: p. 185-191.
57. van Rutten, J.W.T., H.T. Hintzen and R. Metselaar, *Densification behaviour of Ca-α-sialons.* Ceramics International, 2001. **27**: p. 461-466.
58. Riu, D.-H., Y.-M. Kong and H.-E. Kim, *Effect of Cr_2O_3 addition on microstructural evolution and mechanical properties of Al_2O_3.* Journal of the European Ceramic Society, 2000. **20**: p. 1475-1481.
59. Sathiyakumar, M. and F.D. Gnanam, *Influence of MnO and TiO_2 additives on density microstructure and mechanical properties of Al_2O_3.* Ceramics International, 2002. **28**: p. 195-200.
60. Li, J.G. and X. Sun, *Synthesis and sintering behavior of a nanocrystalline α-alumina powder.* Acta Materialia, 2000. **48**: p. 3103-3112.
61. Gerling, R. and F.-P. Schimansky, *Prospects for metal injection moulding using a gamma titanium aluminide based alloy powder.* Materials Science and Engineering A, 2002. **329-331**: p. 45-49.
62. Lance, D., F. Valdivieso and P. Goeuriot, *Correlation between densification rate and microstructural evolution for pure alpha alumina.* Journal of the European Ceramic Society, 2004. **24**: p. 2749-2761.
63. Jayaseelan, D.D., D.A. Rani, T. Nishikawa and H. Awaji, *Powder characteristics, sintering behavior and microstructure of sol-gel derived*

ZTA composites. Journal of the European Ceramic Society, 2000. **20**: p. 267-275.

64. Taruta, S., Y. Itou, N. Takusagawa, K. Okada and N. Otsuka, *Influence of aluminum titanate formation on sintering of bimodal size-distributed alumina powder mixtures.* Journal of the American Ceramic Society, 1997. **80**(3): p. 551-556.
65. Krell, A., *Fracture origin and strength in advanced pressureless-sintered alumina.* Journal of the American Ceramic Society, 1998. **81**(7): p. 1900-1906.
66. Nettleship, I., R.J. McAfee and W.S. Slaughter, *Evolution of the grain size distribution during the sintering of alumina at 1350°C.* Journal of the American Ceramic Society, 2002. **85**(8): p. 1954-1960.
67. Bowen, P. and A. Mocellin, *Pressure filtration of AlN-TiO_2 slurries for the production of reaction hot-pressed Al_2O_3/TiN composites.* Ceramic Transactions, 1995. **51**: p. 427-431.
68. Li, J., L. Gao and J. Guo, *Mechanical properties and electrical conductivity of TiN-Al_2O_3 nanocomposites.* Journal of the European Ceramic Society, 2003. **23**: p. 69-74.
69. Chen, H., M. Suzuki, S. Sodeoka, T. Inoue and K. Ueno, *New approach to $MoSi_2$/SiC intermetallic-ceramic composite with B_4C.* Journal of Materials Science Letters, 2001. **36**: p. 5773-5777.
70. Wang, H.Z., L. Gao and J.K. Guo, *Fabrication and microstructure of Al_2O_3-ZrO_2(3Y)-SiC nanocomposites.* Journal of the European Ceramic Society, 1999. **19**: p. 2125-2131.
71. Klein, R., V. Medri, M. Desmaison-Brut, A. Bellosi and J. Desmaison, *Influence of additives content on the high temperature oxidation of silicon nitride based composites.* Journal of the European Ceramic Society, 2003. **23**: p. 603-611.
72. Biasini, V., M. Parasporo and A. Bellosi, *Fabrication and characterisation of Al_2O_3 porous bodies by hot isostatic pressing.* Thin Solid Films, 1997. **297**: p. 207-211.
73. Beddoes, J.C., W. Wallace and M.C. de Malherbe, *Densification of γ-TiAl powder by hot isostatic pressing.* The International Journal of Powder Metallurgy, 1992. **28**(3): p. 313-325.
74. Sperisen, T. and A. Mocellin, *Investigation of the displacement reaction in mixed AlN+TiO_2 powders Part I Microstructural changes at 1 atm N_2.* Journal of Materials Science Letters, 1992. **27**: p. 1121-1128.
75. Lannutti, J.J., T.A. Deis, M.C. Kong and P. D.H., *Density gradient evolution during dry pressing.* The American Ceramic Society Bulletin, 1997. **76**(1): p. 53-58.
76. Kim, H.G., H.M. Lee and K.T. Kim, *Near-net-shape forming of ceramic powder under cold combination pressing and pressureless sintering.* Journal of Engineering Materials and Technology, 2001. **123**: p. 221-228.
77. Schwattz, M., *Handbook of Structural Ceramics.* 1992, New York: McGraw-Hill.
78. Brook, R.J., R.W. Cahn and M.B. Bever, *Advances in materials science and engineering*, in *Concise encyclopedia of advanced ceramic materials.* 1991, Pergamon Press: Oxford ; New York Cambridge, Mass. p. 219-222.
79. Petrovsky, V.Y. and Z.S. Rak, *Densification, microstructure and properties of electroconductive Si_3N_4-TaN composites Part I:*

Densification and microstructure. Journal of the European Ceramic Society, 2001. **21**(2): p. 219-235.

80. Kim, K.T., Y.S. Kwon and H.G. Kim, *Near-net-shape forming of alumina powder under hot pressing and hot isostatic pressing.* International Journal of Mechanical Sciences, 1997. **39**(9): p. 1011-1022.
81. Ji, Y. and J.A. Yeomans, *Processing and mechanical properties of Al_2O_3-5vol.% Cr nanocomposites.* Journal of the European Ceramic Society, 2002. **22**: p. 1927-1936.
82. Mizuuchi, K., K. Inoue, M. Sugioka, M. Itami and M. Kawahara, *Microstructure and mechanical properties of Ti-aluminides reinforced Ti matrix composites synthesized by pulsed current hot pressing.* Materials Science and Engineering A, 2004. **368**: p. 260-268.
83. Geandier, G., S. Denis, A. Hazotte and A. Mocellin, *Hertzian crack analysis in alumina-chromium composites.* Journal of the European Ceramic Society, 2005. **25**: p. 1119-1132.
84. Hsieh, C.L. and W.H. Tuan, *Elastic properties of ceramic-metal particulate composites.* Materials Science and Engineering A, 2005. **393**: p. 133-139.
85. Subramanian, R., E. Ustundag, S.L. Sass and R. Dieckmann, *In-situ formation of metal-ceramic microstructures by partial reduction reactions.* Solid State Ionics, 1995. **75**: p. 241-255.
86. Ustundag, E., P. Ret, R. Subramanian, R. Dieckmann and S.L. Sass, *In situ metal-ceramic microstructures by partial reduction reactions in the Ni-Al-O system and the role of ZrO_2.* Materials Science and Engineering A, 1995. **195**: p. 39-50.
87. Teng, L.D., F.M. Wang and W.C. Li, *Thermodynamics and microstructure of Ti-ZrO_2 metal-ceramic functionally graded materials.* Materials Science and Engineering A, 2000. **293**: p. 130-136.
88. Ma, J. and G.E.B. Tan, *Processing and characterization of metal-ceramics functionally gradient materials.* Journal of Materials Processing Technology, 2001. **113**: p. 446-449.
89. Sbaizero, O., S. Roitti and G. Pezzotti, *R-curve behavior of alumina toughened with molybdenum and zirconia particles.* Materials Science and Engineering A, 2003. **359**: p. 297-302.
90. Ustundag, E., R. Subramanian, R. Dieckmann and S.L. Sass, *In situ formation of metal-ceramic microstructures in the Ni-Al-O system by partial reduction reactions.* Acta Metallurgica et Materialia, 1995. **43**(1): p. 383-389.
91. Mashl, S.J., J.C. Hebeisen and C.G. Hjorth, *Producing large P/M near-net shapes using hot isostatic pressing.* Journal of Metals, 1998: p. 29-31.
92. Conway, J.J. and F.J. Rizzo, *Hot Isostatic Pressing of Metal Powders*, in *ASM Handbook.* p. 605-620.
93. Fujikawa, T., *Hot isostatic pressing (HIP) of ceramics and HIP equipment for ceramics*, in *Fine Ceramics*, S. Saito, Editor. 1985, Elsevier Applied Science Publishers Ltd. p. 44-53.
94. Larker, H.T. and R. Lundberg, *Neat net shape production of monolithic and composite high temperature ceramics by hot isostatic pressing (HIP).* Journal of the European Ceramic Society, 1999. **19**(13-14): p. 2367-2373.

95. Echeberria, J., J. Tarazona, J.Y. He, T. Butler and F. Castro, *Sinter-HIP of -alumina powders with sub-micron grain sizes.* Journal of the European Ceramic Society, 2002. **22**: p. 1801-1809.
96. Dax, R., R.J. Henry, T. McCabe and P. Barrous-Antolin, *Process modeling and design*, in *ASM Handbook: Powder Metal Technologies and Applications*. p. 23-30.
97. Cahn, R.W., P. Haasen and E.J. Kramer, *Hot isostatic pressing*, in *Materials Science and Technology: Processing of Ceramics Part II.* 1996: Weinheim ; Cambridge. p. 147-157.
98. Sanderow, H.I., *Powder metallurgy methods and design*, in *ASM Handbook: Powder Metal Technologies and Applications*. p. 9-15.
99. Azcona, I., J.M. Sanchez and F. Castro, *Hipping after sintering of titanium diboride cermets.* Powder Metallurgy, 2001. **44**(2): p. 133-138.
100. Ranganath, S., *A review on particulate-reinforced titanium matrix composites.* Journal of Materials Science, 1997. **32**: p. 1-16.
101. Pagounis, E., M. Talvitie and V.K. Lindroos, *Influence of the metal/ceramic interface on the microstructure and mechanical properties of HIPed iron-based composites.* Composites Science and Technology, 1996. **56**: p. 1329-1337.
102. Suresh, S. and A. Mortensen, *Functionally graded metals and metal-ceramic composites: Part 2 Thermomechanical behaviour.* International Materials Reviews, 1997. **42**(3): p. 85-116.
103. Brown, I.W.M. and W.R. Owers, *Fabrication, microstructure and properties of Fe-TiC ceramic-metal composites.* Current Applied Physics, 2004. **4**: p. 171-174.
104. Lin, J.S. and Y. Miyamoto, *Notch effect of surface compression and the toughening of graded Al_2O_3/TiC/Ni materials.* Acta Materialia, 2000. **48**: p. 767-775.
105. Flinn, B.D., F.W. Zok, F.F. Lange and A.G. Evans, *Processing and properties of Al2O3-Al composites.* Materials Science and Engineering A, 1991. **144**: p. 153-157.
106. Steinbrech, R.W., *Toughening mechanisms for ceramic materials.* Journal of European Ceramic society, 1992. **10**: p. 131-142.
107. Sigl, L.S., P.A. Mataga, B.J. Dalgleish, R.M. McMeeking and A.G. Evans, *On the toughness of brittle materials reinforced with a ductile phase.* Acta Metallurgica, 1988. **36**(4): p. 945-953.
108. Flinn, B.D., M. Ruhle and A.G. Evans, *Toughening in composites of Al_2O_3 reinforced with Al.* Acta Metallurgica, 1989. **37**(11): p. 3001-3006.
109. Konopka, K., M. Maj and K.J. Kurzydlowski, *Studies of the effect of metal particles on the fracture toughness of ceramic matrix composites.* Materials Characterization, 2003. **51**: p. 335-340.
110. Hillig, W.B., O. Raddatz, G.A. Schneider and N. Claussen, *Analysis and model of the crack bridging mechanisms in a ductile fiber reinforced ceramic matrix composite.* Journal of Materials Science, 2001. **36**: p. 1653-1663.
111. Lu, J., L. Gao, J. Sun, L. Gui and J. Guo, *Preparation and sintering behavior of Ni-Al_2O_3 nanocermets from coated powders.* Journal of Materials Science Letters, 2001. **20**: p. 1-3.
112. Agrawal, P. and C.T. Sun, *Fracture in metal-ceramic composites.* Composite Science and Technology, 2004. **64**: p. 1167-1178.

113. Kawasaki, A. and R. Watanabe, *Thermal fracture behavior of metal/ceramic functionally graded materials.* Engineering Fracture Mechanics, 2002. **69**: p. 1713-1728.
114. Ji, Y. and J.A. Yeomans, *Microstructure and mechanical propeties of chromium and chromium/nickel partiulate reinforced alumina ceramics.* Journal of Materials Science, 2002. **37**: p. 5229-5236.
115. Mishra, R.S. and A.K. Mukherjee, *Processing of high hardness-high toughness alumina matrix nanocomposites.* Materials Science and Engineering A, 2001. **301**: p. 97-101.
116. Liu, N., C. Han, Y. Xu, S. Chao, M. Shi and J. Feng, *Microstructures and mechanical properties of nanoTiN modified TiC-based cermets for the milling tools.* Materials Science and Engineering A, 2004. **382**: p. 122-131.
117. Hussainova, I., *Microstructure and erosive wear in ceramic-based composites.* Wear, 2005. **258**: p. 357-365.
118. Zalar, A., B.M.M. Baretzky, S. Hofmann, M. Ruhle and P. Panjan, *Interfacial reactions in Al_2O_3/Ti, Al_2O_3/Ti_3Al and Al_2O_3/TiAl bilayers.* Thin Solid Films, 1999. **352**: p. 151-155.
119. Avishai, A., C. Scheu and W.D. Kaplan, *Intergranular films at metal-ceramic interfaces Part I - Interface structure and chemistry.* Acta Materialia, 2005. **53**: p. 1559-1569.
120. Shih, D.S. and R.A. Amato, *Interface reaction between gamma-TiAl alloys and reinforcements.* Scripta Metallurgica, 1990. **24**: p. 2053-2058.
121. Flinn, B.D., C.S. Lo, F.W. Zok and A.G. Evans, *Fracture resistance characteristics of a metal-toughened ceramic.* Journal of the American Ceramic Society, 1993. **76**(2): p. 369-375.
122. Konopka, K., A. Olszowka-Myalska and M. Szafran, *Ceramic-metal composites with an interpenetrating network.* Materials and Physics, 2003. **81**: p. 329-332.
123. Zhang, L.M., J. Liu, R.Z. Yuan and T. Hirai, *Properties of TiC-Ni_3Al composites and structural optimization of TiC-Ni_3Al functionally gradient materials.* Materials Science and Engineering A, 1995. **203**: p. 272-277.
124. Saiz, E., A.P. Tomsia and K. Suganuma, *Wetting and strength issues at Al/α-alumina interfaces.* Journal of the European Ceramic Society, 2003. **23**: p. 2787-2796.
125. Bartolome, J.F., M. Diaz, J. Requena, J.S. Moya and A.P. Tomsia, *Mullite/molybdenum ceramic-metal composites.* Acta Materialia, 1999. **47**(14): p. 3891-3899.
126. Sbaizero, O. and G. Pezzotti, *Residual stresses and R-curve behavior of AlN/Mo composite.* Journal of the European Ceramic Society, 2001. **21**: p. 269-275.
127. Zalar, A., B.M.M. Baretzky, F. Dettenwanger, M. Ruhle and P. Panjan, *Interdiffusion at the Al2O3/Ti interface studied in thin-film structures.* Surface and Interface Analysis, 1998. **26**: p. 861-867.
128. Lu, Y.-C., S.L. Sass, Q. Bai, D.L. Kohlstedt and W.W. Gerberich, *The influence of interfacial reactions on the fracture toughness of Ti-Al_2O_3 interfaces.* Acta Metallurgica et Materialia, 1995. **43**(1): p. 31-41.
129. Chen, Y., D.J. Young and B. Gleeson, *A new Ti-rich ternary phase in the Ti-Al-O system.* Materials Letters, 1995. **22**: p. 125-129.

130. Misra, A.K., *Reaction of Ti and Ti-Al alloys with alumina.* Metallurgical Transactions A, 1991. **22A**: p. 715-721.
131. Lee, B.J. and N. Saunders, *Thermodynamic evaluation of the Ti-Al-O ternary system.* Z. Metallkd., 1997. **88**: p. 152-161.
132. Shemet, V., P. Karduck, H. Hoven, B. Grushko, W. Fischer and W.J. Quadakkers, *Synthesis of the cubic Z-phase in the Ti-Al-O system by a powder metallurgical method.* Intermetallics, 1997. **5**: p. 271-280.
133. Kojima, Y., T. Isobe, M. Senna, M. Sakurai, K. Sumiyama and K. Suzuki, *An XAFS study on reconstruction of short-range order in mechanically alloyed Al-Ti and Al-Ti-O complexes.* Journal of Alloys and Compounds, 1997. **248**: p. 52-58.

CHAPTER TWO:

Experimental Procedure

This chapter describes the experimental procedure during the course of the research undertaken. This includes the materials used, sample preparation and the techniques employed for analysing the samples.

2.1 Powder Preparation

A mixture of Al and TiO_2 was milled using a high-energy discus-milling device as shown in Figure 2.1. The discus mill used at the University of Waikato consisted of two matching hardened steel discuses and a bowl. The capacity of the discus mill ranges from 300 to 1000g of powder per batch. The powder charge in the bowl is required to be no less than 50% of the volume of the bowl because lower powder loadings may cause severe wear and possible breakage of the discuses. Therefore a minimum Al/TiO_2 powder charge of 500g was used for the discus milling in the present experiments.

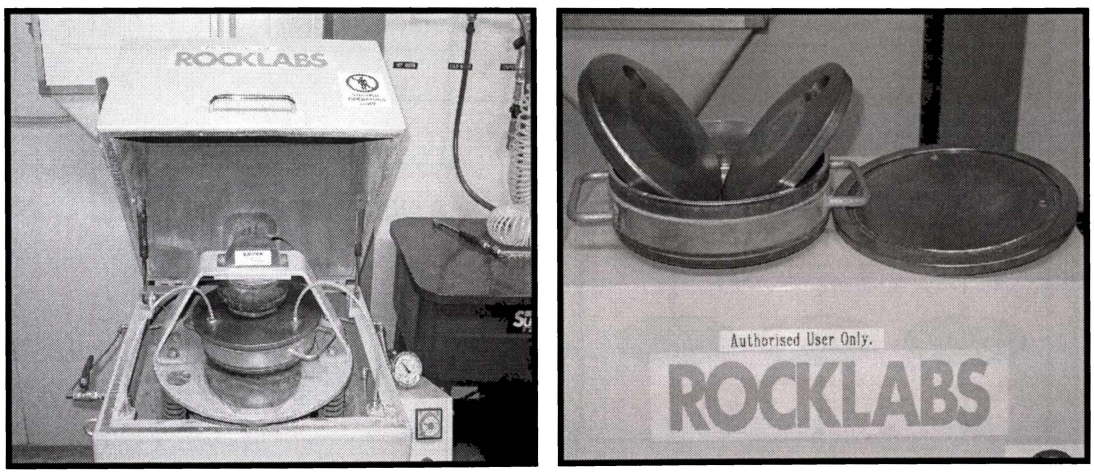

Figure 2.1: High energy discus milling device

The starting materials were Al powder (industrial grade, 99.5% purity, average particle size <60μm) and TiO_2 powder (rutile - 99.5% purity, average particle size 200-300nm or anatase - 99% purity, average particle size 200nm). The milling was carried out under protection of an Ar atmosphere (O_2 content < 8×10^{-2} vol.%). 10ml of isopropyl alcohol was mixed with the powder prior to milling to reduce the tendency of the powder to stick to the discuses.

The quantities of Al and TiO_2 powders were calculated using the following equation, using 5wt% excess of Al powder.

$$3TiO_2 + 4Al \rightarrow 3Ti + 2Al_2O_3 \qquad \textbf{Equation 2.1}$$

A schematic flow chart of the powder preparation is shown in Figure 2.2.

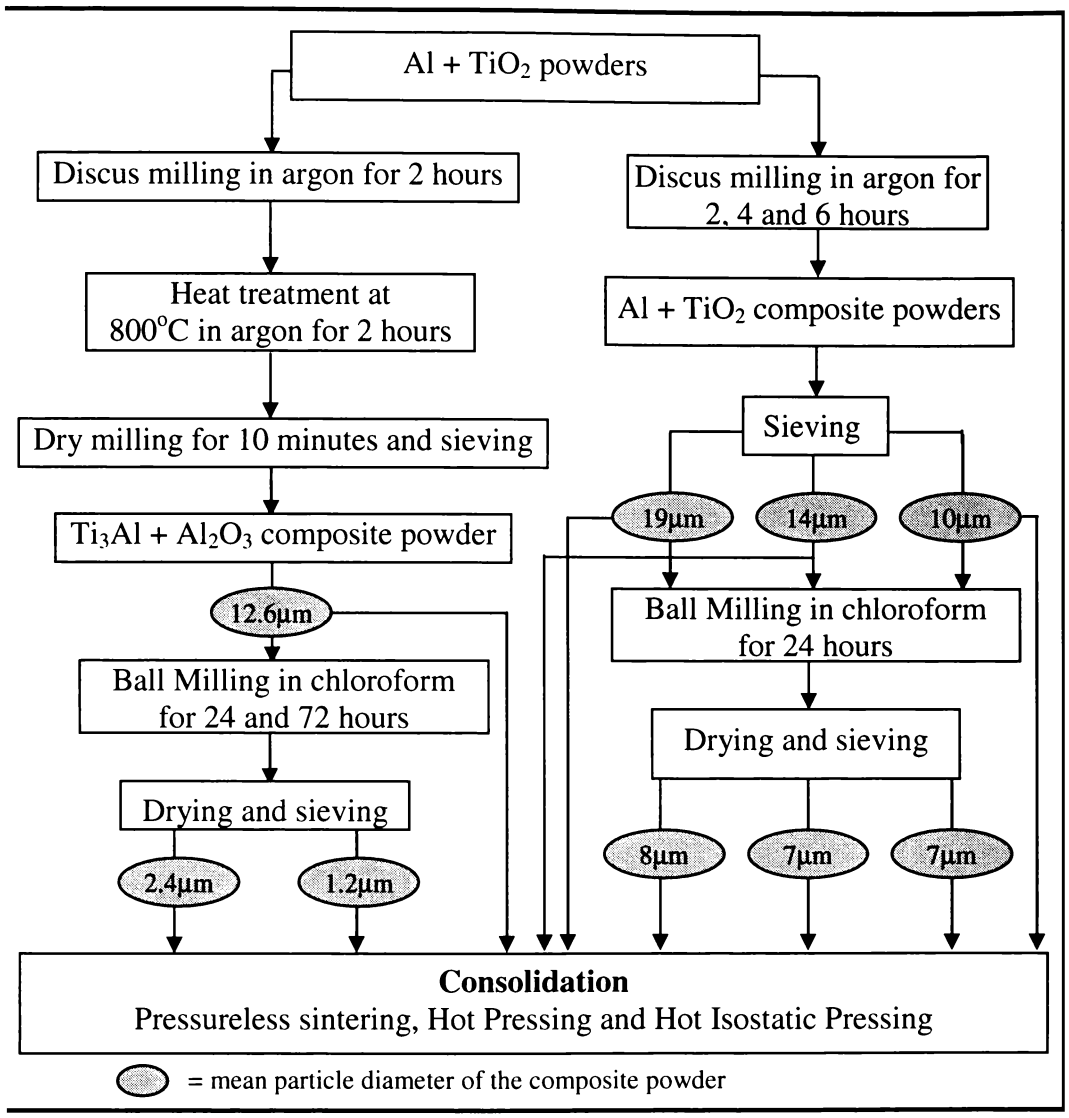

Figure 2.2: Schematic flow sheet of powder preparation

The first part of the experiment in powder preparation involved the discus milled powder being heated at 800°C in argon gas for 2 hours. The powder was then mixed with 2wt% of PVA[1] and 4wt% of PEG[2] for ease of pressing. After pressing, the pellet was heat-treated in air at 400°C to burnout the organic binders. The second part of the experiment in powder preparation involved the powder being discus milled for two, four and six hours. No binders were necessary for compaction in this procedure

The heat treated powders (~30g) were further Si_3N_4 ball milled in chloroform for 24, 48 and 72 hours whereas the discus milled powders were ZrO_2 ball milled in chloroform for 24 hours to further reduce the powder particle sizes. The ball mill set up is shown in Figure 2.3. The weights of the Si_3N_4 and ZrO_2 balls were measured before and after ball milling. No weight loss was recorded in either case.

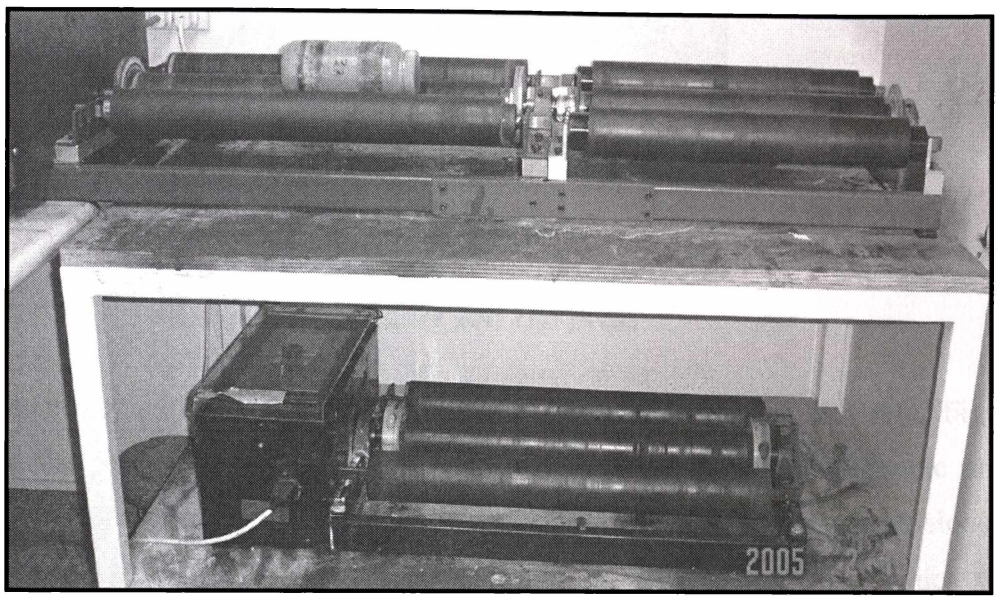

Figure 2.3: Ball milling

2.2 Powder Compaction

Die pressing followed by cold isostatic pressing, CIP, was used for compaction prior to pressureless sintering, hot pressing or hot isostatic pressing, which contributed to net-shape processing, fast operation and more uniform density distributions.

A simple die press involving a hydraulic jack was used to shape a small amount of powder prior to isostatic pressing as shown in Figure 2.4. Pressure of up to 10MPa was used, enough to hold the powder together when it was transferred to the cold isostatic press. Four different hardened steel dies were used ranging from 7.00mm, 10.00mm, 20.10mm and 25.35mm in diameter.

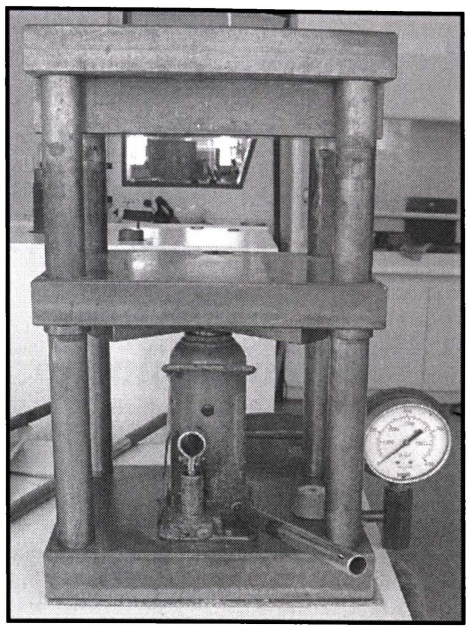

Figure 2.4: Die press

For the preparation of the samples for cold isostatic pressing (CIP) (refer Figure 2.5), the pellets were placed in vacuum-sealed plastic bags. The isostatic press design was of the screw thread closure type, with internal chamber dimensions of 75mmϕ x 300mm deep. The samples were placed in a wire cage, which was suspended in the chamber. Ethylene glycol with corrosion inhibitor additives was used as the pressing fluid. The pressure on the gauge could be set at desired values of up to 350MPa. In these experiments, a pressure of 150MPa was sufficient for cold isostatic pressing.

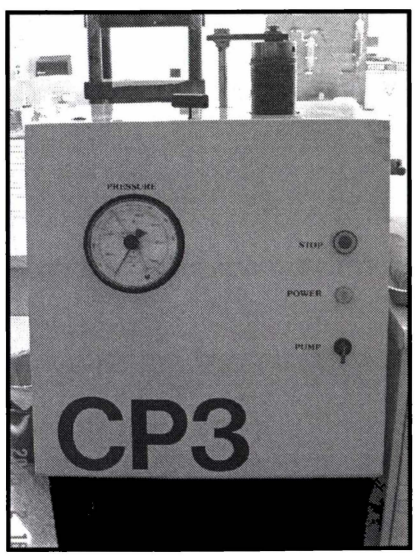

Figure 2.5: Cold Isostatic Press

The dimensions of the sample discs were measured prior to sintering. Typically, green density between 55 to 75% of theoretical density was obtained. The approximate theoretical densities of Ti_3Al-Al_2O_3 and Al-TiO_2 composite powders are 4.235g/cm^3 and 3.39g/cm^3, respectively based on calculations for the densities of the volume fractions of the respective components.

2.3 Powder Consolidation

2.3.1 Pressureless Sintering

Pressureless sintering experiments were undertaken in an alumina tube furnace (refer Figure 2.6) at temperatures of up to 1480°C under argon or in a hot press furnace at temperatures of up to 1600°C under argon or vacuum. The exothermic character of the reactions involved during sintering requires careful process control, which was managed by decreasing the heating rate to between 2 to 15°C/min and using holding periods of 1, 4, 8, 12 and 16 hours.

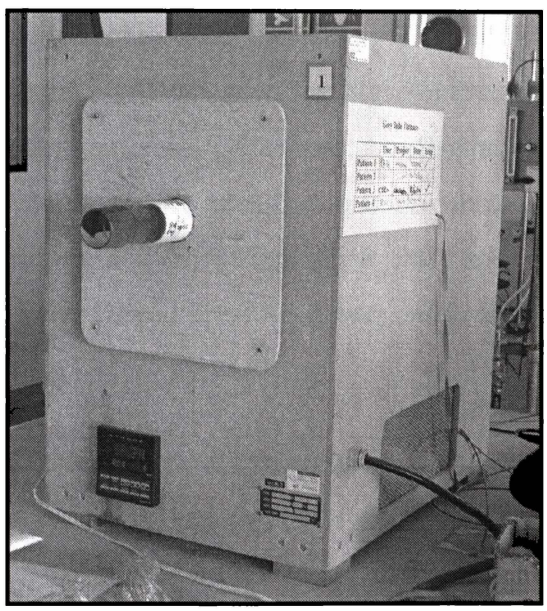

Figure 2.6: Alumina tube furnace

For pressureless sintering using the hot press furnace (refer Figure 2.7), a machined graphite pot was used. The sample was carefully placed on a half full boron nitride powder bed inside the pot and further boron nitride was added to cover the sample. A schematic diagram of the graphite pot set up for pressureless sintering is shown in Figure 2.7. The procedure for chamber evacuation or the operation under gas atmosphere is outlined in Section 2.3.2.

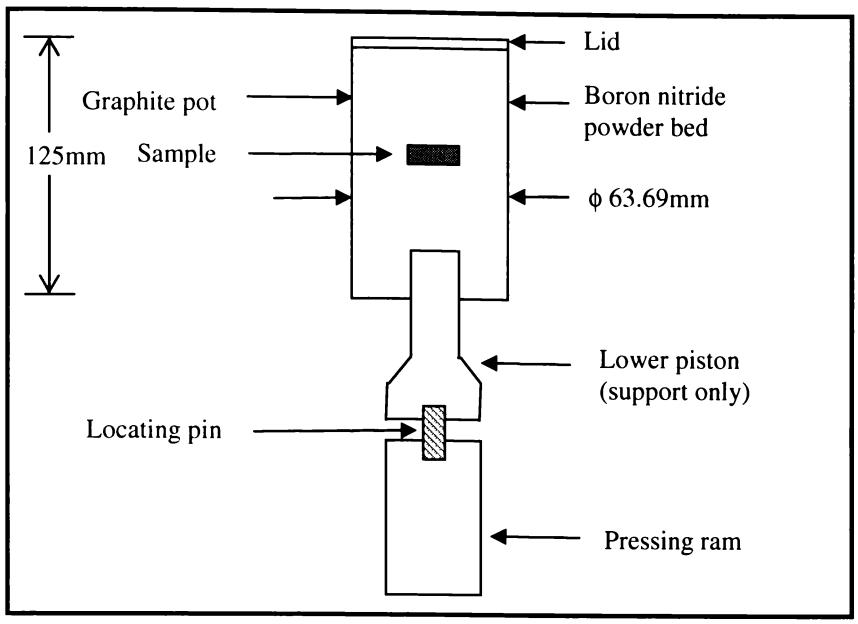

Figure 2.7: Graphite pot set up for pressureless sintering

2.3.2 Hot Pressing

A Thermal Technology Group 1400 Laboratory Hot Press, model HP20-1000-3060 as shown in Figure 2.8 is designed for high temperature and high pressure consolidation of powder materials. The basic configuration of the hot pressing system includes the furnace with standard graphite hot zone constructed with graphite element, furniture and insulation; press load frame with rams; manual power supply with water-cooled flexible power leads and manually controlled hydraulic force system.

The graphite furnace assembly was contained in a water-cooled alloy housing, containing various sight holes and penetrations for thermocouple placements. This is the blue shell suspended in its frame in Figure 2.8. 19mm or 25mm diameter graphite dies were readily available for hot pressing, which were carefully placed on the graphite locating pin. A schematic diagram of the graphite die set up for hot pressing is shown in Figure 2.9. Sufficient pressure was initially applied to hold the die with the sample in place prior to furnace operation by switching on the hydraulic pump elevator. Pressure was not applied at the beginning of the run as sample fracture was a potential problem due to the low green strength of some samples. The desired pressure could be applied manually at any stage of the sintering. The die was centred vertically in the hot zone using

the sight hole as a reference. The dies machined from graphite could sustain a maximum of 1000kg uniaxial force. Sacrificial graphite spacers were used between the pistons and the sample surrounded in powder bed of boron nitride. This minimised the potential for destruction of the die due to undesirable bonding between the sample and the die that might jam the piston.

Figure 2.8: Thermal Technology's Group 1400 Laboratory Hot Press

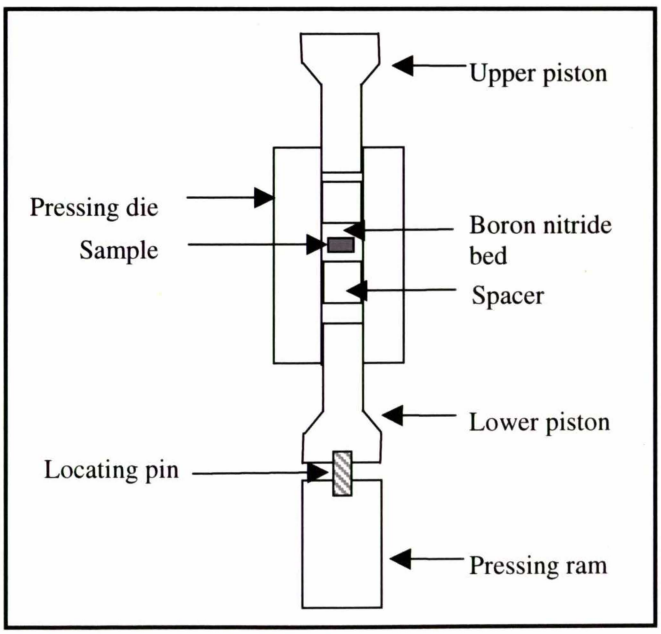

Figure 2.9: Graphite die set up for hot pressing

Care was taken to clean the o-ring and the mating face with a soft hair brush before the furnace was lowered prior to every firing. The initial chamber evacuation was undertaken very slowly to minimise the potential for damage to the sample or powder bed. For operation under gas atmosphere, the evacuated furnace was backfilled with argon and then a constant flow of argon was maintained. A typical gas flow rate was 10-20ml/min.

2.3.3 Hot Isostatic Pressing

The Laboratory Hot Isostatic Press, model CPSI SL-1 as shown in Figure 2.10 is designed for simultaneous high temperature and pressure consolidation of powder materials. Some of the pressureless sintered samples were further densified by hot isostatic pressing. The sample was divided into two pieces; one was hot isostatic pressed and one kept as a control sample for comparison. The samples were hot isostatically pressed at 200MPa in argon for two hours at temperatures of 1100°C, 1200°C, 1300°C and 1350°C. The heating rate used was 3°C/min.

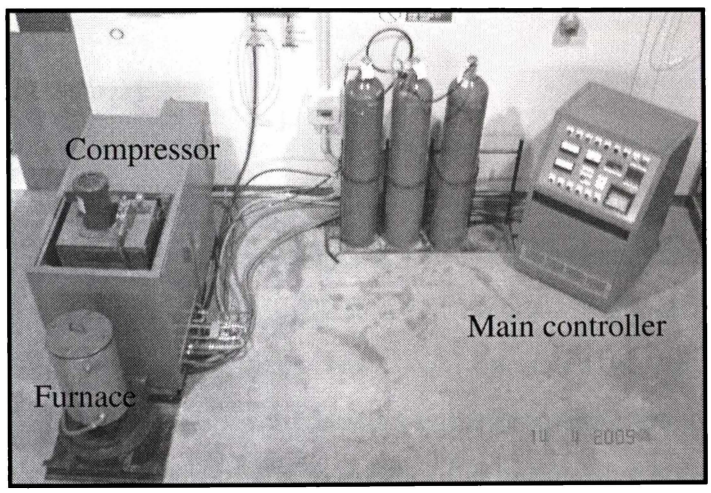

Figure 2.10: Hot isostatic press

2.4 Sample Characterisation

2.4.1 Particle Size Determination

The particle size distributions of the powders were determined using a Shimadzu SALD-2001 laser diffraction instrument. Powders were dispersed ultrasonically in a distilled water or ethanol medium for analysis.

2.4.2 Differential Thermal Analysis

Differential Thermal Analysis (DTA) was undertaken using a STA 1500 TG/DSC Instrument. The powders were loaded into an alumina crucible, which was allowed to equilibrate for ~20 minutes before heating to 1200°C at 15°C/min under flowing argon.

2.4.3 X-Ray Diffraction

X-Ray Diffraction (XRD) was used to study the crystallographic structure of the composite powders and powdered sintered samples. The equipment used was a Philips PW 1729 X-Ray generator with a PW 1710 microprocessor using Co Kα radiation. The x-ray tube was set at 35kV and 40mA. Typical XRD scanning conditions were a scan range of 4-80° 2θ at a scan speed of 3°/min. The results were interpreted using the ICDD Database and proprietary XRD Evaluation Software (EVA). The estimated phase composition of the individual samples was obtained from the major peaks height intensity.

2.4.4 Microscopy

Surface topography and cross sections of the powder particles and bulk samples were studied using optical microscopy (Olympus BX60M) and Scanning Electron Microscopy, SEM (Secondary Electrons, SE and Back Scattered Electrons, AUX). The equipment used was a Philips XL30 SEM coupled with Energy Dispersive Spectroscopy, EDS. The powders were cold mounted in epoxy resin plus hardener. The sintered pellets were mounted with epoxy hot mounting resin. The mounted samples were subjected to a series of grinding and polishing steps as shown in Table 2.1, with grit sizes from 15 to 3μm.

Table 2.1: Grinding and polishing steps

Steps	Grit Sizes (μm)	Materials	Wheel Rotation Speed
Fine grinding	15	MD Allegro/Plan, diamond paste, blue lubricant	100rpm
Initial polishing	9	MD Plan, diamond paste, blue lubricant	100rpm
Intermediate polishing	6	MD Plan, diamond abrasive, blue lubricant	100rpm
Final polishing	3	MD Plan, diamond abrasive, blue lubricant	100rpm

2.4.5 Porosity and Density Measurements

Open porosity, closed porosity, relative density and bulk density of the sintered sample were obtained using a vacuum desiccator apparatus as shown schematically in Figure 2.11, which utilises the Archimedes technique in the calculation as shown in the following.

$$\text{Open Porosity} = \frac{\text{Volume of open pores}}{\text{Vol. of solid material} + \text{vol. of (closed} + \text{open pores)}}$$

$$= \frac{(W_W - W_D)}{W_W - W_S} \times 100\% \qquad \textbf{Equation 2.2}$$

$$\text{Relative Density} = \frac{\text{Dry weight of the porous material}}{\text{Vol. of solid material} + \text{vol. of (closed} + \text{open pores)}}$$

$$= \frac{W_D}{W_W - W_S} \times D \times 100\% \qquad \textbf{Equation 2.3}$$

Where,

W_D = Weight of dry sample

D = Density of water at measurement temperature

W_w = Weight of sample with open pores filled with water after vacuum impregnation

W_S = Weight of sample suspended in water after vacuum impregnation

The sintered sample was dried in oven at 100°C until a constant weight was reached. The dry weight (W_D) of the sample was obtained prior to placing the sample in the desiccator. The desiccator was evacuated with the pump valve on until there was no further drop in pressure, typically 1-2 hours. After that, the water valve was switched on to let the water flow into the desiccator. The pump valve was left on for a couple of hours until there were no air bubbles coming out from the sample. The air was let in gradually by switching on the air valve after the pump valve was turned off. The sample was allowed to stand overnight in water at atmospheric pressure.

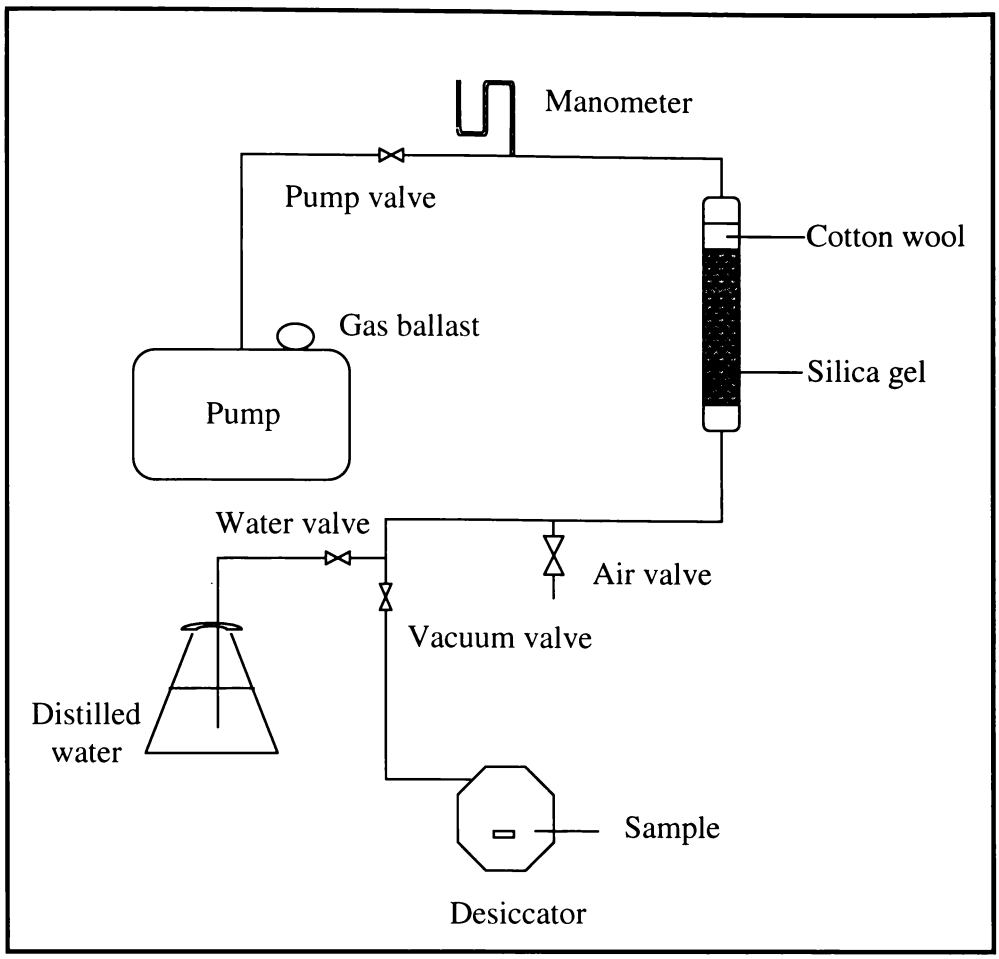

Figure 2.11: Schematic diagram of the vacuum impregnation system used

Figure 2.12 shows a schematic diagram of the apparatus used to measure the suspended weight (W_S) of the sample. The measurement was undertaken in a closed (draught free) environment. Distilled water must cover the glass bucket and the suspension hooks to avoid displacement errors during the measurement. The sample was placed on the glass bridge for measuring. A wet cloth was used to remove excess surface moisture on the sample before the wet weight was measured. Bulk density and apparent porosity were calculated in a spreadsheet using Equation 2.2 and Equation 2.3 following measurements of the dry weight, suspended weight and the wet weight of the sample.

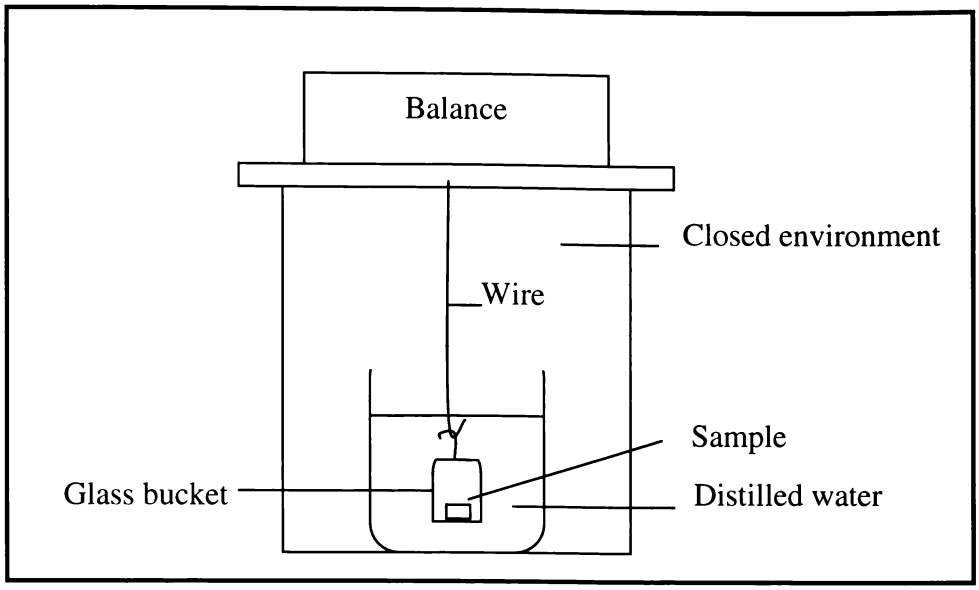

Figure 2.12: Apparatus for suspended weight

2.4.6 Dilatometry

The dimensional change of a powder compact during heating and cooling was studied using a thermal dilatometric analyser, HARROP model TDA-H1-CP6X. The initial length of the samples was typically 7mm. The dilatometry analysis was performed in flowing argon gas using a standard heating/cooling rate of 10°C/min.

2.4.7 Mechanical Properties Measurements

2.4.7.1 Ball-on-ring test

Thin circular discs of approximately 20mm in diameter and up to 2mm thick were fabricated. The disc was supported on a ring and centrally loaded via a ball. The ball-on-ring test jig is shown in Figure 2.13. The support ring is a commercial thrust bearing with its upper race removed with 8 balls on a radius of 8.49mm. This reduced the frictional effects of a fixed support. The support fixture can be placed directly on the plate of a testing machine load cell or it may be supported in turn on a bridge allowing transmission of the deflection of the sample centre to a clip-on strain-gauge type extensometer by a spring-loaded rod touching the disc beneath the central loading ball. The disc is loaded by a 4mm ball in a fixture attached to the crosshead of the testing machine Axial alignment is assured by the

use of an alignment sleeve between the load and support fixtures. A crosshead speed of 0.5mm/min was used.

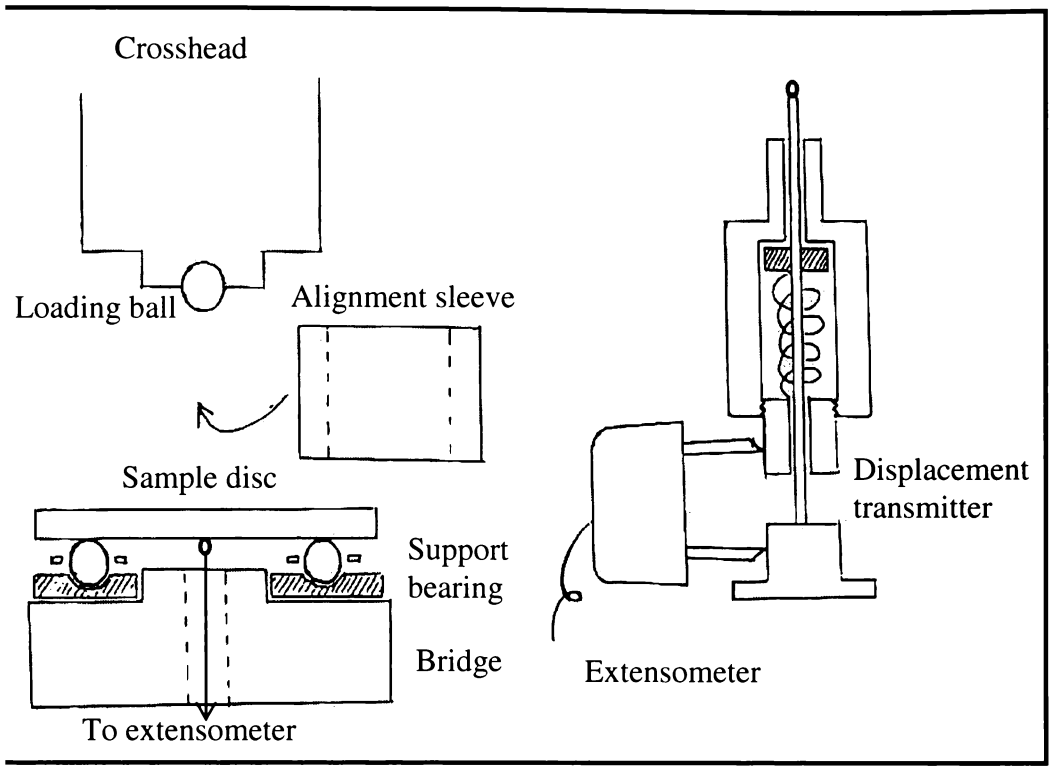

Figure 2.13: Ball on ring biaxial strength test jig[3]

This technique produced the biaxial strength for the test samples. The biaxial strength is calculated using Equation 2.4. The ball on ring test was suitable for material comparisons within the laboratory using the same apparatus and similar specimen dimensions, but comparison with uniaxial test results in the literature may not be valid and was not considered.

$$S = \left(\frac{3P(1+\upsilon)}{4\pi\, t^2}\right)\left\{1 + 2\ln\left(\frac{a}{b}\right) + \left[\frac{(1-\upsilon)a^2}{(1+\upsilon)R^2}\right]\left[1 - \left(\frac{b^2}{2a^2}\right)\right]\right\} \qquad \textbf{Equation 2.4}$$

Where,

P = load (N)

a = radius of ring, mm = 8.49, b = radius of constant stress (= t/3 in mm)

t = disc thickness, mm, R = radius of disc, mm

ν = Poisson's ratio

2.4.7.2 Vickers indentation fracture toughness test

The application of the Vickers indentation fracture toughness test[4-10] has become widespread because (i) it can be used on small samples of material, (ii) specimen preparation is relatively simple requiring only the provision of a polished, reflective plane surface, (iii) the Vickers diamond indenter used to produce the hardness indentations is a standard item used on a dedicated hardness tester or on a universal testing machine, (iv) in many instances the crack lengths can be measured optically and (v) it is both quick and cost effective.

However, there are a number of complications such as (i) the accuracy to which the crack lengths can be measured, (ii) all the indentation fracture models given in the literature assume that idealised crack systems are formed during a Vickers indentation test, which may or may not be the case for the test material, (iii) the diversity of indentation fracture toughness equations reported in the literature and (iv) the often reported discrepancy between the indentation fracture toughness of a material and its fracture toughness as measured by conventional methods such as the single edge notched beam test.

The Vickers hardness test[11, 12] is a static hardness test for ceramics, which employs a square-based diamond pyramid indentor with an angle of 136° between opposing faces. A schematic of the indentation deformation/fracture pattern for the Vickers geometry is shown in Figure 2.14. The Vickers hardness is defined as the applied load P divided by the surface area of the indent impression as shown:

$$H_v = \frac{1854.4P}{(2a)^2} \qquad \textbf{Equation 2.5}$$

The concept of using the indentation cracks size to quantify toughness was recognised by Palmqvist, which leads to one of the numerous equations for evaluating material toughness reported by Anstis et al[126].

$$K_c = 2.263x10^{-8}\sqrt{E*P}*c^{-3/2}*a \qquad \textbf{Equation 2.6}$$

Where E is the elastic modulus, P is the indentation load, a is the average diagonal measurement and c is the crack dimensions.

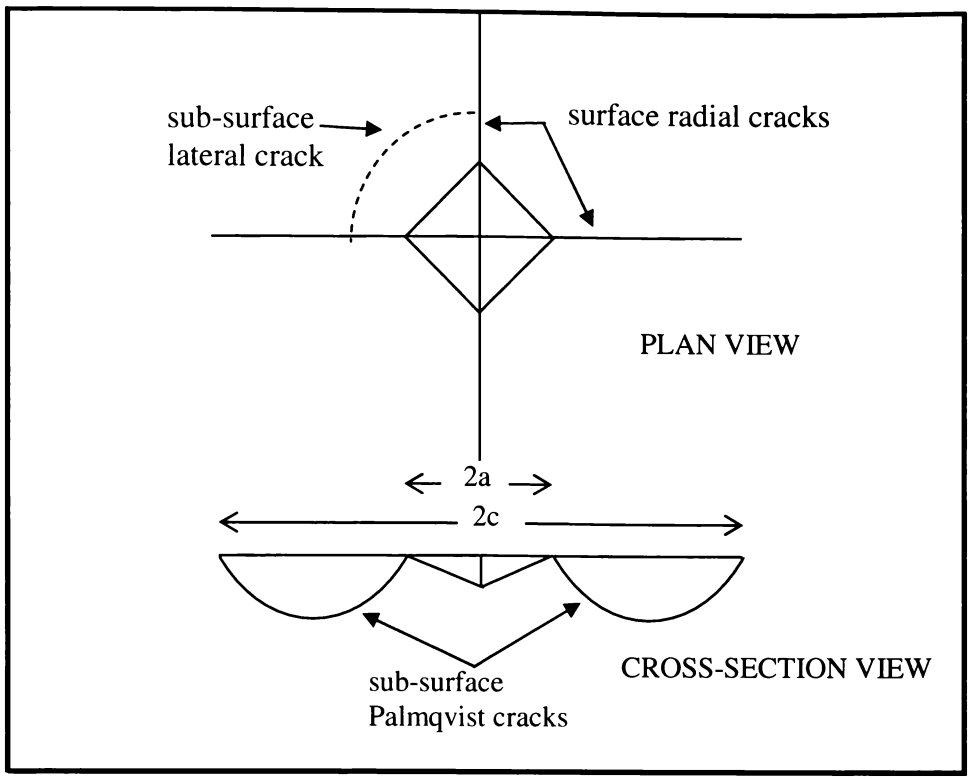

Figure 2.14: Schematic idealised view of Vickers indent radial Palmqvist crack system[129]

Figure 2.15 shows the flow chart of the procedure for fracture toughness measurements. Vickers indentation loads of 10 or 20 kg were used depending on the characteristics of the sample such as composition and porosity. A minimum of five readings were performed across a single sample to give an average of the Vickers hardness number reported in GPa.

The fracture toughness obtained from the Vickers indentation fracture toughness test was an average measurement derived from two to eight indentations. The problems with the measurements include (i) the length measurement errors due to the two-phase system, which interrupt the crack tip determination; (ii) irregular diamond-shaped indentations, chipping and/or the formation of multiple cracks and (iii) surface roughness associated with grain pullout, which could influence crack propagation and hinder crack measurement.

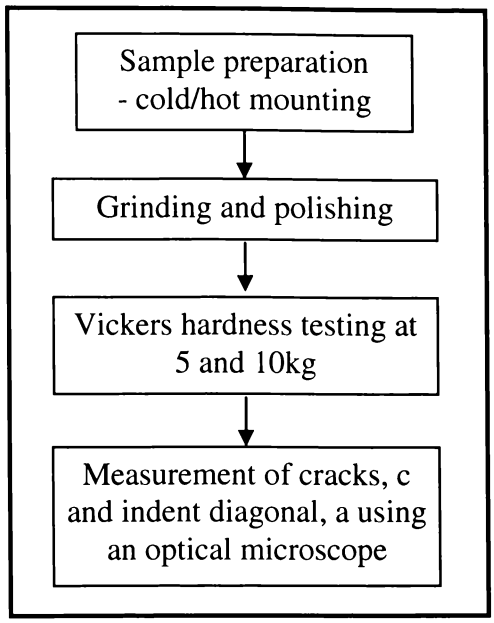

Figure 2.15: Procedure for fracture toughness measurements

The average fracture toughness readings obtained were within 30% of their uncertainty error therefore raised inevitable concerns about comparison with other reported data.

REFERENCES

1. Bassner, S.L. and E.H. Klingenberg, *Using polyvinyl alcohol as a binder.* The American Ceramic Society Bulletin, 1998: p. 71-75.
2. Walker, J., W.J., J.S. Reed and S.K. Verma, *Polyethylene glycol binders for advanced ceramics.* Ceramic Engineering and Science Proceedings, 1993. **14**(11-12): p. 58-79.
3. Ryan, M.J., G.C. Barris, W.R. Owers, C.M. Sheppard and G.V. White, *Mechanical properties of ceramic discs.* IPENZ Annual Conference Proceedings, 1997. **2**: p. 411-413.
4. *Joining of ceramic-metal systems: Procedures and microstructures*, in *Concise Encyclopedia of Advanced Ceramic Materials*, R.J. Brook, Editor. 1991, Pergamon Press: Oxford ; New York Cambridge, Mass. p. 263-271.
5. Ponton, C.B. and R.D. Rawlings, *Vickers indentation fracture toughness test Part 1 Review of literature and formulation of standardised indentation toughness equations.* Materials science and technology, 1989. **5**: p. 865-872.
6. Ponton, C.B. and R.D. Rawlings, *Vickers indentation fracture toughness test Part 2 Application and critical evaluation of standardised indentation toughness equations.* Materials science and technology, 1989. **5**: p. 961-976.
7. Dietz, M. and H.-D. Tietz, *Characterization of engineering ceramics by indentation methods.* Journal of Materials Science, 1990. **25**: p. 3731-3738.
8. Cook, S.G., J.E. King and J.A. Little, *Surface and subsurface Vickers indentation cracks in SiC, Si_3N_4 and sialon ceramics.* Materials science and technology, 1995. **11**: p. 1093-1098.
9. Anstis, G.R., P. Chantikul, B.R. Lawn and D.B. Marshall, *A critical evaluation of indentation techniques for measuring fracture toughness: I, Direct crack measurements.* Journal of the American Ceramic Society, 1981. **64**(9): p. 533-537.
10. Chantikul, P., G.R. Anstis, B.R. Lawn and D.B. Marshall, *A critical evaluation of indentation techniques for measuring fracture toughness: II, Strength method.* Journal of the American Ceramic Society, 1981. **64**(9): p. 539-543.
11. Zussman, J., *Physical methods in determinative mineralogy*: London ; New York. p. 138-147.
12. *Hardness*, in *Concise Encyclopedia of Advanced Ceramic Materials*, R.J. Brook, Editor. 1991, Pergamon Press: Oxford ; New York Cambridge, Mass. p. 206-209.

CHAPTER THREE:

Pressureless Sintering and Hot Pressing of Ti_3Al-Al_2O_3 Composite Powders

Knowledge and control of the solid state reactions that occur during heating of the discus milled powders is essential in order to combine high energy milling and thermal treatment to best effect in powder material processing. Over the past ten years studies have been performed using a combination of high energy milling with thermal treatment to produce a variety of intermetallics and metal matrix composites[1-4]. This chapter describes the results of a study on processing conditions and microstructure relationships for pressureless sintering and hot pressing of Ti_3Al-Al_2O_3 composite powders produced by heat treating the discus milled Al-TiO_2 composite powders in argon.

3.1 Powder Particle Morphology, Microstructure and Size Distribution

The microscopic appearance of the particle surfaces may be described in terms of light reflection (bright or grey) and in terms of texture (smooth or rough). Figure 3.1 shows the morphology of Ti_3Al-Al_2O_3-1 composite powder, produced by heat treating Al-TiO_2 composite powder after two hours of discus milling. The shapes of the particles are irregular and their sizes range from 1 to 20μm in diameter.

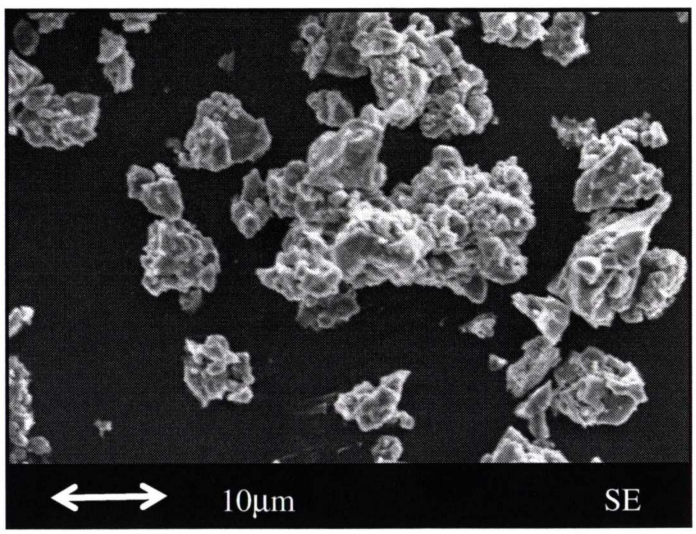

Figure 3.1: Morphology of Ti_3Al-Al_2O_3-1 composite powder

Figure 3.2 shows the morphology of Ti_3Al-Al_2O_3-2 composite powder, produced by heat treating Al-TiO_2 composite powder after two hours of discus milling. The shapes of the particles are irregular and their sizes range from 0.5 to 15μm in diameter, which is slightly finer than Ti_3Al-Al_2O_3-1 composite powder. Figure

3.2 appears to display two different particle forms. The first form labelled (a) in Figure 3.2, is similar to that of Ti_3Al-Al_2O_3-1 powder particles, that is, rough and irregular. These particles may consist of agglomerates of finer particles. The shape of the second form labelled (b) displays a more defined and smooth surface.

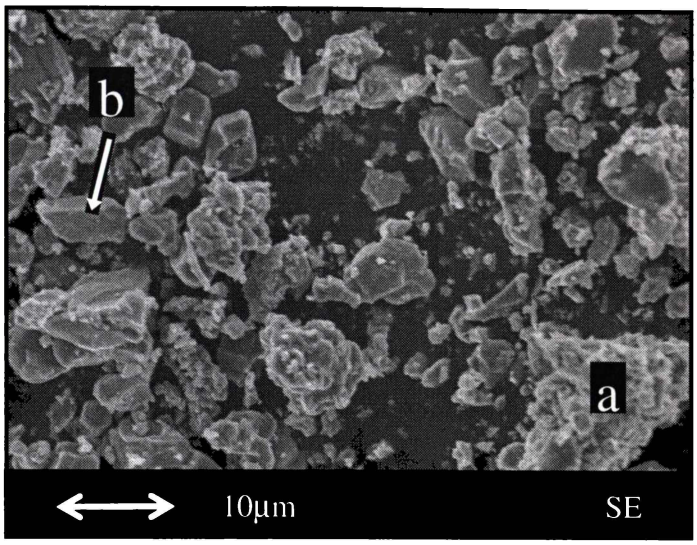

Figure 3.2: Morphology of Ti_3Al-Al_2O_3-2 composite powder

Figure 3.3 shows cross-sections of polished Ti_3Al-Al_2O_3-1 composite powder particles before and after 24 and 72 hours Si_3N_4 ball milling in chloroform. SEM micrographs (a) and (b) in Figure 3.3 show that the particles consist of Al_2O_3 embedded in a Ti_3Al matrix. As noted previously, the size varies from 0.5 to 15μm for the original Ti_3Al-Al_2O_3-1 composite powder before ball milling (a) and from 0.5 to 5μm for the powder after ball milling for 24 hours (b). The smaller particles in (b) retain a similar matrix structure to those in (a). SEM micrograph 3.3(c), on the other hand, shows that the composite particles were broken apart after 72 hours milling time.

Figure 3.4 shows cross sections of polished Ti_3Al-Al_2O_3-2 powder particles (a) before and after (b) 24 hours and (c) 72 hours of Si_3N_4 ball milling in chloroform. The original powder particles consist of Al_2O_3 embedded in a Ti_3Al matrix whose size varied from 0.5 to 20μm. Milling the powder for 24 hours reduced the particle size range from 0.5 to 3μm giving a result equivalent to Ti_3Al-Al_2O_3-1 composite powder that was milled for 72 hours. This highlights the importance of controlling the starting powder particle size distribution.

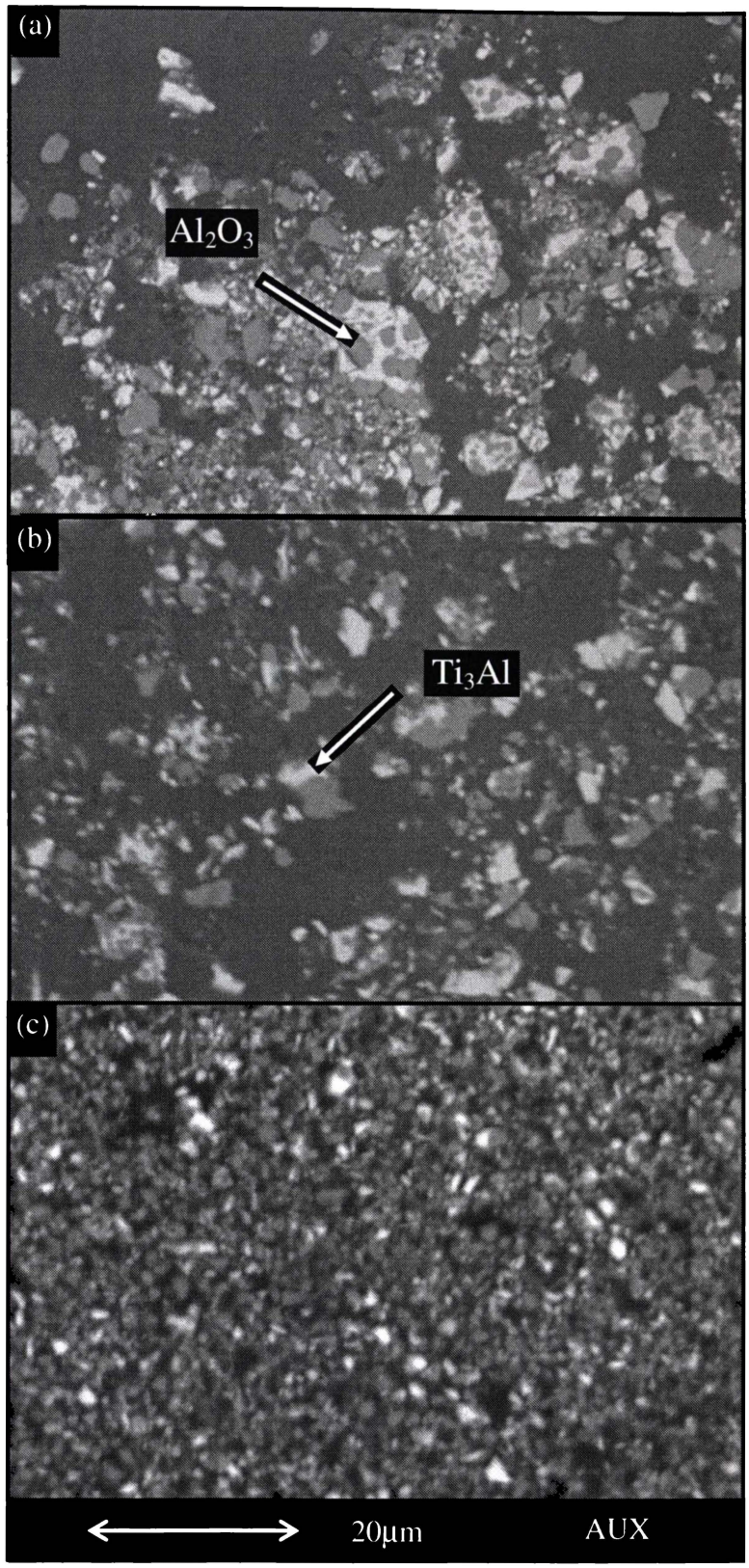

Figure 3.3: Cross sections of polished Ti_3Al-Al_2O_3-1 powder particles (a) before, (b) after 24 hours and (c) 72 hours ball milling

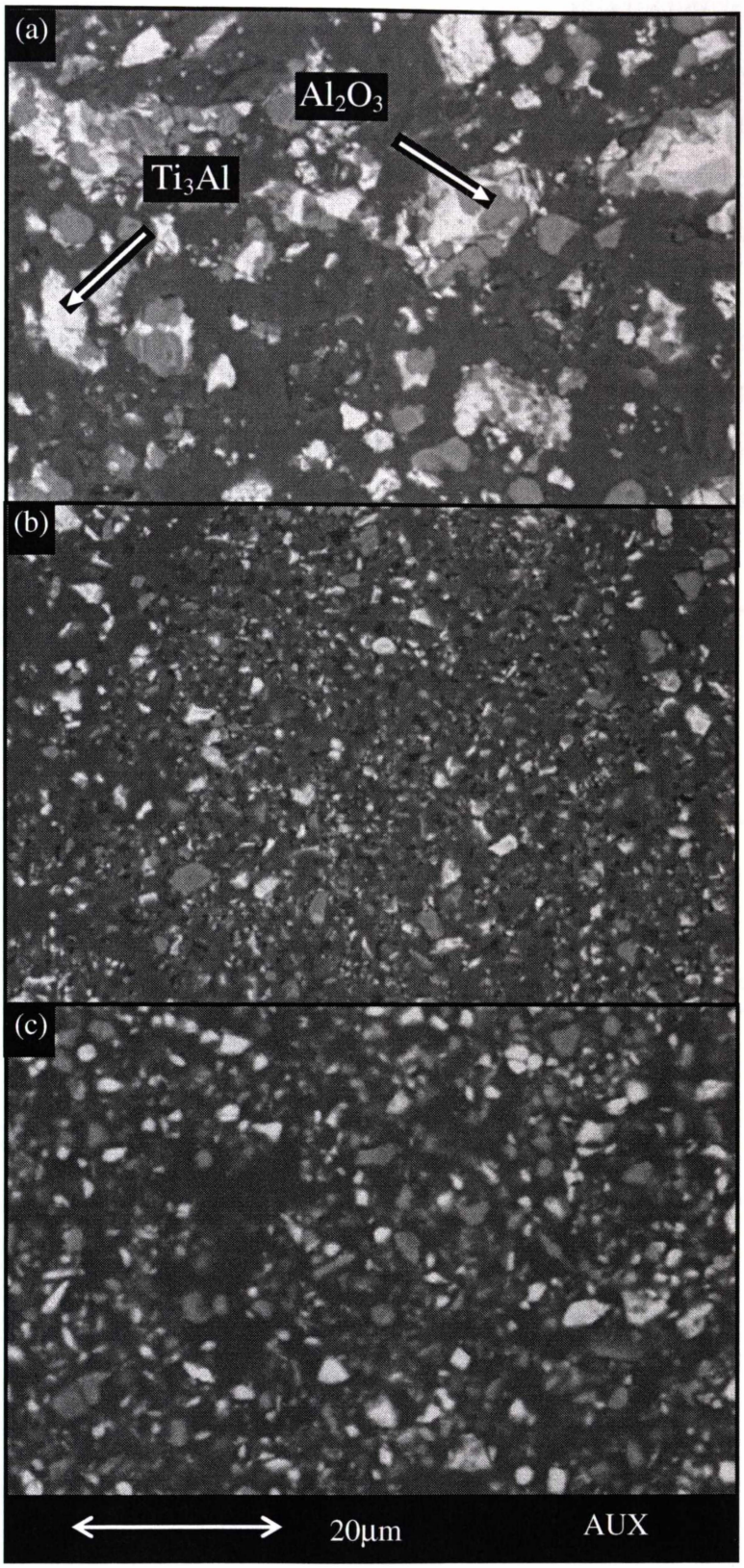

Figure 3.4: Cross sections of polished Ti_3Al-Al_2O_3-2 powder particles (a) before, (b) after 24 hours and (c) 72 hours ball milling

XRD patterns of 12.6, 2.4 and 1.2μm batches of Ti_3Al-Al_2O_3-1 composite powders are shown in Figure 3.5. The powders contain mixtures of rhombohedral corundum (α-Al_2O_3), hexagonal intermetallic aluminium titanium (Ti_3Al) and traces of face-centred cubic titanium oxide (TiO). Previous work on these materials has shown that Ti_3Al contains approximately 17at%O in solid solution by quantitative microanalysis using electron microprobe and wavelength dispersive spectrometry[5], which accounts for the shift in unit cell dimensions of Ti_3Al compared to those in the ICDD database. The increase of unit cell dimensions of Ti_3Al compared with that in the ICDD database implies the possibility of dissolved oxygen incorporated in Ti_3Al during sintering. The solubility of oxygen in Ti_3Al is about 12±3at% for Ti_3Al[6-8].

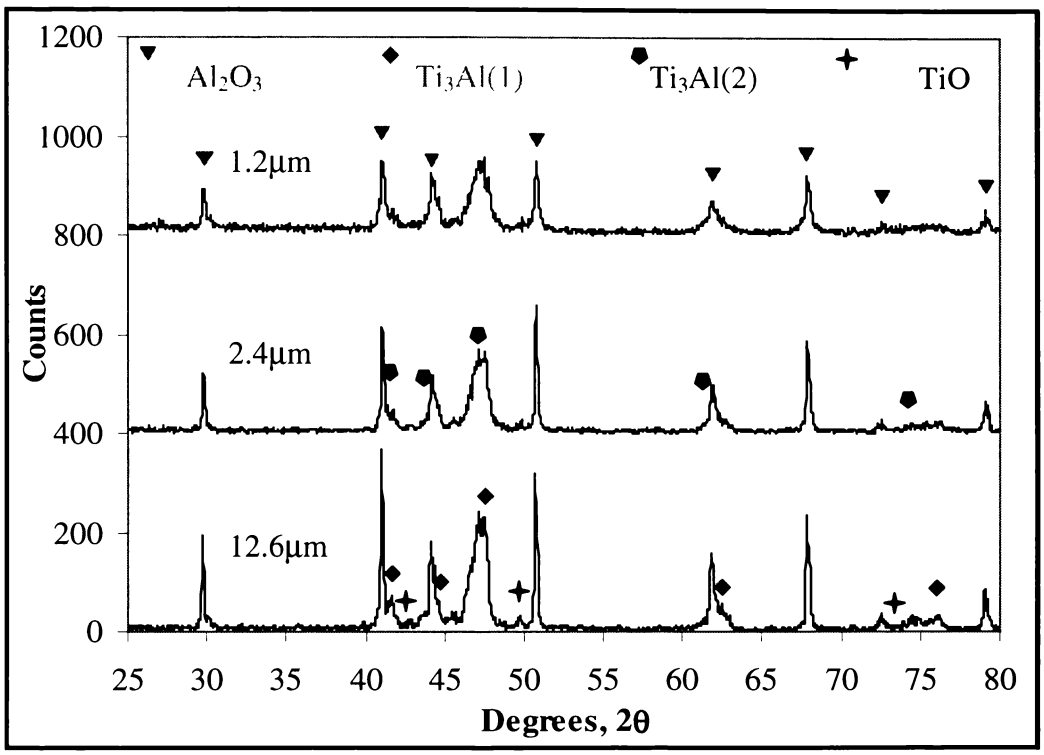

Figure 3.5: XRD patterns of Ti_3Al-Al_2O_3-1 composite powder with 12.6, 2.4 and 1.2μm mean particle sizes

XRD patterns of Ti_3Al-Al_2O_3-1 and Ti_3Al-Al_2O_3-2 composite powders are shown in Figure 3.6. The powders contain mixtures of rhombohedral corundum (α-Al_2O_3), hexagonal intermetallic aluminium titanium (Ti_3Al), traces of face-centred cubic titanium oxide (TiO) and residual rutile (TiO_2). Compared to Ti_3Al-Al_2O_3-1 composite powder, the XRD trace shows two distinct Ti_3Al phases. The explanation is based on the assumption that different amounts of dissolved oxygen

were picked up during sintering. An increase in both unit cell dimensions and hence the cell volume was observed for two Ti_3Al phases compared to those in the ICDD database (Refer Chapter Five). Unit cell dimensions for the standard Ti_3Al phase from ICDD database are a = 5.77Å and c = 4.62Å. The unit cell dimensions of $Ti_3Al(1)$ and $Ti_3Al(2)$ after XRD peak shift adjustments give a = 5.799Å; c = 4.715Å and a = 5.912Å; c = 4.814Å, respectively.

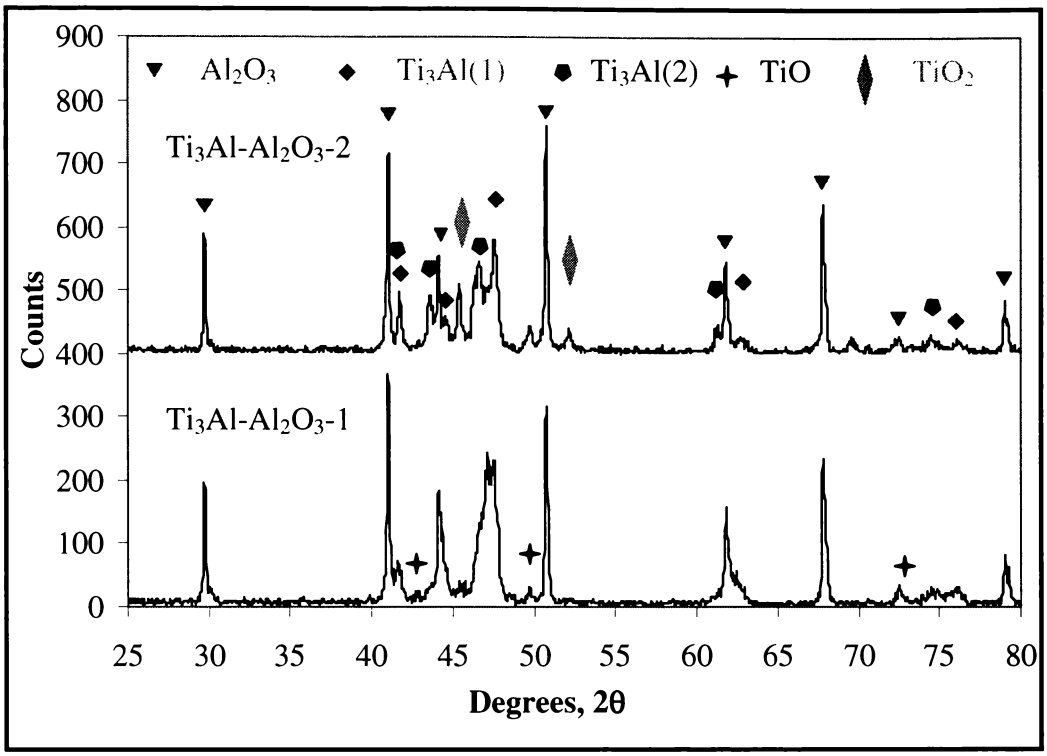

Figure 3.6: XRD patterns of Ti_3Al-Al_2O_3-1 and Ti_3Al-Al_2O_3-2 composite powders

Figure 3.7 and Figure 3.8 show the particle size distributions of Ti_3Al-Al_2O_3-1 composite powder, ball milled at 0, 24 and 72 hours. These curves demonstrated a clear reduction in particle size with increasing milling time. The size ranges from 0.5 to 100μm for the original powder before milling, from 0.1 to 20μm for the powder after 24 hours milling and from 0.2 to 10μm for the Ti_3Al-Al_2O_3-1 composite powder after 72 hours milling in chloroform. The median particle diameters of the Ti_3Al-Al_2O_3-1 particles were determined as 12.6, 2.4 and 1.2μm respectively. These measured particle sizes were comparable to the particle sizes obtained from SEM images

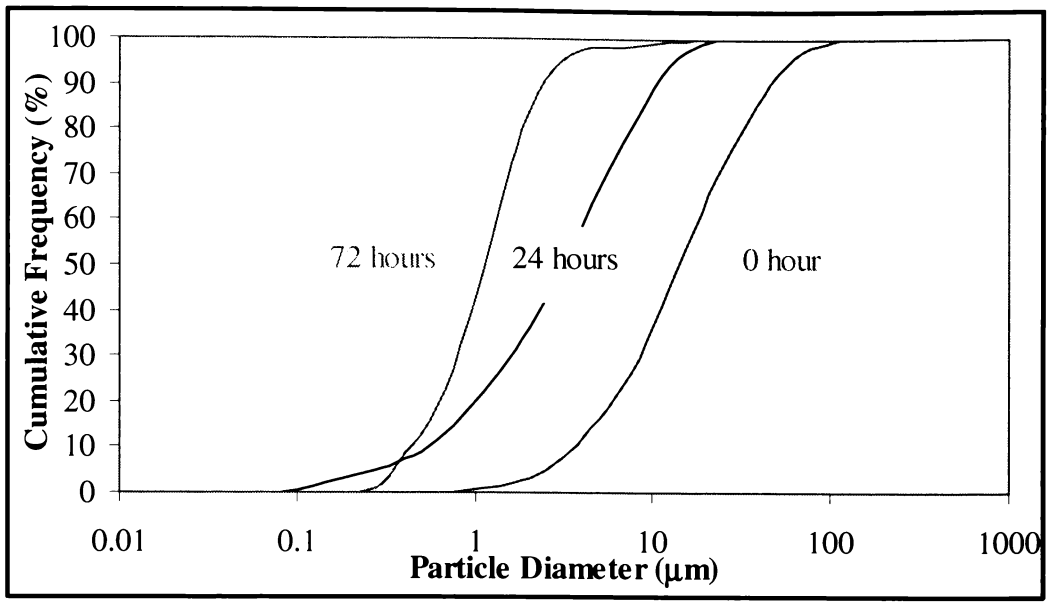

Figure 3.7: Particle size distributions (cumulative frequency) of Ti_3Al-Al_2O_3-1 composite powder after milling for 0, 24 and 72hours

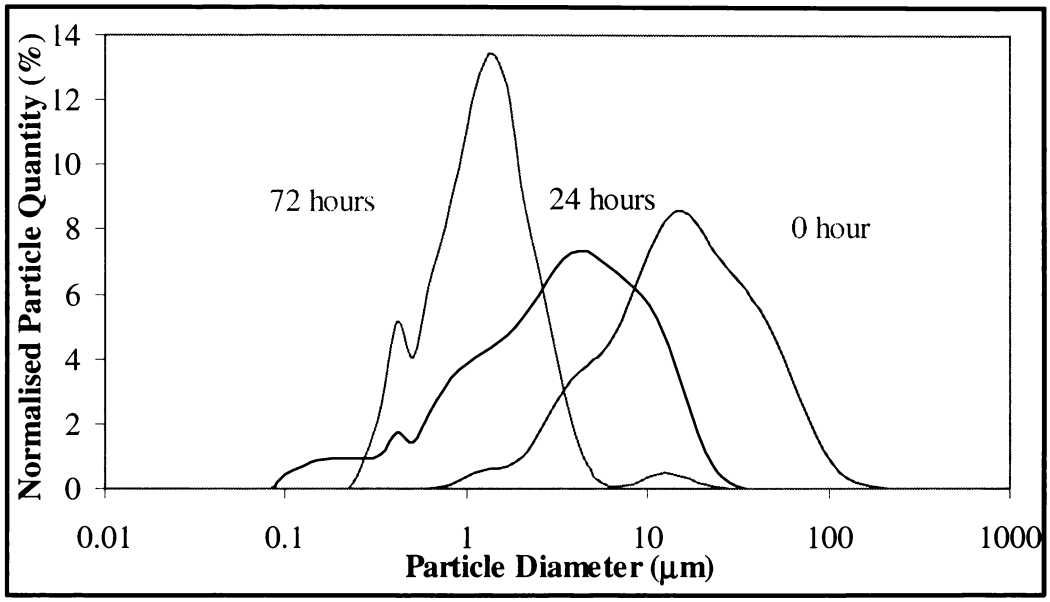

Figure 3.8: Normalised particle size distributions (frequency) of Ti_3Al-Al_2O_3-1 composite powder after milling for 0, 24 and 72hours

From Figure 3.9 and Figure 3.10, the particle size distribution curves of Ti_3Al-Al_2O_3-2 composite powder also demonstrate a reduction of particle size from 0 to 24 hours of ball milling. The size ranges from 0.5 to 100μm for the original composite powder before milling and from 0.2 to 12μm for the composite powder after 24 and 72 hours milling. The median particle diameters of the Ti_3Al-Al_2O_3-2 batch were determined as 11.2 and 2.2 μm (for both 24 and 72 hours milling) respectively. The overlap of 24 and 72 hours milled curves indicates that the

particle size reduction has ceased after 24 hours. As supported by the SEM images, the particle size of Ti_3Al-Al_2O_3-2 composite powder ball milled for 24 hours is very similar to the particle size of the composite powder ball milled for 72 hours.

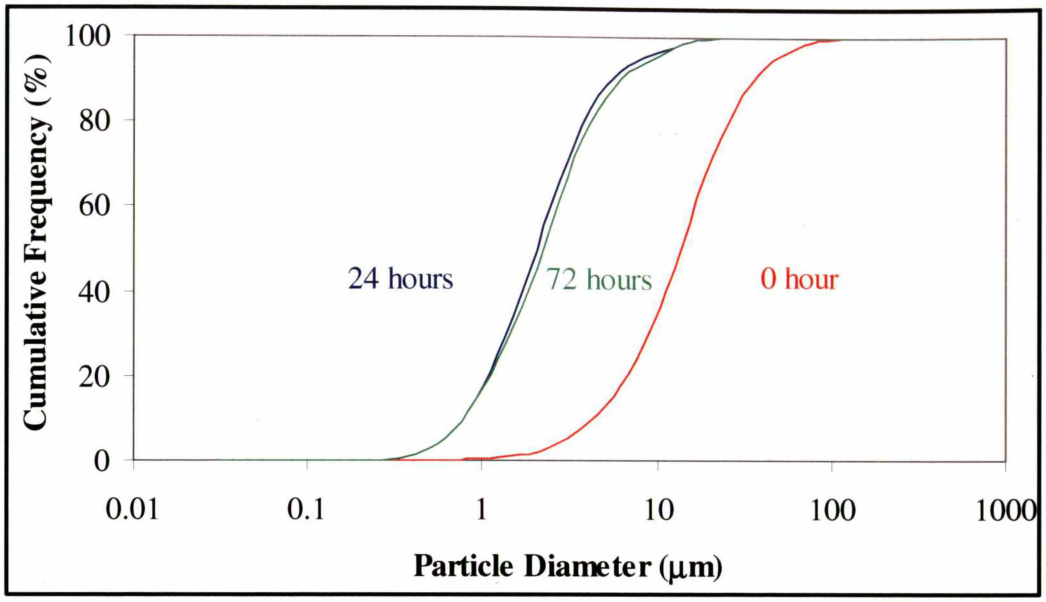

Figure 3.9: Particle size distributions (cumulative frequency) of Ti_3Al-Al_2O_3-2 composite powder after milling for 0, 24 and 72 hours

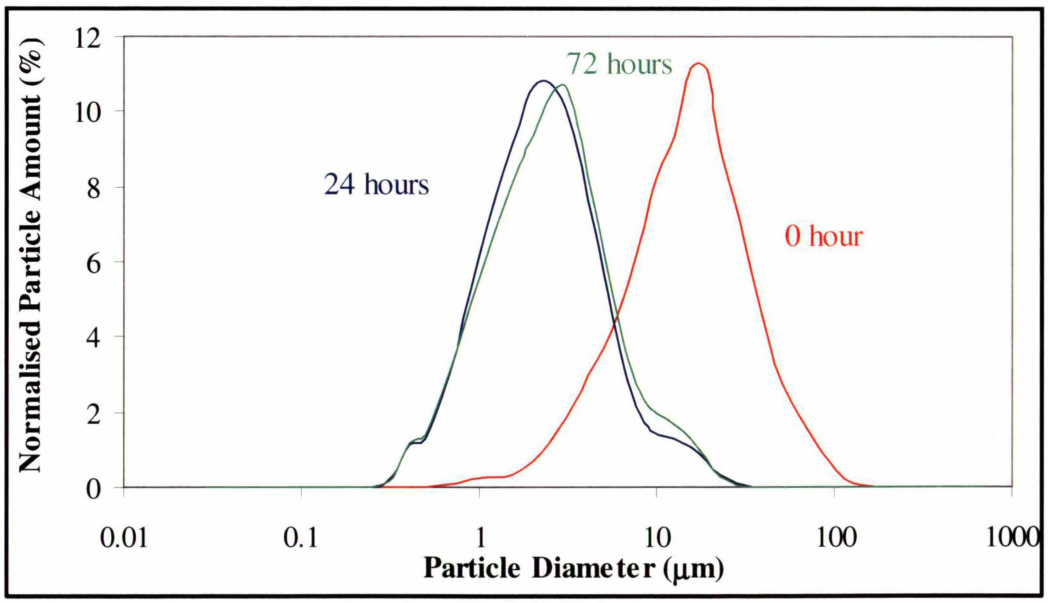

Figure 3.10: Normalised particle size distributions (frequency) of Ti_3Al-Al_2O_3-2 composite powder after milling for 0, 24 and 72 hours

Both Ti_3Al-Al_2O_3-1 and Ti_3Al-Al_2O_3-2 composite powders show limitations on particle size reduction achieved using this milling technique. The mean normalised diameter versus the ball milling time presented in Figure 3.11

demonstrate that the particle size of the composite powder can not be effectively reduced below 1μm mean diameter using Si_3N_4 ball milling in chloroform.

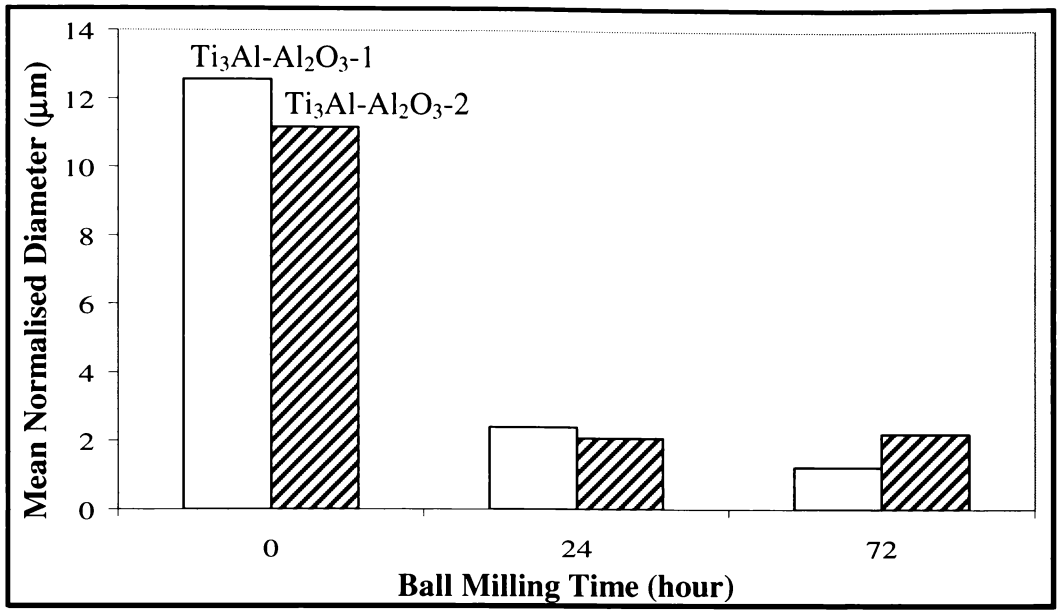

Figure 3.11: Mean normalised diameter of Ti_3Al-Al_2O_3-1 and Ti_3Al-Al_2O_3-2 particles

3.2 Sintering Behaviour of Ti_3Al-Al_2O_3-1

3.2.1 Phase Structure

XRD analyses were performed on powdered samples of the composites produced by hot pressing the Ti_3Al-Al_2O_3-1 composite powders. Figure 3.12, Figure 3.13 and Figure 3.14 show the XRD patterns of the composites produced by hot pressing 12.6, 2.4 and 1.2μm Ti_3Al-Al_2O_3-1 composite powders, respectively. The intensity profiles obtained from the XRD analyses are summarised in Figure 3.15. The intensity of the phases has been calculated by measuring the peak height of the strongest peak of each phase (APPENDIX A). To assist with comparison of X-ray data, all specimens were examined using consistent sample holder and specimen volumes.

For all the 12.6, 2.4 and 1.2 μm samples after hot pressing, the Al_2O_3 phase maintains a reasonable constant level. For the 12.6μm sample, the intensity of Ti_3Al phase vanishes with increasing temperature to coincide with the sharp increase of TiO(1) intensity at 1666°C. The 1.2μm hot pressed samples show a new second TiO(2) phase with different cell dimension in addition to at least a 30wt.% increment in the TiO(1) phase intensity level when compared to both the

12.6 and 2.4 μm samples after hot pressing. This is due to the increased surface area and therefore increased surface oxygen pickup resulting from longer ball milling times. The Ti_3Al phase declines markedly between measurements of the initial untreated composite powder to temperatures exceeding 1400°C as illustrated in Figure 3.14.

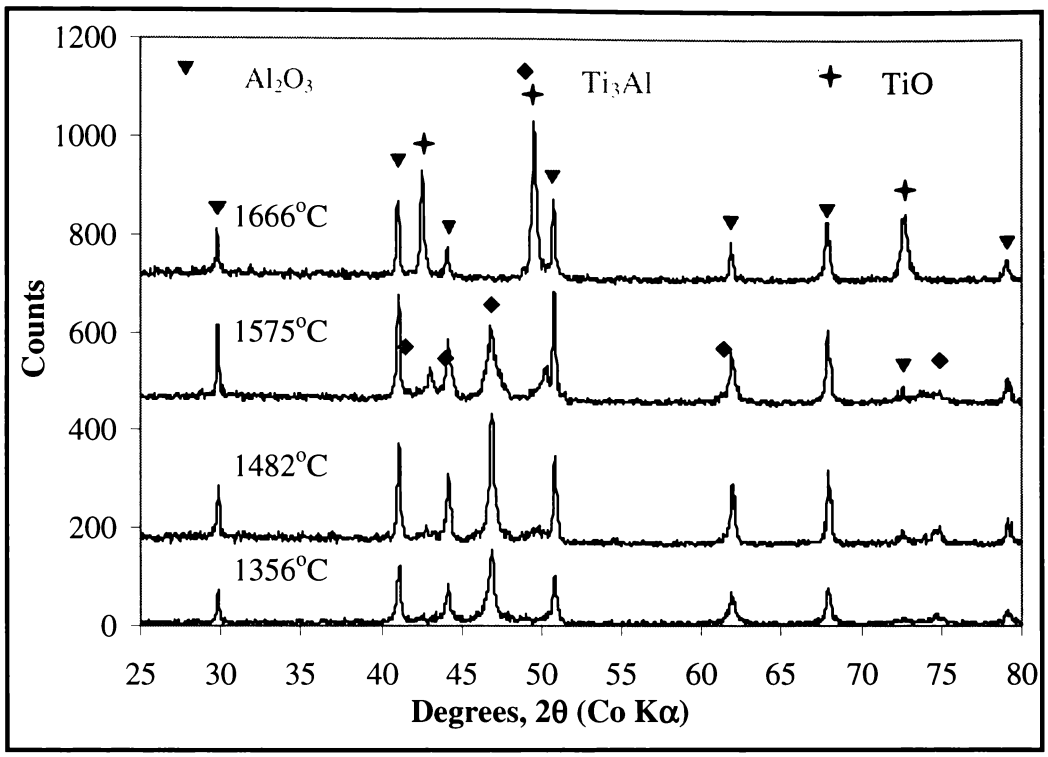

Figure 3.12: XRD patterns of composites produced by hot pressing 12.6μm Ti_3Al-Al_2O_3-1 composite powder under vacuum at different temperatures

The reduction of particle size increases the surface area of the composite powder, which in turn raises the probability of oxygen pickup during sintering. It is likely that the vacuum sintering atmosphere contained a low partial pressure of oxygen. Although thermodynamic data for Ti_3Al does not appear in the international databases, it can be hypothesised that under constrained oxygen environment, some limited oxidation of Ti_3Al will occur, forming TiO. For example this may be represented as: $2Ti_3Al + 4.5O_2 \rightarrow 6TiO + Al_2O_3$, two TiO phases were detected for the 1μm samples after sintering as a result.

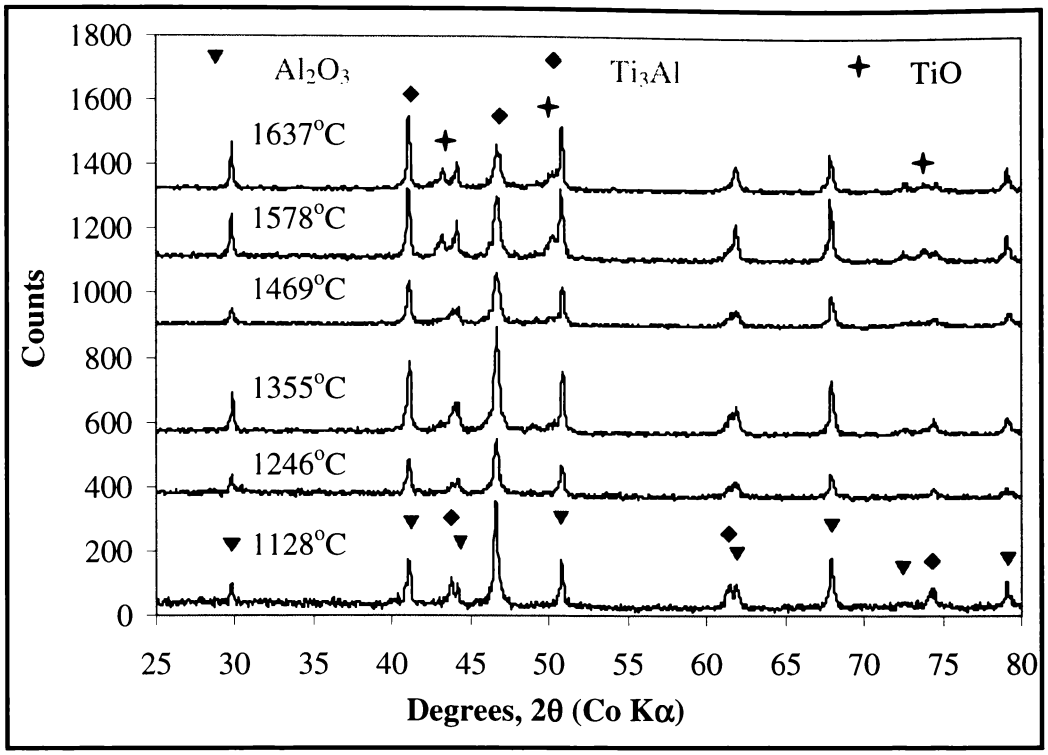

Figure 3.13: XRD patterns of composites produced by hot pressing 2.4μm Ti_3Al-Al_2O_3-1 composite powder under vacuum at different temperatures

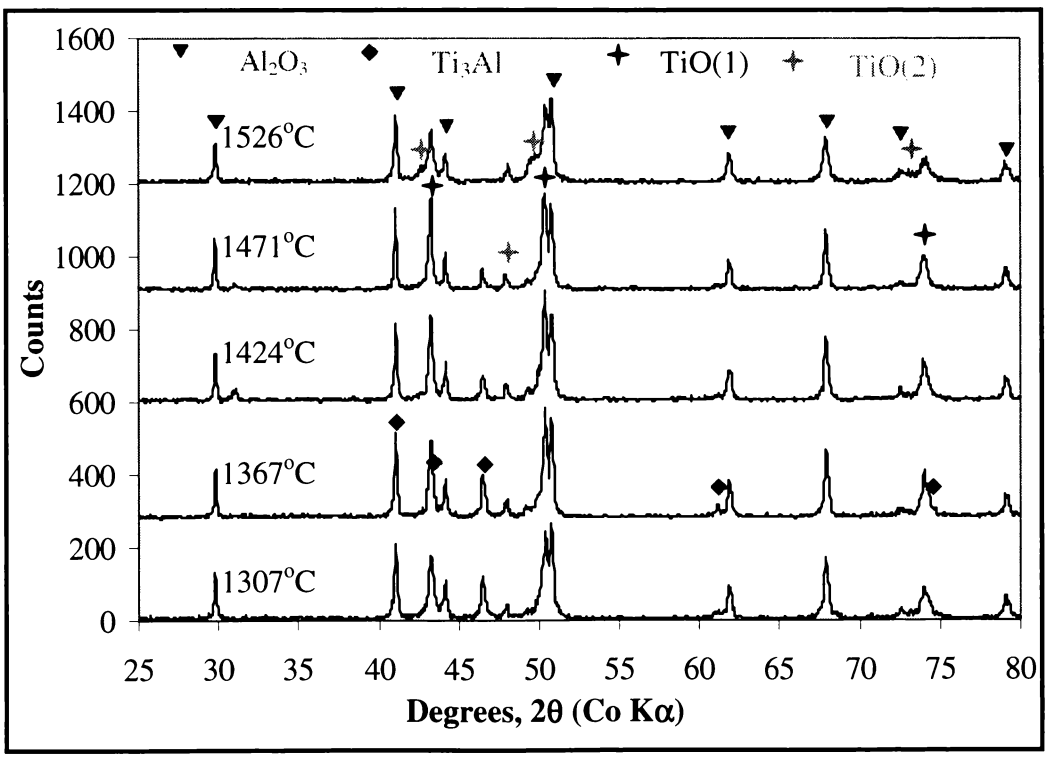

Figure 3.14: XRD patterns of composites produced by hot pressing 1.2μm Ti_3Al-Al_2O_3-1 composite powder under vacuum at different temperature

From Figure 3.16 and Figure 3.17, two TiO phases were detected after pressureless sintering under vacuum for both 12.6 and 2.4μm Ti_3Al-Al_2O_3-1 composite powders, which were not seen in the hot pressing experiments. The intensity profiles in Figure 3.18 and Figure 3.19 obtained from the XRD analyses show that after pressureless sintering, the Al_2O_3 phase content remained reasonably constant. For both the 12.6 and 2.4μm samples, the Ti_3Al phase vanishes with increasing temperature to coincide with the increase of TiO(1) and TiO(2) intensities.

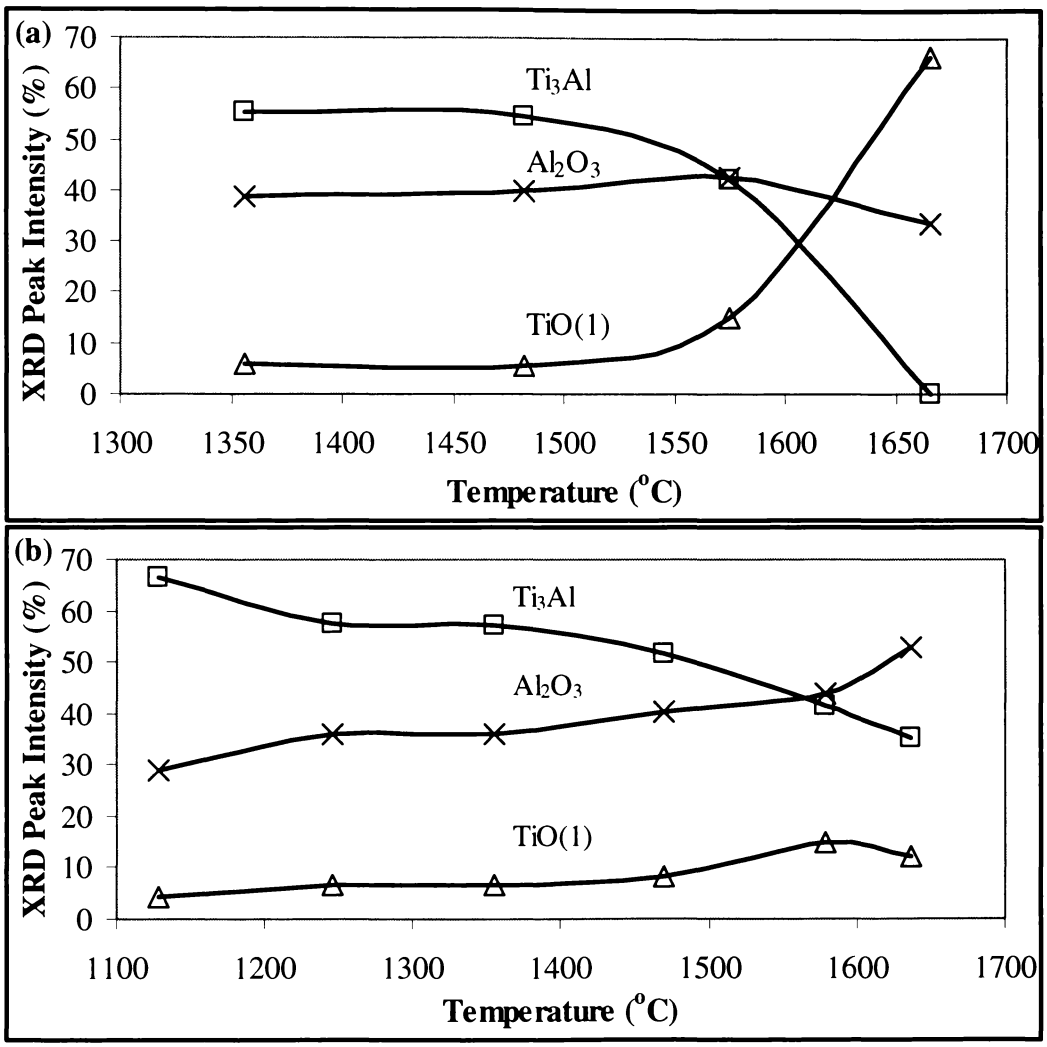

Figure 3.15: XRD phase intensity profile of composites produced by hot pressing (a) 12.6 and (b) 2.4μm Ti_3Al-Al_2O_3-1 composite powders under vacuum at different temperatures

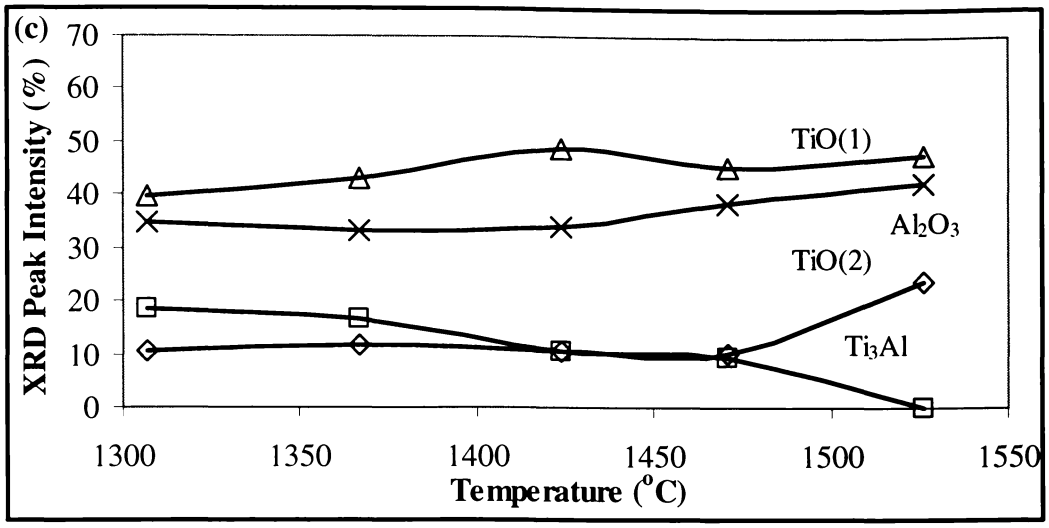

Figure 3.15(c): XRD phase intensity profile of composites produced by hot pressing 1.2μm Ti_3Al-Al_2O_3-1 composite powders under vacuum at different temperatures

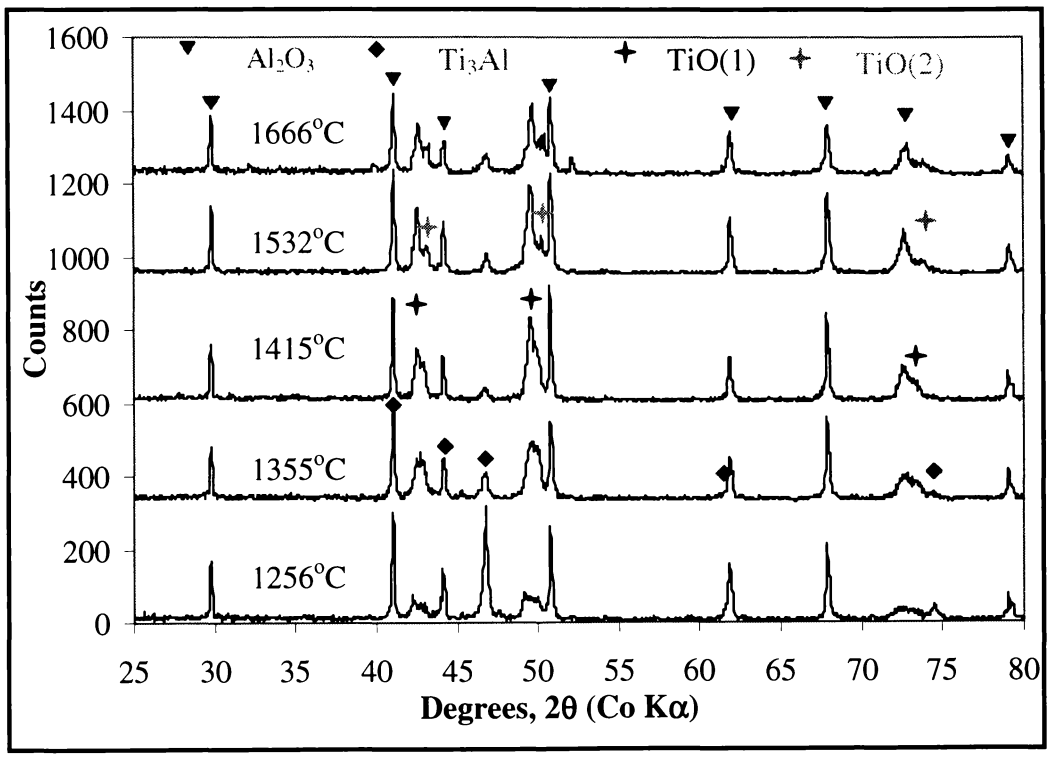

Figure 3.16: XRD phase intensity profile of composites produced by pressureless sintering of 12.6μm Ti_3Al-Al_2O_3-1 composite powder under vacuum at different temperatures

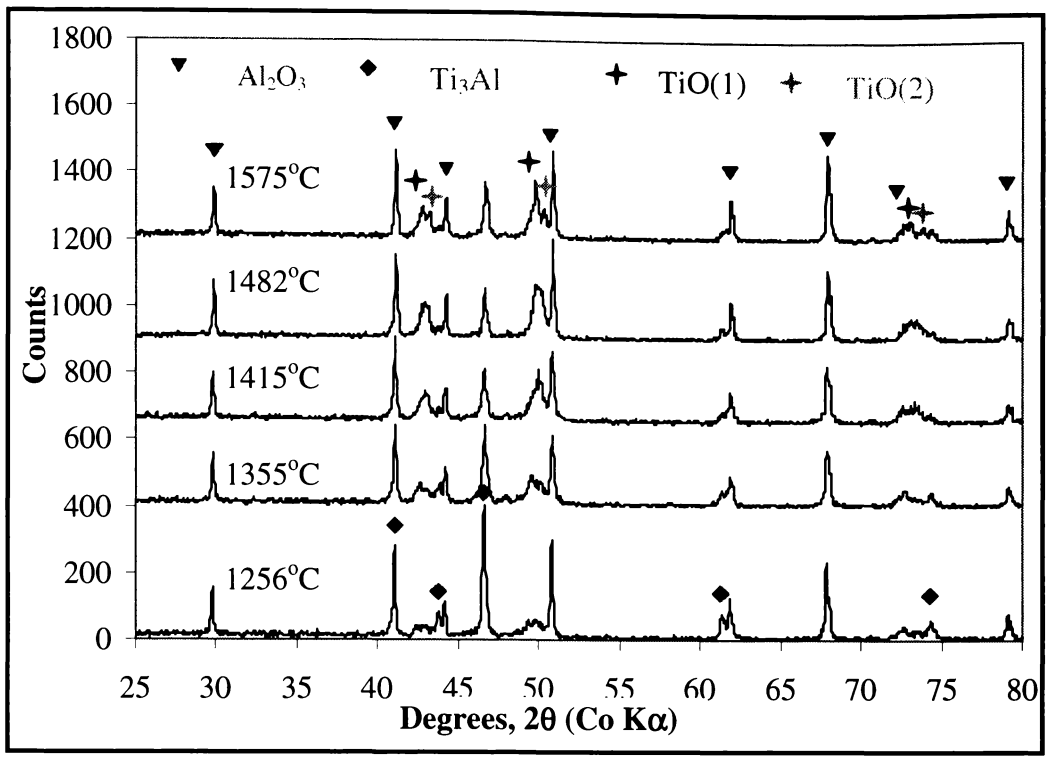

Figure 3.17: XRD phase intensity profile of composites produced by pressureless sintering of 2.4μm Ti_3Al-Al_2O_3-1 composite powder under vacuum at different temperatures

This can be understood by the more open design of the graphite pot used for the pressureless sintering compared to the graphite die used for hot pressing. In the latter case, the samples were tightly shielded from the furnace atmosphere during sintering that may have contained a low partial pressure of oxygen. Refer Figure 2.7 in Chapter Two for the schematic diagram of the graphite die used for hot pressing. The spacers and the pressing die are tightly constricted during compression by the pistons. This design may have constrained oxygen access to the samples.

The loss of intensity of the Ti_3Al phase with increasing temperature, coinciding with the increase of TiO(1) and TiO(2) intensities, was also seen in the pressureless sintering of Ti_3Al-Al_2O_3-2 described in Section 3.3. The formation of TiO from Ti_3Al leads to some improvement in properties such as (1) a reduction in porosity and increase in density of the sintered bodies of the composite powders and (2) an increase in Vickers hardness and biaxial strength, which is discussed later in Chapter Six.

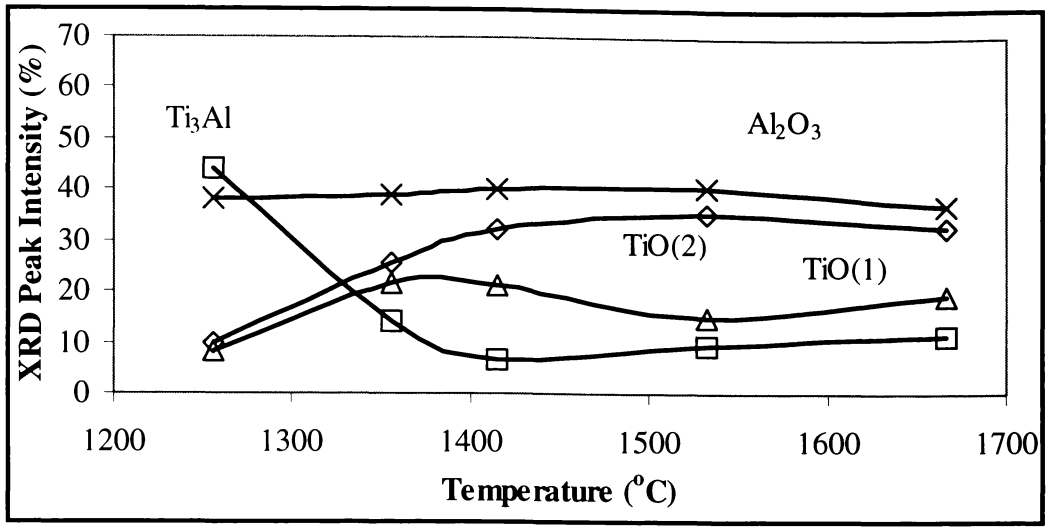

Figure 3.18: XRD phase intensity profile of composites produced by pressureless sintering 12.6μm Ti_3Al-Al_2O_3-1 composite powder under vacuum at different temperatures

Low partial pressure of oxygen present during sintering in the hot press only became a concern in the sintering of the Al-TiO_2 composite powders, which is described in more detail in Chapter Four.

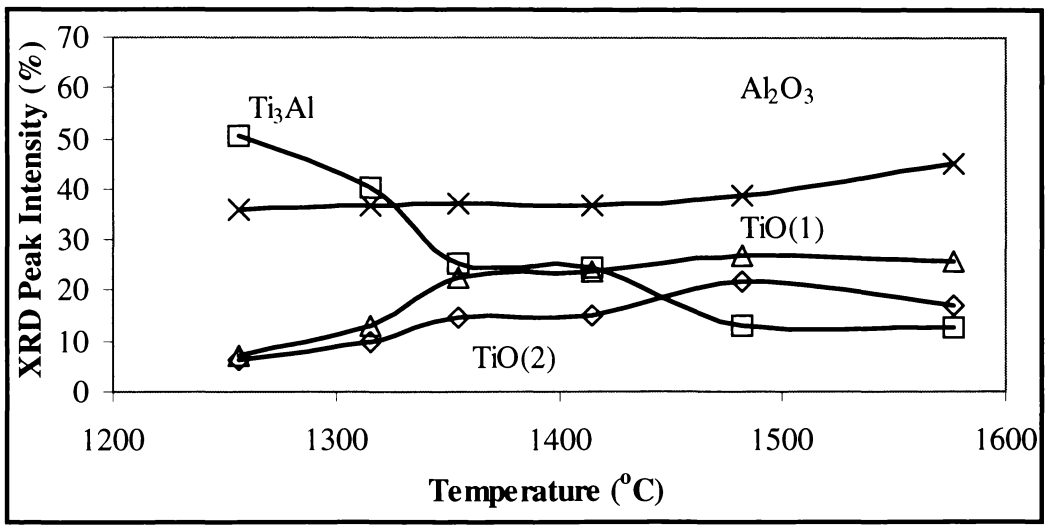

Figure 3.19: XRD phase intensity profile of composites produced by pressureless sintering of 2.4μm Ti_3Al-Al_2O_3-1 composite powder under vacuum at different temperatures

3.2.2 Densification

Figure 3.20 shows the dilatometry curves of the Ti_3Al-Al_2O_3-1 powder compacts during pressureless sintering as a function of temperature. The features of the dilatometry curve are expansion at the initial stage of heating up, followed by

contraction during the sintering and cooling stages after the maximum temperature is reached. The powder compacts made from 12.6, 2.4 and 1.2μm Ti_3Al-Al_2O_3-1 composite powders show similar characteristics with different sintering rates. 1.2μm samples sintered at a much earlier stage and to a much greater extent than 2.4μm sample and 12.6μm samples. This is due to the increased surface area of the finer powders.

EDS and XRD analyses show that the composite consists of Al_2O_3 in a matrix of Ti_3Al and TiO. The volume fraction of Al_2O_3 and the matrix of the composites produced from 12.6, 2.4 and 1.2μm Ti_3Al-Al_2O_3-1 composite powders is calculated based on Equation 2.1, $4Al+3TiO_2 \rightarrow 3Ti+2Al_2O_3$ from Chapter Two. The coefficient of thermal expansion (CTE) of the composites can be calculated from the slope of the linear curve during cooling obtained from Figure 3.20. Using this information and the standard CTE value of Al_2O_3[9], CTE values of the Ti rich matrix are calculated and shown in Table 3.1.

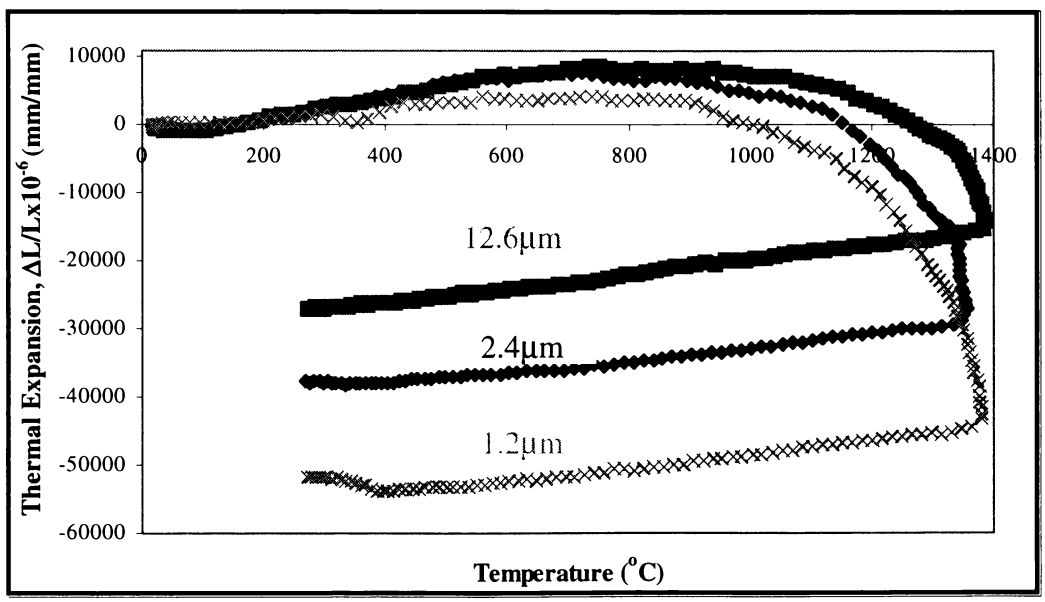

Figure 3.20: Dilatometry curves of Ti_3Al-Al_2O_3-1 composite powder compacts during pressureless sintering in argon

There is a significant contrast between the composites produced by hot pressing 12.6 and 2.4μm Ti_3Al-Al_2O_3-1 composite powders, which exhibit particle growth and microcracking whereas the composites produced by hot pressing 1.2μm Ti_3Al-Al_2O_3-1 composite powder do not. As seen in Table 3.1, the difference between the CTE values of Al_2O_3 and the matrix is clearly greater in the 12.6 and

2.4μm samples, leading to thermal mismatch and microcracking. The lower CTE value achieved for the composites produced by hot pressing 1.2μm is attributed by the higher fraction of TiO phases in the matrix found in the composites as seen earlier in Figure 3.15, compared to the composites produced by hot pressing 12.6μm and 2.4μm Ti_3Al-Al_2O_3 composite powders. Particle growth phenomena are described in more detail in Section 3.2.3.

Table 3.1: Thermal expansion coefficient of 12.6, 2.4 and 1.2μm Ti_3Al/Al_2O_3-1

Composites	Thermal Expansion Coefficient ($x10^{-6}$mm/(mm/°C))		
	Composite	Al_2O_3[9]	Matrix
12.6μm	11.1	8.9	14.6
2.4μm	10.1	8.9	12.1
1.2μm	8.6	8.9	8.1

3.2.3 Pores and Al_2O_3 Particle Morphology

After drying, forming (uniaxial pressing and cold isostatic pressing) and binder burnout, the green bodies have achieved up to 65% of their theoretical density. SEM observations on a green body (12.6μm Ti_3Al-Al_2O_3-1 composite powder) produced from vacuum impregnation of resin into the green compact in a plane perpendicular to the applied stress showed a homogeneous microstructure (Figure 3.21).

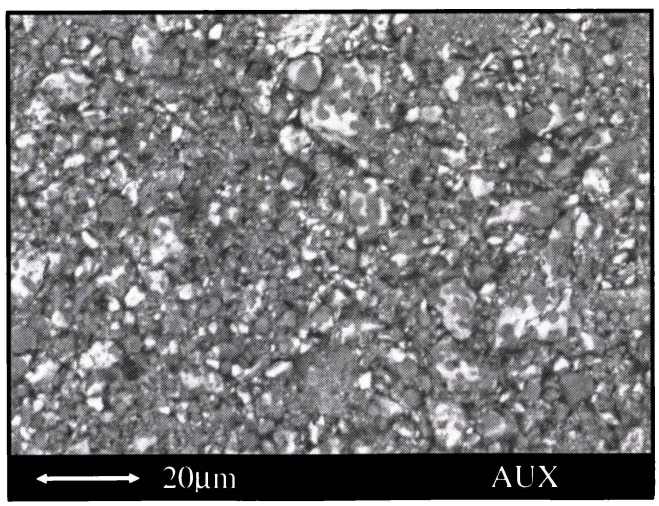

Figure 3.21: SEM micrograph of green body (perpendicular to the applied stress)

Figure 3.22 shows the open porosity of the composites produced by pressureless sintering and hot pressing 12.6, 2.4 and 1.2μm Ti_3Al-Al_2O_3-1 composite powders as a function of temperature for one hour of holding period. The open porosity decreases as the sintering/hot pressing temperature increases. The composites produced by pressureless sintering 12.6μm composite powder have the highest porosity trend compared with the others. The porosity trend data decrease by up to 12% following ball milling, reducing the composite powder mean particle size to 2.4μm.

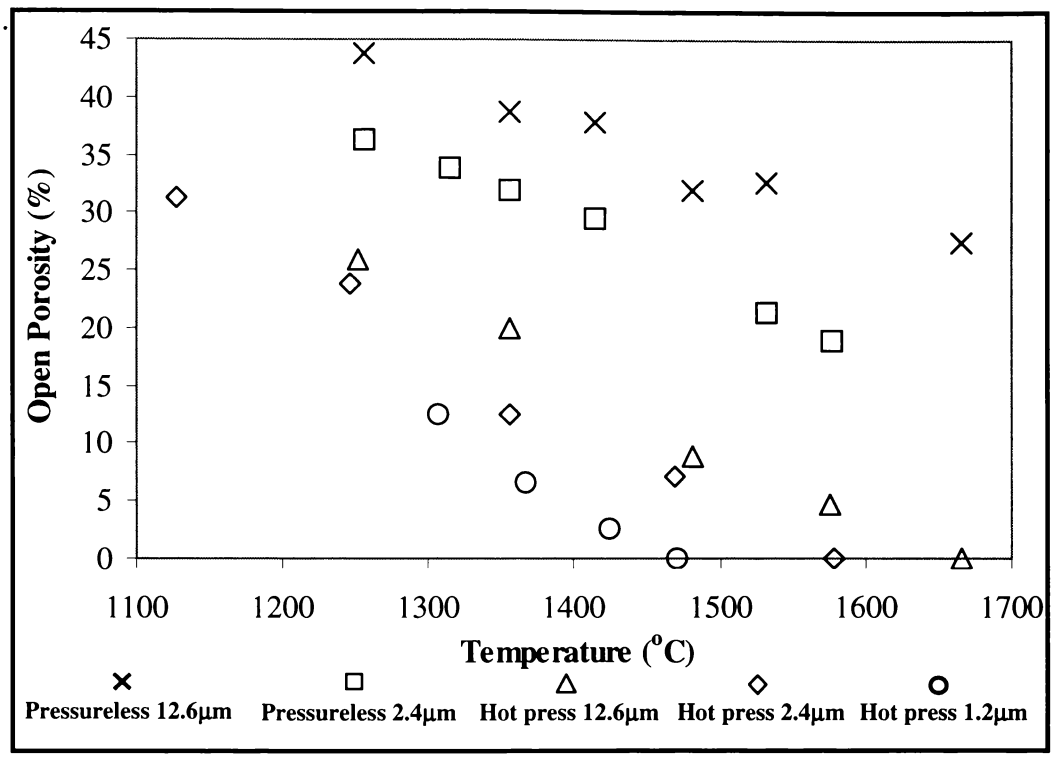

Figure 3.22: Open porosity of composites produced by pressureless sintering and hot pressing Ti_3Al-Al_2O_3-1 composite powders under vacuum as a function of temperature

The hot pressed samples display further reduction in the porosity by up to 20 and 27% for the 2.4 and 12.6μm samples compared to their counterpart pressureless sintered samples. As the particle size decreases, the open porosity of the hot pressed sample tends to 0% at a much lower sintering temperature. The open porosity of the samples reached 0% at approximately 100°C decrements in hot pressing temperature as the particle size was reduced from 12.6 to 2.4 and then to 1.2μm.

Figure 3.23 shows that the bulk density of pressureless sintered and hot pressed samples increases with increasing sintering/hot pressing temperature. As the temperature increases, the bulk density approaches theoretical density. Two factors contribute to the increase of bulk density of Ti_3Al-Al_2O_3-1 samples pressureless sintered and hot pressed under vacuum. The first factor has been discussed earlier, that is the reduction of porosity. The second factor is the undesirable formation of TiO from Ti_3Al, which was discussed in Section 3.2.1.

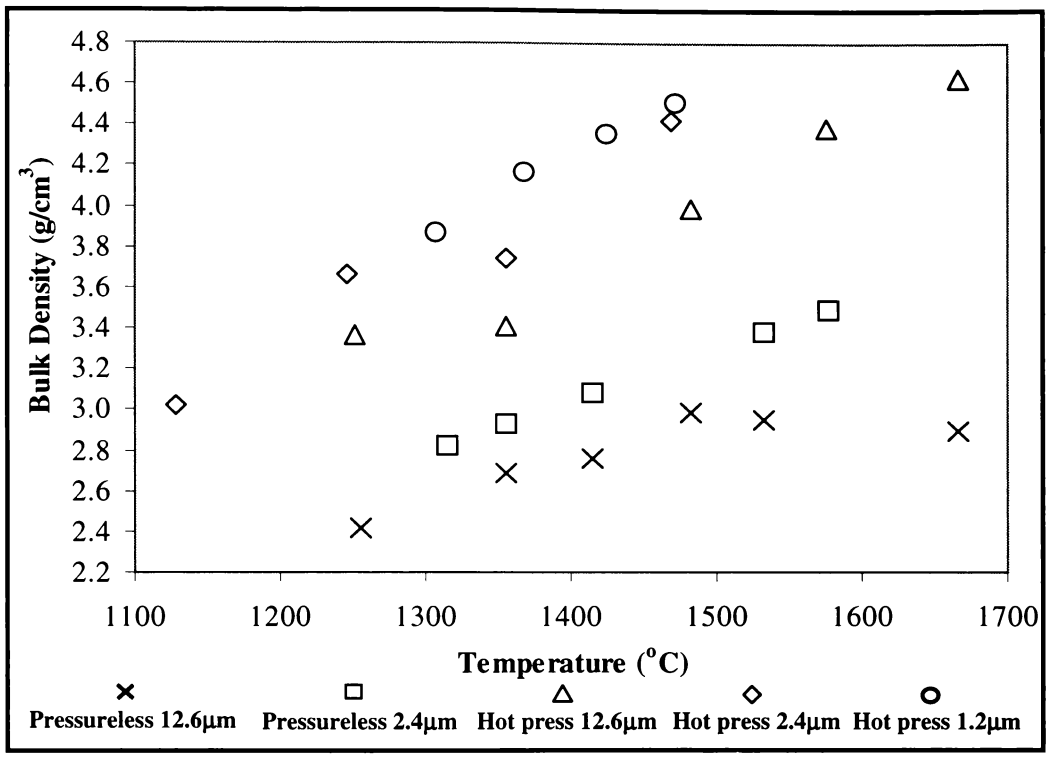

Figure 3.23: Bulk density of composites produced by pressureless sintering and hot pressing Ti_3Al-Al_2O_3-1 composite powders under vacuum as a function of temperature

The bulk density increases with the reduction of starting particle size. By reducing the particle size from 12.6 to 2.4μm, the bulk density improves by up to 12% with increasing sintering temperature. Hot pressing of 12.6μm composite powder improves the bulk density by more than 30% after pressureless sintering or hot pressing at 1666°C. Hot pressed bodies of both 2.4 and 1.2μm composite powders approached theoretical density at some 200°C lower sintering temperatures compared to the 12.6μm hot pressed body. The 12.6μm pressureless sintered samples levelled off at approximately 2.9g/cm^3 with increasing temperature.

Figure 3.24, Figure 3.25 and Figure 3.26 show the SEM micrographs of polished hot pressed 12.6, 2.4 and 1.2μm Ti_3Al-Al_2O_3-1 samples. The dark grey particles are identified as the Al_2O_3 phase embedded in a pale grey matrix identified as a mixture of Ti_3Al and TiO as shown by the XRD patterns in Figure 3.12, Figure 3.13 and Figure 3.14. The quantity of pores decreases with increasing hot pressed temperature for both 12.6 and 2.4μm samples up to approximately 1575°C and both 12.6 and 2.4μm samples show abrupt particle growth above 1500°C. The effect of impurities brought in by starting materials such as Y and La, which play significant roles in influencing the grain growth and densification behaviour of alumina during sintering was expected to be insignificant in this study. This is because the sintering behaviour of the titanium based intermetallic-alumina composites is dominated by the sintering behaviour of the intermetallic phases rather than that of the alumina phase in the composites. For sintering of metallic or intermetallic phases, the existence of impurities such as Y or La would not have an important effect on their densification behaviour.

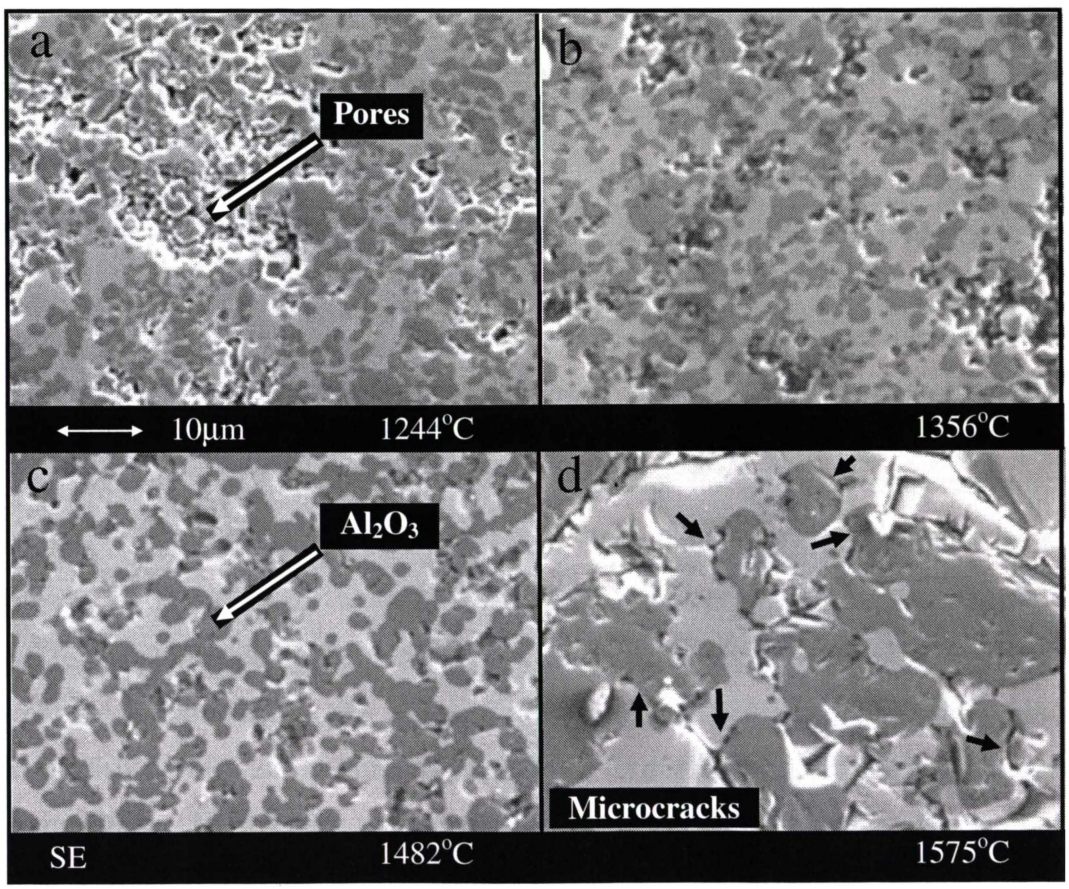

Figure 3.24: Hot pressed 12.6μm Ti_3Al-Al_2O_3-1 samples at (a) 1244, (b) 1356, (c) 1482 and (d) 1575°C at 31MPa

Figure 3.24(d) and Figure 3.25(d) show a combination of microcracks (as indicated by the arrows) and grain pullouts. Microcracks are observed around the grain boundaries on the hot pressed 12.6μm and 2.4μm samples at 1575°C. This is due to the large difference in the thermal expansion coefficients between the Al_2O_3 particles and Ti_3Al/TiO matrix (refer section 3.2.2).

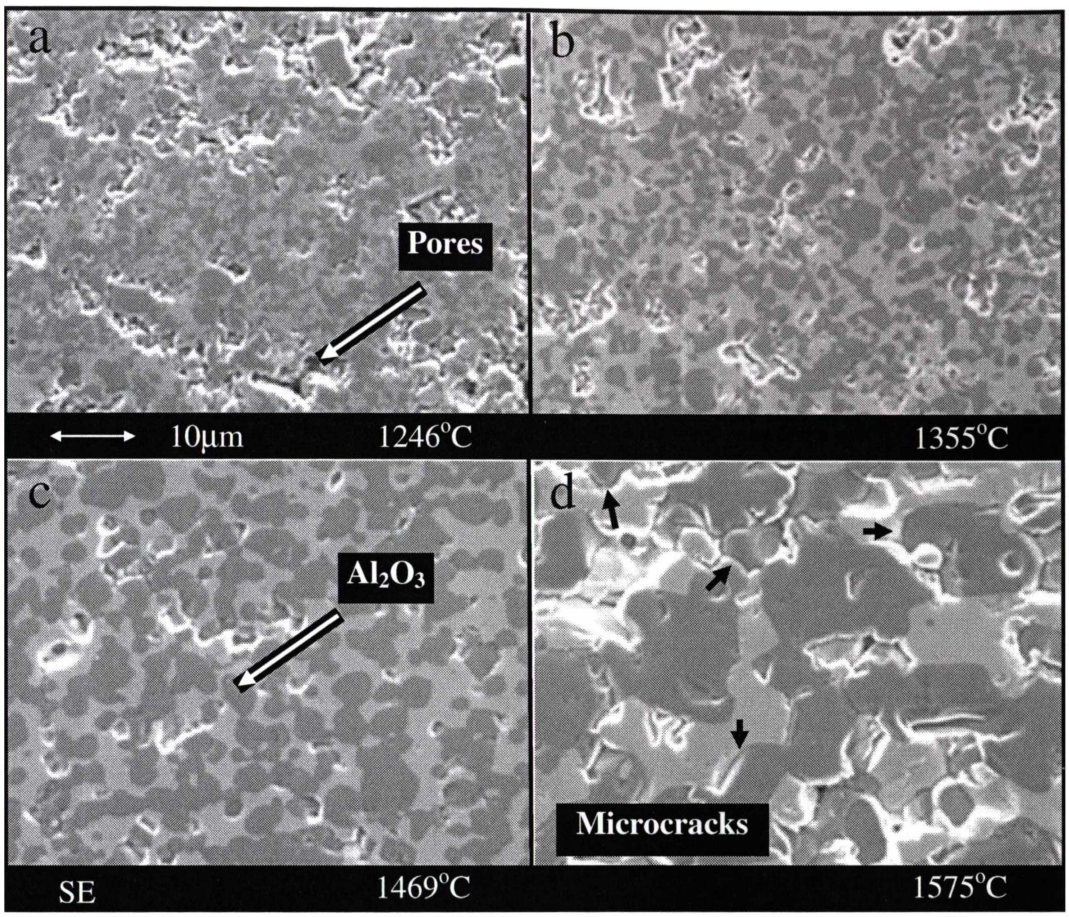

Figure 3.25: Hot pressed 2.4μm Ti_3Al-Al_2O_3-1 samples at (a) 1246, (b) 1355, (c) 1469 and (d) 1575°C at 31MPa

The quantity of pores decreases with increasing hot pressed temperature for 1.2μm samples up to approximately 1471°C forming fully dense composites as shown in Figure 3.26. Closed pores are observed in 1.2μm Ti_3Al-Al_2O_3-1 samples hot pressed at 1526 and 1574°C as shown in Figure 3.26(e) and (f). This can be interpreted as (1) gases resulting from agglomeration, which have expanded during hot pressing to cause pore formation or (2) segregation of the intermetallic Ti_3Al phase under pressure as seen in Figure 3.27. Figure 3.27 shows the phases are inhomogeneously distributed from the surface to the centre of the sample. The structure is porous toward the middle of the sample; however it is almost fully dense between this porous region and the surface. Moreover,

particle growth is observed in this surface area where the pores are absent suggesting that the occurrence of pores may have inhibited the particle growth in addition to the higher TiO content seen earlier in Figure 3.15(c) that make the diffusion of Al^{3+} and O^{2-} more difficult.

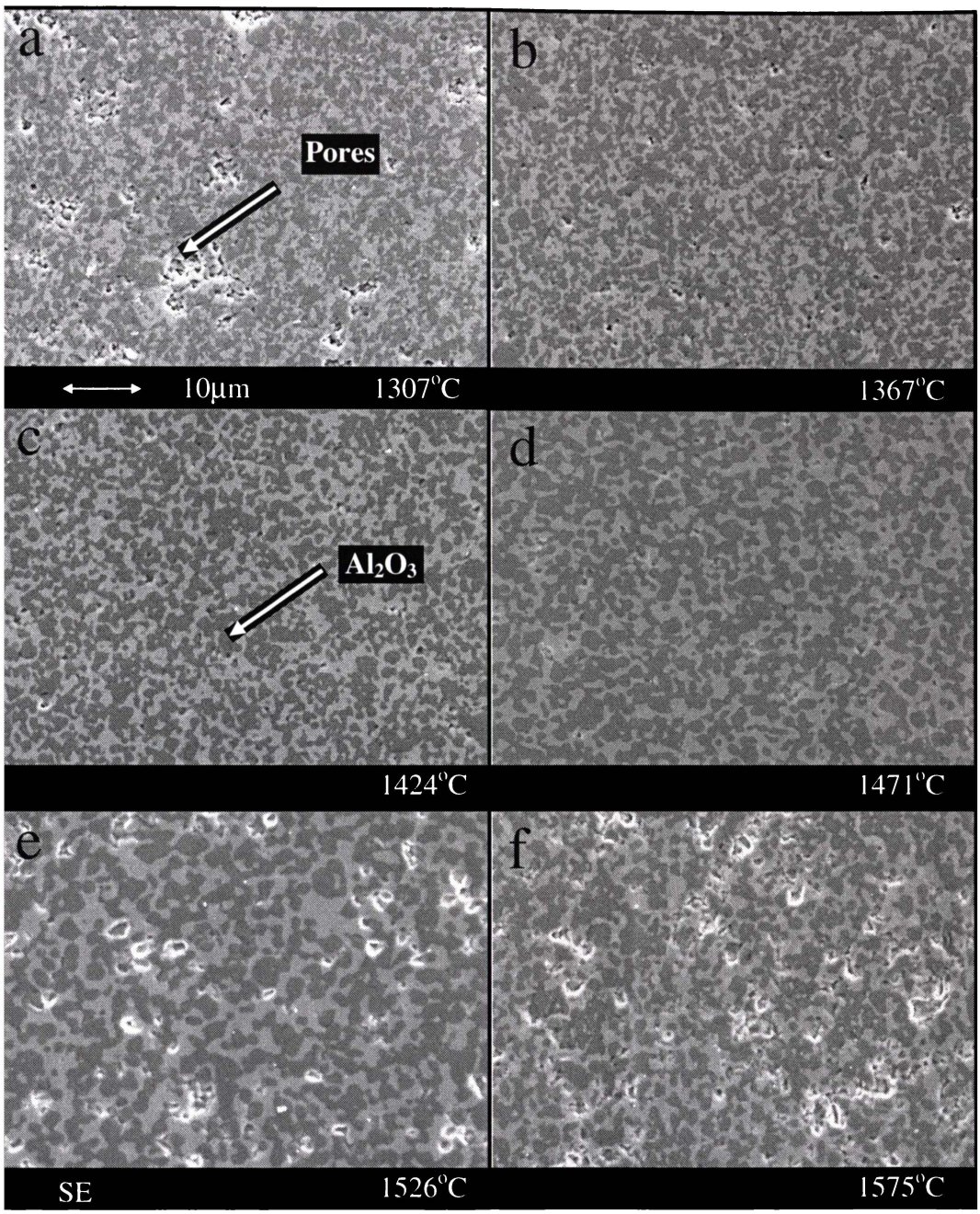

Figure 3.26: Hot pressed 1.2μm samples at (a) 1307, (b) 1367, (c) 1424, (d) 1471, (e) 1526 and (f) 1575°C at 31MPa

The relationship between the Al_2O_3 particle size and the temperature for hot pressed Ti_3Al-Al_2O_3-1 composite powder is shown in Figure 3.28. There is evidence of accelerating and undesirable particle growth after hot pressing above 1500°C for both 12.6 and 2.4μm samples as seen in Figure 3.24 and Figure 3.25.

All three sets of samples show repression of particle growth at hot pressing temperatures below 1500°C. There is no abrupt particle growth above 1500°C for the hot pressed 1.2μm samples compared to both the 2.4 and 12.6μm samples. As noted in the previous paragraph, this may be explained by the occurrence of pores, which have inhibited the particle growth activity as shown earlier in Figure 3.26(e) and (f) and the higher TiO content that suppress the diffusion of Al^{3+} and O^{2-}.

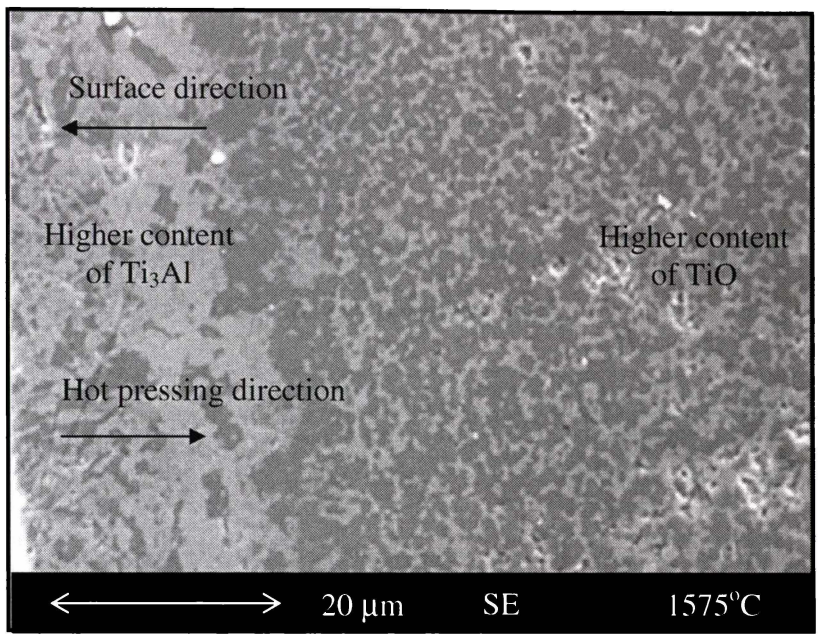

Figure 3.27: Hot pressed 1.2μm sample at 1575°C at 31MPa

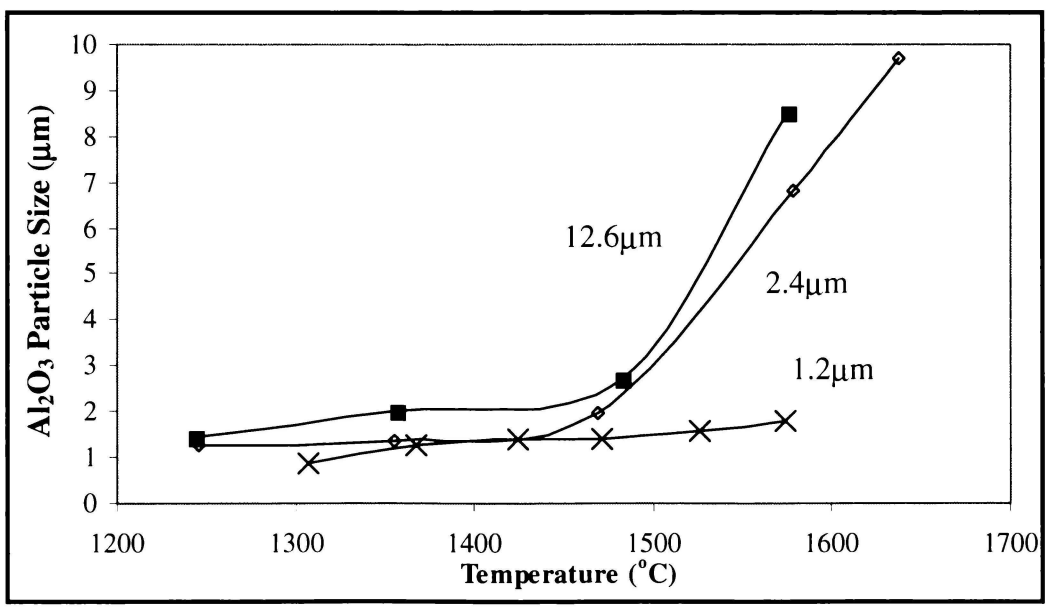

Figure 3.28: Particle size of Al_2O_3 versus temperature of hot pressed Ti_3Al-Al_2O_3-1 composite powder

Dense, fine-grained intermetallic-ceramic Ti_3Al-TiO-Al_2O_3 composites fabricated during hot pressing of Ti_3Al-Al_2O_3 composite powders should offer greatly enhanced mechanical properties and engineering performance. Ceramic-ceramic, Al_2O_3-TiO composites with a low level of Ti_3Al, which were also formed after pressureless sintering of Ti_3Al-Al_2O_3 composite powders under vacuum, should also display improved mechanical properties such as hardness and strength since significant densification of the composites was observed with increasing sintering temperature, which is discussed in Chapter Six.

3.3 Sintering Behaviour of Ti_3Al-Al_2O_3-2

3.3.1 Phase Structure

Figure 3.29 and Figure 3.31 show the XRD patterns of 11.2μm and 2.2μm Ti_3Al-Al_2O_3-2 samples after pressureless sintering under vacuum for one hour of holding period.

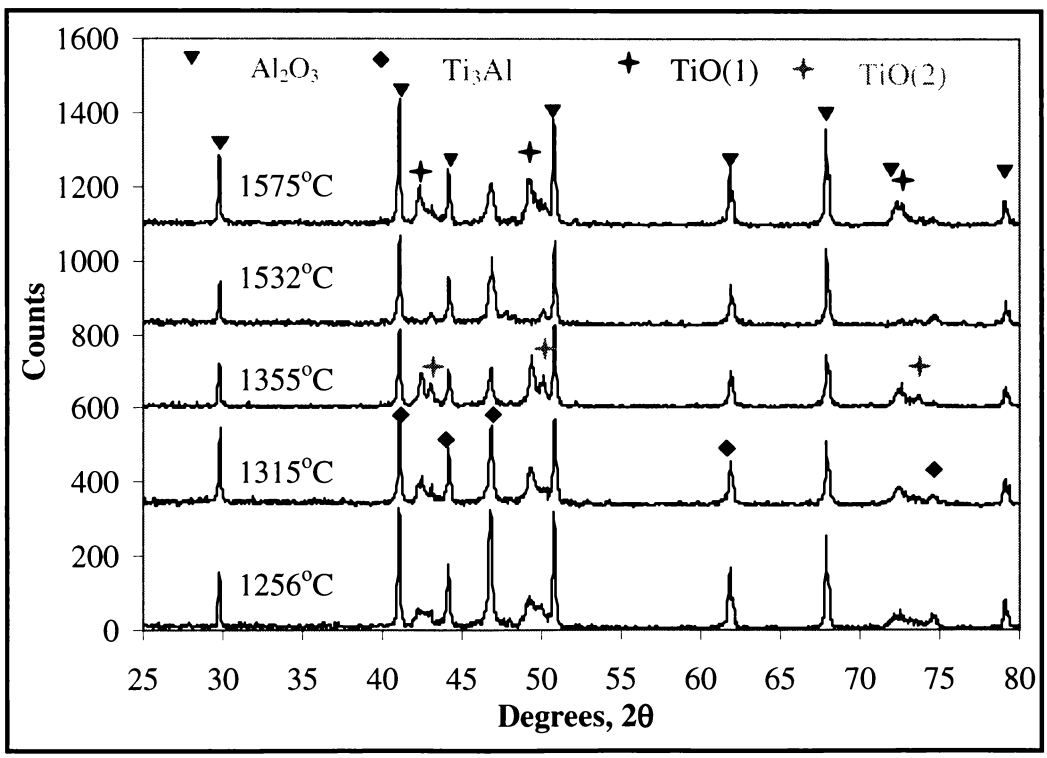

Figure 3.29: XRD patterns of composites produced by pressureless sintering 11.2μm Ti_3Al-Al_2O_3-2 composite powder under vacuum at different temperatures

The XRD phase intensity profiles for the pressureless sintered 11.2μm and 2.2μm Ti_3Al-Al_2O_3-2 samples as shown in Figure 3.30 and Figure 3.32 are comparable with the pressureless sintered Ti_3Al-Al_2O_3-1 samples as described in Section

3.2.1. That is, two TiO phases were detected coinciding with the reduction of Ti_3Al after sintering. In summary, the sintering behaviour of Ti_3Al-Al_2O_3 is reproducible and strongly dependent on the starting particle size distribution of the composite powders.

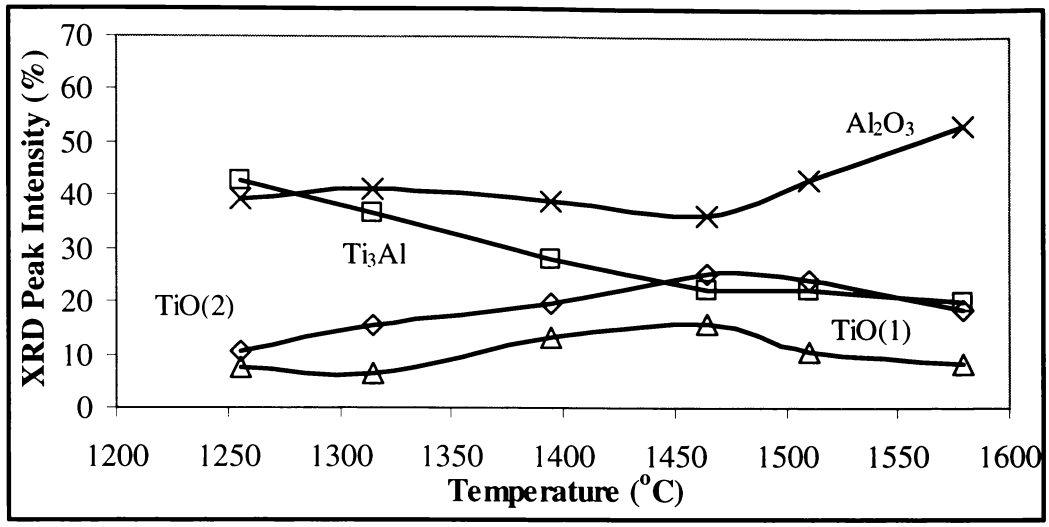

Figure 3.30: XRD phase intensity profile of composites produced by pressureless sintering 11.2μmTi_3Al-Al_2O_3-2 composite powder under vacuum at different temperatures

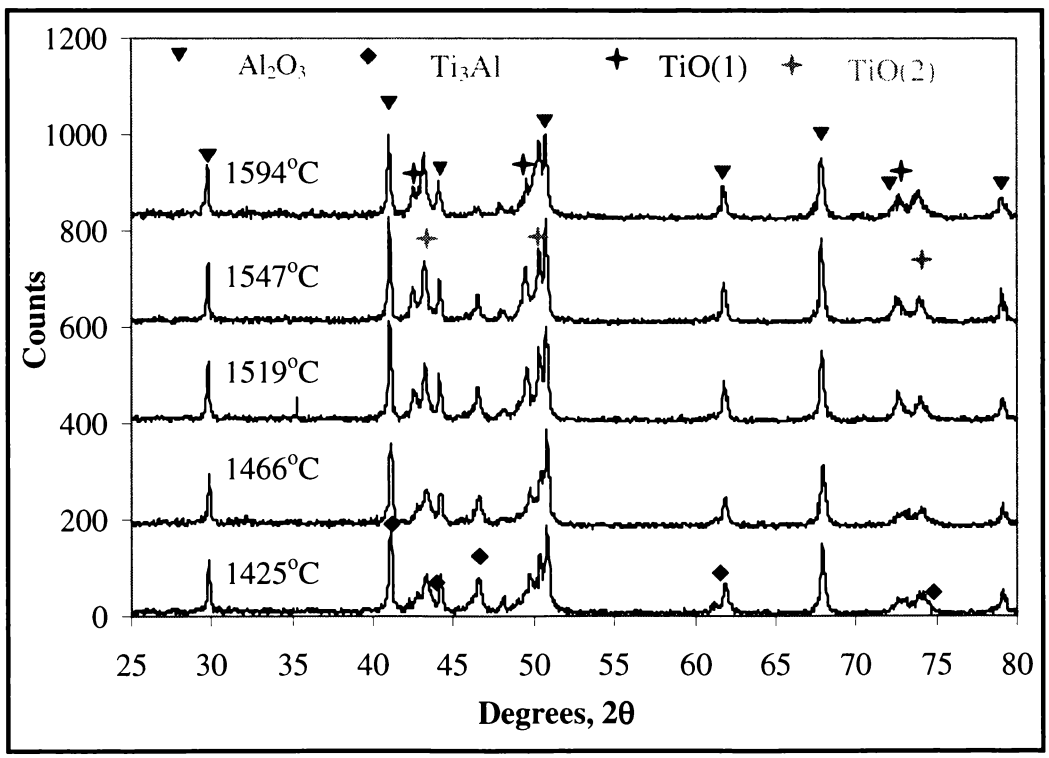

Figure 3.31: XRD patterns of composites produced by pressureless sintering 2.2μm Ti_3Al-Al_2O_3-2 composite powder under vacuum at different temperatures

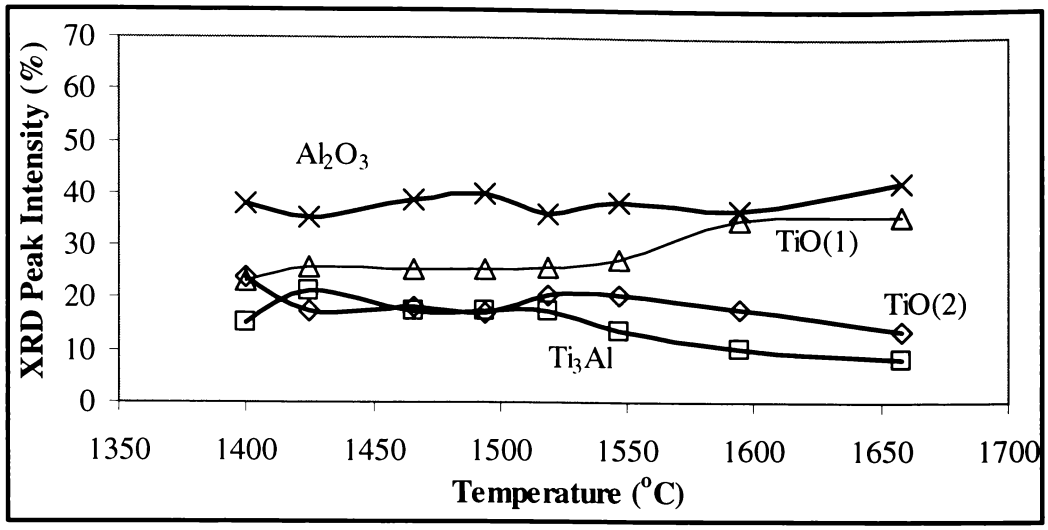

Figure 3.32: XRD phase intensity profile of composites produced by pressureless sintering 2.2μm Ti_3Al-Al_2O_3-2 composite powder under vacuum at different temperatures

3.3.2 Pores and Al_2O_3 Particle Morphology

The open porosity and bulk density of composites produced by pressureless sintering Ti_3Al-Al_2O_3-2 composite powder showed similar trends to samples produced from Ti_3Al-Al_2O_3-1 composite powder as shown in Figure 3.33 and Figure 3.34. However, the samples produced from 24 hours ball milled Ti_3Al-Al_2O_3-2 composite powder were quite different from those produced from the 24 hours ball milled Ti_3Al-Al_2O_3-1 composite powder despite both being ball milled and pressed under the same conditions. This is due to the local differences in particle size distributions as a result of variations in powder processing technique during the original powder manufacture.

The bulk density of composites produced by pressureless sintering Ti_3Al-Al_2O_3-2 composite powder under vacuum improves with increasing sintering temperature as shown in Figure 3.34. As mentioned before, two factors contribute to the increase of bulk density of Ti_3Al-Al_2O_3-2 samples pressureless sintered and hot pressed under vacuum. The first factor is the reduction of porosity whereas the second factor is the undesirable formation of TiO phase from Ti_3Al phase, which was discussed in Section 3.3.1. The reduction of powder particle size from 11.2 to 2.1-2.2μm (from both 24 and 72 hours ball milled powders) has an enormous effect on the bulk density, that is, the bulk density is further improved with decreasing particle size of the composite powders.

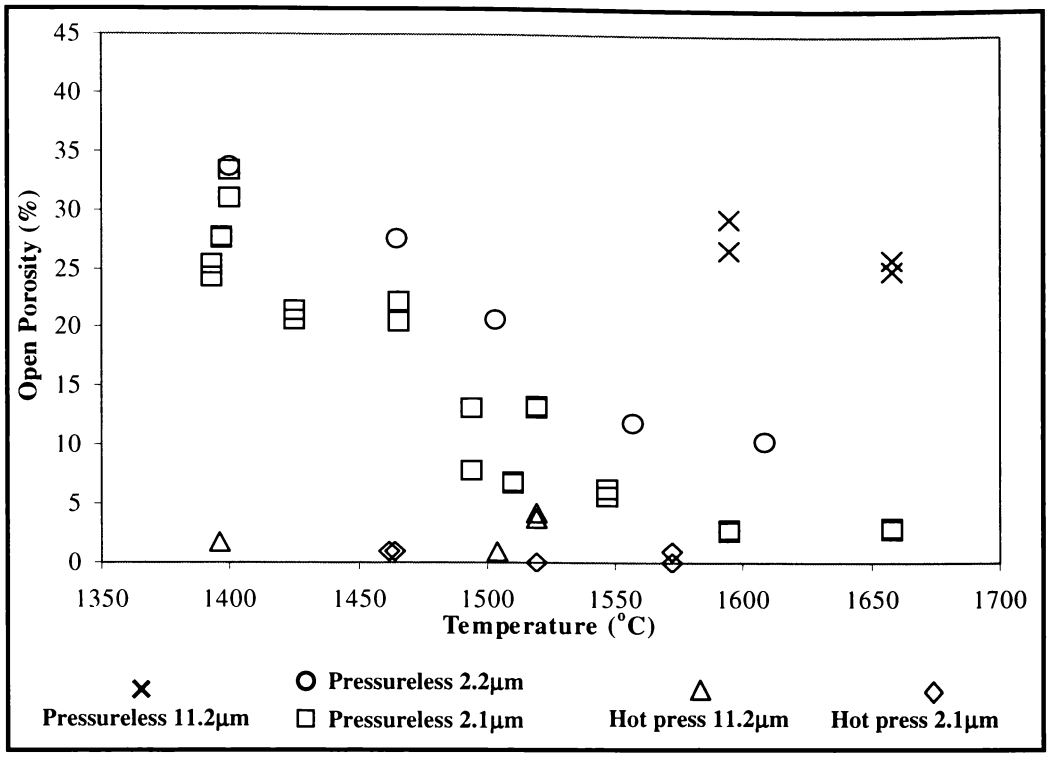

Figure 3.33: Open porosity of composites produced by pressureless sintering and hot pressing Ti_3Al-Al_2O_3-2 composite powders under vacuum at different temperatures

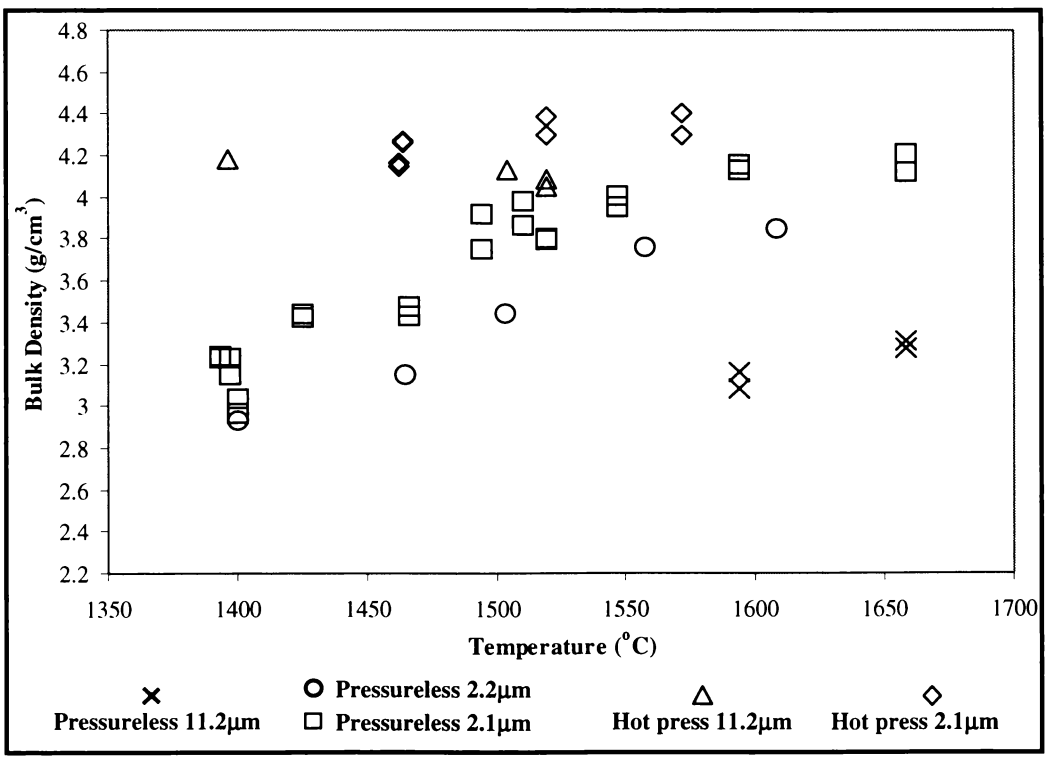

Figure 3.34: Bulk density of composites produced by pressureless sintering and hot pressing Ti_3Al-Al_2O_3-2 composite powders under vacuum at different temperatures

The hot pressed bodies display further improvement in their open porosity compared to the pressureless sintered bodies as shown in Figure 3.33. The open porosity of the hot pressed 11.2 and 2.2μm Ti_3Al-Al_2O_3-2 composite powders are below 5% compared to the pressureless sintered samples at the same temperature, which display values up to 40%. As a result of the improvement in open porosity with the application of pressure, it is expected that densification will have a significant effect on the bulk density of the materials especially for the 11.2μm Ti_3Al-Al_2O_3-2 samples as shown in Figure 3.34. This figure shows that the bulk density of the pressureless sintered 11.2μm Ti_3Al-Al_2O_3-2 samples has improved from 2.6-3.3g/cm^3 to 4-4.5g/cm^3, which could otherwise only be achieved by hot pressing. Hot pressed and pressureless sintered samples of both 24 and 72 hours ball milled powders approach theoretical density at significantly lower sintering temperatures compared to the samples produced from Ti_3Al-Al_2O_3-2 composite powder without ball milling.

Figure 3.35 shows the SEM micrographs of polished 2.1μm Ti_3Al-Al_2O_3-2 samples pressureless sintered at different temperatures under vacuum. The dark grey particles are identified as the Al_2O_3 phase embedded in a pale grey matrix identified as a mixture of Ti_3Al and TiO phases as shown by the XRD patterns in Figure 3.29 and Figure 3.31. The quantity of pores decreases with increasing temperature. Again the composites are showing particle growth and microcracks at sintering temperatures above 1500°C as seen earlier in the hot pressed 12.6μm and 2.4μm Ti_3Al-Al_2O_3-1 samples in Section 3.2.3.

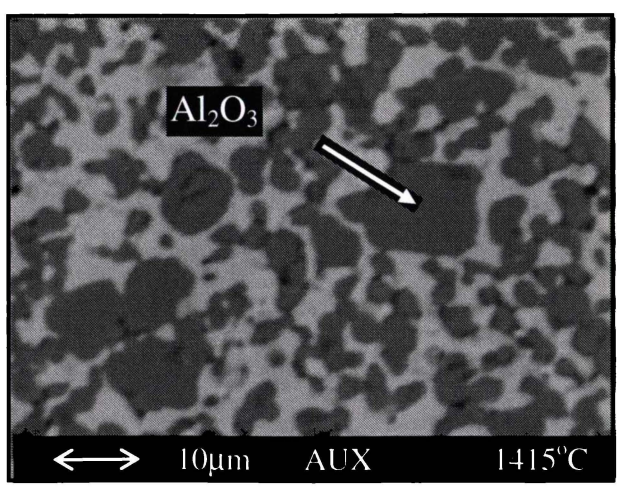

Figure 3.35(a): Pressureless sintered 2.1μm Ti_3Al-Al_2O_3-2 samples at 1415°C

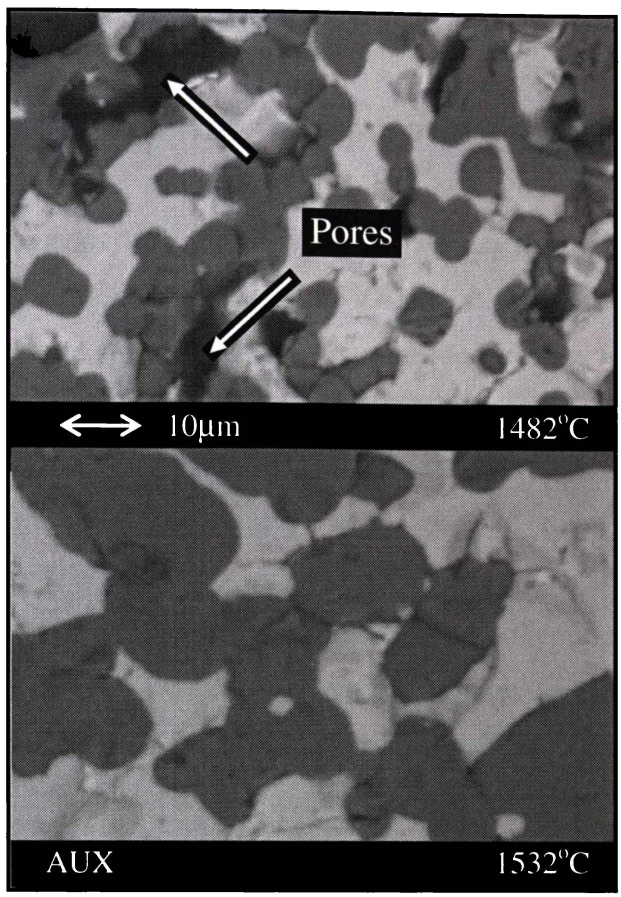

Figure 3.35: Pressureless sintered 2.1μm Ti_3Al-Al_2O_3-2 samples at (b) 1482 and (c) 1532°C

3.4 Discussion

3.4.1 Effect of Phase Structure on the Composites

Different compositions within the intermetallic and ceramic phases Ti_3Al-TiO-Al_2O_3 and Ti_3Al-Al_2O_3 composites were obtained by heat treatment of Al-TiO_2 composite powders produced from discus and ball milling. The two hours discus milled composite powders after heat treatment in argon at 800°C for 2 hours contained mixtures of Ti_3Al, Al_2O_3 and trace amounts of TiO. The microstructure of the composite powders shows Al_2O_3 is embedded in a Ti_3Al matrix. XRD analysis shows that the Ti_3Al phase diminished gradually with increasing sintering temperature during hot pressing under vacuum. This is consistent with the reaction: $2Ti_3Al + 4.5O_2 \rightarrow 6TiO + Al_2O_3$. The sintering atmosphere is believed to contain low partial pressure of oxygen which explains the formation of TiO after sintering. It was found that Ti_3Al diminished markedly when the particle

size of the Ti_3Al-Al_2O_3-1 composite powder was reduced, due to the increased surface area of the powder after 72 hours of ball milling.

3.4.2 Effects of Sintering Temperature and Particle Size

Diffusion in ceramics and metals is a thermally activated process with a strong dependence on temperature[10]. This is demonstrated by the reduction of open and closed porosity for the sintered Ti_3Al-TiO-Al_2O_3 composites with different compositions produced from Ti_3Al-Al_2O_3 composite powders with respect to the increased sintering temperature. The densification of the Ti_3Al-TiO-Al_2O_3 composite was further improved with the reduction of mean particle size from 12.6-1.2μm for the Ti_3Al-Al_2O_3-1 composite powder and from 11.2-2.2μm for the Ti_3Al-Al_2O_3-2 composite powder, which increased the contact area between particles. This allows for improved diffusion in all directions simultaneously. The increased surface area provides a higher driving force for the sintering process and the smaller particles lead to shortening of the diffusion paths, so that these small particles take less time to achieve high sintered density than the larger particles[10, 11].

From the experiments, it was found that 1600°C of pressureless sintering temperature is required for achieving >95% theoretical density. Higher pressureless sintering temperature, lower mean particle size or the application of pressure is essential to produce near fully densified composites with >95% theoretical density in this research. This limitation is comparable to the pressureless sintering of Al_2O_3-Cr and Al_2O_3-NbC composite powders studied elsewhere. That is, ≤94.2% theoretical density of Al_2O_3-Cr composites were prepared by pressureless sintering Al_2O_3 and Cr powders with <5μm starting particle size at 1500°C for one hour[12]. And ~89.6% and ~96.2% theoretical density of Al_2O_3-NbC composites were produced by pressureless sintering Al_2O_3 and NbC powders with 2.3μm starting particle size at 1650°C (30mins) and 1800°C (15mins), respectively. Whereas higher density (98.2% of theoretical density) of Al_2O_3-NbC composites were prepared by hot pressing Al_2O_3 and Cr powders with 2.3μm starting particle size at 1650°C for 30 minutes[13].

3.4.3 Effect of Pressure

The effect of applied pressure on the sintering behaviour has shown that the densification of the hot pressed samples was improved compare to the pressureless sintered composites. The application of pressure at the sintering temperature accelerates the kinetics of densification by increasing the contact stress between particles and by rearranging particle positions to improve packing[11]. This is desirable in that it eliminates the need for very fine particle materials and also removes large pores caused by non-uniform mixing[11, 14]. This study shows that applying pressure during sintering is essential for achieving high density of the Ti_3Al-TiO-Al_2O_3 composite. The dramatic beneficial effect of applying pressure to sintering of the Ti_3Al-Al_2O_3 composite powder can be attributed to its microstructural features. The composite contains 50-60 wt.% of Al_2O_3 particles, which have a very high melting point of over 2300°C, so the movement of Ti_3Al phase through solid state diffusion would be greatly impaired by the presence of large fraction of relatively immobile Al_2O_3 particles. The interaction between the Ti_3Al matrix and Al_2O_3 particles would make the sintering of the composite more difficult than the Ti_3Al or Al_2O_3 powder alone. Therefore the application of pressure causes plastic deformation and plastic flow of the matrix aiding the diffusion of Al^{3+} and O^{2-}. This experimental program has demonstrated that a fully dense microstructure can be produced for 1.2μm Ti_3Al-Al_2O_3-1 composite powder by hot pressing at 1471°C under vacuum for one hour of holding period.

Hot pressing above 1500°C resulted in Ti_3Al segregation in the hot pressing of 1.2μm Ti_3Al-Al_2O_3 composite powder. This is also seen in the Ni_3Al/Al_2O_3 composites produced by hot pressing above the melting point of Ni_3Al, which resulted in Ni_3Al being exuded from the composite. The densification of the composites by hot pressing below 1500°C assisted particle growth and pore suppression. The suppression of grain growth is seen for the development of alumina-metal nanocomposites by combining the "nanocomposite effect" with the ductility of the metallic phase[15].

3.4.4 Microcracking during Hot Pressing

The observation of microcracks at the Ti_3Al-Al_2O_3 interfaces at the same time as the observation of coarsening of Al_2O_3 particles in the Ti_3Al-TiO-Al_2O_3 composite is interesting and important. To date, the exact mechanism of the microcrack development is unknown. A plausible mechanism is that the microcracks are caused by the thermal stress developed at the interface because of the difference in thermal expansion coefficient between the Al_2O_3 and matrix phase. The thermal expansion coefficients of Al_2O_3 and Ti_3Al are calculated and shown in Table 3.1. There are other studies on composites such as Al_2O_3/Al with interpenetrating networks that exhibit thermal stress due to thermal expansion mismatch between multiphase materials[16]. The microcracks are absent in the microstructure of the composite produced at relatively low sintering temperature when the Al_2O_3 particles are much smaller. This may be due to the fact that for small Al_2O_3 particles, it is difficult to nucleate cracks along the matrix/particle interface. No microcracks were observed in the hot pressed samples produced by hot pressing the 1.2μm composite powder, which is explained by the small difference in thermal expansion coefficients of Al_2O_3 ($8.9x10^{-6}$mm/(mm/°C)) and the matrix ($8.1x10^{-6}$mm/(mm/°C)) as seen in Table 3.1. As discussed earlier, the lower thermal expansion coefficient is due to the higher TiO content found in the matrix.

3.5 Summary

This study has clearly demonstrated the benefit of reducing the particle size of the starting Ti_3Al-Al_2O_3 composite powders from 12.6μm to 1.2μm of median particle diameter in the sintering and densification processes. Full density of the composite cannot be achieved by pressureless sintering but much more effective densification was obtained at lower temperature through hot pressing for one hour of holding period. In general, the open porosity and bulk density decreased and increased, respectively with increasing temperature for pressureless sintering and hot pressing under vacuum. *Fully dense microstructures* could be produced by hot pressing the 1.2μm Ti_3Al-Al_2O_3 composite powder at 1471°C with a pressure of 31MPa. Substantial Al_2O_3 particle growth and microcracking at the Ti_3Al-

Al_2O_3 interfaces were triggered above 1500°C for both pressureless sintering and hot pressing.

REFERENCES

1. Cardellini, F., G. Mazzone, A. Montone and M.V. Antisari, *Solid state reactions between Ni and Al powders induced by plastic deformation.* Acta Metallurgica et Materialia, 1994. **42**(7): p. 2445-2451.
2. Welham, N.J., *Mechanical activation of the formation of an alumina-titanium trialuminide composite.* Intermetallics, 1998. **6**: p. 363-368.
3. Ying, D.Y., *Effects of high energy mechanical milling on the kinetics of solid state reaction*, PhD Thesis. 2000, The University of Waikato: Hamilton. p. 177.
4. Liu, L., F. Padella, W. Guo and M. Magini, *Solid state reactions induced by mechanical alloying in metal-silicon (metal = Mo, Nb) systems.* Acta Metallurgica et Materialia, 1995. **43**(10): p. 3755-3761.
5. Ying, D.Y., D.L. Zhang and M. Newby, *Solid-state reactions during heating mechanically milled Al/TIO_2 composite powders.* Metallurgical and Materials Transactions A, 2004. **35**(7): p. 2115-2125.
6. Zalar, A., B.M.M. Baretzky, S. Hofmann, M. Ruhle and P. Panjan, *Interfacial reactions in Al_2O_3/Ti, Al_2O_3/Ti_3Al and Al_2O_3/TiAl bilayers.* Thin Solid Films, 1999. **352**: p. 151-155.
7. Zhang, M.-X., K.-C. Hsieh, J. DeKock and Y.A. Chang, *Phase Diagram of Ti-Al-O at 1100°C.* Scripta Metallurgica et Materialia, 1992. **27**: p. 1361-1366.
8. Chen, Y., D.J. Young and B. Gleeson, *A new Ti-rich ternary phase in the Ti-Al-O system.* Materials Letters, 1995. **22**: p. 125-129.
9. Amatuni, A.N., T.I. Malyutina, C. V.Ya. and V.A. Petukhov, *Standard samples for dilatometry.* High Temperatures - High Pressures, 1976. **8**: p. 565-570.
10. Brook, R.J., ed. *Concise Encyclopedia of Advanced Ceramic Materials.* 1986, Pergamon Press: Oxford. 120-122, 454-458.
11. Richerson, D.W., *Modern ceramic engineering : properties, processing, and use in design*, in *Materials engineering (Marcel Dekker, Inc.).* 1992, New York : M. Dekker. p. 552-556.
12. Ji, Y. and J.A. Yeomans, *Microstructure and mechanical propeties of chromium and chromium/nickel partiulate reinforced alumina ceramics.* Journal of Materials Science, 2002. **37**: p. 5229-5236.
13. Acchar, W., P. Greil, A.E. Martinelli, C.A.A. Cairo, A.H.A. Bressiani, and J.C. Bressiani, *Sintering behaviour of alumina-niobium carbide composites.* Journal of the European Ceramic Society, 2000. **20**: p. 1765-1769.
14. Wulff, J., *Powder Metallurgy*, in *The American Society for Metals.* 1942, Materials Park, Ohio. p. 244-245.
15. Ji, Y. and J.A. Yeomans, *Processing and mechanical properties of Al_2O_3-5vol.% Cr nanocomposites.* Journal of the European Ceramic Society, 2002. **22**: p. 1927-1936.
16. Hoffman, M., S. Skirl, W. Pompe and J. Rodel, *Thermal residual strains and stresses in Al_2O_3/Al composites with interpenetrating networks.* Acta Materialia, 1999. **47**(2): p. 565-577.

CHAPTER FOUR:

Pressureless Sintering of Discus Milled Al-TiO_2 Composite Powders

Reaction sintering of mechanically milled powder mixtures or composite powders made from relatively low cost raw materials such as Al and TiO_2 to produce aluminide-alumina composites has been studied widely[1-8]. Solid-state reactions of this composite powder system have demonstrated critical milling times beyond which the first reaction occurs within seconds during heating, whilst other reactions proceed more slowly with the extent of reaction being a function of milling time[9-15]. This chapter describes the effect of processing conditions on microstructure and phase relationships in Ti_3Al-TiO-Al_2O_3 and Ti_3Al-Al_2O_3 composites prepared by pressureless sintering of the Al-TiO_2 composite powders.

4.1 Powder Characteristics

4.1.1 Aluminium-Rutile Composite Powders

Two hours discus milled aluminium-rutile (Al-TiO_2) composite powder was produced at the University of Waikato. The shapes of Al-TiO_2 powder particles are irregular and range from <1μm to up to 20μm as shown in the Scanning Electron Micrograph in Figure 4.1.

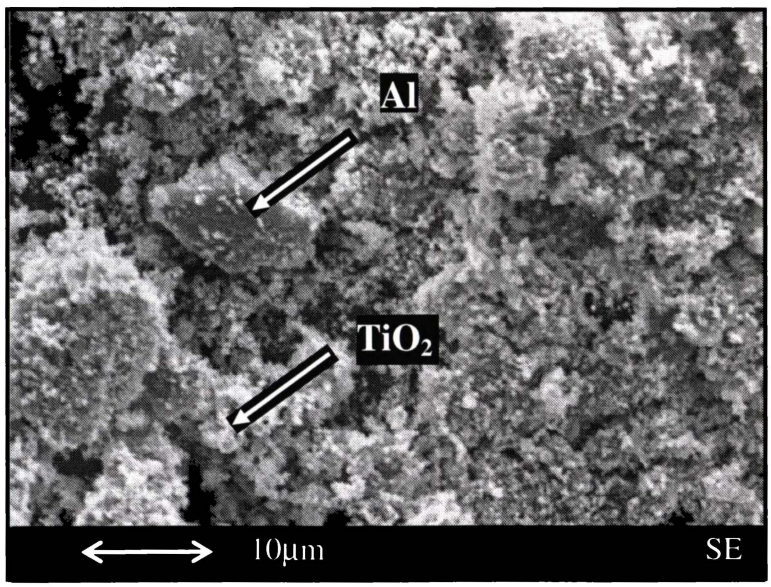

Figure 4.1: Morphology of Al-TiO_2 composite powder particles discus milled for two hours

Figure 4.2 shows the cross section of the Al-TiO_2 composite powder particles discus milled for two hours. The fine particles (<1μm) are TiO_2 (rutile) and the larger platelike particles are Al (around 15μm).

Figure 4.3 shows cross sections of Al-TiO_2 composite powder particles before and after different durations of ZrO_2 ball milling in chloroform. Size reduction of the platelike Al particles was apparent after 4 hours of ball milling and continued through to reach a minimum size after 24 hours milling exposure.

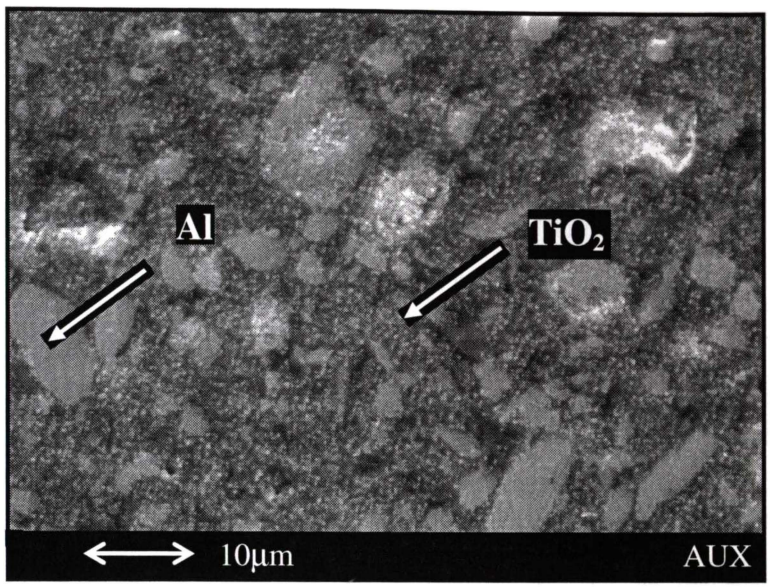

Figure 4.2: Cross section of Al-TiO_2 composite powder particles discus milled for two hours

Figure 4.4 shows the particle size distributions of Al-TiO_2 composite powder before and after different ball milling times. The distributions show there is an obvious reduction of particle diameter from 35 to 10μm in the 90% percentile for 0 and 24 hours ball milled powders. The particle size distributions for the powders ball milled for 4, 8, 10, 12, 16 and 20 hours are very similar and all give a reading of 14 to 18μm in the 90% percentile. The median particle diameters of Al-TiO_2 composite powders are shown in Table 4.1 and exhibit a very narrow range from 4 to 5μm after ball milling. All particle size data display bimodal distributions as shown in Figure 4.5.

Figure 4.6 shows the XRD pattern of Al-TiO_2 composite powder. After two hours discus milling the powder consisted of face centred cubic Al and tetragonal TiO_2 (rutile).

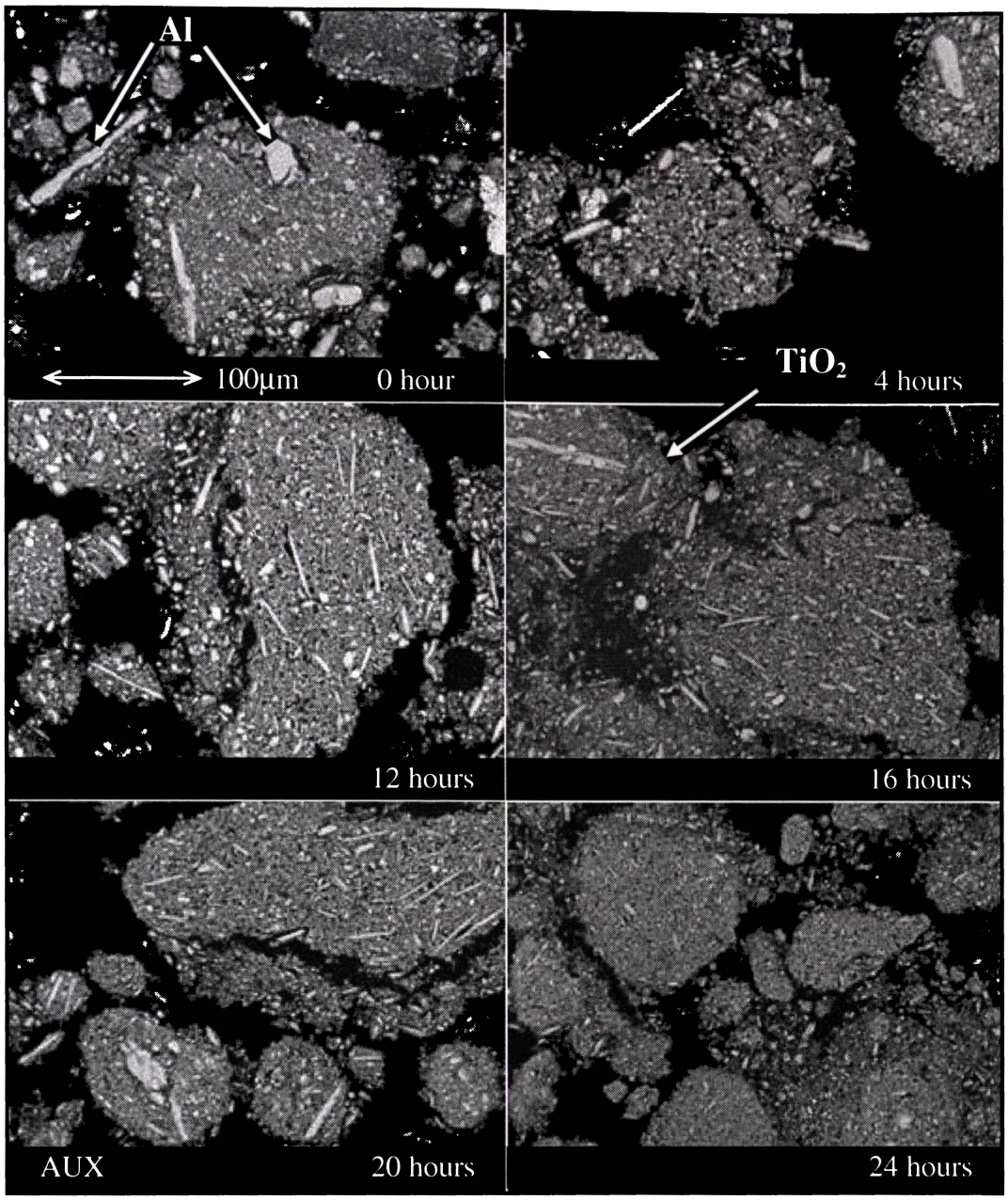

Figure 4.3: Cross sections of Al-TiO_2 composite powder particles before and after various hours of ball milling

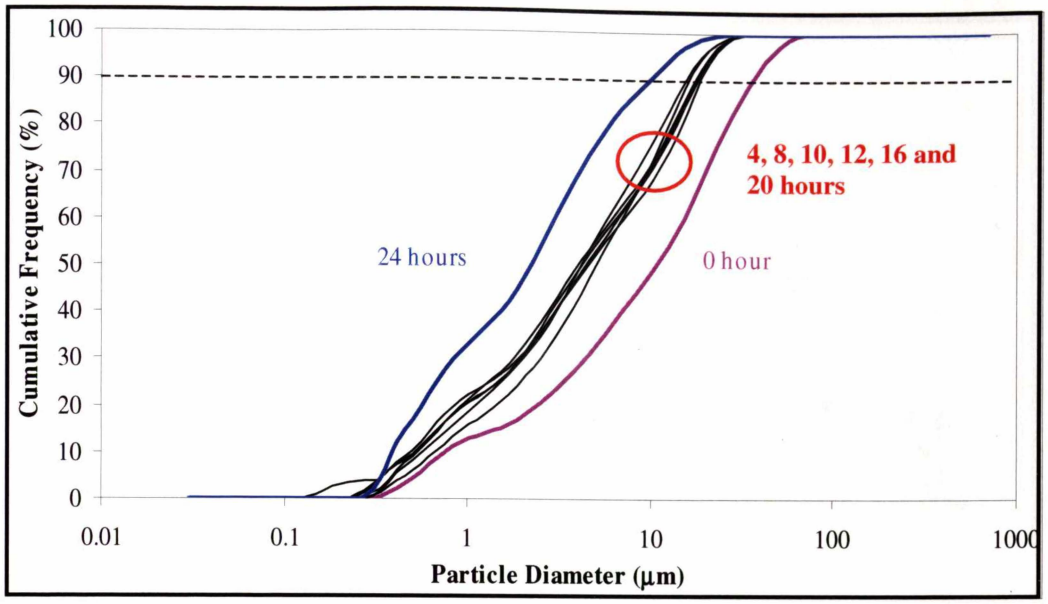

Figure 4.4: Particle size distributions (cumulative frequency) of Al-TiO_2 composite powder from 0-24 hours of ball milling

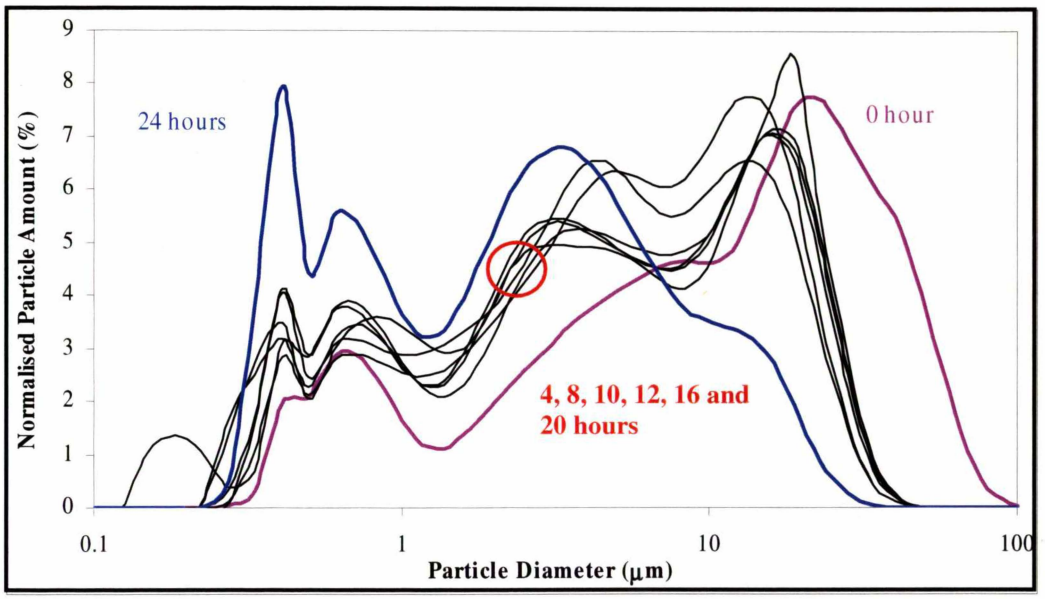

Figure 4.5: Particle size distributions (frequency) of Al-TiO_2 composite powder from 0-24 hours of ball milling

Table 4.1: Median particle diameter of Al-TiO_2 composite powders

Al-TiO_2-2 after ball milling (hours)	Median Particle Diameter (μm)
0	11
4	5
8	4
10	4
12	4
16	4.5
20	4
24	2

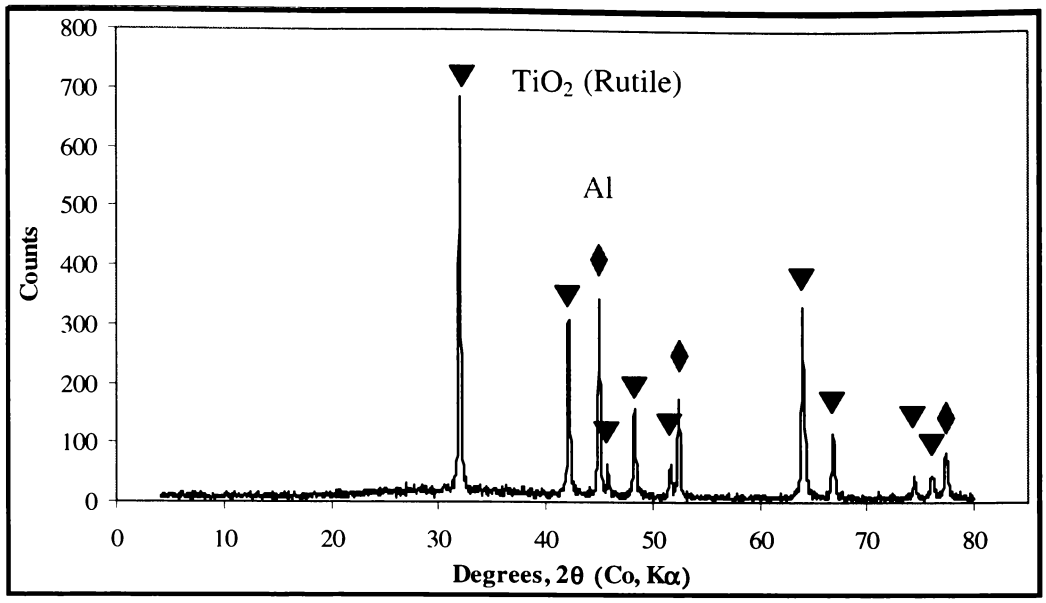

Figure 4.6: XRD pattern of Al-TiO_2 composite powder discus milled for two hours

4.1.2 Aluminium-Anatase Composite Powders

Al-TiO_2 composite powders were produced by discus milling an Al/TiO_2 powder mixture for two, three, four and six hours. The molar ratio between Al and TiO_2 in the mixture is 4:3. The powders are named 2(Al-TiO_2), 3(Al-TiO_2), 4(Al-TiO_2) and 6(Al-TiO_2) respectively (Note: the sample coding used here is that the number in front of Al-TiO_2 is the number of hours of discus milling). Figure 4.7 shows the cross sections of (a) 2(Al-TiO_2), (b) 3(Al-TiO_2) and (c) 4(Al-TiO_2) composite powders particles etched with NaOH solution (~10% NaOH in distilled water, 30s). The removal of Al by etching revealed that discus milling not only reduced the particle sizes but also improved the microstructural homogeneity of the composite powder particles. The Al platelike particles curled up after discus milling.

Ball milling was employed to further reduce the particle sizes. The composite powders were ball milled for 24 hours in chloroform (refer Chapter Two) and the cross sections of the particles after etching are shown in Figure 4.8 and are termed 2(Al-TiO_2)-24, 3(Al-TiO_2)-24 and 4(Al-TiO_2)-24. Ball milling has straightened the Al platelike particles as seen in the figures. The homogeneity of the phases was the most important factor in the enhancement of the reaction with both increased interfacial area and shortened diffusional pathlength playing a major

role in lowering the reaction temperature[14]. The decrease in reaction temperature observed after hours of ball milling described later in this chapter implies that milling has enhanced the phase homogeneity.

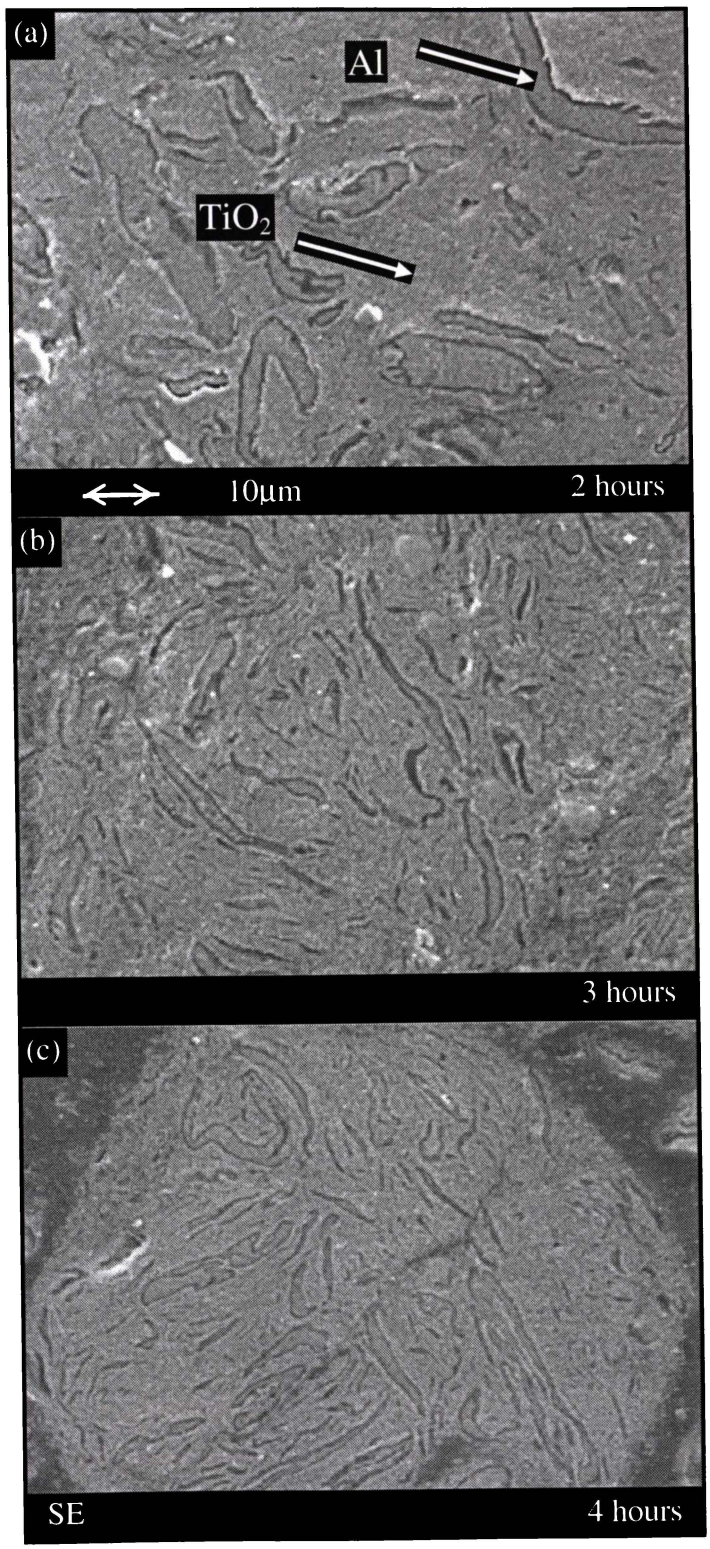

Figure 4.7: Cross sections of (a) 2(Al-TiO_2), (b) 3(Al-TiO_2) and (c) 4(Al-TiO_2) composite powders particles etched with NaOH solution (~10% NaOH in distilled water)

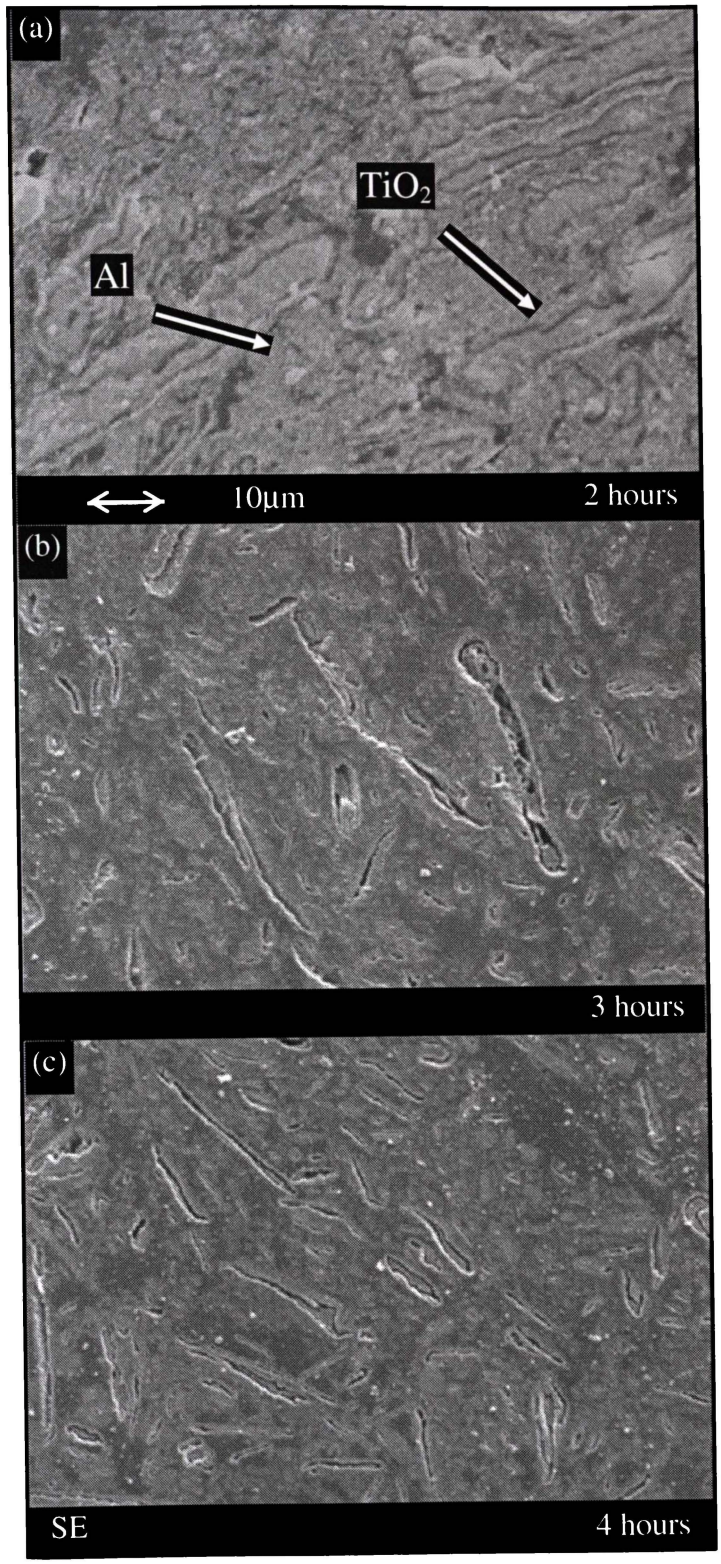

Figure 4.8: Cross sections of (a) 2(Al-TiO_2)-24, (b) 3(Al-TiO_2)-24 and (c) 4(Al-TiO_2)-24 composite powders particles etched with NaOH solution (~10% NaOH in distilled water)

Figure 4.9 and Figure 4.10 show the particle size distributions of 2(Al-TiO_2), 4(Al-TiO_2) and 6(Al-TiO_2) composite powders before and after 24 hours of ball milling. These curves demonstrate a clear reduction of particle size with increasing discus milling time. The median particle diameters of the composite powders are shown in Table 4.2. The overlap of 4(Al-TiO_2)-24 and 6(Al-TiO_2)-24 median particle diameters of approximately 7μm indicates that the particle size reduction probably has ceased after 24 hours of ball milling for the four hours discus milled Al-TiO_2 composite powder. All powders displayed bimodal distributions as shown in Figure 4.10.

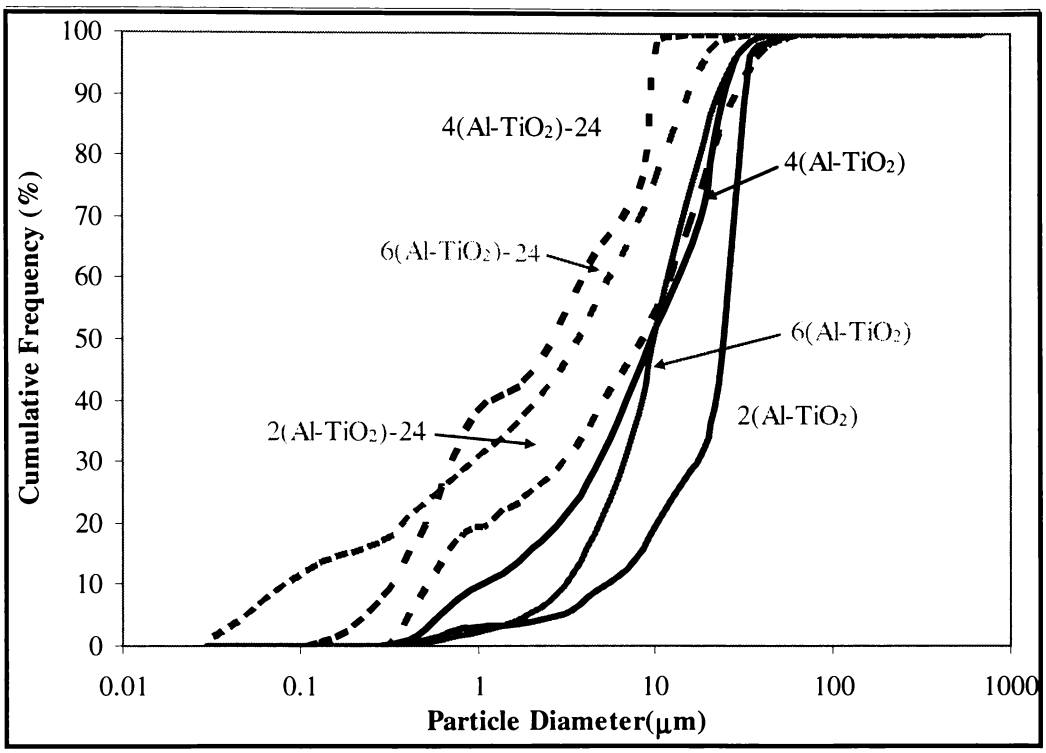

Figure 4.9: Particle size distributions (cumulative frequency) of 2(Al-TiO_2), 4(Al-TiO_2) and 6(Al-TiO_2) composite powders before and after 24 hours of ball milling

Table 4.2: Median particle diameter of the aluminium-anatase composite powders

Composite Powder	Milling (hour)		Median Particle Diameter (μm)
	Discus	Ball	
2(Al-TiO_2)	2	0	19
4(Al-TiO_2)	4	0	14
6(Al-TiO_2)	6	0	10
2(Al-TiO_2)-24	2	24	8
4(Al-TiO_2)-24	4	24	7
6(Al-TiO_2)-24	6	24	7

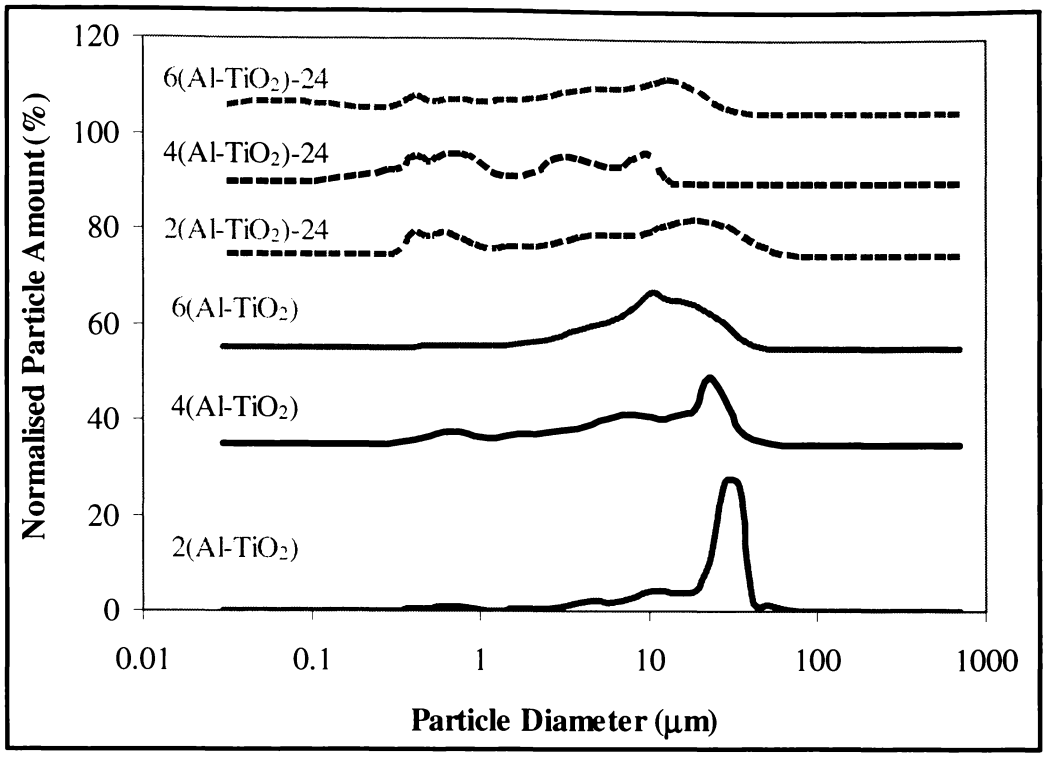

Figure 4.10: Particle size distributions (frequency) of 2(Al-TiO_2), 4(Al-TiO_2) and 6(Al-TiO_2) composite powders before and after 24 hours of ball milling

Figure 4.11 shows the XRD pattern of one of the composite powders – 4(Al-TiO_2). The XRD patterns of other Al-TiO_2 composite powders before and after ball milling are very similar to this XRD pattern. The powder after different times of discus milling up to six hours consists of face centred cubic Al and body centred tetragonal TiO_2 (anatase).

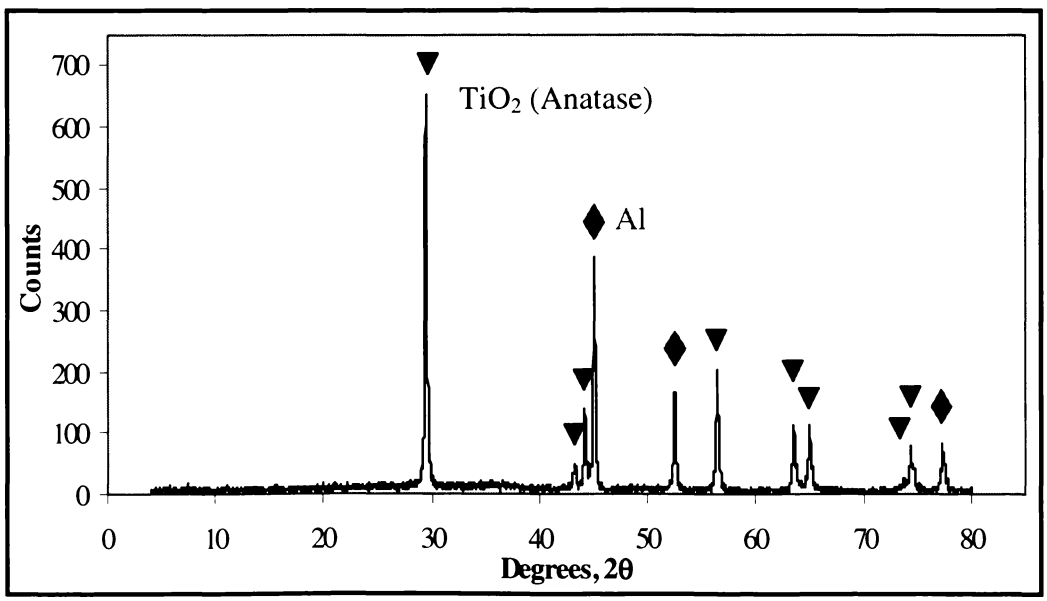

Figure 4.11: XRD pattern of 4(Al-TiO_2) composite powder

4.2 Reactions between Al and TiO_2

Figure 4.12 shows the DTA traces of the Al-TiO_2 composite powder subjected to ball milling for different times up to 24 hours after two hours of discus milling, normalised to equal mass of Al-TiO_2. The heating traces of the discus milled and ball milled powders show an endothermic event at approximately 670°C due to aluminium melting. This melting endothermic reaction was followed by a first exothermic reaction labelled (□), which took place at approximately 680°C. The first exothermic reaction was followed by a second broader exothermic peak. There is a peak shift from 880°C to 740°C for this second exothermic reaction labelled (✣).

Previous work from Ying et al.[15] showed that the powder consists of only Al and TiO_2 phases after heating at 500°C. At 700°C, $TiAl_3$ peaks appeared in the XRD pattern suggesting that the first exothermic event was caused by the reaction between Al and TiO_2, forming $TiAl_3$. From 740 to 880°C, Al and TiO_2 phases disappeared while α-Al_2O_3 phase appeared suggesting the second exothermic reaction was caused by the reaction between $TiAl_3$ and TiO_2, forming α-Al_2O_3 and Ti_3Al phases. Third and fourth exothermic events were evident for the 12, 20 and 24 hours ball milled powders from 900 to 1100°C. This third exothermic event labelled (▽) was identified as the formation of Ti_3Al while α-Al_2O_3 peaks became stronger in the XRD pattern. The origin of the fourth exothermic event labelled (○) is unclear. The second, third and fourth exothermic events all show a peak shift from higher temperature to lower temperature with increasing milling time.

Bruhn et al.[2] reported the formation of γ-Al_2O_3 from the reaction between Al and TiO_2 below 700°C although this is not observed here. Pan et al.[16] also reported the formation of this phase through the interfacial reaction between Al and TiO_2 initiated at ~588°C. The transformation of γ-Al_2O_3 to α-Al_2O_3 is understandable because this phase is thermodynamically less stable than α-Al_2O_3 upon heating.

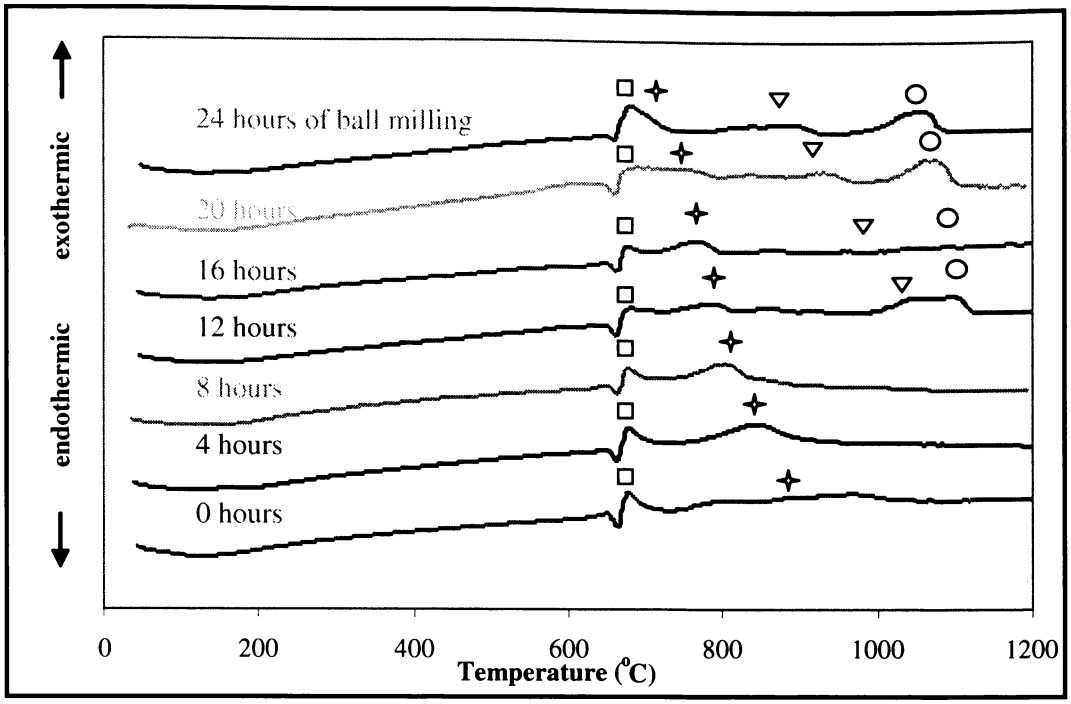

Figure 4.12: Differential thermal analysis traces of ball milled Al-TiO_2 samples heated at 15°C/min in argon (symbols described in text)

Peak integration of exothermic portions of the traces showed lower energy evolution for lower milling times. The reaction was certainly slower and less extensive than that at longer milling times. The increased Al/TiO_2 interfacial area of the composite powder particles due to longer ball milling time is responsible for the extensive exothermic reactions compared to shorter milling time.

4.3 Compact Morphology

Figure 4.13 and Figure 4.14 show the physical appearance of pressureless sintered samples produced from the two hours discus milled Al-TiO_2 composite powder subjected to ball milling for different times under vacuum at 1510°C (except the 24 hours ball milled sample at 1423°C) and heating rate of 15°C/min. After pressureless sintering of the powder before and after 4 hours ball milling, the shape of the pellets distorted from a round to an oval shape. After 8 hours of ball milling, the sintered pellet displayed a "less oval" shape and bloating appeared at the surface. The bloating became more severe as the ball milling time was increased finally resulting in fragmentation of the surface for pellets prepared from 24 hours ball milled powder, heated to just 1423°C.

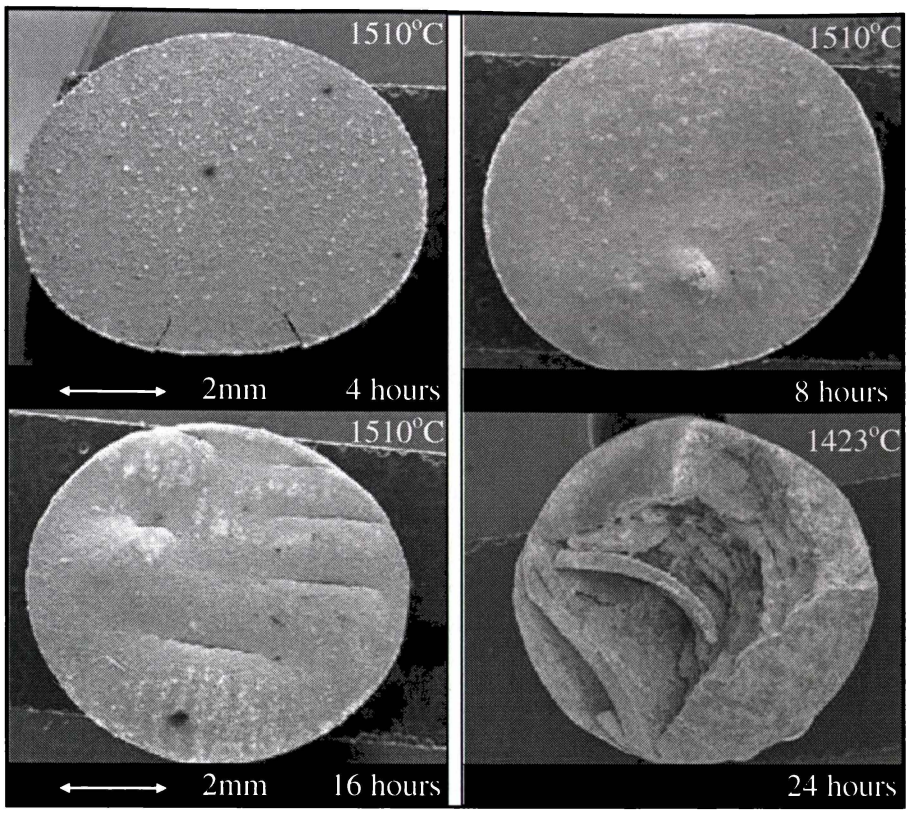

Figure 4.13: Physical appearance (top view) of the samples, pressureless sintered at 1423 and 1510°C under vacuum

Bloating occurs when the surface layer is either (1) very dense or (2) has a 'plastic' or 'viscous' component, in addition to some evolved gas from the body as a result of some chemical process. Fine particles lead to early sintering forming a 'skin' on the surface before the body reaction has been completed, hence causing bloating. Moreover, the DTA traces show the exothermic reactions at 15°C/min heating rate took place from 680 to 880°C for the Al-TiO_2 powders ball milled for 0, 4 and 8 hours and from 680 to 1100°C for the powder ball milled for 12, 20 and 24 hours also support this phenomenon (refer Figure 4.12).

The Al-TiO_2 system exhibits relatively low reaction enthalpies(ΔH = -258.6kJ/mol; ΔG = -248.2kJ/mol for the reaction: $4Al+3TiO_2 \rightarrow 3Ti+2Al_2O_3$[17]), therefore the reaction velocity and maximum heat evolved during reaction synthesis can be controlled by using a low heating rate. With reduction of the heating rate to 3-5°C/min, the explosive bloating caused by the exothermic reactions during sintering was overcome.

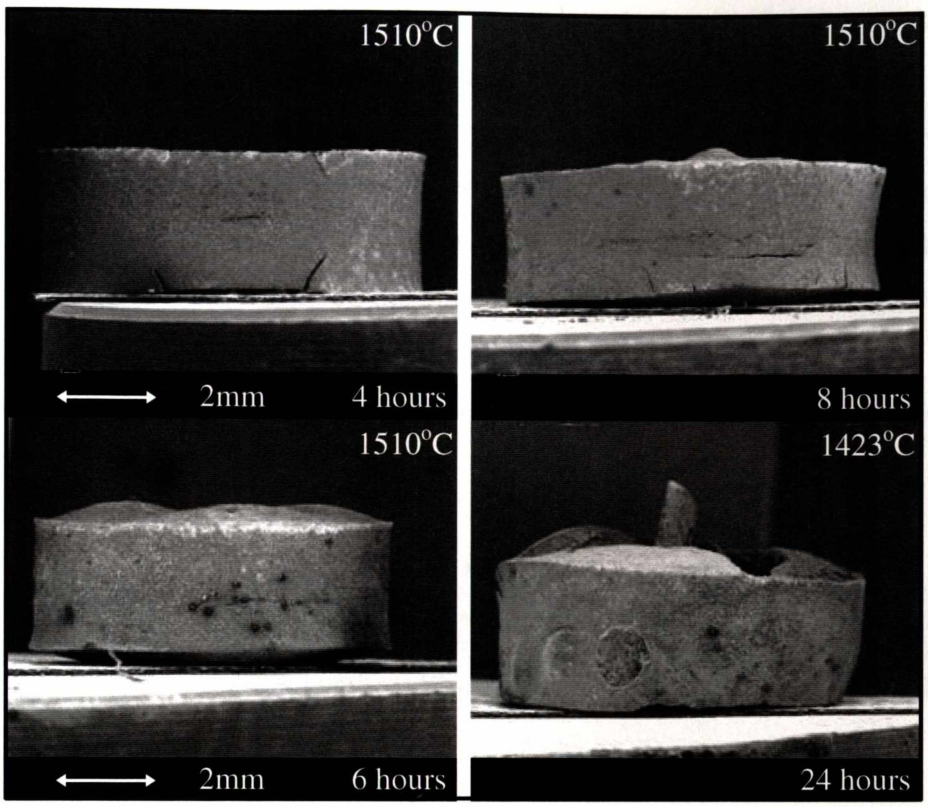

Figure 4.14: Physical appearance (side view) of the samples, pressureless sintered at 1423 and 1510°C under vacuum

Sintering of the Al-TiO_2 powder compacts using different powder beds was examined in an attempt to manage the shape distortion and bloating problem. However, the problem with the shape distortion remained irrespective of the powder beds, at 3-5°C/min as shown in Figure 4.15.

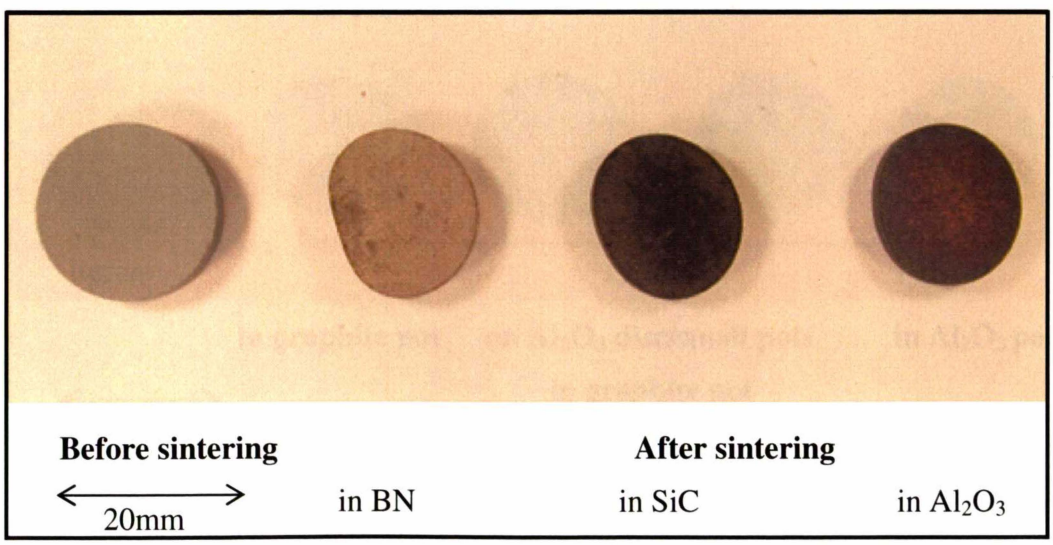

Figure 4.15: Physical appearance of the samples pressureless sintered in different powder beds at 1423°C under vacuum at 3-5°C/min

Powder beds of boron nitride, silicon carbide and alumina were used but all resulted shape distortion after sintering at 3 to 5°C/min as shown in Figure 4.15. Figure 4.16 and Figure 4.17 show the physical appearance of the samples after sintering without the use of a powder bed. The removal of the powder bed and its replacement with Al_2O_3 discs and calcined Al_2O_3 powder in Al_2O_3 small pots, as shown in Figure 4.18, improved the sintering of the samples compacted from the discus milled Al-TiO_2 composite powders under vacuum or argon.

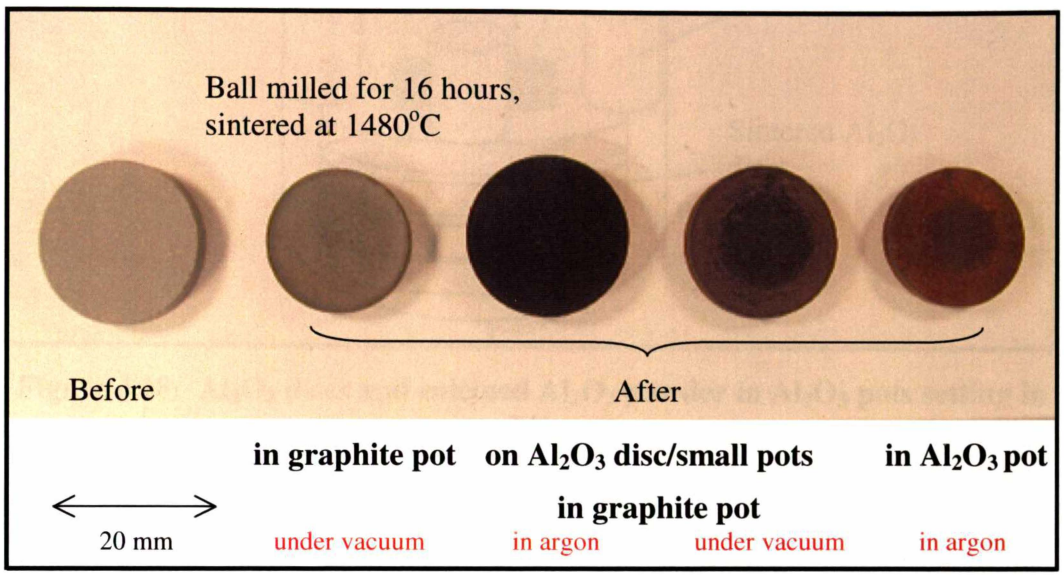

Figure 4.16: Physical appearance (top view) of the samples pressureless sintered at 1300°C with heating rate of 5-15°C/min in different environment

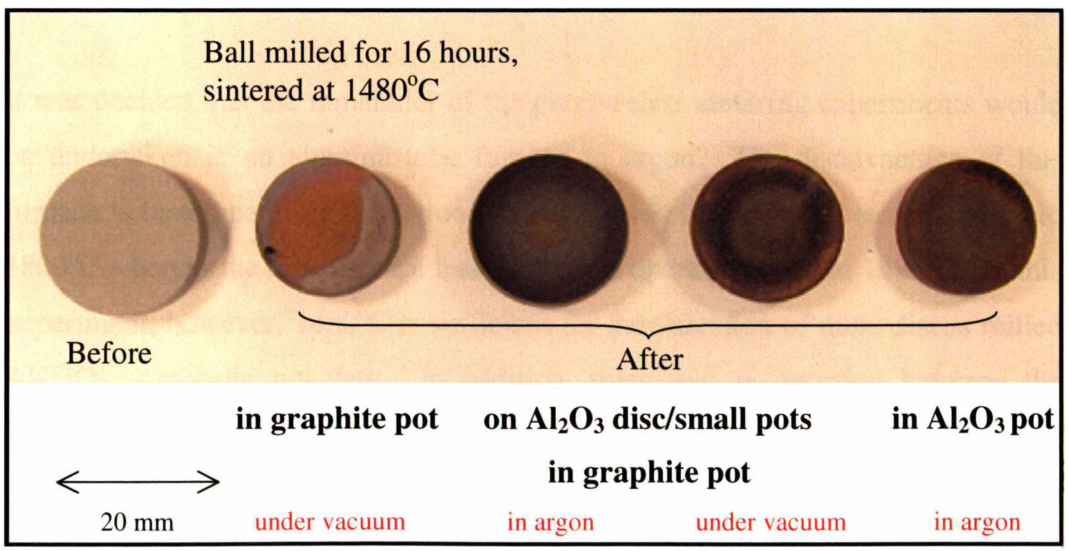

Figure 4.17: Physical appearance (bottom view) of the samples pressureless sintered at 1300°C with heating rate of 5-15°C/min in different environment

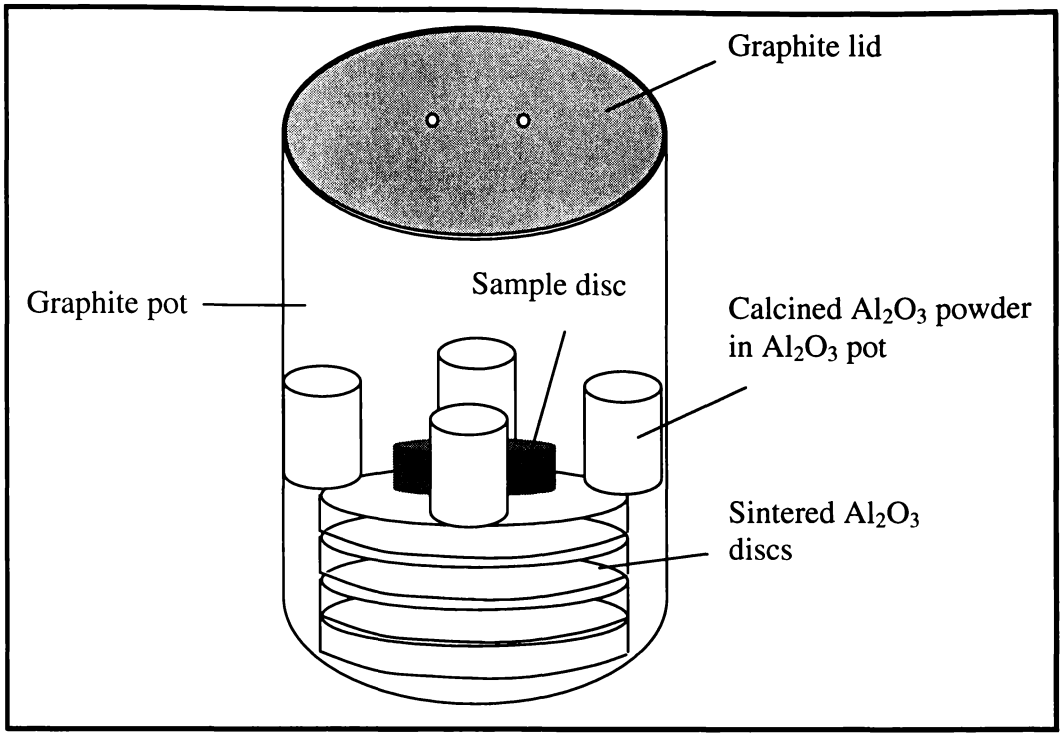

Figure 4.18: Al_2O_3 discs and calcined Al_2O_3 powder in Al_2O_3 pots setting in graphite pot

However, the EDS analysis shows some carbon contamination on all the surfaces of the samples. Due to the reactive nature of Al-TiO_2 composite powder, pressureless sintering of this powder in a furnace with graphite components and insulation was discontinued.

It was decided that the remainder of the pressureless sintering experiments would be undertaken in an alumina tube furnace in argon. The disadvantage of this furnace is its temperature limitation. The hot press furnace can be operated up to 1800°C whereas the tube furnace had a practical operating limit of 1480°C. In this experiment, however, 1480°C is sufficient for densification of most discus milled Al-TiO_2 composite powders. In addition, there was no reaction between the alumina tube and the sample in argon and less contamination between the environment and the sample. Figure 4.19 shows the physical appearance of the sample before and after sintering at 1480°C in argon. A thin surface oxidation layer of Al_2TiO_5 was detected, which could not be avoided due to low level of oxygen in the argon gas atmosphere. This thin layer was easily removed by surface grinding.

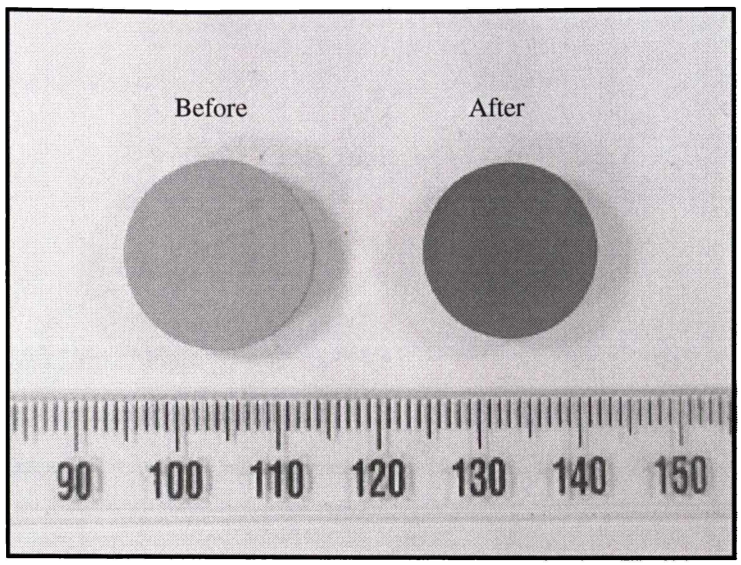

Figure 4.19: The samples before and after sintering at 1480°C in argon in the alumina tube furnace with a heating rate of 15°C/min

Three different heating schedules were established to sinter the discus milled and ball milled Al-TiO_2 composite powders according to their particle size distributions as shown in Figure 4.20. Previous problems associated with the oxidising atmosphere and oval shape distortions were eliminated by running the experiments in the alumina tube furnace in argon at heating rates slower than 15°C/min.

Edge curvature occurred after sintering as shown in Figure 4.21, when sample diameter was scaled up from 15 to 25mm for ball on ring mechanical tests. With this edge curvature, it took much longer times to grind the surface to a plane parallel finish as a basic requirement for the ball on ring test and often it was impossible.

Figure 4.22 shows the technique used to eliminate the edge curvature after sintering. It was found that by cold isostatically pressing two pellets together, the edge curvature was removed. The only difficulty was to separate the samples after sintering without damaging them.

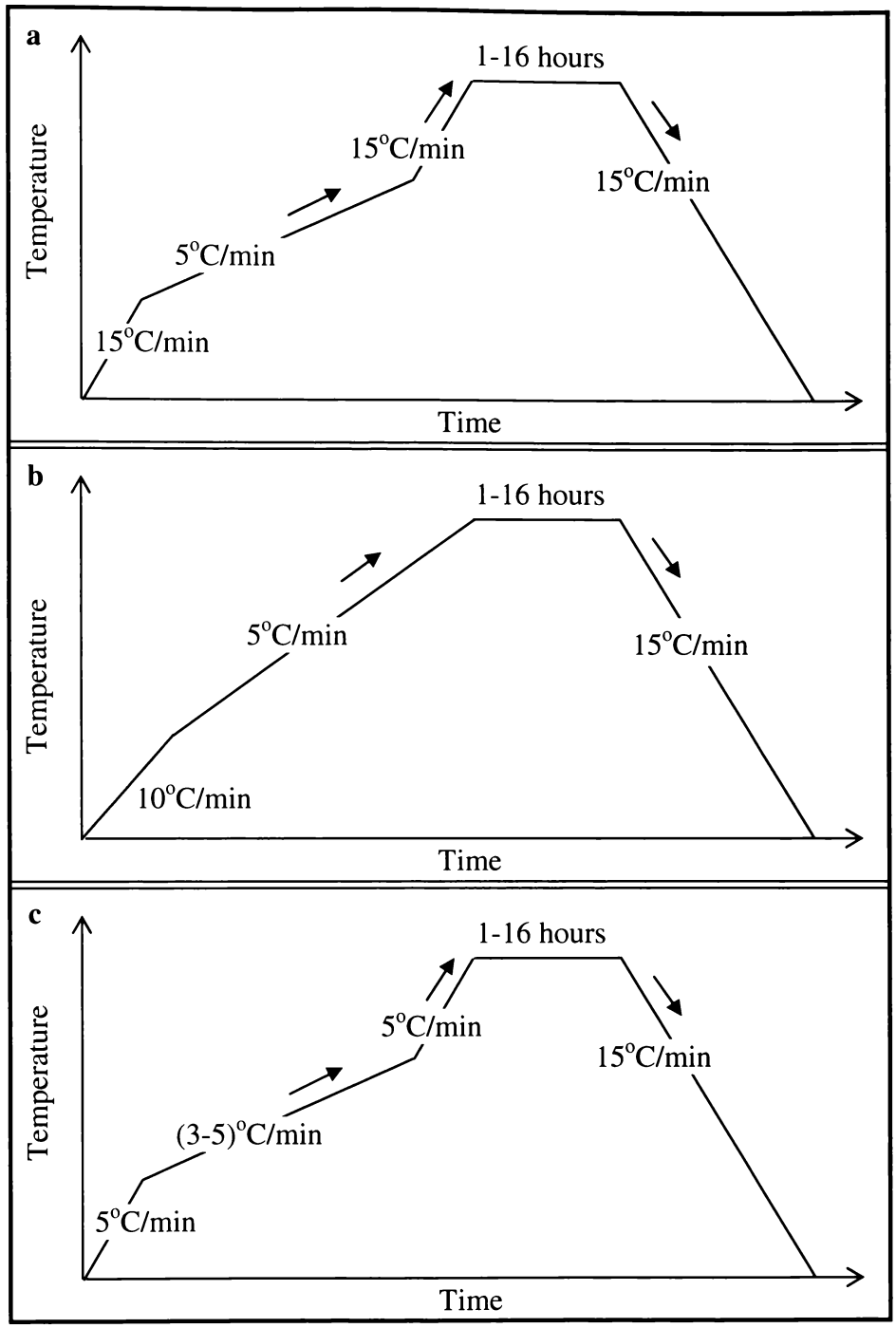

Figure 4.20: Sintering schedules of Al-TiO_2 samples in the alumina tube furnace for (a) 0, 4, (b) 8, 12, 16 and (c) 20 and 24 hours ball milled powders

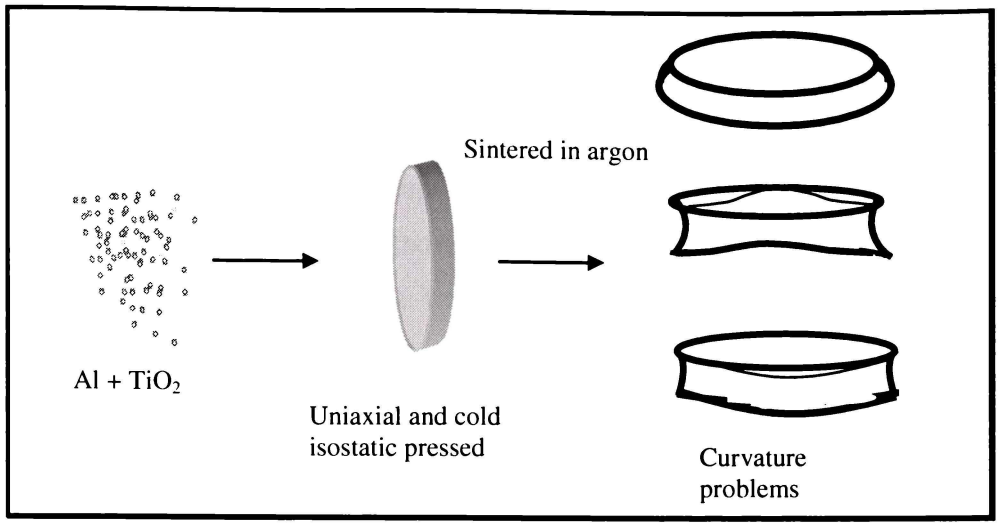

Figure 4.21: Edge curvature after sintering in argon in the alumina tube furnace

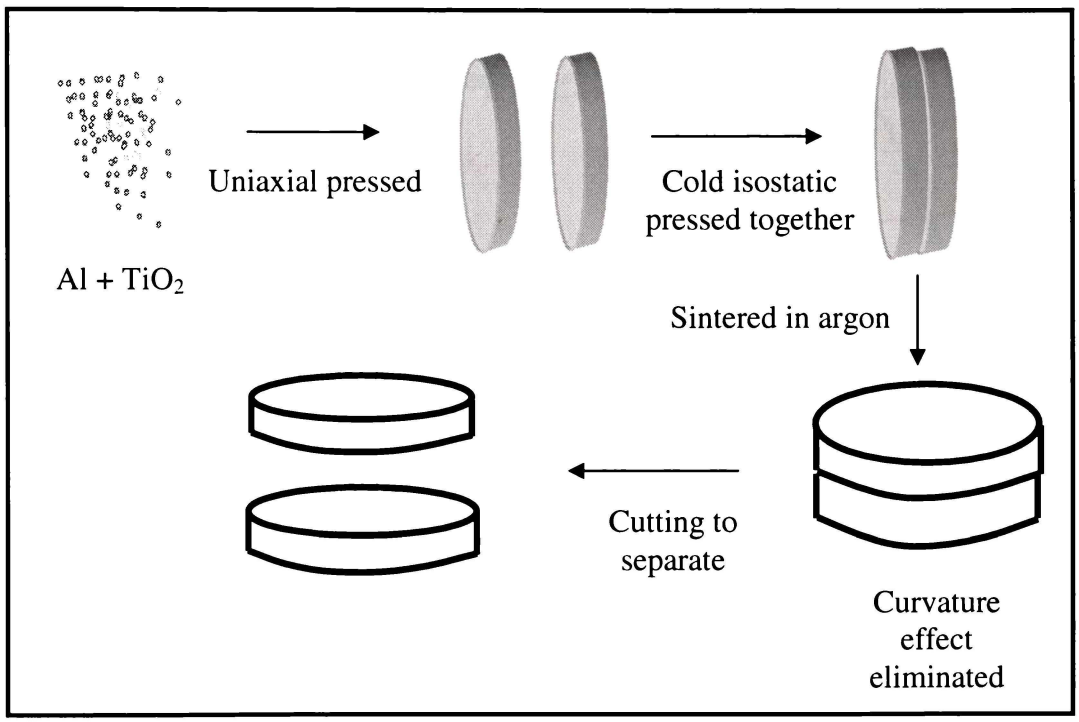

Figure 4.22: Technique for eliminating edge curvature of pellets after sintering in argon in the alumina tube furnace

4.4 Dilatometry Analysis

Figure 4.23 shows the dilatometry curves of the Al-TiO_2 powder compacts made using powders with different particle sizes. The dilatometry curves show that the sintering stage commenced around 1000°C and continued until 1400°C was reached. Al-TiO_2 powder compacts consisting of finer powder particles sintered at a much earlier stage than compacts with coarser powder particles. This can be

explained by the increased surface area of the powder. The decrease in reaction temperature observed after hours of ball milling implies that milling has enhanced the homogeneity of the compacts. All the samples show similar characteristics with different sintering rate, except for the Al-TiO_2 composite powder after 20 and 24 hours of ball milling showing expansion between 800-1100°C. The expansion of the compacts prior to the densification can be explained by the exothermic reactions between Al and TiO_2 forming new phases, hence led to volume change. Greater expansion was noted for compact with finer powder particle sizes, which is explained by the extensive exothermic reactions seen in Figure 4.12.

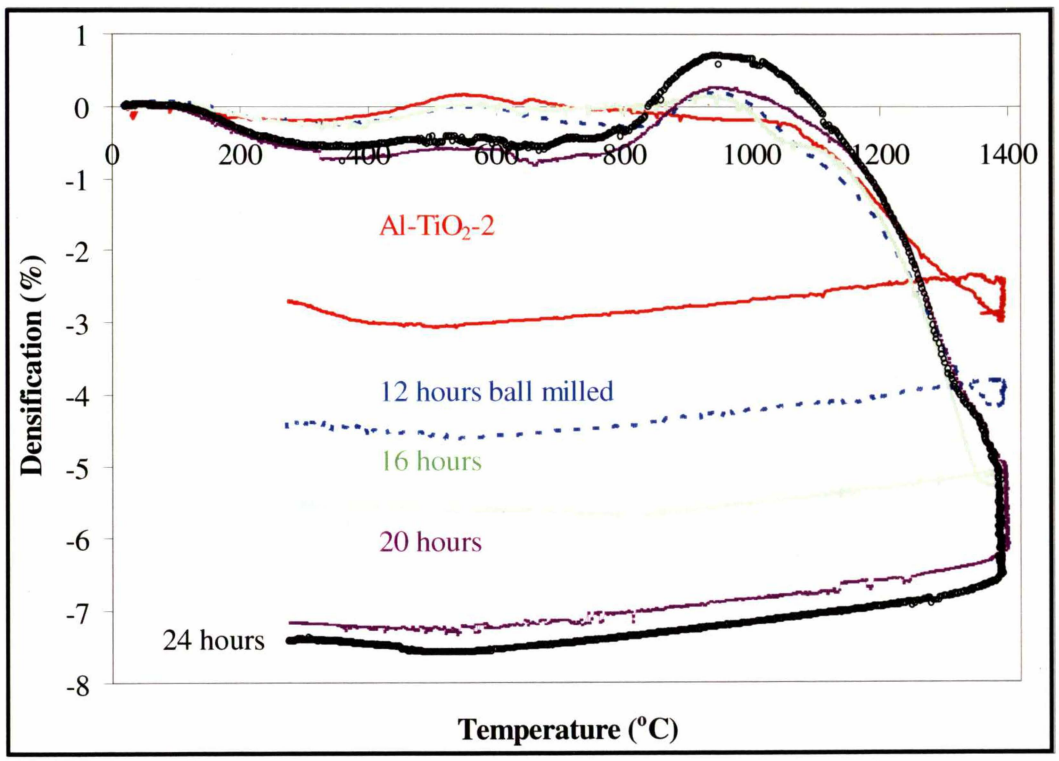

Figure 4.23: Dilatometry curves of the Al-TiO_2 powder compacts in argon up to 1400°C

4.5 Phase Structure-Densification Relationship

4.5.1 Ti_3Al-TiO-Al_2O_3 Composites

After sintering, the samples consist of mixtures of Al_2O_3, Ti_3Al and two TiO phases. The increase of unit cell dimensions of Ti_3Al compared with that in the ICDD database implies the possibility of dissolved oxygen incorporated in Ti_3Al during sintering. The solubility of oxygen in Ti_3Al is about 12±3at% for Ti_3Al[18-20].

Figure 4.24 and Figure 4.25 show the XRD patterns and the intensity profiles of the Ti_3Al-TiO-Al_2O_3 composites produced by pressureless sintering Al-TiO_2 (rutile) at a heating rate of 15°C/min under vacuum. The XRD traces show that the intensity of the Ti_3Al peak decreases with increasing sintering temperature, which is offset by the increment of titanium oxide phases (two TiO phases). The XRD peak intensity of the Ti_3Al phase is reduced from 55% at 1318°C to 4% at 1627°C, which can be understood by hypothesising a small partial pressure of residual oxygen in the vacuum environment of the graphite furnace.

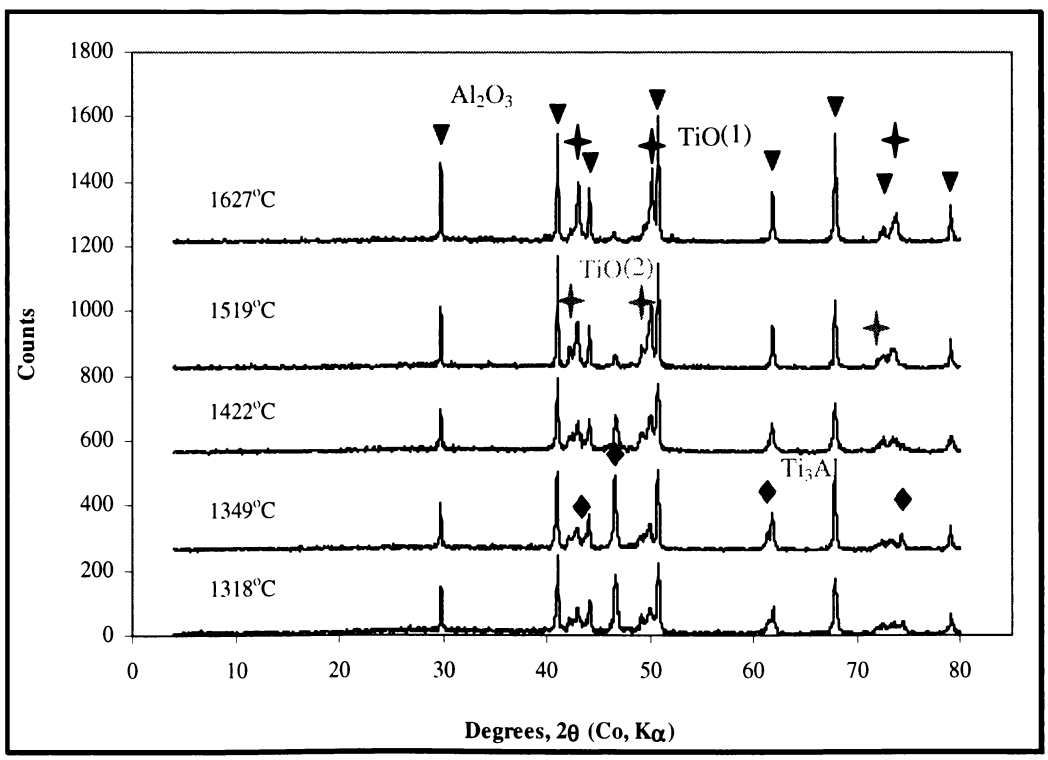

Figure 4.24: XRD patterns of Ti_3Al-TiO-Al_2O_3 composites produced by pressureless sintering Al-TiO_2 composite powder at 15°C/min under vacuum

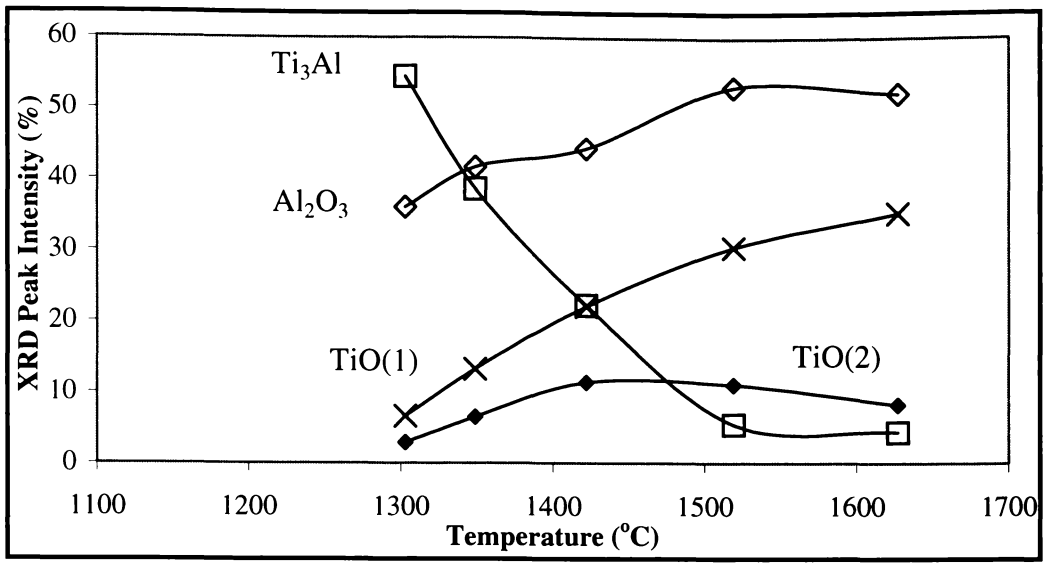

Figure 4.25: Intensity profile of Ti_3Al-TiO-Al_2O_3 composites produced by pressureless sintering Al-TiO_2 composite powder at different temperatures under vacuum

Figure 4.26 and Figure 4.27 show the intensity profile of Ti_3Al-TiO-Al_2O_3 composites produced by pressureless sintering Al-TiO_2 composite powder subjected to various ball milling times, under vacuum at 1510°C and in argon at 1480°C respectively. Heating rates from 5-15°C/min were used in these experiments depending on the various particle size distributions. Ball milling time has an important effect on the pressureless sintering of Al-TiO_2 samples under vacuum, potentially due to a small partial pressure of oxygen in the vacuum atmosphere during sintering. The intensity of the Ti_3Al phase decreases sharply while both TiO phases increase with respect to the ball milling time up to 24 hours with the increased surface area of the particles due to longer ball milling time. On the contrary, the intensity of Ti_3Al phase is maintained around the same level without the formation of additional TiO phase when pressureless sintered in argon as shown in Figure 4.27.

Another batch of two hours discus milled aluminium and rutile composite powder was produced and designated Al-TiO_2-3. This batch of Al-TiO_2-3 composite powder with starting median particle diameter of 7.7μm was pressureless sintered in argon forming Ti_3Al-TiO-Al_2O_3 composites prior to hot isostatic pressing, which is discussed in Chapter Five. Figure 4.28 and Figure 4.29 show the XRD patterns and intensity profile of the samples, respectively, after sintering in argon.

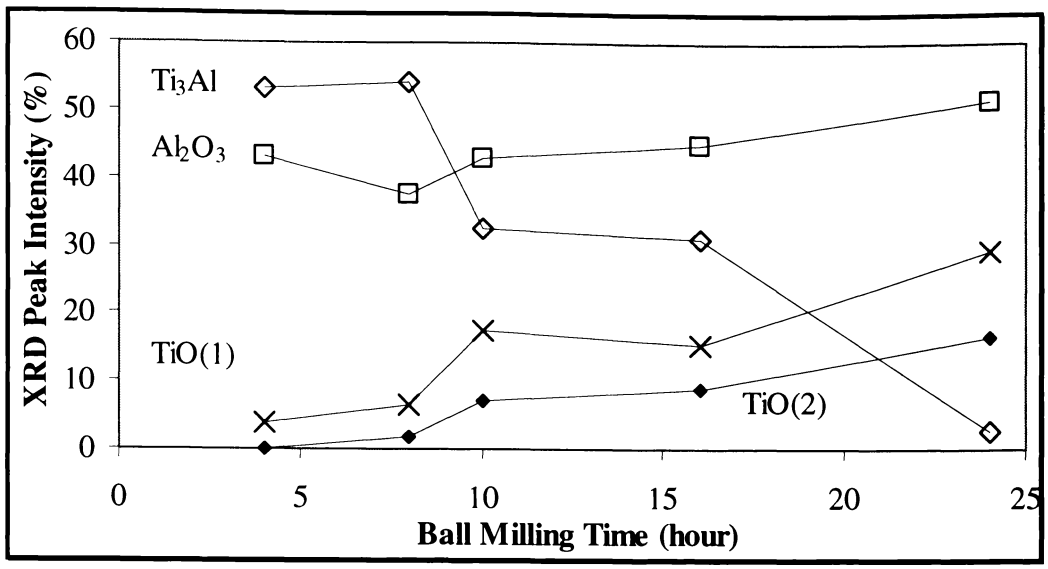

Figure 4.26: Intensity profile of Ti_3Al-TiO-Al_2O_3 composites produced by pressureless sintering Al-TiO_2 composite powder (subjected to various ball milling times) at 1510°C under vacuum

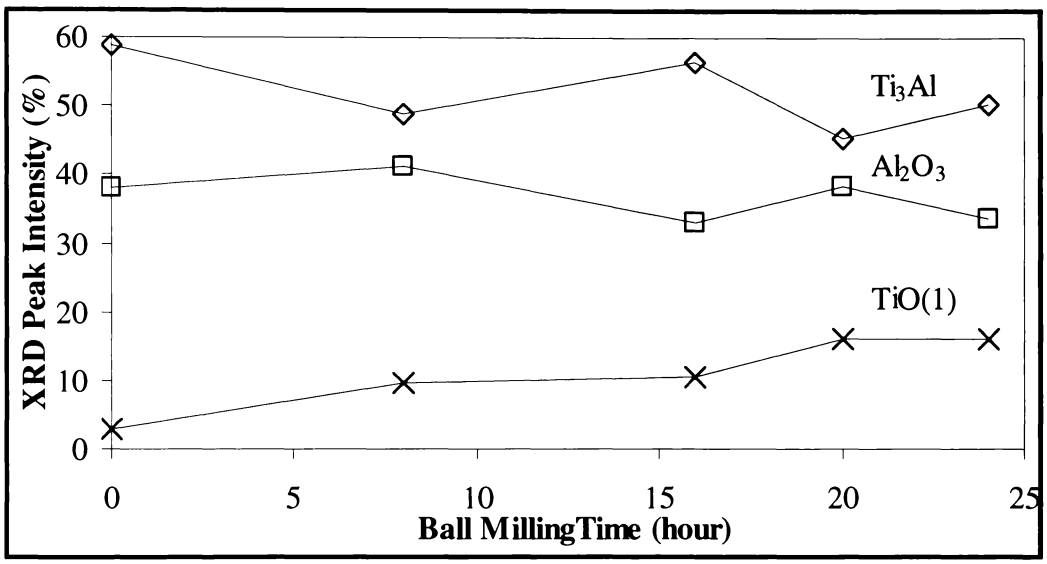

Figure 4.27: Intensity profile Ti_3Al-TiO-Al_2O_3 composites produced by pressureless sintering Al-TiO_2 composite powder (subjected to various ball milling times) at 1480°C in argon

The Ti_3Al-TiO-Al_2O_3 composites produced by pressureless sintering Al-TiO_2-3 composite powder consist of mixtures of Al_2O_3, two Ti_3Al and low level of TiO phases. Previous work on these materials has shown that Ti_3Al contains approximately 17at%O in solid solution by quantitative microanalysis using electron microprobe and wavelength dispersive spectrometry[15]. The explanation of two distinct Ti_3Al phases is based on the assumption that different amounts of dissolved oxygen were picked up during sintering.. That is, an increase of two different unit cell dimensions was observed for Ti_3Al phase compared to those in

the ICDD database giving two Ti_3Al XRD patterns. This is also seen later in the sintering of Al-TiO_2 (anatase) composite powder described in Section 4.5.2.

The XRD traces show that all the phases maintained around the same intensity level from 1330°C to 1480°C in argon. The intensity of the Ti_3Al phase displayed here in Figure 4.29 is a sum of the two Ti_3Al phases.

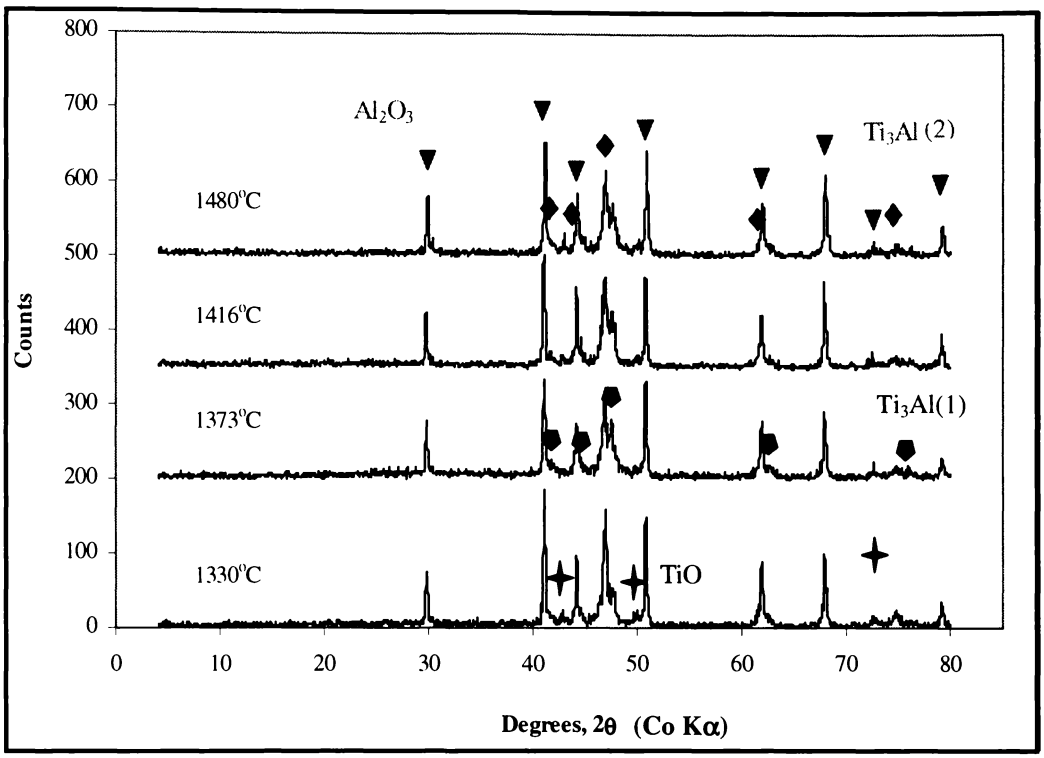

Figure 4.28: XRD patterns of Ti_3Al-TiO-Al_2O_3 composites produced by pressureless sintering Al-TiO_2-3 composite powder at different temperatures in argon

Figure 4.30 shows the open porosity and bulk density of Ti_3Al-TiO-Al_2O_3 composites produced by pressureless sintering Al-TiO_2 composite powder in argon at 1480°C as a function of holding period. The open porosity of the pressureless sintered Al-TiO_2 composite decreased as the particle size decreased. Al-TiO_2 samples with 0 hour ball milling time has the highest porosity trend with increasing holding period compared to the other data. With the same pressureless sintering condition, the open porosity decreased by up to 5-13% when the powder particle size decreased from 35 to 10μm in the 90 percentile from 0 to 24 hours of ball milling. The bulk density, on the other hand, was improved from 3.5 to as high as 4.2 g/cm^3 with both the reduction of starting particle size and increase of holding period.

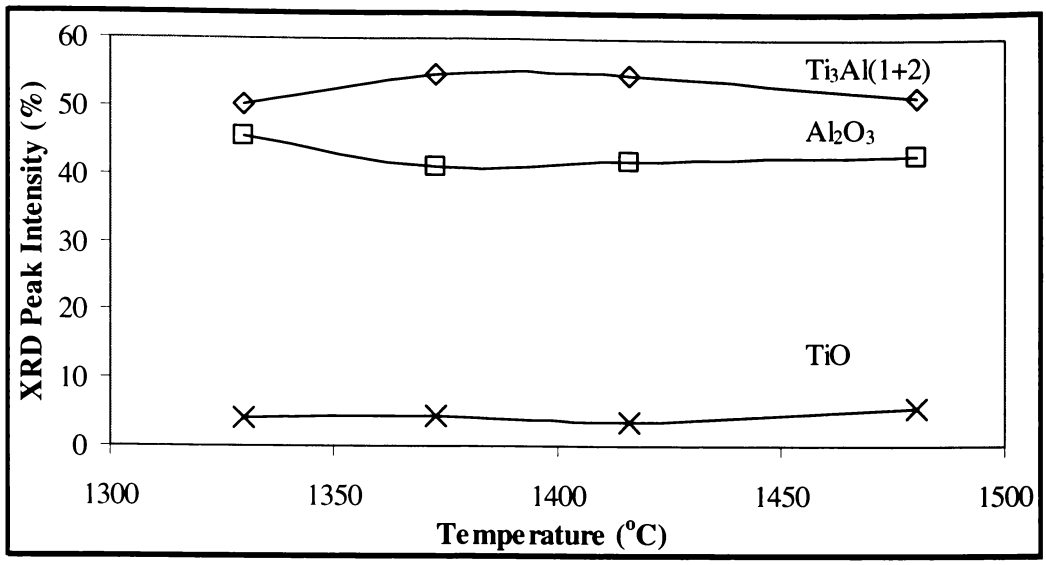

Figure 4.29: Intensity profile of Ti_3Al-TiO-Al_2O_3 composites produced by pressureless sintering Al-TiO_2-3 composite powder at different temperatures in argon

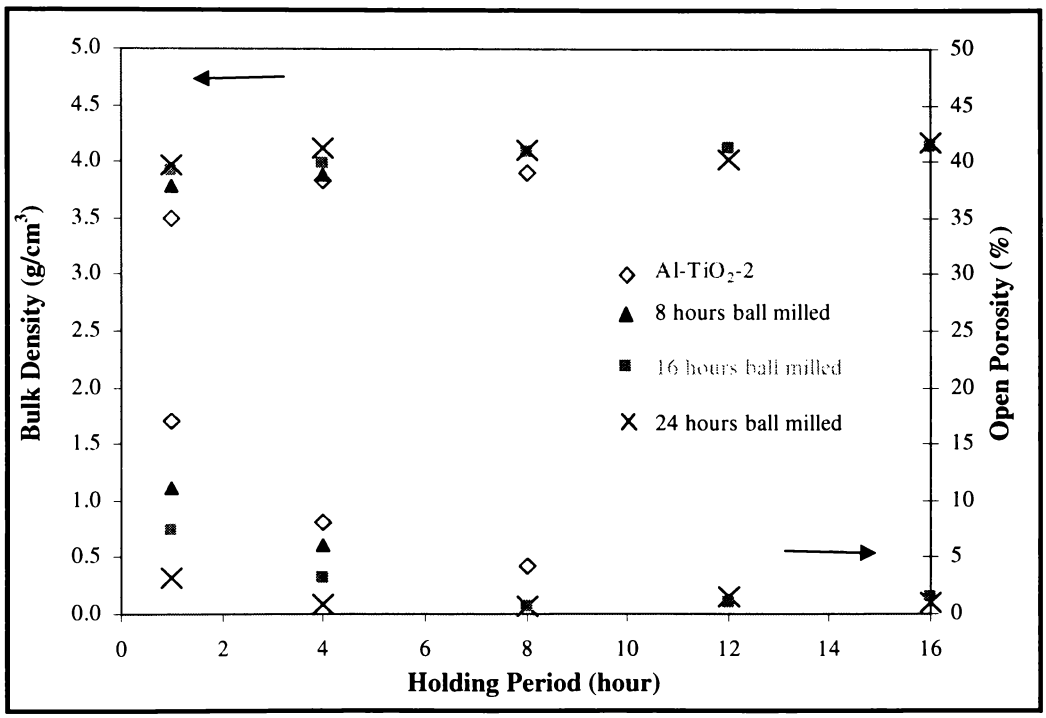

Figure 4.30: Open porosity and bulk density of Ti_3Al-TiO-Al_2O_3 composites produced by pressureless sintering Al-TiO_2 composite powder in argon at 1480°C as a function of holding period

Figure 4.31 shows the closed porosity of the Ti_3Al-TiO-Al_2O_3 composites produced by pressureless sintering Al-TiO_2 composite powders subjected to different ball milling times. The closed porosity is maintained around 5% except for the Al-TiO_2 composite sintered at 1480°C for 1 hour, which shows approximately 12% of closed porosity in the body.

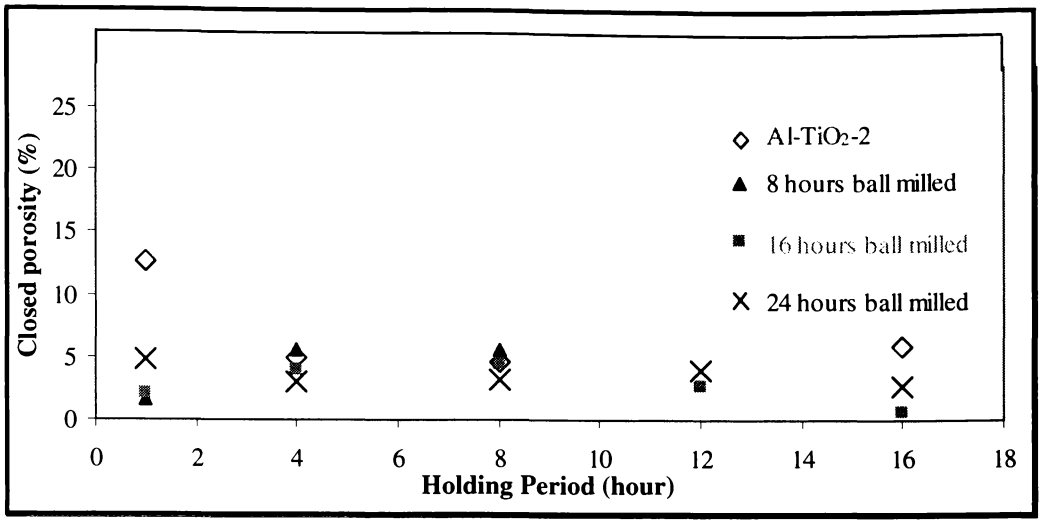

Figure 4.31: Closed porosity of Ti_3Al-TiO-Al_2O_3 composites produced by pressureless sintering Al-TiO_2 composite powder in argon at 1480°C as a function of holding period

4.5.2 Ti_3Al-Al_2O_3 Composites

Pressureless sintering of two, four and six hours discus milled Al-TiO_2 (anatase) composite powders was performed in an alumina tube furnace. Figure 4.32 and Figure 4.33 show the XRD patterns of Ti_3Al-Al_2O_3 composites produced by pressureless sintering 4(Al-TiO_2) and 4(Al-TiO_2)-24 composite powders in argon. The sintered composites consist of mixtures of Al_2O_3 and Ti_3Al phases. The XRD traces show that all the phases maintained similar intensity levels from 1380°C to 1480°C in argon. Figure 4.34 and Figure 4.35 show the XRD patterns of Ti_3Al-Al_2O_3 composites produced by pressureless sintering 6(Al-TiO_2) and 6(Al-TiO_2)-24 composite powders in argon. The compositions of the sintered composites were comparable to those produced from 4(Al-TiO_2) composite powder. That is, only Al_2O_3 and Ti_3Al phases were detected after pressureless sintering up to 1480°C in argon.

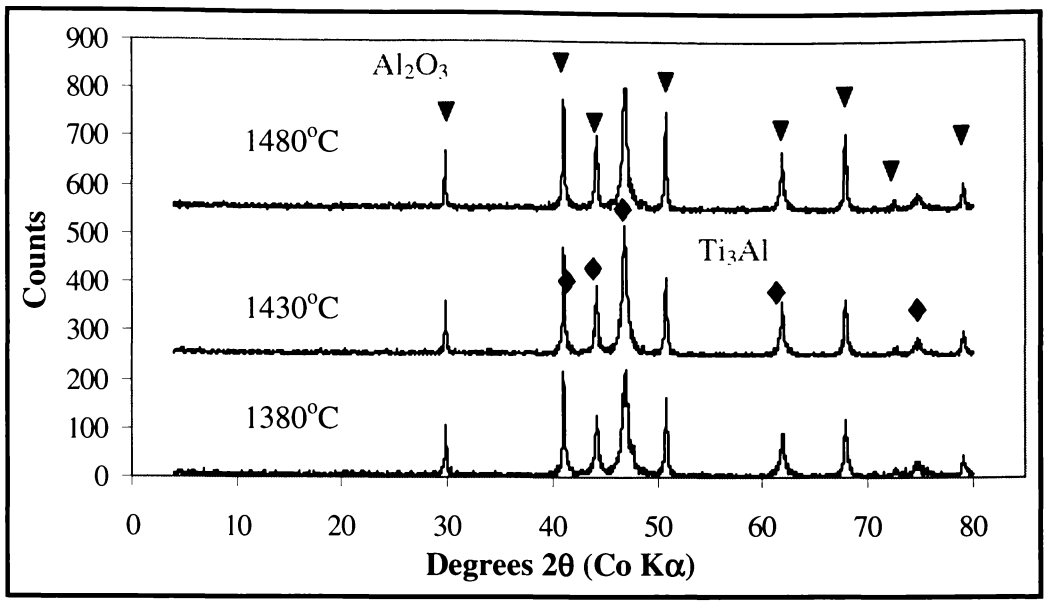

Figure 4.32: XRD patterns of Ti_3Al-Al_2O_3 composites produced by pressureless sintering 4(Al-TiO_2) composite powder at different temperatures in argon

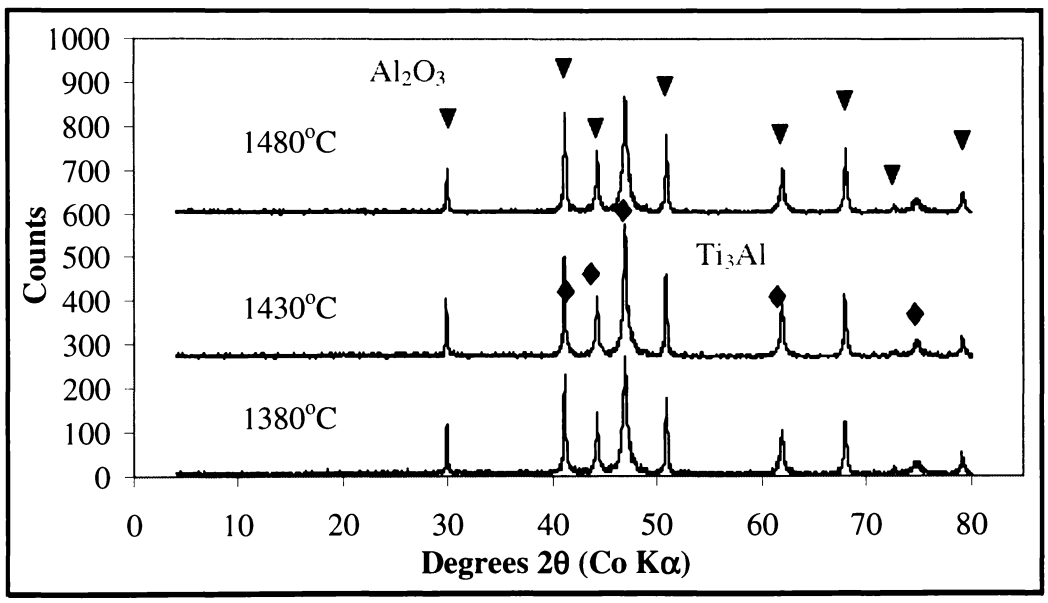

Figure 4.33: XRD patterns of Ti_3Al-Al_2O_3 composites produced by pressureless sintering 4(Al-TiO_2)-24 composite powder at different temperatures in argon

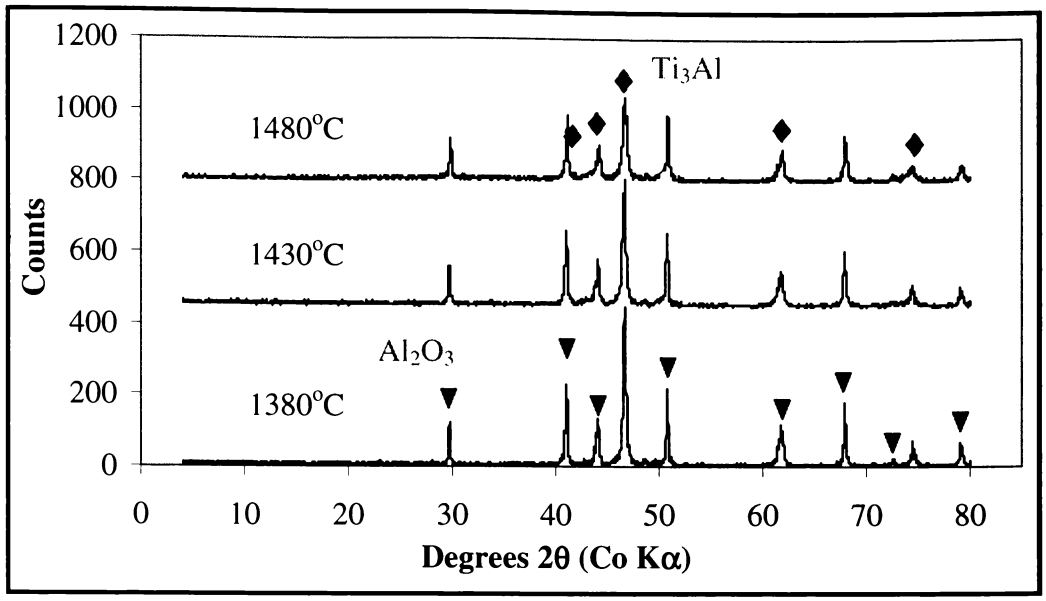

Figure 4.34: XRD patterns of Ti_3Al-Al_2O_3 composites produced by pressureless sintering 6(Al-TiO_2) composite powder at different temperatures in argon

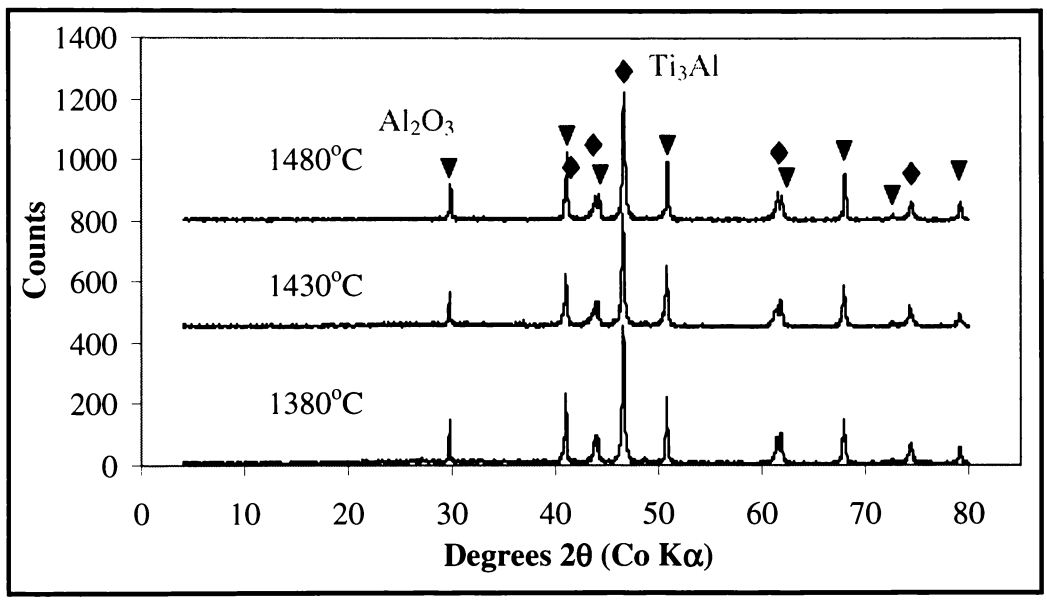

Figure 4.35: XRD patterns of Ti_3Al-Al_2O_3 composites produced by pressureless sintering 6(Al-TiO_2)-24 composite powder at different temperatures in argon

Figure 4.36 shows the total porosity and bulk density of Ti_3Al-Al_2O_3 composites produced by pressureless sintering Al-TiO_2 (anatase) composite powders in argon as a function of their sintering temperature. Total porosity of the pressureless sintered composite decreases whereas the bulk density increases with both the reduction of particle size and the increase of sintering temperature.

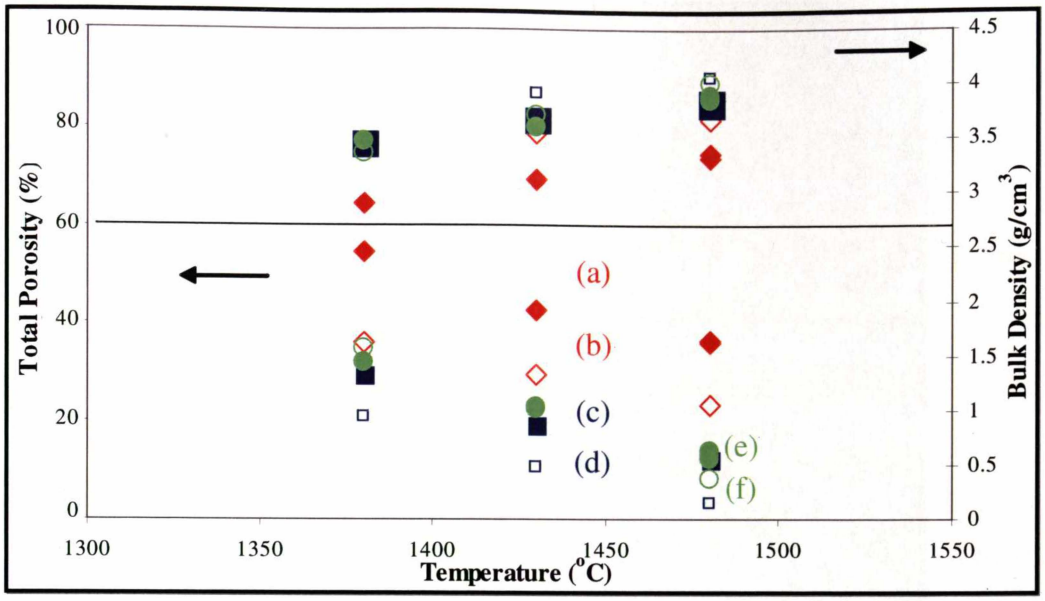

Figure 4.36: Total porosity and bulk density of Ti_3Al-Al_2O_3 composites produced by pressureless sintering (a) 2(Al-TiO_2), (b) 2(Al-TiO_2)-24, (c) 4(Al-TiO_2) (d) 4(Al-TiO_2)-24, (e) 6(Al-TiO_2) and (f) 6(Al-TiO_2)-24 composite powders in argon as a function of temperature

4.6 *Processing-Microstructure Relationship*

Figure 4.37 shows the SEM micrographs of the Ti_3Al-TiO-Al_2O_3 composites produced by pressureless sintering the two hours discus milled Al-TiO_2 composite powder subjected to (i) 16 and (ii) 24 hours of ball milling at 1480°C in argon. The dark grey particles were identified as Al_2O_3 phase embedded in a pale grey matrix of Ti_3Al/TiO phases with black residual pores. The quantity of pores decreased whereas the Al_2O_3 grains increased with increasing holding period for both sets of samples. After 8 hours of holding, the open porosity of both 16 and 24 hours of ball milled samples appeared to be close to 0% (Figure 4.30). On the other hand, closed pores were observed in the microstructure, which is also seen in the porosity measurement shown in Figure 4.31. All the samples produced from Al-TiO_2 composite powders show control of particle growth after pressureless sintering up to 1480°C as shown in Figure 4.38. This is similar to the results for the hot pressed Ti_3Al/Al_2O_3-1 samples below 1500°C shown in Figure 3.28 in Chapter Three. The average Al_2O_3 particle size in the microstructure after pressureless sintering is in the range of 1.4-3.5μm (grain size of 1-3μm is categorised as fine grain size[21]).

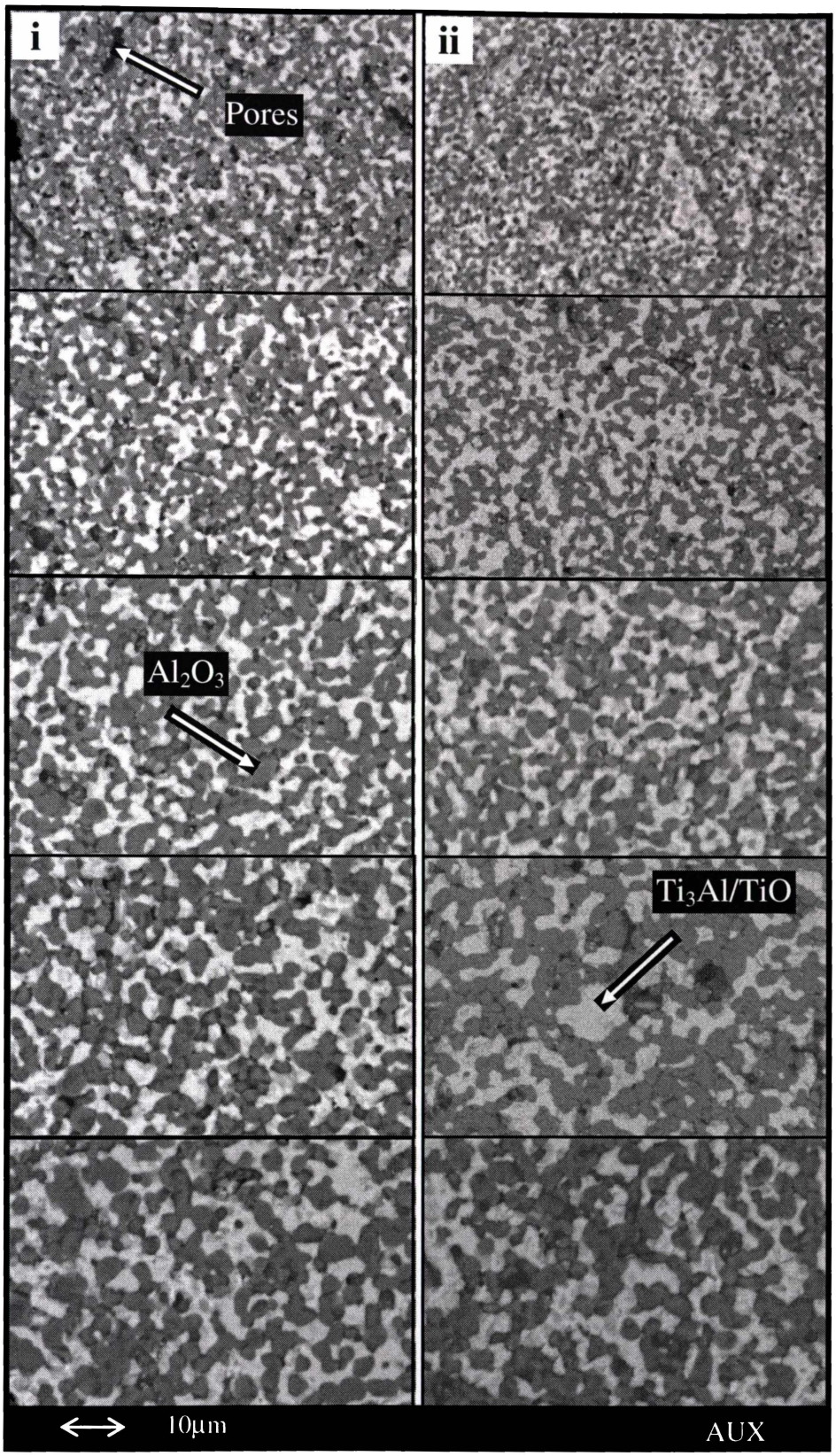

Figure 4.37: Microstructure of Ti_3Al-TiO-Al_2O_3 composites produced by pressureless sintering the discus milled Al-TiO_2 composite powders subjected to (i) 16 and (ii) 24 hours of ball milling for different holding periods

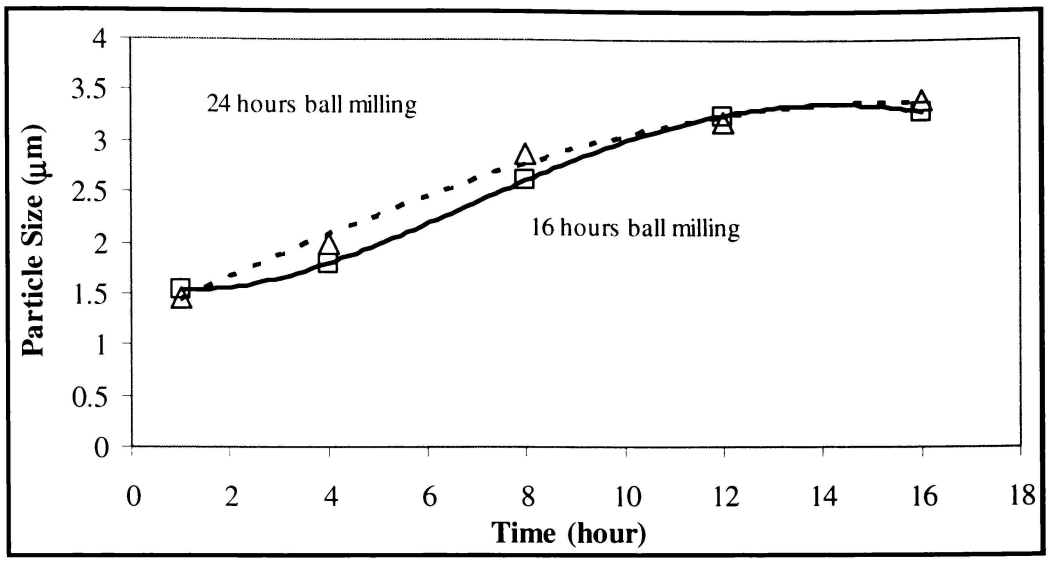

Figure 4.38: Particle size of Al_2O_3 as a function of time for Ti_3Al-TiO-Al_2O_3 composites produced by pressureless sintering Al-TiO_2 composite powder

A near fully densified microstructure was achieved at 1480°C in which the Al_2O_3 particles are embedded in the Ti_3Al/TiO matrix as shown in Figure 4.39. Both phases are continuous and hence exhibit an interpenetrating network.

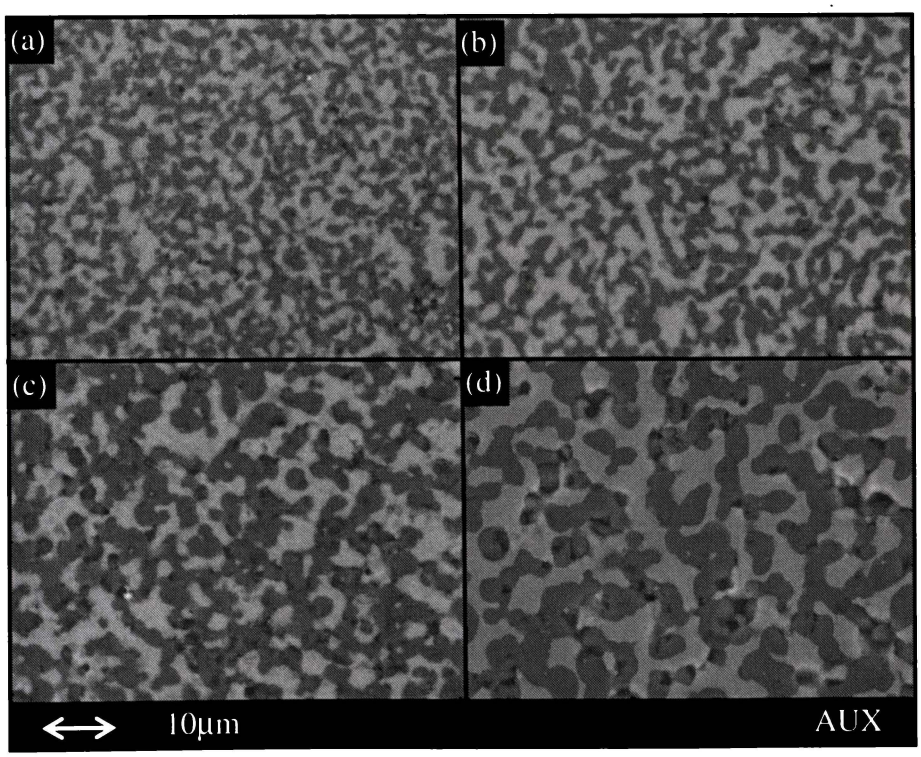

Figure 4.39: Ti_3Al-TiO-Al_2O_3 composites produced from pressureless sintering of Al-TiO_2-3 with interpenetrating network at (a)1330°C, (b)1373°C, (c)1416°C and (d)1480°C in argon

For Al-TiO_2-3 composite powder pressureless sintered from 1330°C to 1480°C in argon, the composites consist of around 50% XRD peak intensity of Ti_3Al phase as shown in Figure 4.29. An increase in Al_2O_3 particle size in the microstructure was observed with increasing sintering temperature. Figure 4.40 shows the microstructure of Ti_3Al-TiO-Al_2O_3 composites at a lower magnification than the previous figure. With increasing temperature, the Al_2O_3 particles become separated whereas the pores reduced dramatically from 18% to 4% obtained from the porosity measurement using Archimedes method. The average Al_2O_3 particle sizes of the pressureless sintered Al-TiO_2-3 composites are shown in Figure 4.41. The Al_2O_3 particle size increased from 1.2μm to 3.9μm with temperature increased from 1330°C to 1480°C.

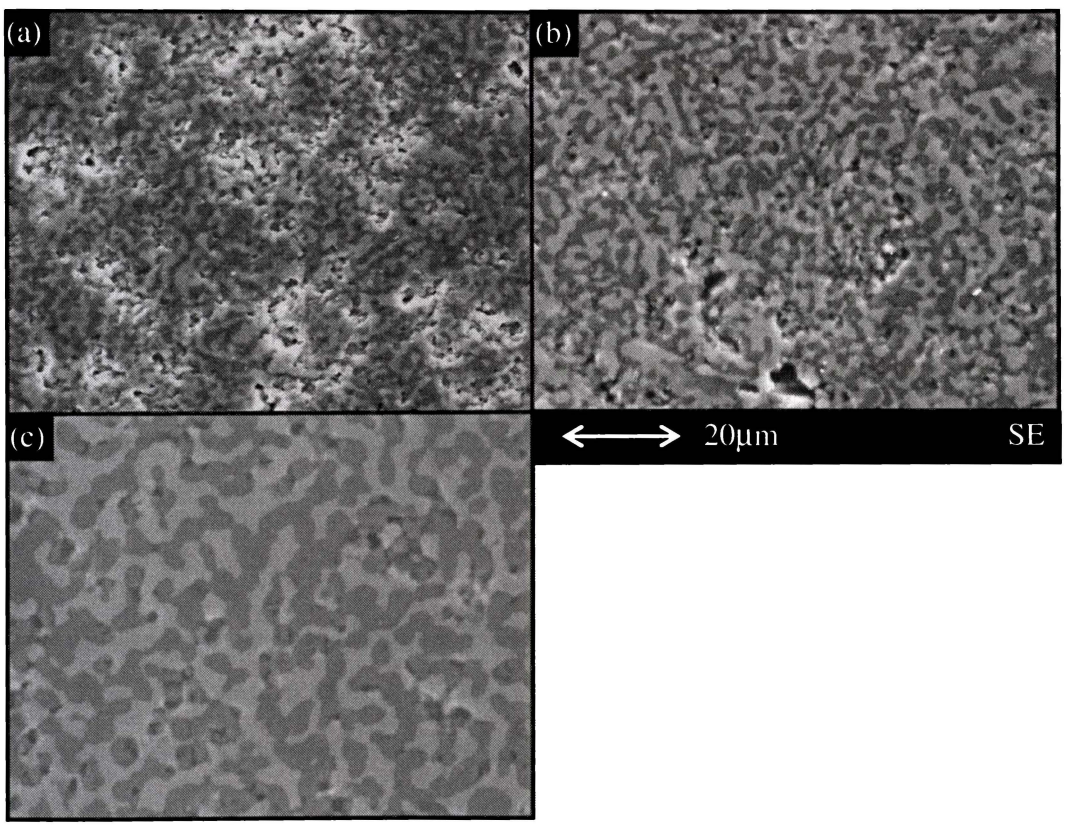

Figure 4.40: SEM images of Ti_3Al-TiO-Al_2O_3 composites prepared by pressureless sintering Al-TiO_2-3 composite powder at (a)1330, (b)1373 and (c) 1480°C in argon

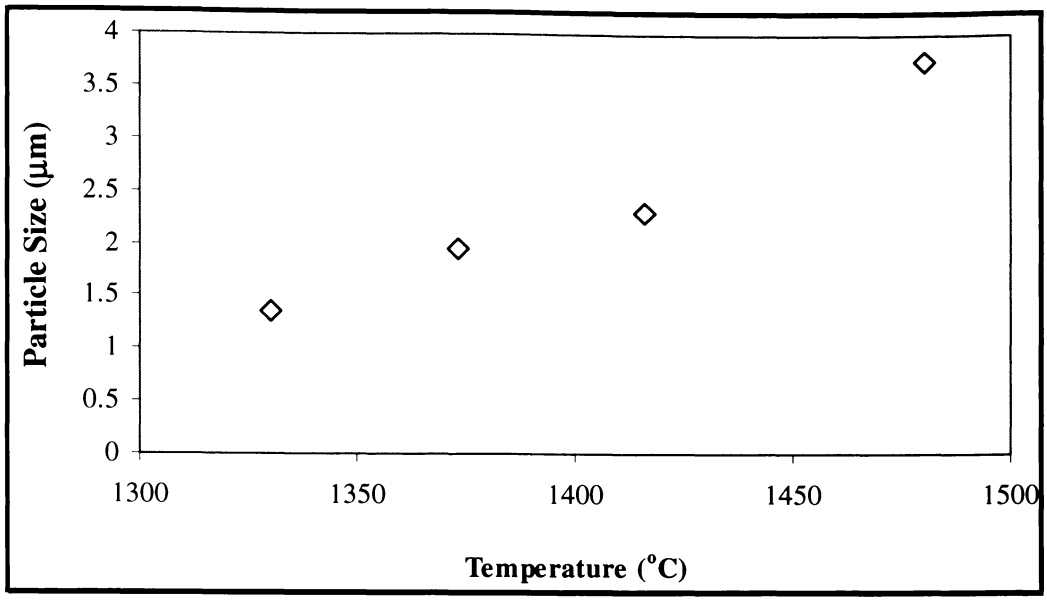

Figure 4.41: Effect of sintering temperature on the Al_2O_3 particle size in Ti_3Al-TiO-Al_2O_3 composites produced by pressureless sintering Al-TiO_2-3 composite powder

4.7 Discussion

4.7.1 Sintering Mechanism

Ti_3Al-TiO-Al_2O_3 and Ti_3Al-Al_2O_3 composites with different fractions of intermetallic and ceramic phases were fabricated by pressureless sintering Al-TiO_2 composite powders produced from discus and ball milling. Bulk density, closed and open porosity and microstructural development of the composites were studied.

Aluminium has lower density than Ti_3Al and Al_2O_3 hence the reaction between Al and TiO_2 will cause a volume change of the powder compact. The decrease in volume during Al/TiO_2 reaction can make the sintering process more difficult. A large number of open pores were present in the Ti_3Al-TiO-Al_2O_3 composites pressureless sintered at 1330°C and 1373°C as seen in Figure 4.40. This indicates that the sintering effect at these temperatures was limited. Although the reaction between Al and TiO_2 is highly exothermic, the evolved heat is insufficient to achieve sintering at 1400°C[1]. Therefore, ball milling to reduce the particle size of Al-TiO_2 and a temperature of 1480°C were used to fabricate near fully densified composites. After sintering at 1480°C, the intermetallic Ti_3Al phase became fully dense with residual pores in the Al_2O_3 particles. This is expected

since the melting temperature of Ti_3Al (1600°C) is comparatively lower than Al_2O_3 (2300°C).

Although solid state reactions of the 3A process have been studied widely, pressureless densification of fully dense bodies with fine microstructure has not been achieved. To date, only near fully densified bodies were fabricated by pressureless sintering these materials. For examples, ≤97% theoretical density of Al_2O_3-Fe_3Al composites with alumina grain size of 10-15μm[22] and very fine grained (<1μm) Al_2O_3-$NbAl_3$ composites with <95% theoretical density[23] were produced by pressureless sintering at 1500°C and 1550°C, respectively. Cai reported that 1650°C was an effective pressureless sintering temperature of Ti_3Al-Al_2O_3 composites forming ≤96% theoretical density. However, at 1650°C, the coarsening of Al_2O_3 particles from ~2-35μm was observed[1].

In this study, near fully densified Ti_3Al-TiO-Al_2O_3 and Ti_3Al-Al_2O_3 composites of 96% of theoretical density with ≤4μm Al_2O_3 particle size in the composites could be achieved for pressureless sintering at 1480°C in argon with five hours of holding period. Fine Al_2O_3 particle size was maintained at 1480°C. The Al_2O_3 particle size in Ti_3Al-TiO-Al_2O_3 composites increased from 1.2μm to 3.9μm with sintering temperature increased from 1330°C to 1480°C (grain size of 1-3μm is categorised as fine grain size[10])

4.7.2 Effect of Powder Characteristics on Sintering Behaviour

The reaction of unmilled powder is controlled by solid-state diffusion at point contacts. In the unmilled powder, the extent of contact between Al and TiO_2 particles was limited. The longer the milling time, the smaller the particles became. Therefore the reaction between Al and TiO_2 for the 24 hours ball milled powder occurred faster than the unmilled powder. However, with the reduction of particle size, the exposed surface area significantly increases, leading to the possibility of higher amount of atmospheric oxygen being absorbed. This might explains the decreased fraction of Ti_3Al phase (as reflected by the change of the Ti_3Al XRD peak intensity) and the corresponding increase of TiO phases with respect to the ball milling time up to 24 hours (Figure 4.26).

At least two exothermic peaks appeared in the DTA traces of Al-TiO_2 powders ball milled up to 24 hours as shown in Figure 4.12. With increasing ball milling time, the first exothermic peak at 680°C remained unchanged whereas the second, third and fourth exothermic peaks all show a peak shift from higher temperature to lower temperature with increasing milling time. This shows that the increase of milling time causes the reaction temperature to decrease slightly until a minimum reaction temperature was achieved. Hence the extended milling can not cause any further decrease in the reaction temperature. The decrease in reaction temperature observed after hours of ball milling implies that milling has played a major role in lowering the reaction temperature by enhancing the reaction due to increased interfacial area and shortened diffusional pathlength [14].

The increased surface area of the particles due to longer milling time was responsible for the extensive exothermic reactions compared to those at lower milling times. In general, it is clear that integration of exothermic portions of the traces showed lower heat release for lower milling time. The reaction was certainly less extensive at shorter milling times. Due to the highly exothermic character of these reactions, the temperature increase within the sample can cause distortion during pressureless sintering, which was observed in Figure 4.13 and Figure 4.14. Systems like Al-TiO_2 exhibit relatively low reaction enthalpies (ΔH = -258.6kJ/mol; ΔG = -248.2kJ/mol for the reaction: $4Al+3TiO_2 \rightarrow 3Ti+2Al_2O_3$ [17]), reaction velocity and maximum heat during reaction synthesis in the temperature range between 650 to 850°C (650 to 1050°C for 24 hours milled powder) and the reactions can easily be controlled by using low heating rates.

Discus and ball milling not only reduced the particle sizes but also improved the microstructural homogeneity of the composite powder particles. Al-TiO_2 powder compacts consisting of finer powder particles sintered at a much earlier stage than compacts with coarser powder particles as seen in Figure 4.23. This can be explained by the increased surface area of the powder. The decrease in reaction temperature observed after hours of ball milling implies that milling has enhanced the homogeneity of the compacts. Total porosity of the pressureless sintered composite decreases whereas the bulk density increases with both the reduction of

particle size and the increase of sintering temperature as seen in Figure 4.30 and Figure 4.31.

Overall, near fully densified Ti_3Al-TiO-Al_2O_3 and Ti_3Al-Al_2O_3 composites (≤96% of theoretical density) with interpenetrating network were fabricated by pressureless sintering Al-TiO_2 composite powder with starting median particle diameter of 2μm and 7μm, respectively, in argon at 1480°C for holding period of 4-5 hours.

4.8 Summary

Batches of Al-TiO_2 (rutile or anatase) composite powders were prepared by two, four and six hours of discus milling in argon. Different compositions of intermetallic and ceramic phases Ti_3Al-TiO-Al_2O_3 and Ti_3Al-Al_2O_3 composites were fabricated by pressureless sintering Al-TiO_2 composite powders produced from discus and ball milling. The particle size of the powders could be reduced by ZrO_2 ball milling in chloroform for 24 hours. It was found that TiO_2 used in the experiments, either rutile or anatase, produced similar composites on the subsequent solid state sintering of Al and TiO_2.

The XRD results show that all the phases maintained around the same intensity level from 1330°C to 1480°C during pressureless sintering in argon for the Ti_3Al-TiO-Al_2O_3 and Ti_3Al-Al_2O_3 composites. For pressureless sintering in argon, the Ti_3Al phase is maintained around 50% of XRD peak intensity up to 1480°C. The Ti_3Al and Al_2O_3 phases are continuous and hence exhibit an interpenetrating network.

The open porosity and bulk density decreased and increased respectively with increasing temperature for pressureless sintering in argon. As a result of increased density, reduced porosity and fine Al_2O_3 particle size, *near fully densified intermetallic-ceramic* Ti_3Al-TiO-Al_2O_3 and Ti_3Al-Al_2O_3 composites (≤96% of theoretical density) with *interpenetrating network* were fabricated.

REFERENCES

1. Cai, Z.H., *Processing, microstructure and mechanical properties of Ti_xAl_y/Al_2O_3 and $Al_2Ti_4C_2/Ti_xAl_y/Al_2O_3/TiC$ composites*, PhD Thesis. 2003, The University of Waikato: Hamilton. p. 110.
2. Bruhn, J., S. Schicker, D.E. Garcia, R. Jansen, F. Wagner, and N. Claussen, *Novel reaction-based processing of co-continuous ceramic-metal composites.* Key engineering materials, 1997. **127-131**: p. 73-80.
3. Claussen, N., D.E. Garcia and R. Jansen, *Reaction sintering of alumina-aluminide alloys (3A).* Journal of Materials Research, 1996. **11**(11): p. 2884-2888.
4. Feng, C.F. and L. Froyen, *Formation of Al_3Ti and Al_2O_3 from an Al-TiO_2 system for preparing in-situ aluminium matrix composites.* Composite Part A: Applied Science and Manufacturing, 2000. **31**: p. 385-390.
5. Gaus, S.P., M.P. Harmer, H.M. Chan, H.S. Caram and N. Claussen, *Alumina-aluminide alloys (3A) technology: II, Modeling of Ti_xAl_y-Al_2O_3 composite formation.* Journal of the American Ceramic Society, 2000. **83**(7): p. 1606-1612.
6. Han, C.Z., I.W.M. Brown and D.L. Zhang. *Consolidation and properties of a Ti3Al/Al2O3 advanced composite material.* in *8th Engineering and Technology Postgraduate Conference.* 2001. Hamilton, New Zealand: University of Waikato.
7. Han, C.Z., I.W.M. Brown and D.L. Zhang, *Effect of powder characteristics on microstructural development in bodies produced by pressureless sintering of Al/TiO2 composite powder.* Materials Science Forum, 2003. **437-438**: p. 173-176.
8. Zhang, D.L., D.Y. Ying and P. Munroe, *Formation of Al_2O_3 during heating an Al/TiO_2 nanocomposite powder.* Journal of Materials Research, 2005. **20**: p. 307-313.
9. Schaffer, G.B. and P.G. McCormick, *Combustion and resultant powder temperatures during mechanical alloying.* Journal of Materials Science Letters, 1990. **9**: p. 1014-1016.
10. Schaffer, G.B. and P.G. McCormick, *On the kinetics of mechanical alloying.* Metallurgical Transaction A, 1992. **23**: p. 1285-1290.
11. Welham, N.J., *Mechanical activation of the solid-state reaction between Al and TiO_2.* Materials science and technology, 1998. **255**: p. 81-89.
12. Wang, G.M., S.J. Campbell, A. Calka and W.A. Kaczmarek, *Ball-milling of Fe-C (20-75% Fe).* Nanostructured Materials, 1995. **6**(1-4): p. 389-392.
13. Calka, A. and J.I. Nikolov, *Direct synthesis of AlN and Al-AlN composites by room temperature magneto ball milling: the effect of milling condition on formation of nanostructures.* Nanostructured Materials, 1995. **6**(1-4): p. 409-412.
14. Han, C.Z., I.W.M. Brown and D.L. Zhang. *Effect of powder characteristics on the solid state reaction during sintering of Al/TiO_2 composite powder.* in *9th Engineering and Technology Postgraduate Conference.* 2002. Auckland, New Zealand: Auckland University of Technology.

15. Ying, D.Y., D.L. Zhang and M. Newby, *Solid-state reactions during heating mechanically milled Al/TIO_2 composite powders.* Metallurgical and Materials Transactions A, 2004. **35**(7): p. 2115-2125.
16. Pan, J., H. Li, H. Fukunage, X.G. Ning, H.Q. Ye, Z.K. Yao, and D.M. Yang, *Microstructural study of the interface reaction between titania whiskers and aluminium.* Composites Science and Technology, 1997. **57**: p. 319-325.
17. Schicker, S., D.E. Garcia, J. Bruhn, R. Jansen and N. Claussen, *Reaction synthesized Al_2O_3-based intermetallic composites.* Acta Materialia, 1998. **46**(7): p. 2485-2492.
18. Zalar, A., B.M.M. Baretzky, S. Hofmann, M. Ruhle and P. Panjan, *Interfacial reactions in Al_2O_3/Ti, Al_2O_3/Ti_3Al and Al_2O_3/TiAl bilayers.* Thin Solid Films, 1999. **352**: p. 151-155.
19. Zhang, M.-X., K.-C. Hsieh, J. DeKock and Y.A. Chang, *Phase Diagram of Ti-Al-O at 1100°C.* Scripta Metallurgica et Materialia, 1992. **27**: p. 1361-1366.
20. Chen, Y., D.J. Young and B. Gleeson, *A new Ti-rich ternary phase in the Ti-Al-O system.* Materials Letters, 1995. **22**: p. 125-129.
21. Nakahigashi, J. and H. Yoshimura, *Ultra-fine grain refinement and tensile properties of titanium alloys obtained through protium treatment.* Journal of Alloys and Compounds, 2002. **330-332**: p. 384-388.
22. Schicker, S., D.E. Garcia, J. Bruhn, R. Jansen and N. Claussen, *Reaction processing of Al_2O_3 composites containing iron and iron aluminides.* Journal of American Ceramic Society, 1997. **80**(9): p. 2294-2300.
23. Garcia, D.E., S. Schicker, J. Bruhn, R. Janssen and N. Claussen, *Synthesis of novel niobium aluminide-based composites.* Journal of American Ceramic Society, 1997. **80**(9): p. 2248-2252.

CHAPTER FIVE:

Pressure-Assisted Sintering of Discus Milled Al-TiO_2 Composite Powders

Solid-state reactions of Al-TiO_2 (rutile) composite powders have demonstrated the benefit of reaction sintering of intensively milled powder mixtures to form alumina-aluminide composites whose interpenetrating networks offer the possibility of greatly enhanced mechanical properties and engineering performance[1-8]. In addition to reaction sintering, the application of pressure may further improve the densification of the composites. This chapter describes the effect of processing conditions on microstructure and phase relationships in Ti_3Al-TiO-Al_2O_3 and Ti_3Al-Al_2O_3 composites prepared by hot pressing and sinter-HIP.

5.1 Hot Pressing

5.1.1 Ti_3Al-TiO-Al_2O_3 Composites

Figure 5.1 shows the XRD patterns of Ti_3Al-TiO-Al_2O_3 composites produced by hot pressing Al-TiO_2 (rutile) composite powder under vacuum at heating rate of 15°C/min. The XRD traces show that the intensity of the Ti_3Al phase decreases with increasing temperature as shown in Figure 5.2. The XRD peak intensity of Ti_3Al phase decreased from 63% at 1293°C to 26% at 1633°C under vacuum. No second TiO phase was detected in these samples compared to the second TiO detected in the pressureless sintered samples seen in Figure 4.25 in Chapter Four. Both of these phenomena can be explained by the design of the graphite die, which shields the samples from outside atmosphere during sintering discussed earlier in Chapter Three.

Figure 5.3 shows the open porosity of the Ti_3Al-TiO-Al_2O_3 composites produced by hot pressing Al-TiO_2 composite powder under vacuum as a function of sintering temperature. The pressureless sintered composites show no sign of densification under vacuum with open porosity as high as 32% described earlier in Chapter Four. On the other hand, the hot pressed samples display reduction in the open porosity to approximately 3% at 1633°C.

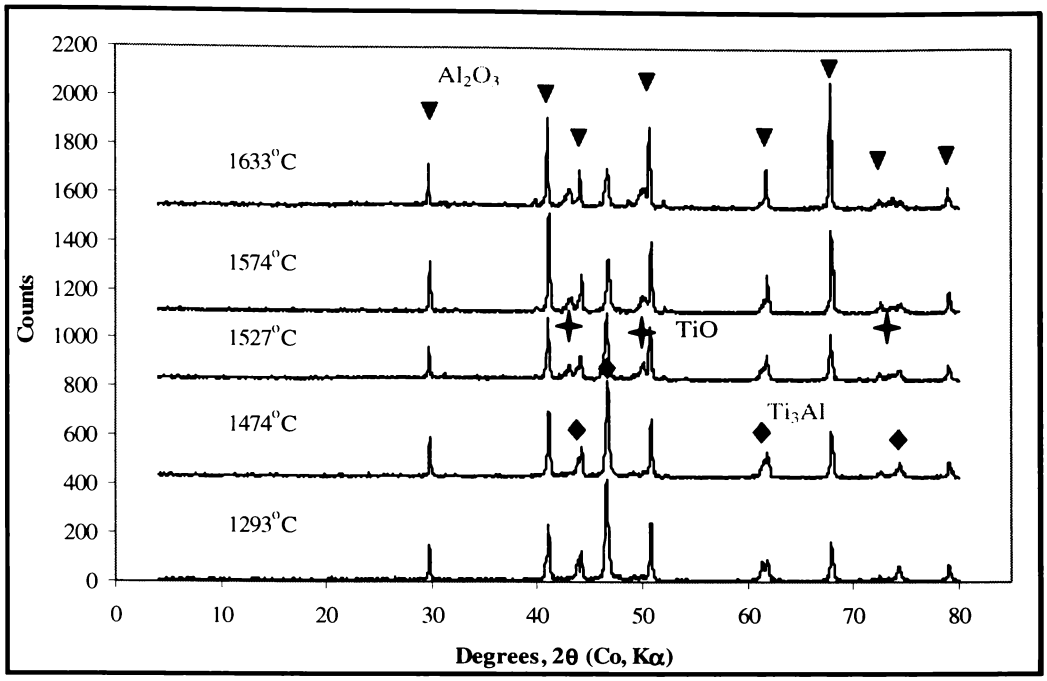

Figure 5.1: XRD patterns of Ti_3Al-TiO-Al_2O_3 composites produced by hot pressing Al-TiO_2 composite powder under vacuum

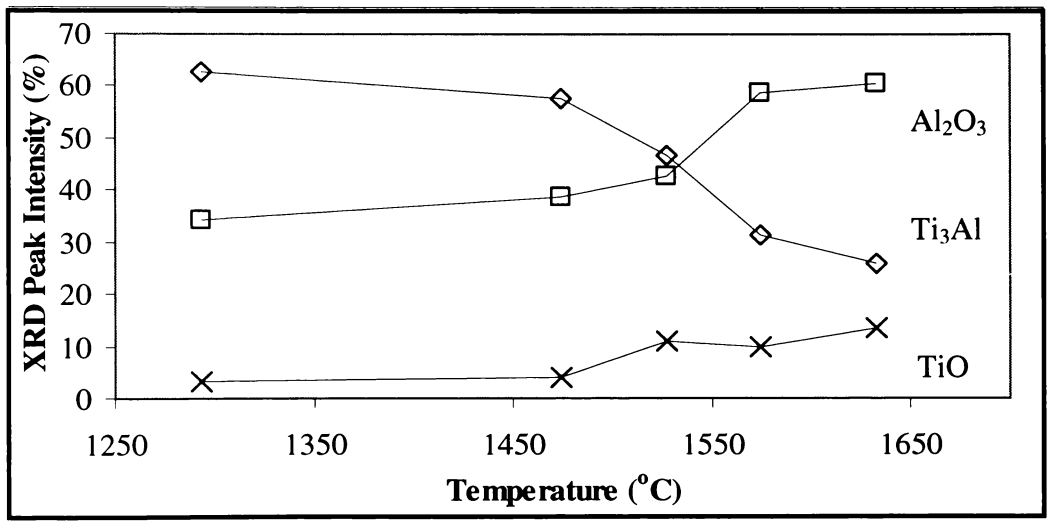

Figure 5.2: Intensity profile of Ti_3Al-TiO-Al_2O_3 composites produced by hot pressing Al-TiO_2 composite powder at different temperatures under vacuum

Figure 5.4 shows the microstructure of polished composites produced from the hot pressing of Al-TiO_2 (rutile) composite powders. The dark grey particles are identified as the Al_2O_3 phase embedded in a Ti_3Al/TiO matrix with some black residual pores. The quantity of pores decreases with increasing hot pressing temperature from 1293°C to 1574°C. The microstructure of the composite hot pressed at 1574°C shows abrupt particle coarsening similar to the hot pressing of Ti_3Al-Al_2O_3 composite powders above 1500°C discussed earlier in Chapter Three. The Al_2O_3 particle size of the Ti_3Al-TiO-Al_2O_3 composites is 1.5μm to 13μm.

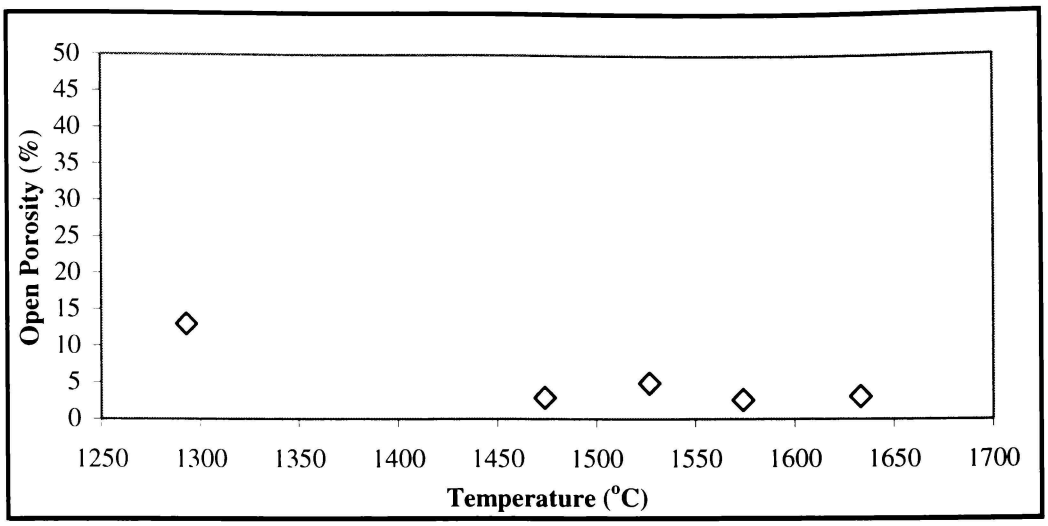

Figure 5.3: Open porosity of Ti_3Al-TiO-Al_2O_3 composites produced by hot pressing Al-TiO_2 under vacuum as a function of sintering temperature

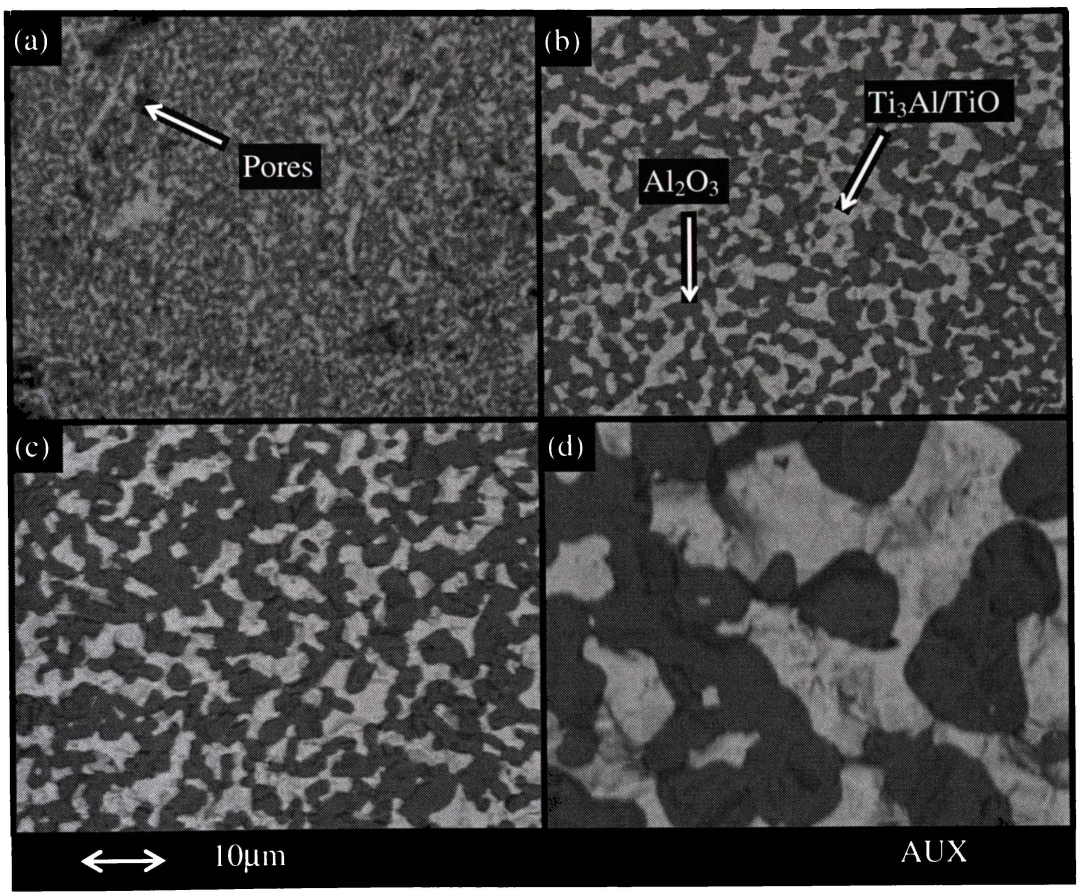

Figure 5.4: SEM images of Ti_3Al-TiO-Al_2O_3 composites produced by hot pressing Al-TiO_2 composite powder at (a) 1293, (b) 1474, (c) 1527 and (d) 1574°C under vacuum

5.1.2 Ti_3Al-Al_2O_3 Composites

Powder characteristics of the two, four and six hours discus milled Al-TiO_2 (anatase) composite powder before and after ball milling is discussed earlier in

Chapter Four. Figure 5.5 and Figure 5.6 show the XRD patterns of the Ti_3Al-Al_2O_3 composites produced by hot pressing 2(Al-TiO_2) and 2(Al-TiO_2)-24 composite powders in argon, respectively. It shows that the samples produced from both 2(Al-TiO_2) and 2(Al-TiO_2)-24 composite powders after hot pressing contain only Al_2O_3 and Ti_3Al unlike in the earlier studies reported in Chapter Four where the samples contain additional phases such as TiO after sintering.

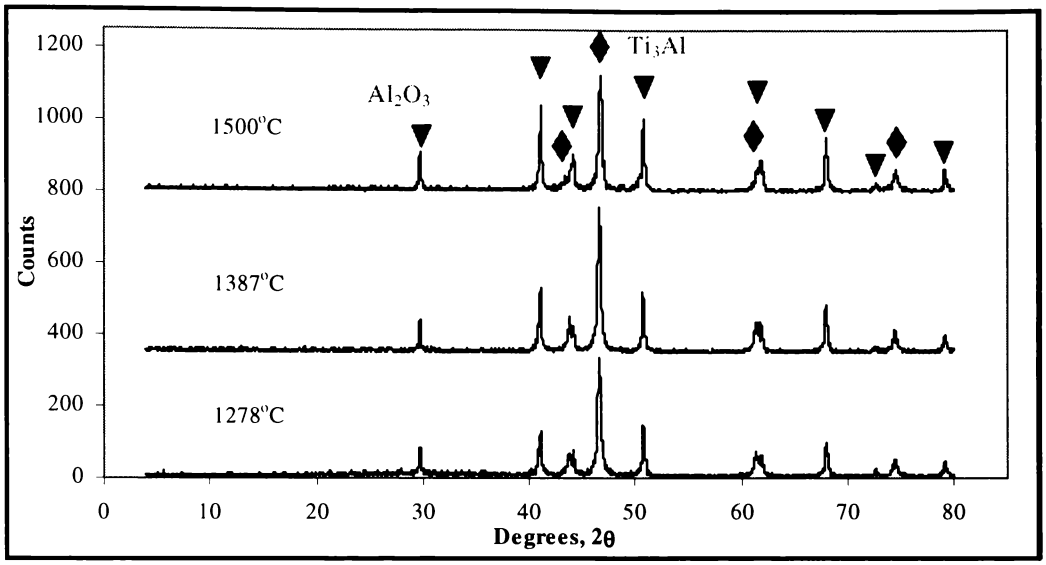

Figure 5.5: XRD patterns of Ti_3Al-Al_2O_3 composites produced by hot pressing 2(Al-TiO_2) composite powder under vacuum

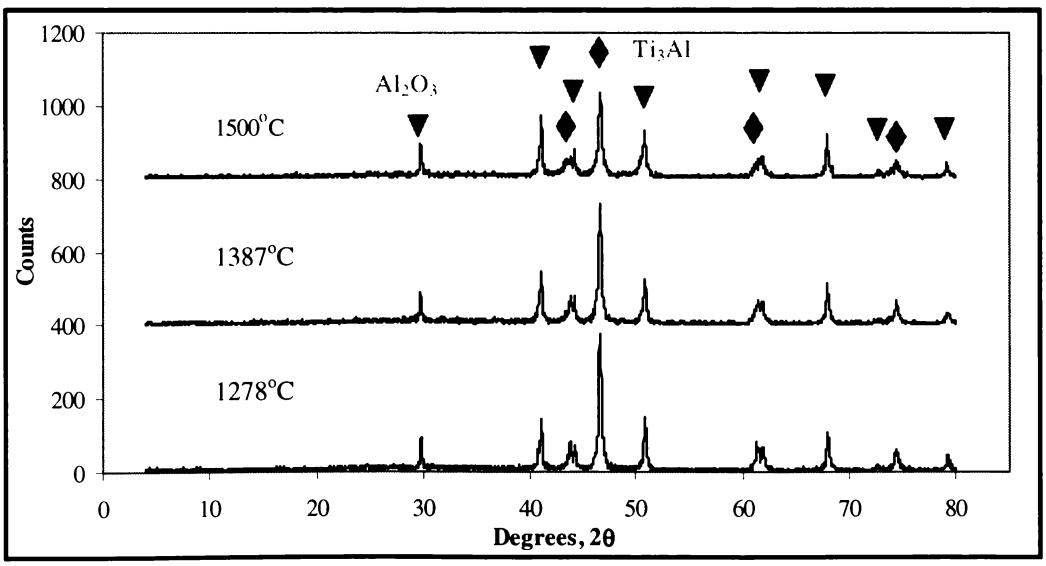

Figure 5.6: XRD patterns of Ti_3Al-Al_2O_3 composites produced by hot pressing 2(Al-TiO_2)-24 composite powder under vacuum

Figure 5.7 and Figure 5.8 show the XRD patterns of hot pressed 4(Al-TiO_2) and 4(Al-TiO_2)-24 in argon respectively. These show that the hot pressed samples contain two Ti_3Al phases. The explanation is based on the assumption that two

Ti_3Al phases with different amounts of dissolved oxygen formed during sintering. This is an increase of two different unit cell dimensions was observed for two Ti_3Al phase compared to those in the ICDD database (refer Chapter Three). Unit cell dimensions for the standard Ti_3Al phase from ICDD database are a = 5.77Å and c = 4.62Å. The unit cell dimensions of Ti_3Al(a) and Ti_3Al(b) after XRD peak shift adjustments give a = 5.883Å; c = 4.802Å, and a = 5.799Å; c = 4.715Å, respectively.

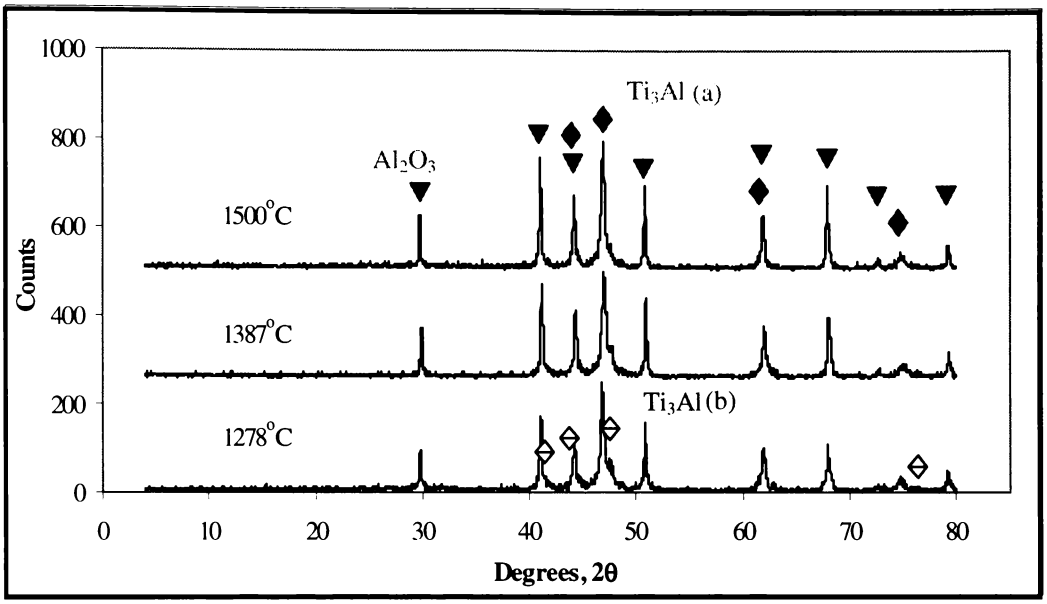

Figure 5.7: XRD patterns of Ti_3Al-Al_2O_3 composites produced by hot pressing 4(Al-TiO_2) composite powder under vacuum

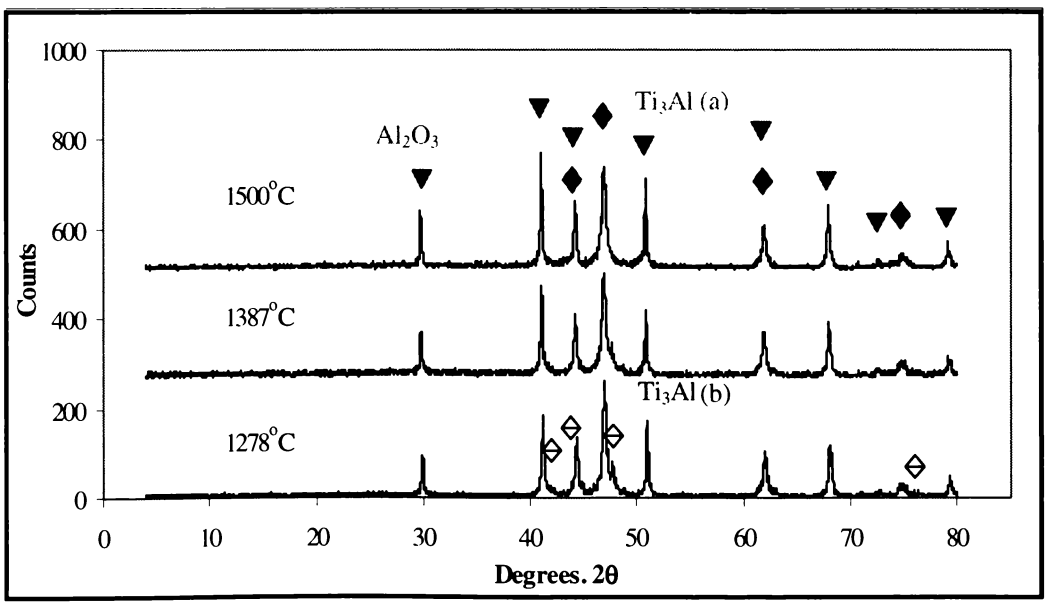

Figure 5.8: XRD patterns of Ti_3Al-Al_2O_3 composites produced by hot pressing 4(Al-TiO_2)-24 composite powder under vacuum

The Ti_3Al phase [or a mixture of two Ti_3Al phases for both the 4(Al-TiO_2) and 4(Al-TiO_2)-24] is maintained above 50% of XRD peak intensity in the composites after hot pressing as shown in Figure 5.9. Hot pressed samples display further improvement in their porosity shown in Figure 5.10 compared to the pressureless sintered samples shown in Figure 4.36 in Chapter Four. The application of pressure at the sintering temperature accelerates the kinetics of densification by increasing the contact packing[9]. The porosity of the hot pressed samples shifts towards 0% at a much lower sintering temperature. This research has demonstrated that fully dense Ti_3Al-Al_2O_3 composites can be obtained using hot pressing.

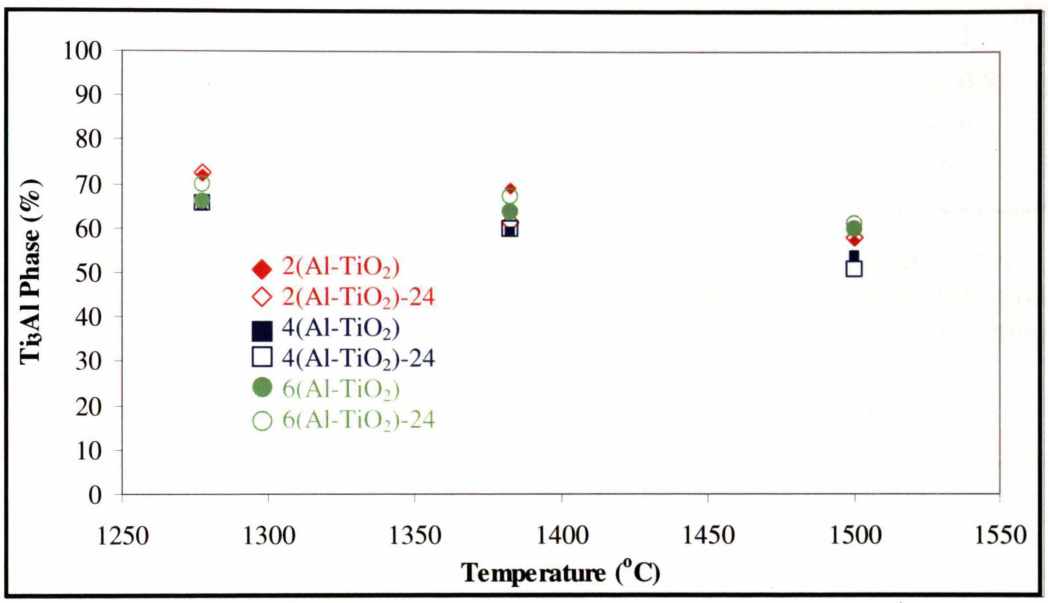

Figure 5.9: Intensity profile of Ti_3Al-Al_2O_3 composites produced by hot pressing Al-TiO_2 (anatase) composite powder as a function of hot pressing temperature

The densification of the composites improved with the increase of discus milling time from two to six hours as shown in Figure 5.10. The particle size of the composite powders decreased from a median particle diameter of 19μm to 7μm as seen earlier in Table 4.2 in Chapter Four with increasing discus milling time from two to six hours. This leads to a significant increase of bulk density and a decrease of the total porosity of the hot pressed Ti_3Al-Al_2O_3 composites.

Figure 5.11, Figure 5.12 and Figure 5.13 show the microstructure of polished composites produced by hot pressing Al-TiO_2 (anatase) composite powders. The dark grey particles are identified as the Al_2O_3 phase embedded in a Ti_3Al matrix

with some black residual pores. The pores seem to be concentrated around the Al_2O_3 particles. The Al_2O_3 particles become more separated with increasing hot pressing temperature as shown in these figures.

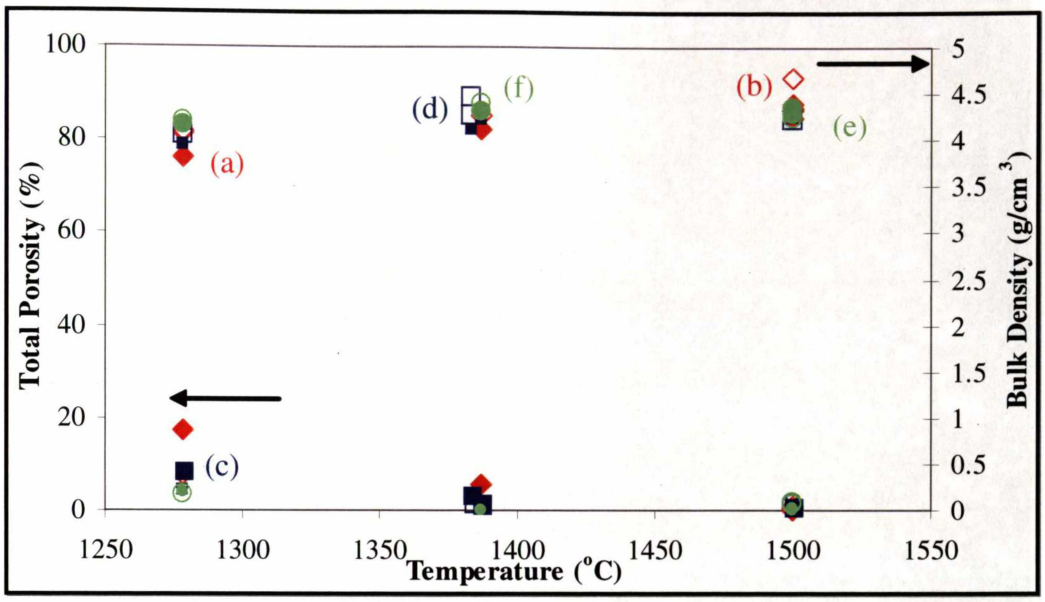

Figure 5.10: Total porosity and bulk density of Ti_3Al-Al_2O_3 composites produced by hot pressing (a) 2(Al-TiO_2), (b) 2(Al-TiO_2)-24, (c) 4(Al-TiO_2) (d) 4(Al-TiO_2)-24, (e) 6(Al-TiO_2) and (f) 6(Al-TiO_2)-24 composite powders under vacuum as a function of hot pressing temperature

The homogeneity of the microstructures of the composites becomes more uniform and increases with the increasing discus milling time from two to six hours. The uniformity of the microstructure is also seen in the composites produced from the composite powders after 24 hours of ball milling. The quantity of pores observed in the microstructure decreased with both increasing discus and ball milling, which is supported by the porosity measurement seen earlier in Figure 5.10. The Al_2O_3 particles are much finer for most of the samples produced from the composite powders that were subjected to 24 hours of ball milling. However, at hot pressing temperature of 1500°C, the Al_2O_3 particles become significantly coarsened compared to the hot pressed samples at both 1278°C and 1387°C.

The phases are continuous and hence exhibit an interpenetrating network, which is expected to enhance the mechanical properties. Grain pullout after polishing is one of the problems encountered as shown in Figure 5.11, Figure 5.12 and Figure 5.13. This affects the mechanical property measurements such as Vickers hardness and fracture toughness, described in more detail in Chapter Six.

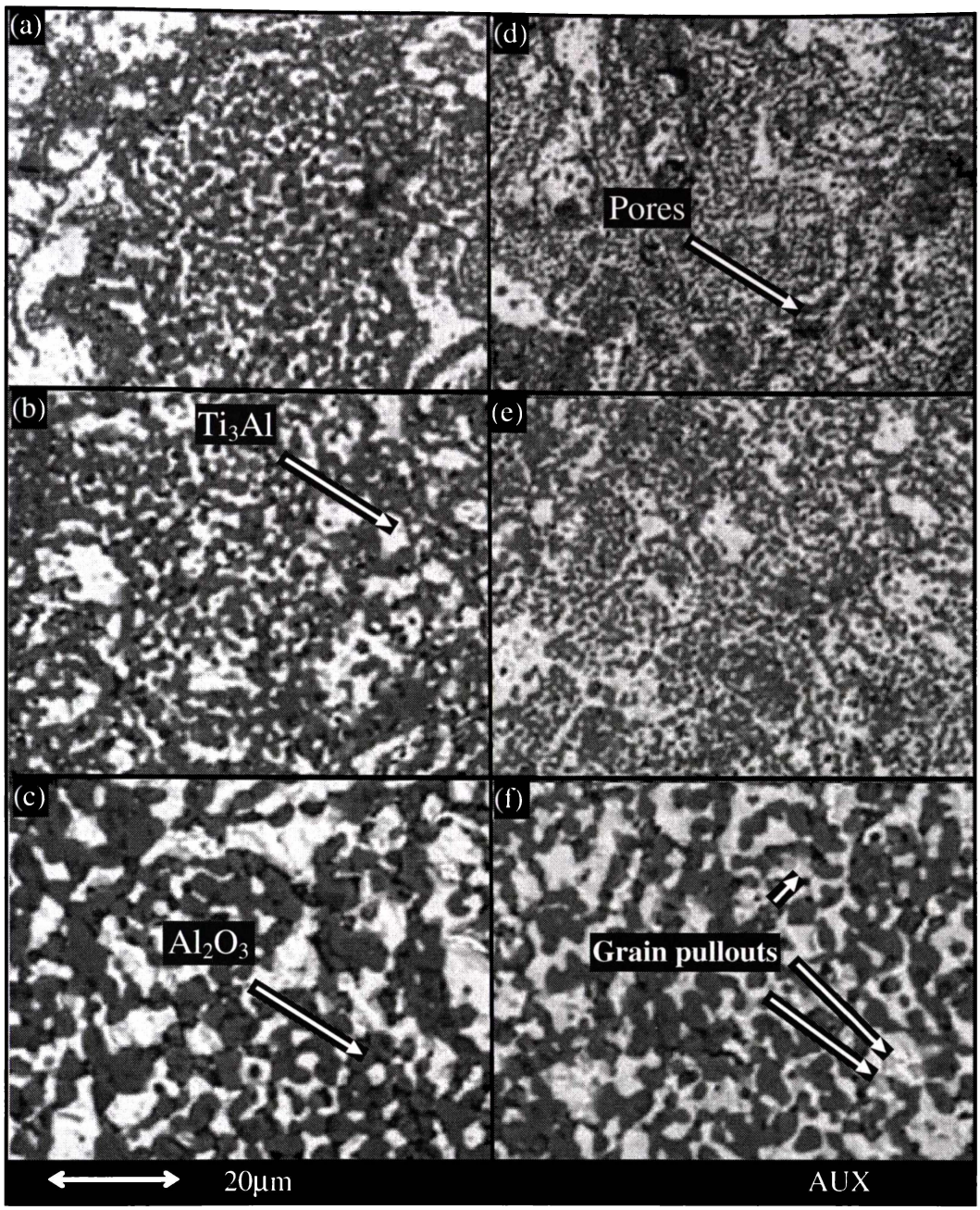

Figure 5.11: SEM images of Ti_3Al-Al_2O_3 composites produced by hot pressing (i) 2(Al-TiO_2) at (a) 1278, (b) 1387 and (c) 1500°C and (ii) 2(Al-TiO_2)-24 composite powders at (d) 1278, (e) 1387 and (f) 1500°C

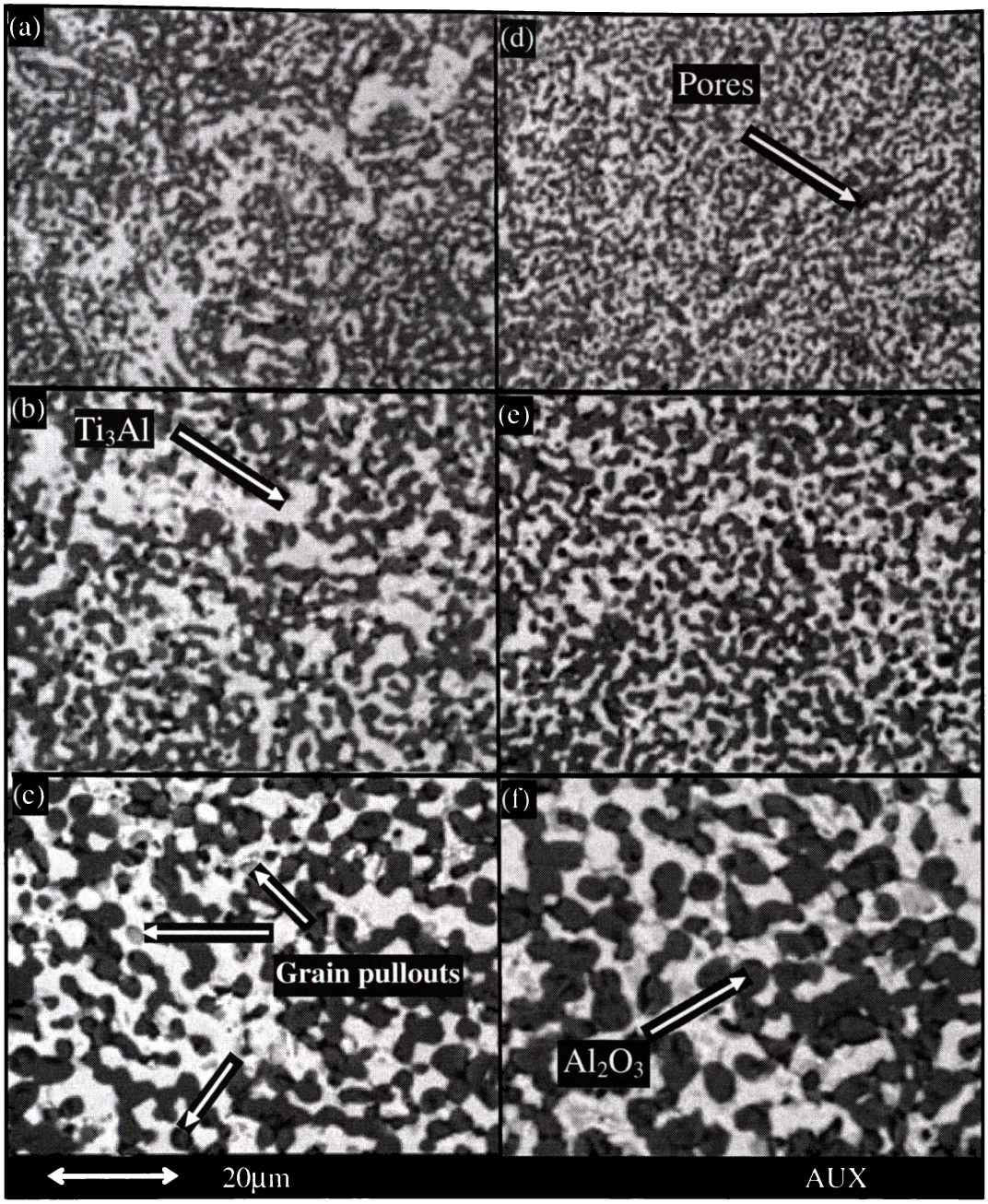

Figure 5.12: SEM images of Ti_3Al-Al_2O_3 composites produced by hot pressing (i) 4(Al-TiO_2) at (a) 1278, (b) 1387 and (c) 1500°C and (ii) 4(Al-TiO_2)-24 composite powders at (d) 1278, (e) 1387 and (f) 1500°C

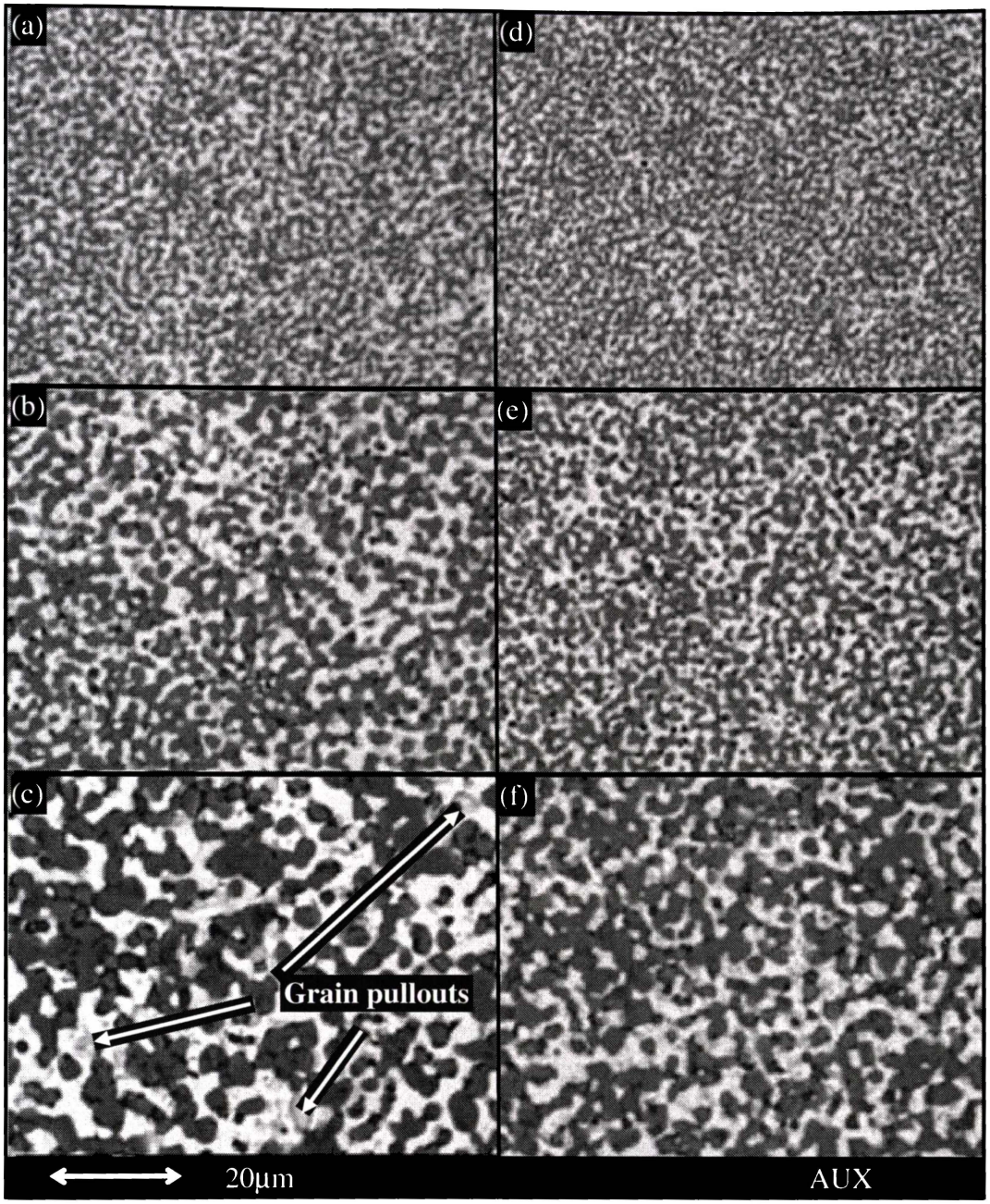

Figure 5.13: SEM images of Ti_3Al-Al_2O_3 composites produced by hot pressing (i) 6(Al-TiO_2) at (a) 1278, (b) 1387 and (c) 1500°C and (ii) 6(Al-TiO_2)-24 composite powders at (d) 1278, (e) 1387 and (f) 1500°C

All the hot pressed samples produced from the Al-TiO_2 (anatase) composite powders show control of Al_2O_3 particle growth after hot pressing below 1500°C as shown in Figure 5.14. This is similar to the results for the hot pressed Ti_3Al-Al_2O_3-1 samples shown in Figure 3.28 in Chapter Three. The average Al_2O_3 particle size in the microstructure after hot pressing is in the range of 0.8-4μm (grain size of 1-3μm is categorised as fine grain size[10]).

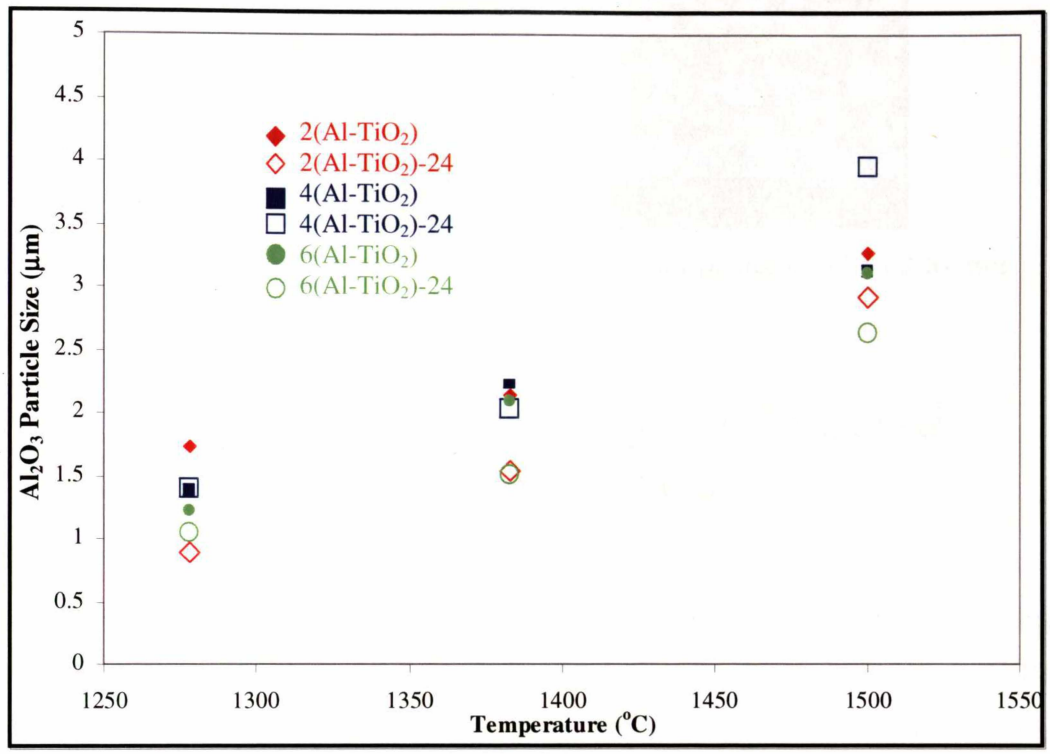

Figure 5.14: Particle size of Al_2O_3 as a function of temperature for hot pressed aluminium-anatase samples

Fully dense Ti_3Al-Al_2O_3 composite microstructures could be achieved by hot pressing 4(Al-TiO_2)-24 composite powder at 1387°C under vacuum. Figure 5.15 shows the microstructure of a fully densified composite in which the Al_2O_3 particles are embedded in the Ti_3Al matrix. The phases are continuous and hence exhibit an interpenetrating network. The average particle size of Al_2O_3 is approximately 2μm.

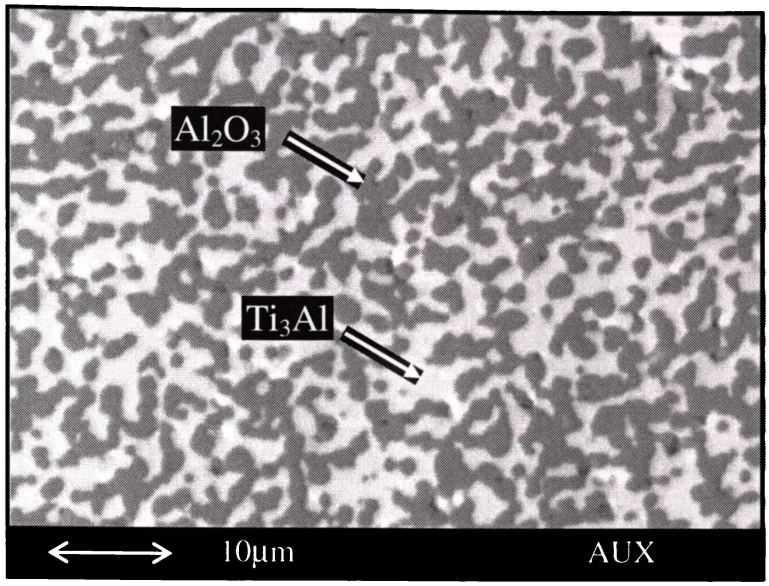

Figure 5.15: Microstructure of Ti_3Al-Al_2O_3 composite produced by hot pressing at 1387°C

5.2 *Hot Isostatic Pressing of Pre-Sintered Ti_3Al-TiO-Al_2O_3 Composites*

This section describes the densification of Ti_3Al-TiO-Al_2O_3 composites produced by pressureless sintering (PS) Al-TiO_2-3 (rutile) composite powder with starting median particle diameter of 7.7μm, before and after hot isostatic pressing (HIP). The phase composition-densification relationship during pressureless sintering is described in Chapter Four. After pressureless sintering in argon, Ti_3Al-TiO-Al_2O_3 composites were further subjected to hot isostatic pressing.

Figure 5.16 shows the closed porosity of Ti_3Al-TiO-Al_2O_3 composites produced by pressureless sintering Al-TiO_2-3 composite powder in argon at 1480°C versus holding period before and after hot isostatic pressing at 200MPa for two hours. The figure shows that the closed porosity was reduced when the hot isostatic pressing temperature increased to 1300°C from 1100°C. However, HIP temperatures of 1100°C and 1200°C were insufficient to reduce the closed porosity of the composite.

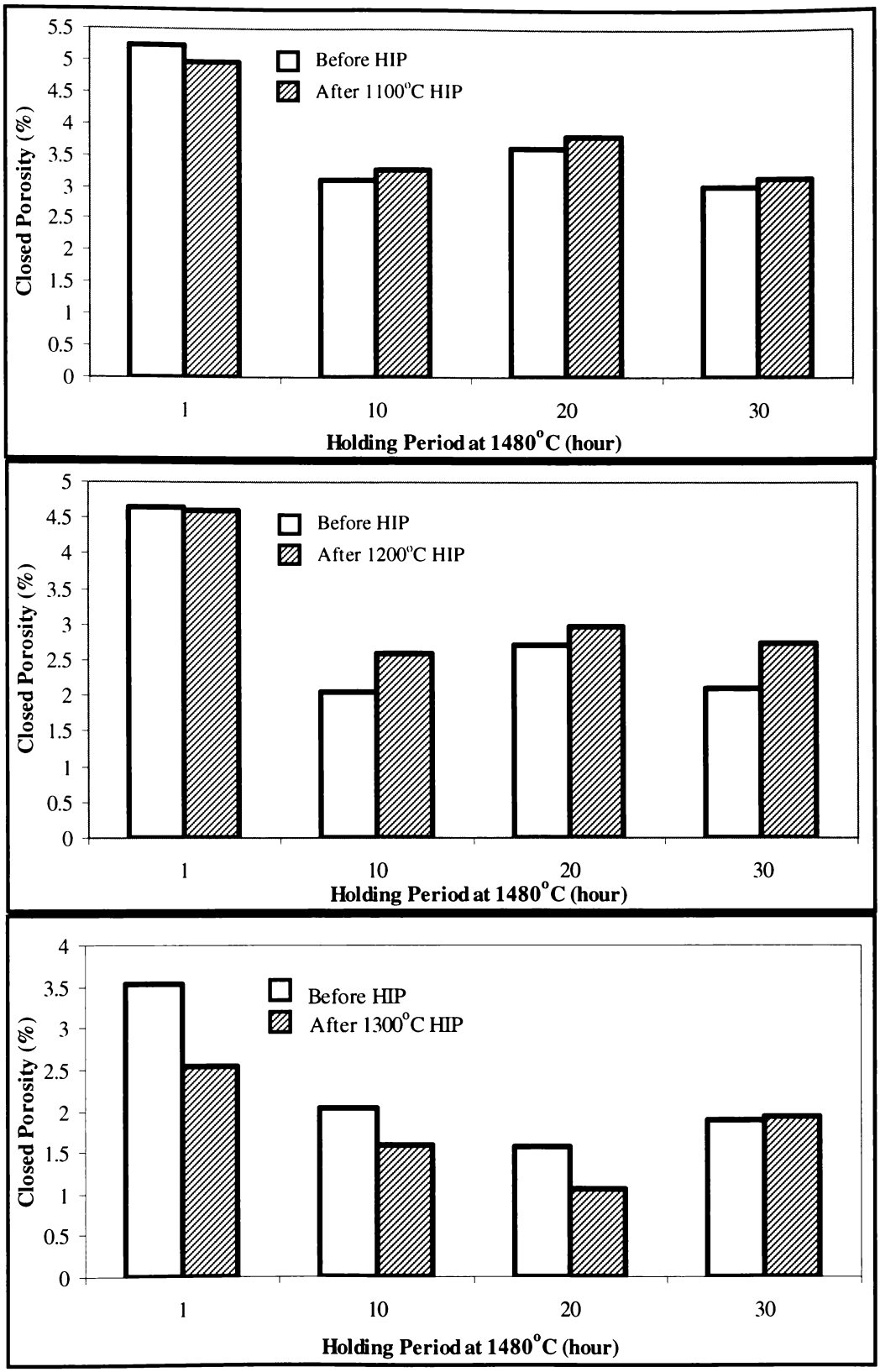

Figure 5.16: Closed porosity of Ti_3Al-TiO-Al_2O_3 composites produced by pressureless sintering Al-TiO_2-3 composite powder at various holding period at 1480°C in argon before and after hot isostatic pressing at 200MPa for two hours

Figure 5.17 and Figure 5.18 show the open porosity of the pressureless sintered Al-TiO_2-3 in argon at 1480°C versus holding period before and after hot isostatic pressing at 1100, 1200 and 1300°C, at 200MPa for two hours. The open porosity of the samples after 1100°C and 1200°C increased more than the closed porosity, which was expected since the 1200°C temperature was insufficient to cause any plastic deformation during hot isostatic pressing at 200MPa. Although hot isostatic pressing at 200MPa was sufficient to reduce the closed porosity at 1300°C, the open porosity of the samples increased, thereby undoing the densification of the pressureless sintered composites. The likely mechanism is that the application of pressure during hot isostatic pressing causes plastic flow of the intermetallic phases, causing the closed pores to shrink and the open pores to become enlarged.

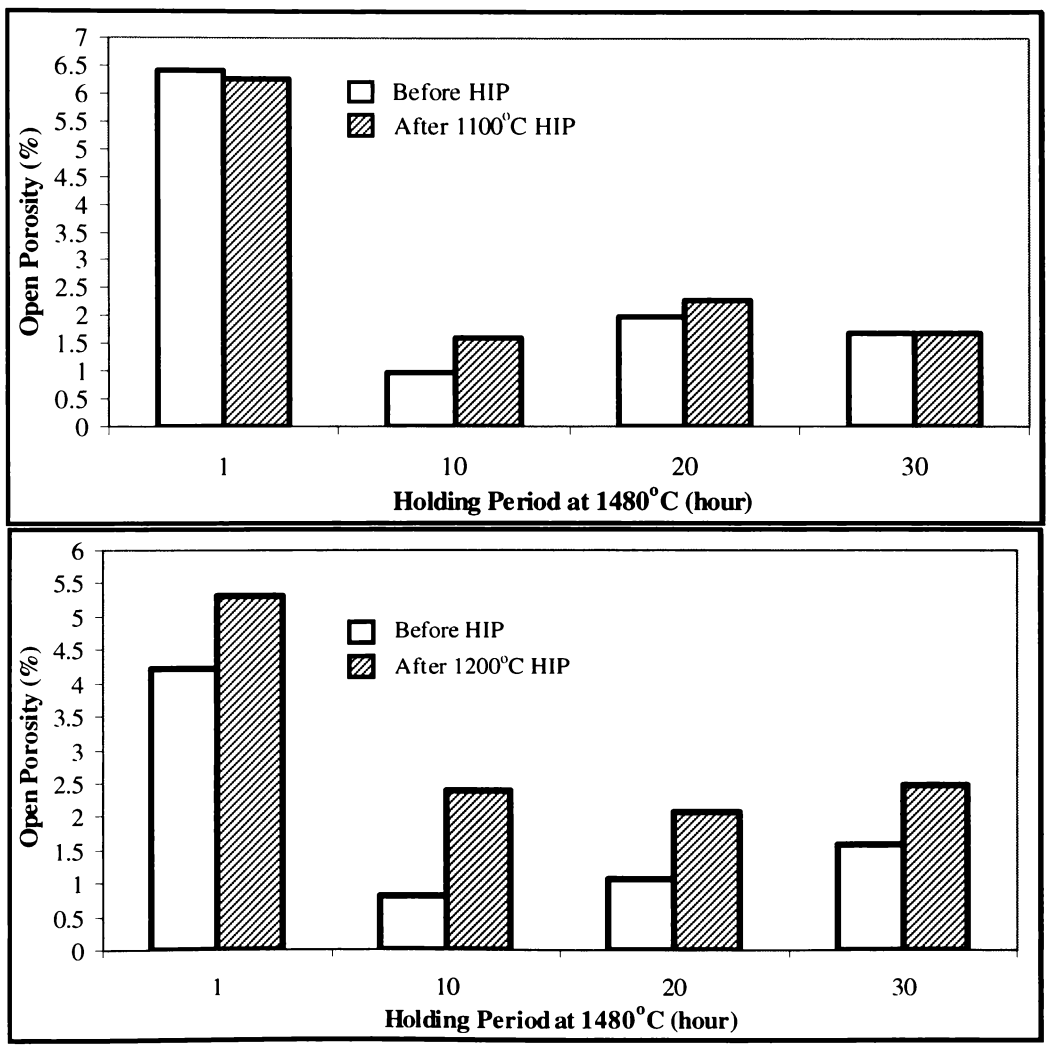

Figure 5.17: Open porosity of Ti_3Al-TiO-Al_2O_3 composites produced by pressureless sintering Al-TiO_2-3 composite powder at various holding period at 1480°C in argon before and after hot isostatic pressing at 1100 and 1200°C under 200MPa for two hours

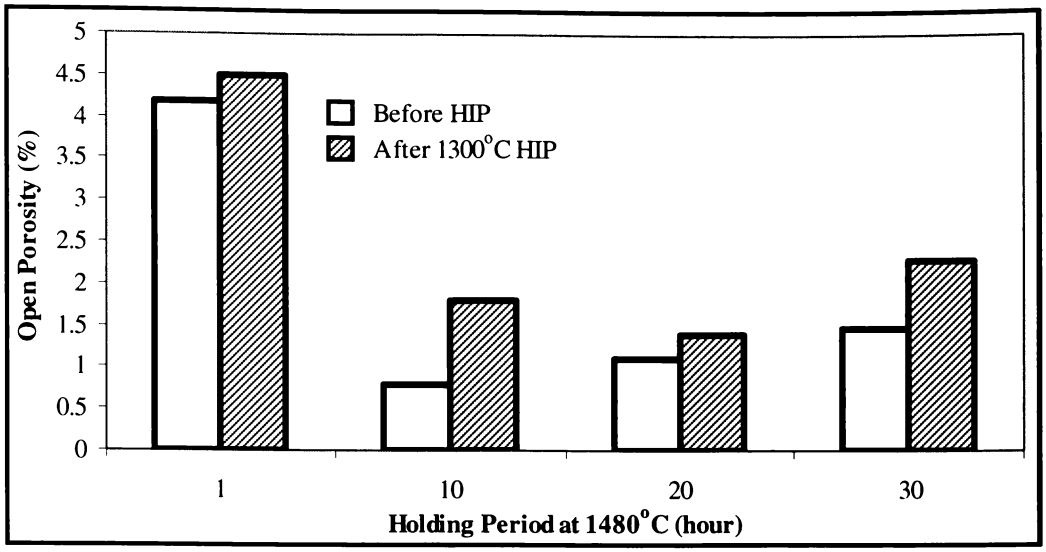

Figure 5.18: Open porosity of Ti_3Al-TiO-Al_2O_3 composites produced by pressureless sintering Al-TiO_2-3 composite powder at various holding period at 1480°C in argon before and after hot isostatic pressing at 1300°C under 200MPa for two hours

A similar outcome showing reduced closed porosity was obtained when Al-TiO_2-3 samples pressureless sintered at various temperatures were hot isostatic pressed at 200MPa for two hours at 1350°C in argon as shown in Figure 5.19. However, unlike the previous experimental results shown in Figure 5.18 where the open porosity increased after hot isostatic pressing at 1300°C, some samples hot isostatic pressed at 1350°C showed reduced open porosity.

The microstructures of Ti_3Al-TiO-Al_2O_3 composites produced by pressureless sintering Al-TiO_2-3 composite powder at 1330°C, 1373°C, 1416°C and 1480°C, before and after hot isostatic pressing are shown in Figure 5.20, Figure 5.21 and Figure 5.22. In general, only reduction of porosity and no Al_2O_3 particle coarsening were observed after hot isostatic pressing at 1350°C and 200MPa for 2 hours as supported by the porosity measurement using the Archimedes method displayed in Figure 5.19. The results also show that changing the cold isostatic pressing (CIP) pressure from 150-325MPa for the compaction of Al-TiO_2-3 composite powder does not have a significant effect on the pressureless sintered composites or the pressureless sintered composites after HIP. This is expected since the CIP pressure from 150-325MPa shows little effect on the green density of the samples prior to pressureless sintering, which is 62-65% of theoretical density as shown in Figure 5.23.

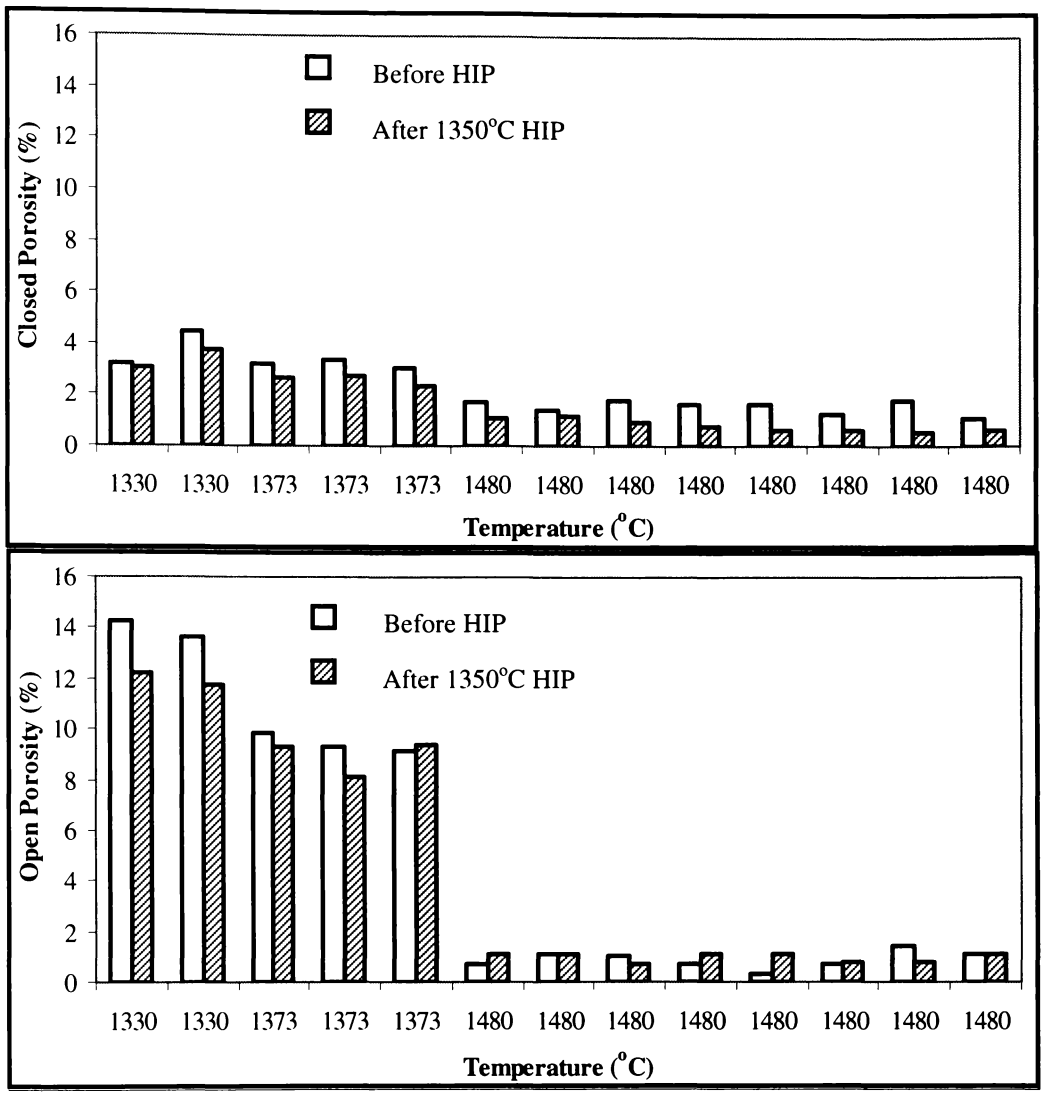

Figure 5.19: Closed and open porosity of Ti_3Al-TiO-Al_2O_3 composites produced by pressureless sintering Al-TiO_2-3 composite powder at various temperatures in argon before and after hot isostatic pressing at 200MPa for two hours

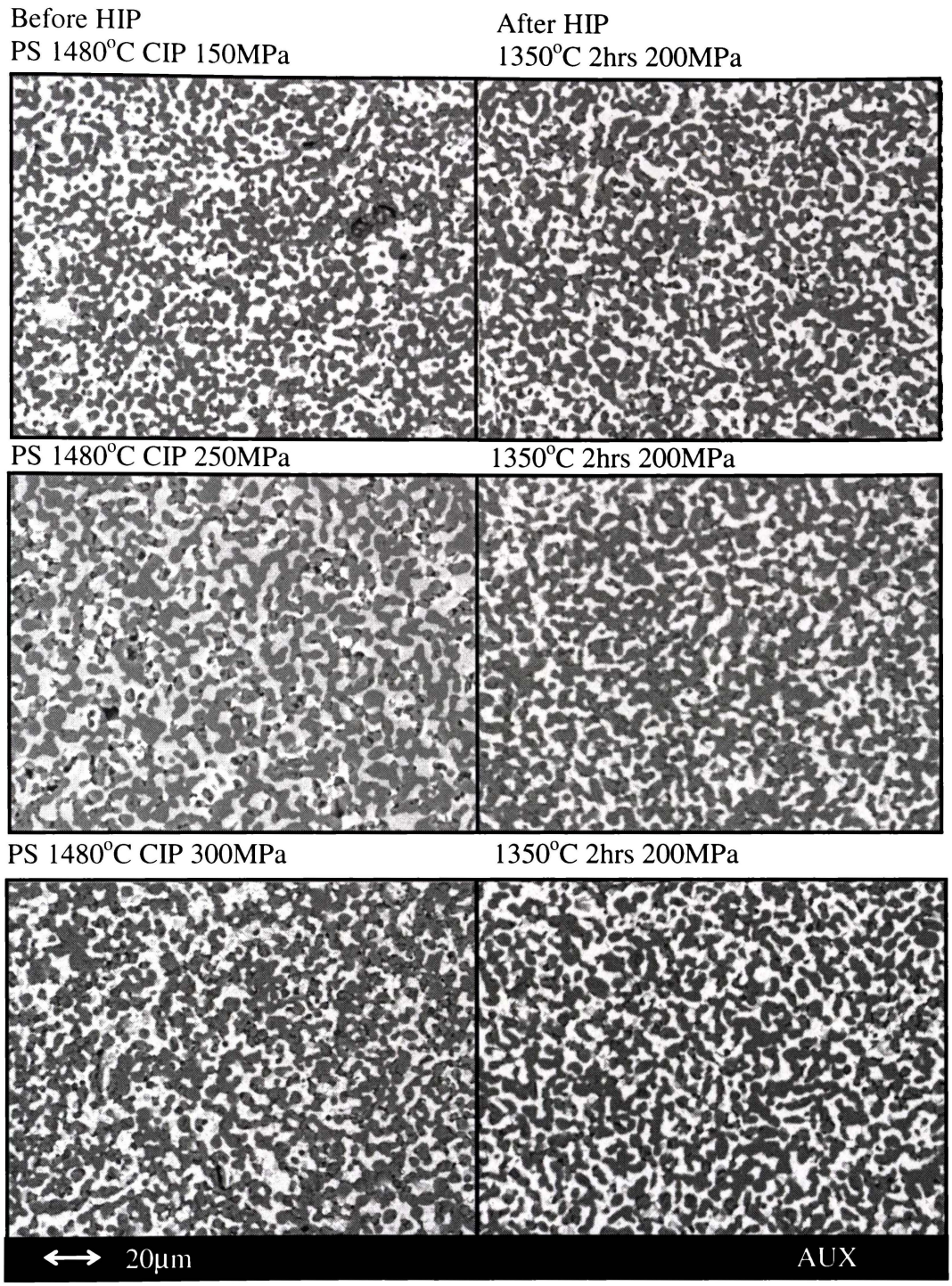

Figure 5.20: SEM images of Ti_3Al-TiO-Al_2O_3 composites produced by pressureless sintering Al-TiO_2-3 composite powder at 1480°C before and after hot isostatic pressing

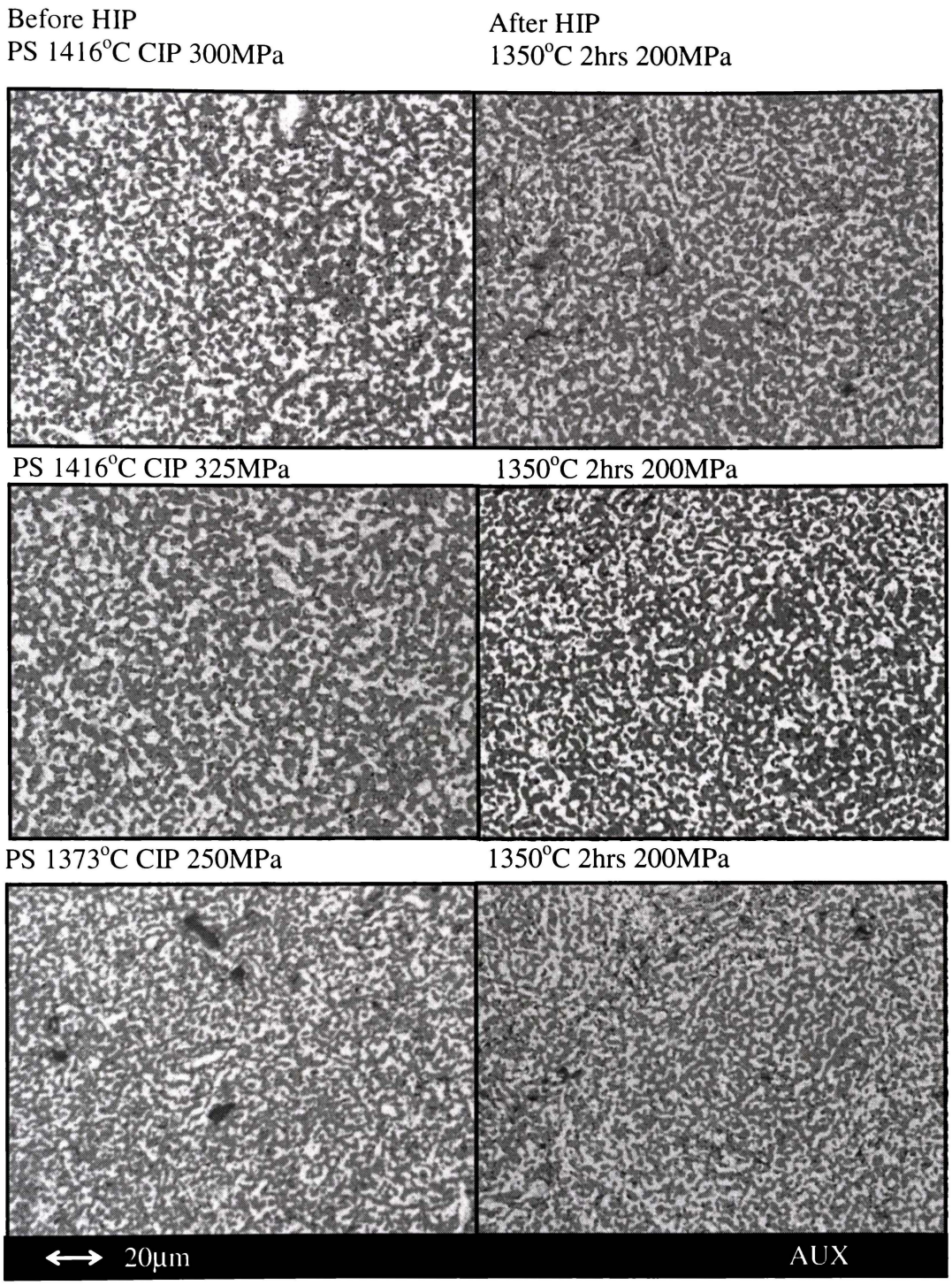

Figure 5.21: SEM images of Ti_3Al-TiO-Al_2O_3 composites produced by pressureless sintering Al-TiO_2-3 composite powder at 1373°C and 1416°C before and after hot isostatic pressing

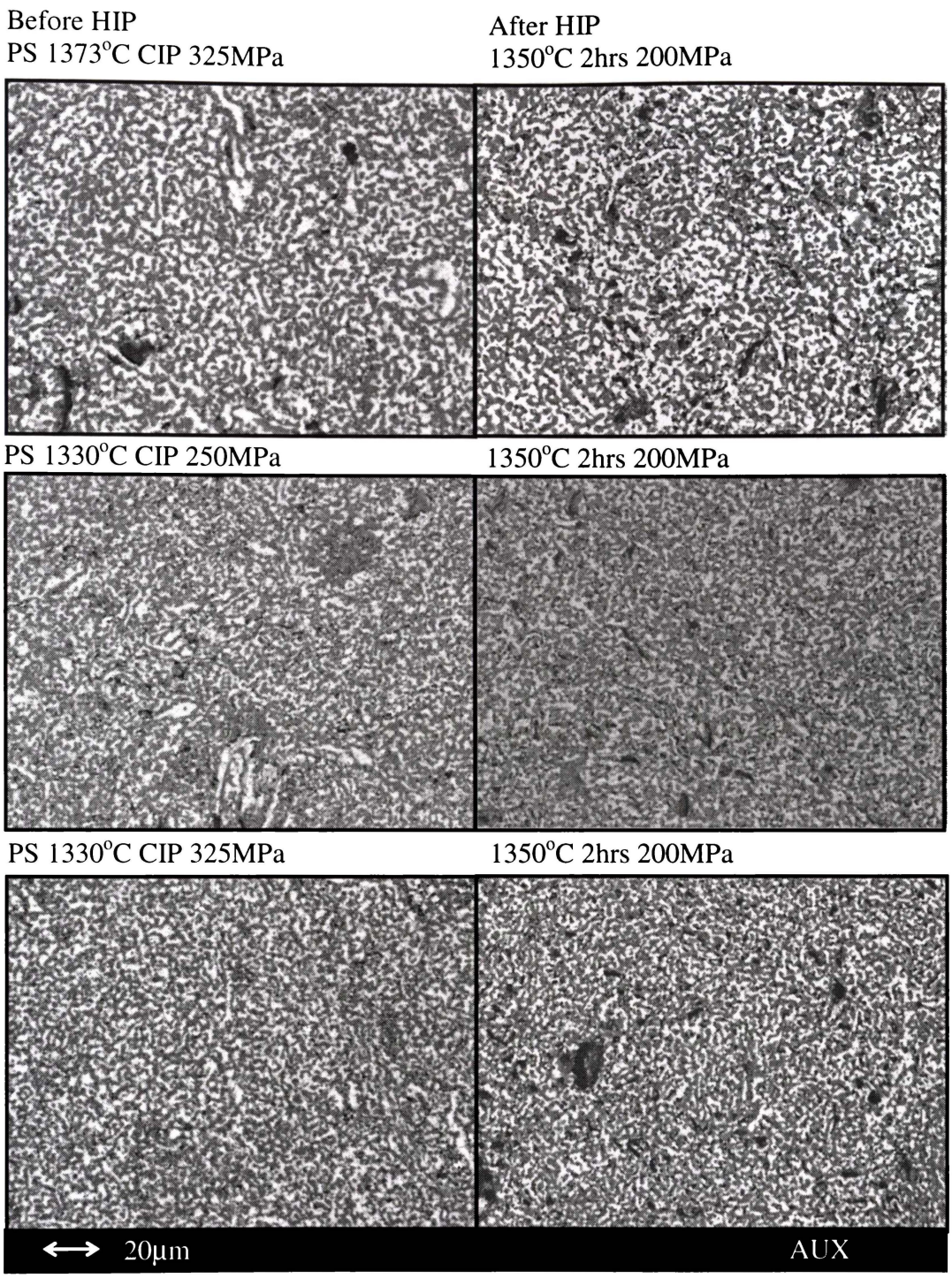

Figure 5.22: SEM images of Ti_3Al-TiO-Al_2O_3 composites produced by pressureless sintering Al-TiO_2-3 composite powder at 1330°C and 1373°C before and after hot isostatic pressing

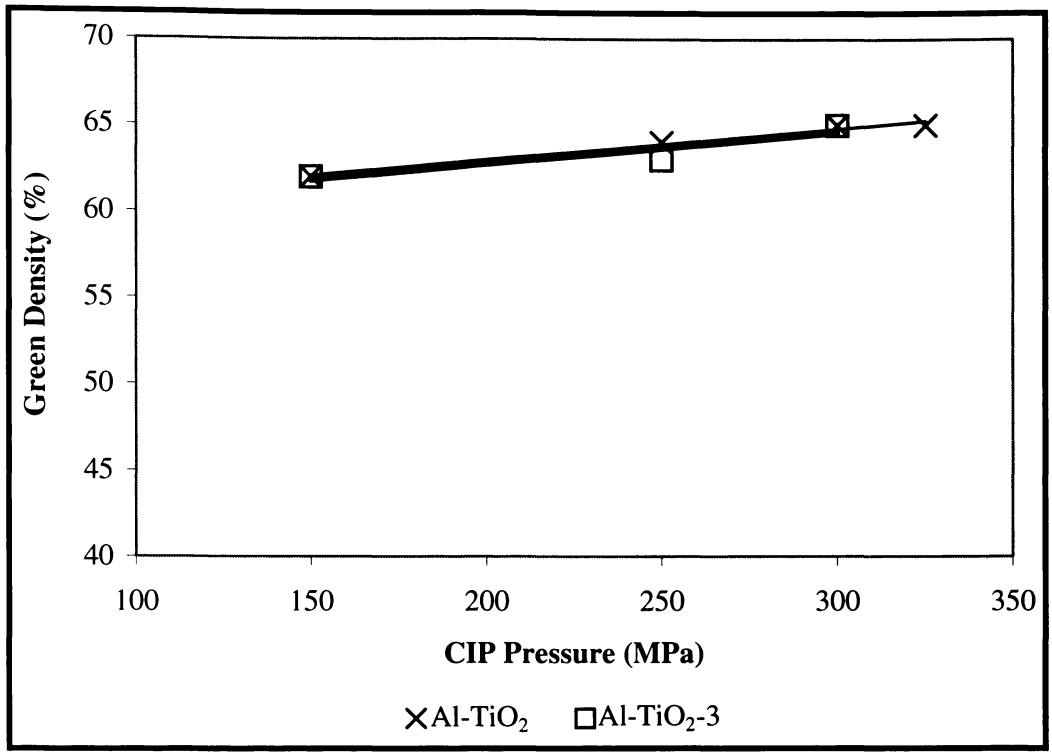

Figure 5.23: Green density of cold isostatic pressed Al-TiO_2 and Al-TiO_2-3 powder compacts at different pressure

Overall, near fully densified microstructures with ceramic-intermetallic interpenetrating networks could also be achieved by sinter-HIP at pressureless sintering temperature of 1480°C followed by hot isostatic pressing at 1350°C in argon as shown in Figure 5.24. These images show the cross sections of three different Ti_3Al-TiO-Al_2O_3 composites produced by pressureless sintering Al-TiO_2-3 composite powder at 1480°C before and after hot isostatic pressing at 1350°C under 200MPa for two hours. The dark grey particles are identified as Al_2O_3 embedded in the Ti_3Al matrix. The average particle size of Al_2O_3 is approximately 3.8μm.

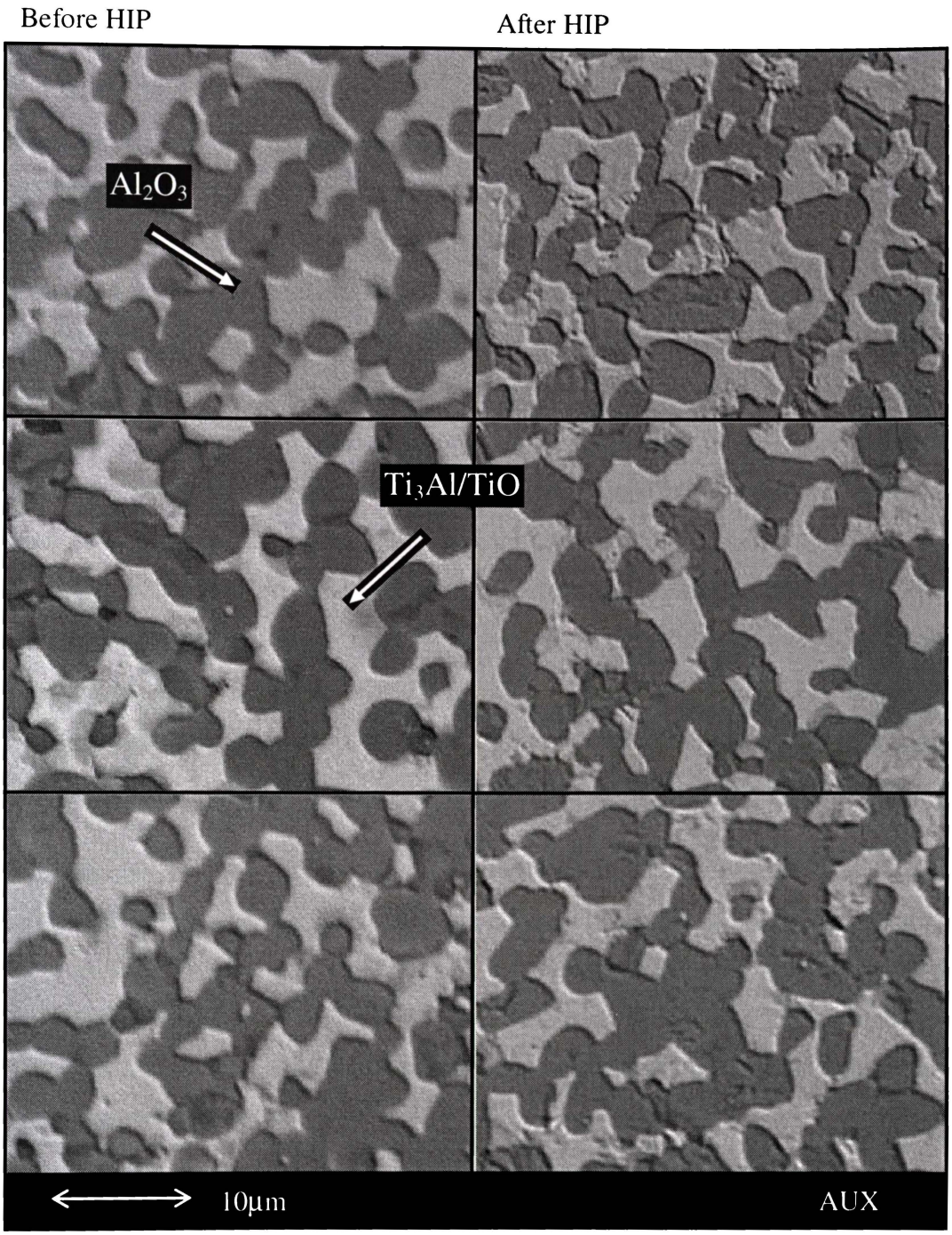

Figure 5.24: Microstructure of three different Ti_3Al-TiO-Al_2O_3 composites produced by pressureless sintering Al-TiO_2-3 composite powder at 1480°C before and after hot isostatic pressing at 1350°C under 200MPa for two hours

5.3 Discussion

5.3.1 Hot Pressing

High energy discus milling has been shown to greatly enhance the sintering behaviour of Ti_3Al-Al_2O_3 composites prepared from these Al-TiO_2 composite powders. The interface between Al and TiO_2 particles increases with the discus milling time from two to six hours. This study has shown that sintering and densification processes are accelerated by the reducing particle size of the starting discus milled Al-TiO_2 composite powders from 19μm to 10μm of median particle diameter. The increase of discus milling time causes the reaction temperature to decrease slightly due to the reduced particle size. After 24 hours of ball milling, there was significant microscale mixing between Al and TiO_2 and an accompanying reduction in particle size. However, the extended ball milling did not cause any further reduction of the particle size. A minimum median particle diameter of 7μm was reached for the six hours discus milled Al-TiO_2 composite powder subjected to 24 hours of ball milling as seen earlier in Table 4.2 in Chapter Four.

The volume fraction of the ductile intermetallic Ti_3Al in the Ti_3Al-Al_2O_3 composite is important in controlling the composite toughness. The XRD traces show that the Ti_3Al phase is maintained above 50% XRD peak intensity up to a hot pressing temperature of 1500°C. The composite microstructure demonstrates that both the Al_2O_3 and Ti_3Al phases are continuous and hence exhibit an interpenetrating network.

The advantage of hot pressing in this study is the improvement in the densification kinetics of Al and TiO_2 composite powders. The application of pressure causes plastic deformation and plastic flow of the matrix aiding to the diffusion of Al^{3+} and O^{2-}. Hot pressing above 1500°C was avoided to reduce the possibility of segregation of Ti_3Al causing inhomogeneous microstructure. In addition, the reaction sintering of Al and TiO_2 was controlled by hot pressing which allowed particle growth and pore suppression at a much lower temperature. That is, the densification phase and the operation temperatures are much more desirable than those achieved using pressureless sintering. Other research such as that on the Al_2O_3-Cr composites produced by pressureless sintering at 1500°C

achieved ~98.9% theoretical density whereas the composites produced by hot pressing at 1400°C under 20MPa reached ~99.1% theoretical density with 1.9μm Al_2O_3 particle size[11]. In this study, fully dense Ti_3Al-Al_2O_3 composites were achieved below 1400°C compared to pressureless sintered Ti_3Al-Al_2O_3 composites, which could only reach full density at 1650°C from previous study[12]. The average particle size of Al_2O_3 in Ti_3Al-Al_2O_3 composites produced by hot pressing Al-TiO_2 composite powder at 1387°C under vacuum for five hours of holding period is approximately 2μm, which is categorised as fine grain size[10].

5.3.2 Sinter-HIP

One of the advantages of sinter-HIP process is its ability to create near-net shapes that require little machining. In this project, near fully densified Ti_3Al-TiO-Al_2O_3 composites were fabricated by sinter-HIP of Al-TiO_2 composite powder with starting median particle diameter of 7.7μm, which had been discus milled for two hours. The composite microstructure shows that both the Al_2O_3 and Ti_3Al phases are continuous and hence exhibit an interpenetrating network. Overall, sinter-HIP at 1100°C and 1200°C was insufficient to cause any plastic deformation to improve the densification of the pressureless sintered composites. That is, both the closed and open porosity increased after hot isostatic pressing as shown in Figure 5.16 and Figure 5.17, respectively. Although at 1300°C, the closed porosity of the pressureless sintered composites was slightly reduced, the open porosity was increased after hot isostatic pressing as seen in Figure 5.18. Only at 1350°C under 200MPa, the pressureless sintered bodies were starting to decrease in both the open and closed porosity forming ≤98% theoretical density of Ti_3Al-TiO-Al_2O_3 composites.

Hot pressing and sinter-HIP assist sintering and densification processes allowing the reduction of temperature that leads to particle growth and pore suppression. Sinter-HIP in contrast to hot pressing permits the production of components with complex and precisely defined shapes. Besson reported that grain growth in alumina is accelerated by high pressure[13]. Studies by Cai reported that the Al_2O_3 particles in the composites coarsened after hot isostatic pressing for pre-sintered samples produced at 1550°C[12]. In this study, the coarsening of the Al_2O_3 particles was suppressed after hot isostatic pressing of the Ti_3Al-TiO-Al_2O_3

composites prepared by pressureless sintering Al-TiO_2 composite powder at 1480°C.

One of the essential pre-requisites of successful sinter-HIP is that ≥95% theoretical density of the pre-sintered composites must be obtained before hot isostatic pressing[14]. Therefore in order to achieve ≥95% of pre-sintered composites, the starting powder mixtures should be reactive and fine grained (~1μm)[5] with an accurate starting molar ratio, which adds to the need for better processing of Al-TiO_2 composite powder. To achieve ≥95% theoretical density of Ti_3Al-TiO-Al_2O_3 composites, a pressureless sintering temperature of at least 1480°C for five hours is necessary to make sinter-HIP without canning more effective.

5.4 Summary

In this chapter, the densification and microstructural development during pressure-assisted sintering such as hot pressing and sinter-HIP of Al-TiO_2 composite powders produced from high energy discus milling were investigated. Hot pressing of two, four and six hours discus milled composite powders containing Al and TiO_2 (anatase) before and after 24 hours of ball milling has been carried out under vacuum for five hours of holding period at temperatures between 1278°C and 1500°C and a heating rate of 5°C/min. Densification of the composites was investigated as a function of temperature. It was shown that lower porosity was obtained by hot pressing the composite powder and by hot isostatic pressing of the pre-sintered composites compared to pressureless sintering of the composite powder. *Fully dense microstructures* could be achieved by hot pressing Al-TiO_2 composite powder with starting median particle diameter of 7μm at 1387°C for five hours of holding period under vacuum at 10MPa. *Near fully densified* Ti_3Al-TiO-Al_2O_3 composites *(≤98% of theoretical density)* were fabricated by hot isostatic pressing of the pre-sintered Ti_3Al-TiO-Al_2O_3 composite *(96% of theoretical density)*, produced by pressureless sintering Al-TiO_2 composite powders with starting median particle diameter of 7.7μm. Interpenetrating phase Ti_3Al-TiO-Al_2O_3 and Ti_3Al-Al_2O_3 composites have been

fabricated by hot pressing and sinter-HIP, using controlled heat-treatment in non-oxidising atmospheres.

REFERENCES

1. Bruhn, J., S. Schicker, D.E. Garcia, R. Jansen, F. Wagner, and N. Claussen, *Novel reaction-based processing of co-continuous ceramic-metal composites.* Key engineering materials, 1997. **127-131**: p. 73-80.
2. Gunther, R., T. Klassen, B. Dickau, F. Gartner, A. Bartels, and R. Bormann, *Advanced alumina composites reinforced with titanium-based alloys.* Journal of American Ceramic Society, 2001. **84**(7): p. 1509-1513.
3. Pan, J., H. Li, H. Fukunage, X.G. Ning, H.Q. Ye, Z.K. Yao, and D.M. Yang, *Microstructural study of the interface reaction between titania whiskers and aluminium.* Composites Science and Technology, 1997. **57**: p. 319-325.
4. Zhang, D.L., D.Y. Ying and P. Munroe, *Formation of Al_2O_3 during heating an Al/TiO_2 nanocomposite powder.* Journal of Materials Research, 2005. **20**: p. 307-313.
5. Claussen, N., D.E. Garcia and R. Jansen, *Reaction sintering of alumina-aluminide alloys (3A).* Journal of Materials Research, 1996. **11**(11): p. 2884-2888.
6. Schicker, S., D.E. Garcia, J. Bruhn, R. Jansen and N. Claussen, *Reaction synthesized Al_2O_3-based intermetallic composites.* Acta Materialia, 1998. **46**(7): p. 2485-2492.
7. Klassen, T., R. Gunther, B. Dickau, F. Gartner, A. Bartels, R. Bormann, and H. Mecking, *Processing and properties of intermetallic/ceramic composites with interpenetrating microstructure.* Journal of the American Ceramic Society, 1998. **81**(9): p. 2504-2506.
8. Travitzky, N., I. Gotman, E.Y. Gutmanas and N. Claussen, *Alumina-Ti aluminide interpenetrating composites: microstructure and mechanical properties.* Materials Letters, 2003. **57**: p. 3422-3426.
9. Richerson, D.W., *Modern ceramic engineering : properties, processing, and use in design*, in *Materials engineering (Marcel Dekker, Inc.).* 1992, New York : M. Dekker. p. 552-556.
10. Nakahigashi, J. and H. Yoshimura, *Ultra-fine grain refinement and tensile properties of titanium alloys obtained through protium treatment.* Journal of Alloys and Compounds, 2002. **330-332**: p. 384-388.
11. Ji, Y. and J.A. Yeomans, *Microstructure and mechanical propeties of chromium and chromium/nickel partiulate reinforced alumina ceramics.* Journal of Materials Science, 2002. **37**: p. 5229-5236.
12. Cai, Z.H., *Processing, microstructure and mechanical properties of Ti_xAl_y/Al_2O_3 and $Al_2Ti_4C_2/Ti_xAl_y/Al_2O_3/TiC$ composites*, PhD Thesis. 2003, The University of Waikato: Hamilton. p. 110.
13. Besson, J. and M. Abouaf, *Grain growth enhancement in alumina during hot isostatic pressing.* Acta Metallurgica et Materialia, 1991. **39**(10): p. 2225-2234.
14. Azcona, I., J.M. Sanchez and F. Castro, *Hipping after sintering of titanium diboride cermets.* Powder Metallurgy, 2001. **44**(2): p. 133-138.

CHAPTER SIX:

Mechanical Properties of Ti_3Al-Al_2O_3 and Ti_3Al-TiO-Al_2O_3 Composites

In this chapter, the results of a study on the mechanical properties of Ti_3Al-Al_2O_3 and Ti_3Al-TiO-Al_2O_3 composites such as Vickers hardness, biaxial strength and fracture toughness are presented and discussed. These composites are formed using different processing conditions, namely (1) hot pressing of Ti_3Al-Al_2O_3 composite powders; (2) pressureless sintering of discus milled Al-TiO_2 composite powders before and after ball milling; (3) hot pressing of discus milled Al-TiO_2 composite powders before and after ball milling and (4) combination of sintering and hot isostatic pressing of Al-TiO_2 composite powder, which have been described in previous chapters. The phase composition-densification-mechanical properties relationships of Ti_3Al-Al_2O_3 and Ti_3Al-TiO-Al_2O_3 composites are discussed.

6.1 Ti_3Al-TiO-Al_2O_3 Composites

6.1.1 Effect of Composition

Vickers hardness measurements of Ti_3Al-TiO-Al_2O_3 composites produced by hot pressing 2.4μm and 1.2μm Ti_3Al-Al_2O_3 composite powders at 31MPa or 4MPa are plotted against their sintering temperature as shown in Figure 6.1. The open porosity and Al_2O_3 particle size of these composites are set between 0-3% and 1-2.5μm, respectively for comparison in this figure. The Vickers hardness of the Ti_3Al-TiO-Al_2O_3 composites produced from 1.2μm Ti_3Al-Al_2O_3 composite powders was generally higher than that of the composites produced from 2.4μm Ti_3Al-Al_2O_3 composite powder, both hot pressed at 31MPa. This can be explained by the fraction of Ti_3Al in the composites. It was described earlier in Chapter Three that the composites produced by hot pressing 1.2μm Ti_3Al-Al_2O_3 composite powder contained only up to 25% XRD phase intensity of Ti_3Al phase whereas the composites produced by hot pressing 2.4μm Ti_3Al-Al_2O_3 samples contained up to 58% XRD phase intensity of Ti_3Al phase as seen in Figure 3.15. That is, the higher content of the intermetallic Ti_3Al phase in the hot pressed composite contributed to lower Vickers hardness. Vickers hardness of approximately 17.5GPa was achieved for the fully densified Ti_3Al-TiO-Al_2O_3 composite produced by hot pressing 1.2μm Ti_3Al-Al_2O_3 composite powder at 1474°C under vacuum at 4MPa.

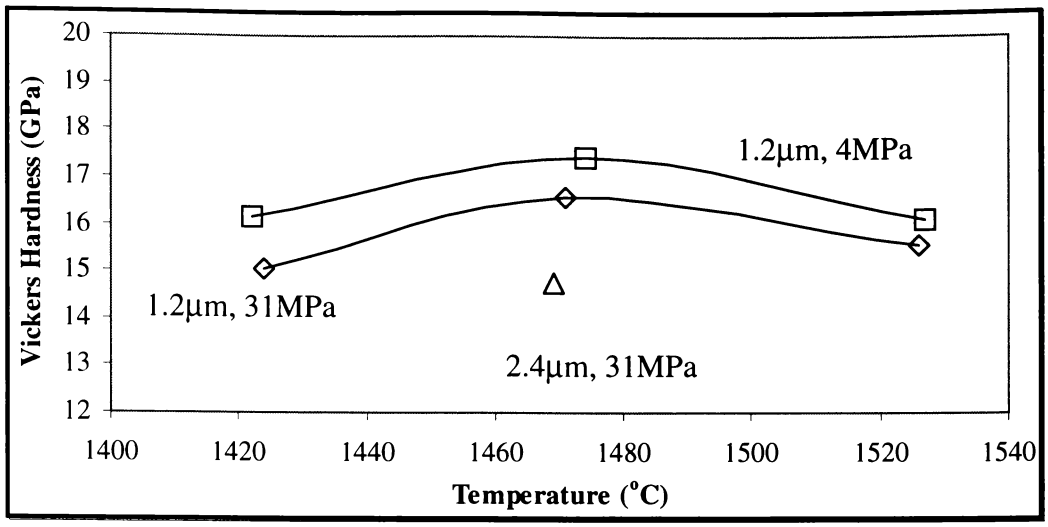

Figure 6.1: Vickers hardness as a function of sintering temperature of Ti_3Al-TiO-Al_2O_3 composites produced from hot pressing Ti_3Al-Al_2O_3-1 composite powder under vacuum

Figure 6.2 shows the biaxial strength, XRD peak intensity of Ti_3Al phase and open porosity of the Ti_3Al-TiO-Al_2O_3 composites produced by hot pressing Al-TiO_2 composite powders hot pressed under vacuum.

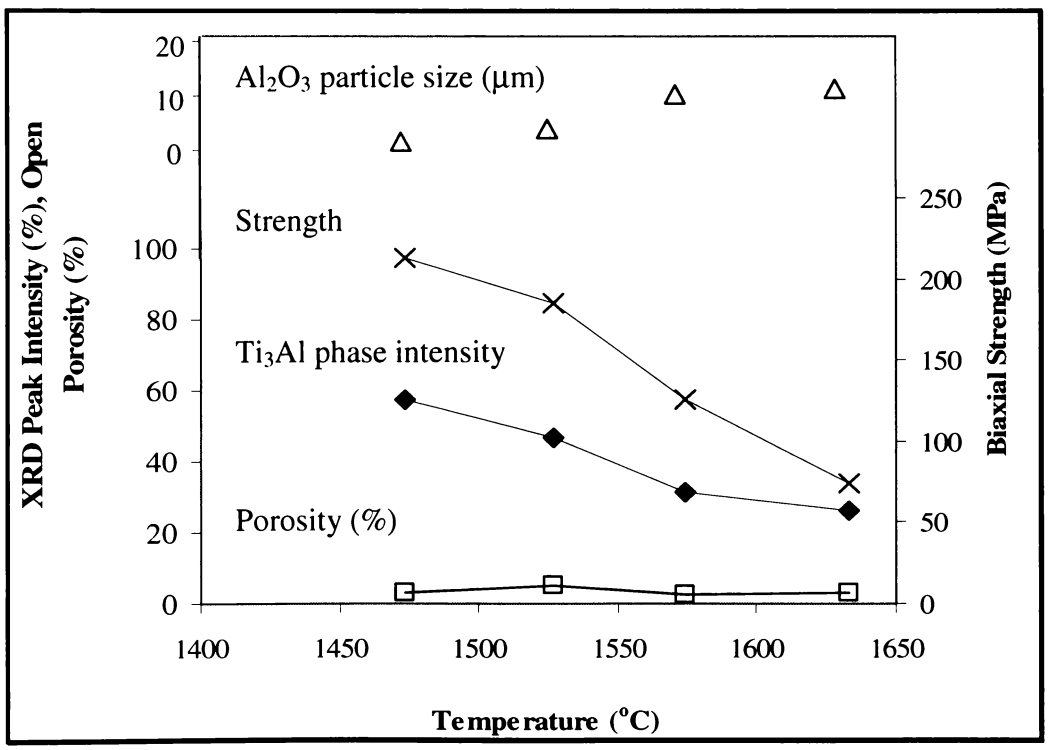

Figure 6.2: Biaxial strength, Ti_3Al phase intensity, Al_2O_3 particle size and open porosity as a function of temperature for Ti_3Al-TiO-Al_2O_3 composites produced by hot pressing Al-TiO_2 composite powder under vacuum

The biaxial strength of the composites decreased with increasing hot pressing temperature, increasing Al_2O_3 particle size and the reduction of the Ti_3Al

intermetallic phase content. This shows that the effect of the Ti_3Al intermetallic phase and the Al_2O_3 particle size are important in controlling the mechanical properties of the composite. In these experiments, the biaxial strength was decreased due to the reduction of Ti_3Al intermetallic phase content even though the open porosity in the bodies remained below 5%, as shown in Figure 6.2.

6.1.2 Effect of Starting Particle Size

Starting particle size can be reduced by ball milling for up to 24 hours. Vickers hardness of the Ti_3Al-TiO-Al_2O_3 composites prepared by pressureless sintering Al-TiO_2 composite powder at 1480°C in argon is shown in Figure 6.3. The figure shows Vickers hardness could be doubled by increasing the ball milling time of the starting powder from 0 to 24 hours. The increased ball milling time led to decreased starting particle size of the Al-TiO_2 composite powder as seen in Table 4.1 in Chapter Four, which produced lower open porosity and higher Vickers hardness. From 1 to 4 hours of holding period, Vickers hardness was improved by approximately 2GPa and from 4 to 8 hours of holding period, Vickers hardness was improved by approximately 1GPa. The hardness trends can be seen to be increasing with holding period. Vickers hardness of 15.9GPa was achieved for the fully densified Ti_3Al-TiO-Al_2O_3 composite produced by pressureless sintering Al-TiO_2 composite powder in argon at 1480°C for 8 hours.

Figure 6.4 shows the biaxial strength of Ti_3Al-TiO-Al_2O_3 composites produced by pressureless sintering Al-TiO_2-2 composites powder after 0, 8, 16 and 24 hours of ball milling, in argon, as a result of porosity reduction. The Ti_3Al intermetallic phase in the compacts was maintained at around 50% XRD phase intensity after sintering at 1480°C as shown in Figure 6.4. The biaxial strength of the near densified Ti_3Al-TiO-Al_2O_3 composites formed by pressureless sintering Al-TiO_2 composite powder after 24 hours ball milling can reach as high as 350MPa.

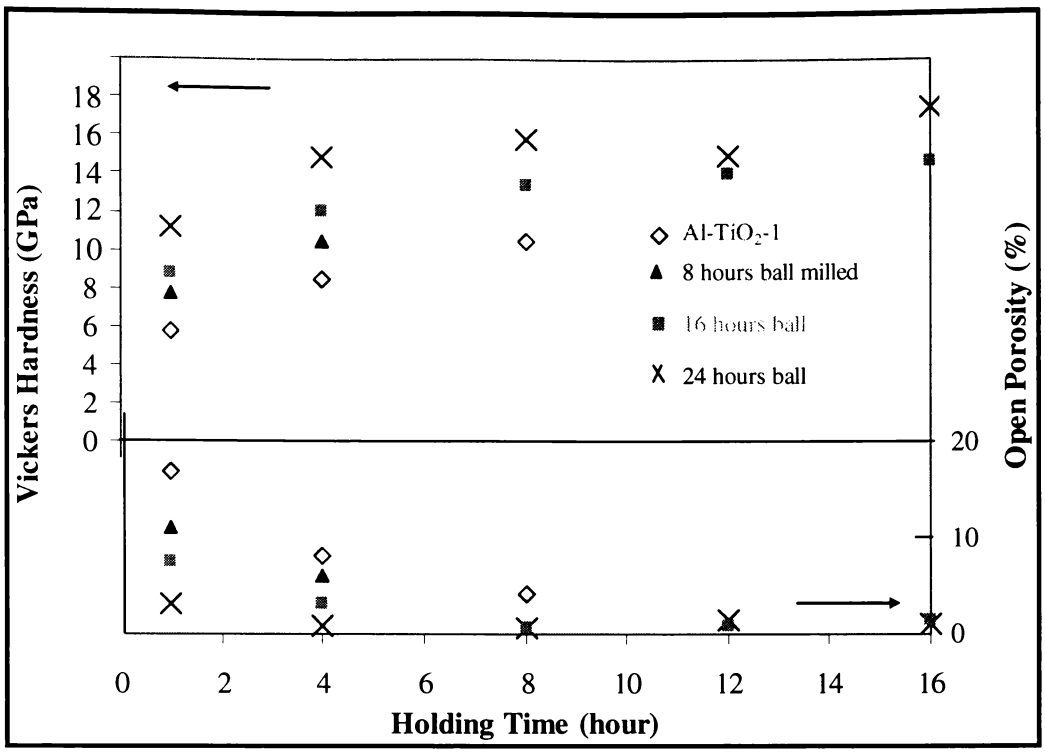

Figure 6.3: Vickers hardness and open porosity of Ti_3Al-TiO-Al_2O_3 composites produced by pressureless sintering Al-TiO_2 composite powder as a function of holding time in argon at 1480°C

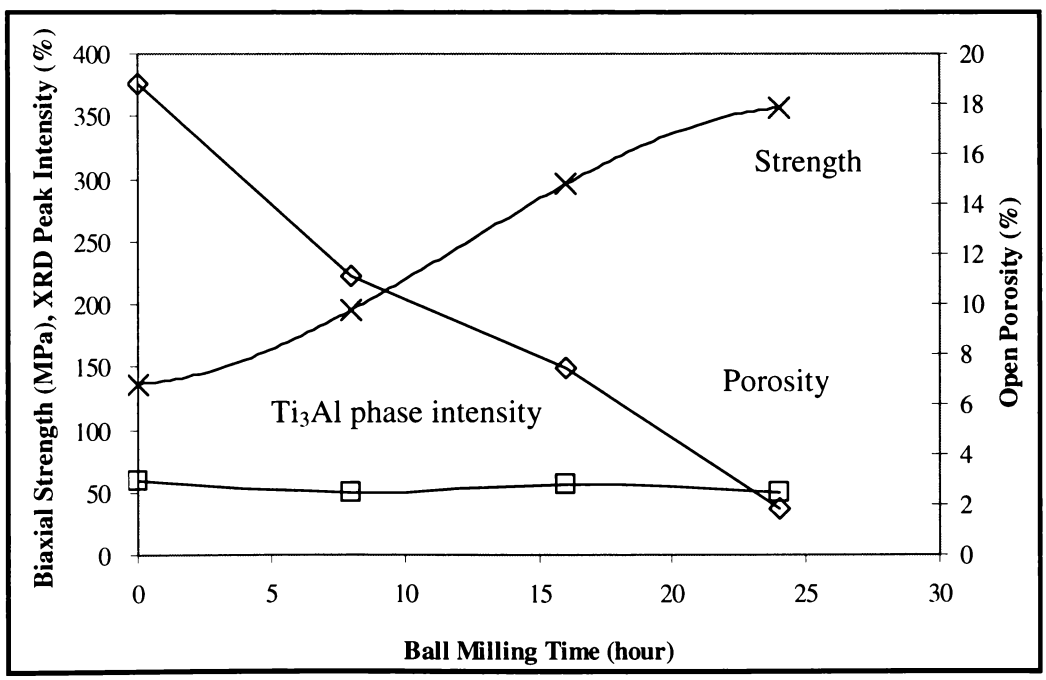

Figure 6.4: Biaxial Strength, XRD peak intensity of Ti_3Al phase and open porosity as a function of ball milling time for Ti_3Al-TiO-Al_2O_3 composites produced by pressureless sintering of Al-TiO_2 composite powder in argon at 1480°C

6.2 Ti_3Al-TiO-Al_2O_3 and Ti_3Al-Al_2O_3 Composites Produced by Pressureless Sintering and Hot Pressing

6.2.1 Pressureless Sintering

Vickers hardness measurements of Ti_3Al-Al_2O_3 composites produced by pressureless sintering of Al-TiO_2 composite powders are plotted against the sintering temperature in Figure 6.5. Vickers hardness increased with respect to the sintering temperatures for the pressureless sintered samples. Vickers hardness of the pressureless sintered samples achieved up to 10GPa. The higher Vickers hardness is due to the increased densification with increasing temperature for the pressureless sintering while maintaining the Ti_3Al above 50% XRD peak intensity.

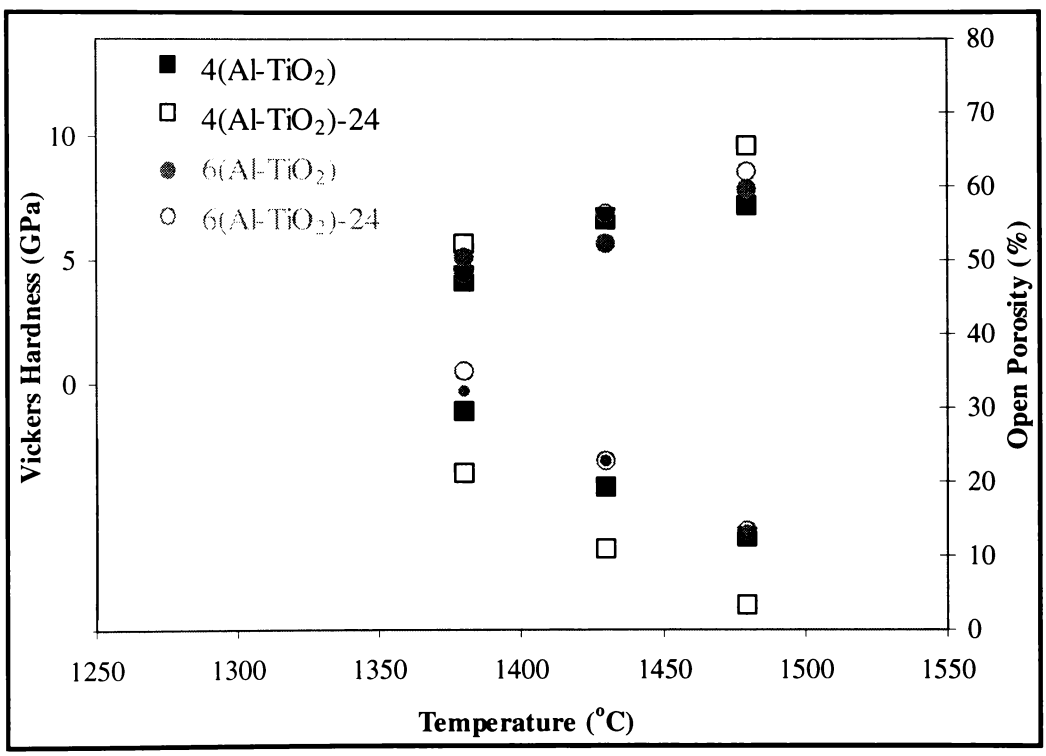

Figure 6.5: Vickers hardness and open porosity of Ti_3Al-Al_2O_3 composites produced by pressureless sintering Al-TiO_2 composite powder under vacuum as a function of temperature

6.2.2 Ti_3Al-TiO-Al_2O_3 and Ti_3Al-Al_2O_3 Composites produced by Hot Pressing

Vickers hardness, Al_2O_3 particle size and open porosity measurements of Ti_3Al-TiO-Al_2O_3 composites produced by hot pressing 2.4μm and 1.2μm Ti_3Al-Al_2O_3 composite powders under vacuum are plotted against the sintering temperature as shown in Figure 6.6. The Vickers hardness of the Ti_3Al-TiO-Al_2O_3 composites produced from 1.2μm Ti_3Al-Al_2O_3 composite powders was generally higher than that of the composites produced from 2.4μm Ti_3Al-Al_2O_3 composite powder, both hot pressed at 31MPa. This can be explained by the lower porosity level obtained from the hot pressed 1.2μm Ti_3Al-Al_2O_3 samples. The Vickers hardness increased with increasing hot pressing temperature up to approximately 1500°C then decreased with respect to the hot pressing temperature. The improvement of Vickers hardness is due to the increasing composite densification with increasing hot pressing temperature as shown in Figure 6.6. The reduction of Vickers hardness above 1500°C can be interpreted by the increase in Al_2O_3 particle size seen in Figure 6.6 and microcracking observed in the 2.4μm samples as seen earlier in Figure 3.25 and the high temperature development of pores in the 1.2μm samples as seen earlier in Figure 3.26(e) and (f) in Chapter Three.

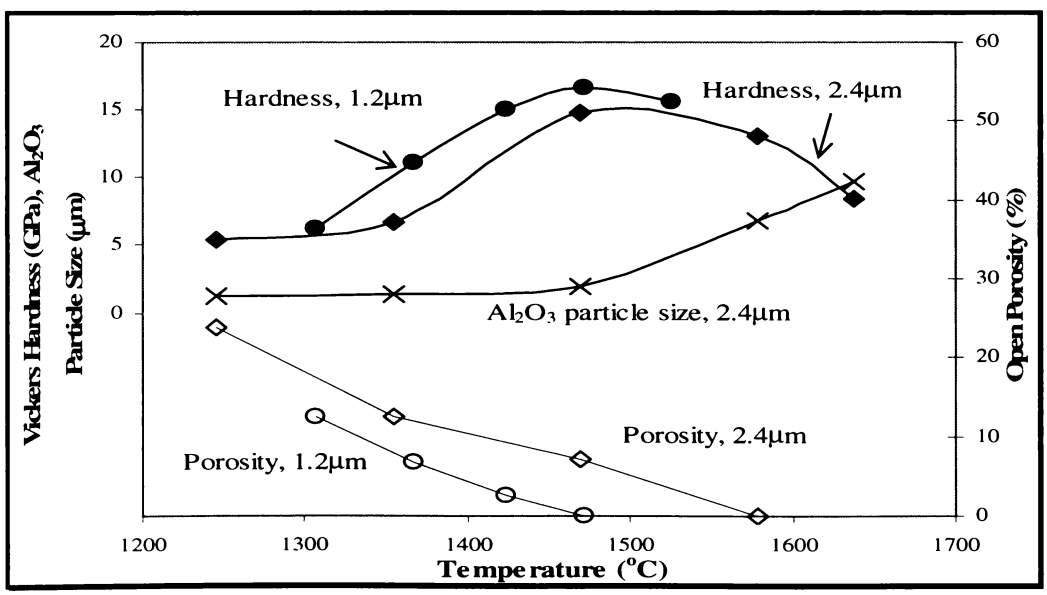

Figure 6.6: Vickers hardness, Al_2O_3 particle size and open porosity as a function of hot pressing temperature for Ti_3Al-Al_2O_3 composites produced by hot pressing Ti_3Al-Al_2O_3 composite powder under vacuum

Figure 6.7 shows Vickers hardness measurements of Ti_3Al-Al_2O_3 composites produced by hot pressing Al-TiO_2 composite powders as a function of hot pressing temperature. Vickers hardness of the hot pressed samples achieved 12 to 15GPa. The higher Vickers hardness compared to the pressureless sintered samples is due to Ti_3Al-Al_2O_3 composites produced from hot pressing being significantly denser. The Vickers hardness of the hot pressed composites was almost at the same level, i.e. within 1-2GPa of each other for the same set of composite powders. This can be explained by the fine particle size (0.8-4μm) of the Al_2O_3 particles after hot pressing and around 50% XRD peak intensity of Ti_3Al phase being maintained in the composite as discussed earlier in Chapter Five. Higher Vickers hardness of 15.1GPa was achieved for the fully densified Ti_3Al-Al_2O_3 composite produced by hot pressing 2(Al-TiO_2) composite powder at 1500°C under vacuum compared to the fully densified Ti_3Al-Al_2O_3 composites produced by hot pressing 4(Al-TiO_2) and 6(Al-TiO_2) with finer starting median particle diameters. This is due to the larger Al_2O_3 particle size in the composite, hence larger contact areas of Al_2O_3 particles.

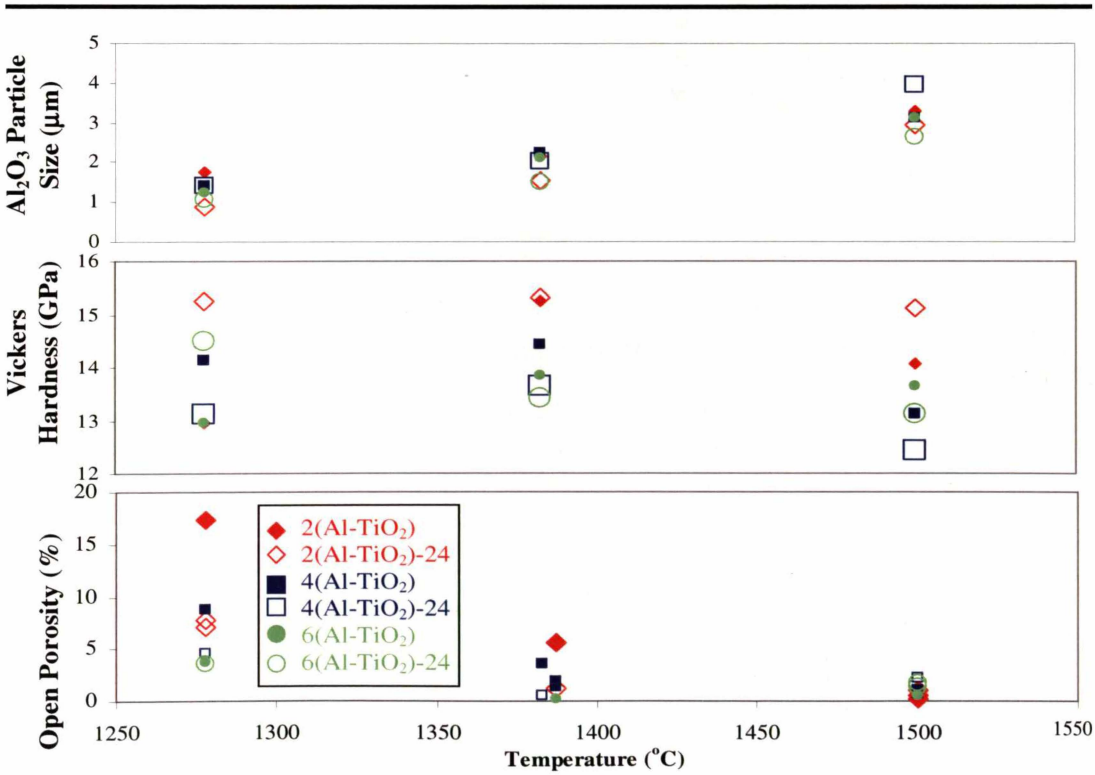

Figure 6.7: Vickers hardness, Al_2O_3 particle size and open porosity as a function of temperature for Ti_3Al-Al_2O_3 composite produced by hot pressing under vacuum

Biaxial strength of the Ti_3Al-Al_2O_3 composites fabricated by hot pressing Al-TiO_2 composite powders as a function of the hot pressing temperature is shown in Figure 6.8. The biaxial strength increased from 139 to 278MPa. The starting median particle diameters of the two, four and six hours discus milled Al-TiO_2 composite powders before and after ball milling range from 19μm to 10μm and from 8μm to 7μm, respectively. There is no clear trend in the biaxial strength versus the hot pressing temperature between the Ti_3Al-Al_2O_3 composites produced by hot pressing the Al-TiO_2 composite powder with different starting median particle diameters. In general, the biaxial strength increased with increasing hot pressing temperature. The increase of biaxial strength was proportional to the reduction of porosity as shown in Figure 5.10 seen earlier in Chapter Five.

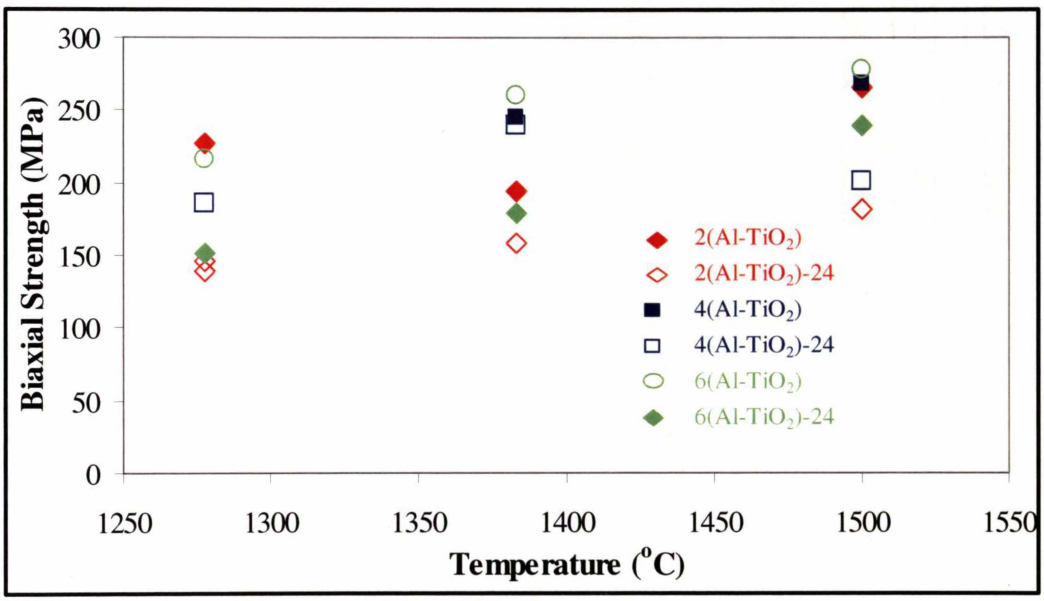

Figure 6.8: Biaxial strength of Ti_3Al-Al_2O_3 composites produced by hot pressing Al-TiO_2 composites powders as a function of temperature

6.2.3 Ti_3Al-TiO-Al_2O_3 Composites Produced by Sinter-HIP of Al-TiO_2 Composite Powder

For the sinter-HIP method to be beneficial, green bodies should contain only closed porosity, that is >95% theoretical density[1]. One of the benefits shown in the Ti_3Al-TiO-Al_2O_3 composites produced by pressureless sintering of Al-TiO_2-3 composite powder is the increased Vickers hardness after hot isostatic pressing. The Vickers hardness of the sintered composites displayed improvement provided that the bodies had greater than 95% theoretical densities before hot isostatic

pressing. That is, the Vickers hardness increased by up to 2GPa due to the decreased total porosity (original total porosity of ≤4%, refer Figure 5.19) of the composites pressureless sintered at 1480°C after hot isostatic pressing at 1350°C and 200MPa for two hours as shown in Figure 6.9. This was not demonstrated by the samples pressureless sintered at 1330°C and 1373°C after hot isostatic pressing at 1350°C regardless of the reduction of both closed and open porosity (original total porosity of ≥12%, refer Figure 5.19). In fact the Vickers hardness was maintained around the same level before and after hot isostatic pressing as shown in Figure 6.9.

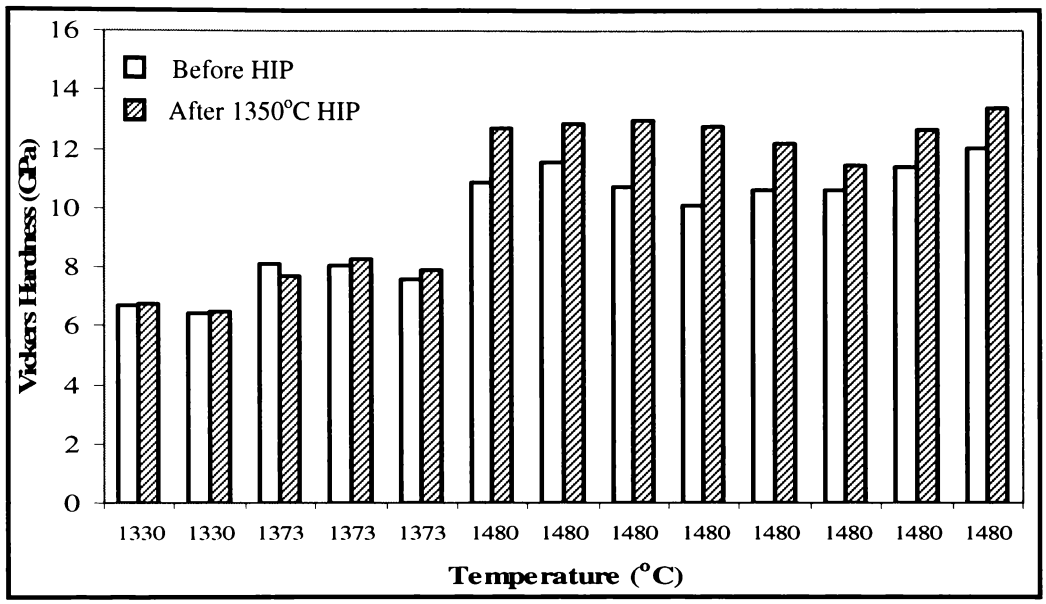

Figure 6.9: Vickers hardness of Al-TiO_2-2 composites pressureless sintered at various temperature subjected to hot isostatic pressing at 1350°C and 200MPa for two hours

Overall, sinter-HIP at 1100°C and 1200°C is insufficient to improve the densification of the pressureless sintered composites. That is, as discussed in Chapter Five, both the closed and open porosity increased after hot isostatic pressing as shown in Figure 5.16, Figure 5.17 and Figure 5.18. Although at 1300°C, the closed porosity of the pressureless sintered composites was slightly reduced, the open porosity was increased after hot isostatic pressing as seen in Figure 5.16 and Figure 5.18, respectively. This was discussed in more detail in Chapter Five.

6.3 Al_2O_3 Particle Size-Porosity-Ti_3Al Phase-Mechanical Properties Relationship

Vickers hardness of Ti_3Al-Al_2O_3 composites produced by hot pressing 2.4 and 1.2μm Ti_3Al-Al_2O_3 composite powders increased initially with increasing temperature but then decreased with further increase in temperature, as seen earlier in Figure 6.6. The increase of the hardness below 1500°C can be attributed to the increase of density and the decrease of the level of porosity with increasing hot pressing temperature. The decrease of Vickers hardness for the samples produced by hot pressing 2.4 and 1.2μm Ti_3Al-Al_2O_3 composite powders above 1500°C can be understood by two observations: (i) The abrupt increase in Al_2O_3 particle size (Figure 3.25) and (ii) the development of pores (Figure 3.26) and increased TiO phase (Figure 3.15(c)) in the composites, occurring following high temperature sintering seen earlier in Chapter Three. Kingery states that once the porosity has decreased to a value such that secondary particle growth can occur, extensive particle growth may result at high sintering temperatures[2]. For the composites produced by hot pressing 2.4μm composite powder, the decline of Vickers hardness is probably due to the abrupt increase in particle growth, which leads to microcracks around the particle boundary as seen earlier in Figure 3.25(d). Particle growth phenomena causing microcracks are described more in detail in Chapter Three.

Mechanical properties such as biaxial strength are influenced by the level of sample porosity, such that higher porosity gives lower biaxial strength. For a Ti_3Al-Al_2O_3 composite, the biaxial strength increases when the Ti_3Al phase content increases. Figure 6.10 and Figure 6.11 show the biaxial strength of hot pressed composites produced from 2(Al-TiO_2), 4(Al-TiO_2) and 6(Al-TiO_2) before and after 24 hours of ball milling. The mechanical behaviour exhibited by the composites can be understood when the composites display one or more of the factors noted above. For example, Figure 6.10(b) shows that the biaxial strength is dominated by the increase of Al_2O_3 particle size. On the other hand, Figure 6.10(c), Figure 6.11(a) and (b) show that the increase of strength is dominated by the decrease of porosity level. The best biaxial strength achieved was 278MPa.

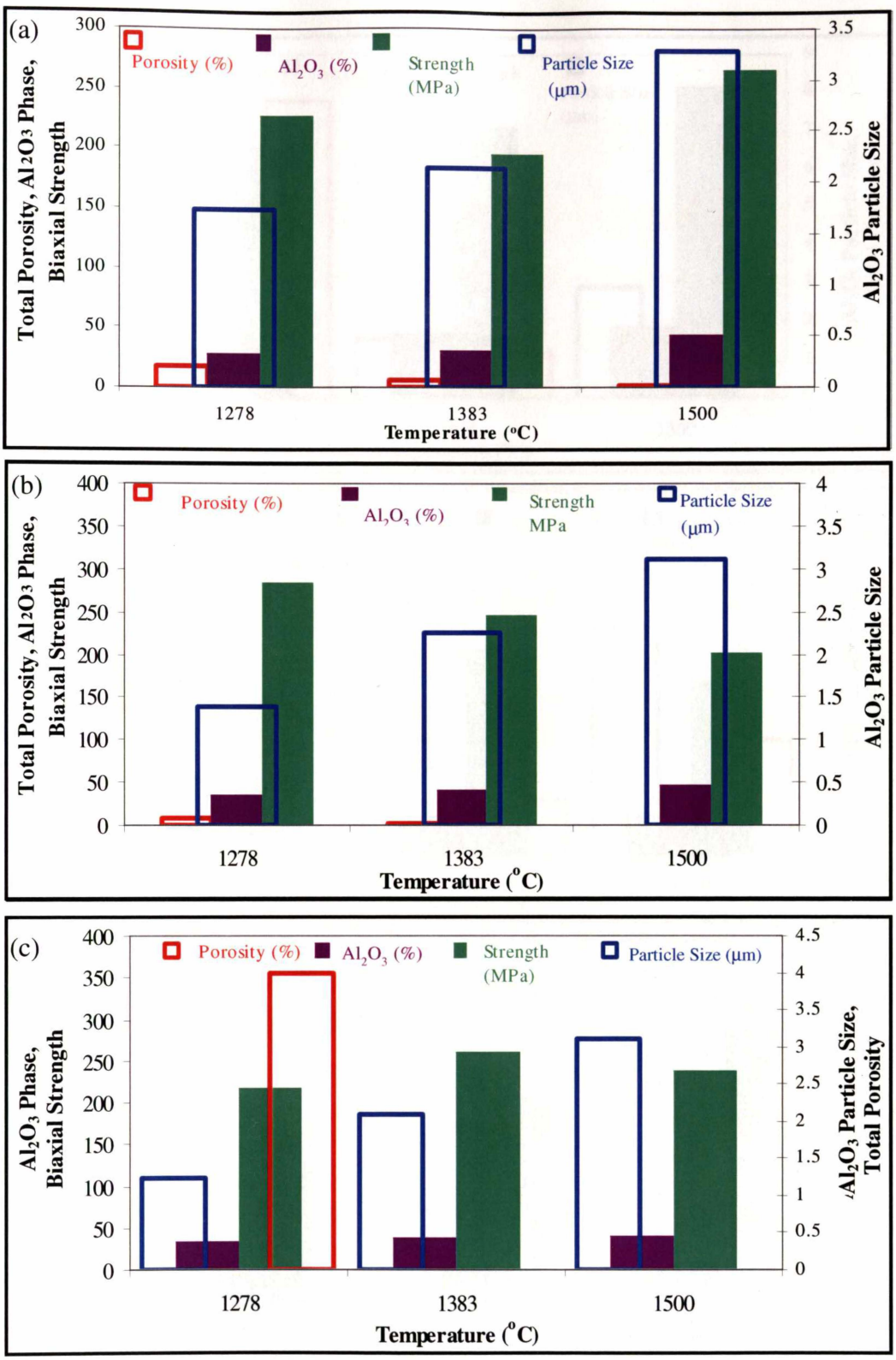

Figure 6.10: Phase-porosity-Al_2O_3 particle size-strength of Ti_3Al-Al_2O_3 composite produced by hot pressing (a) 2(Al-TiO_2), (b) 4(Al-TiO_2) and (c) 6(Al-TiO_2) composite powders under vacuum as a function of temperature

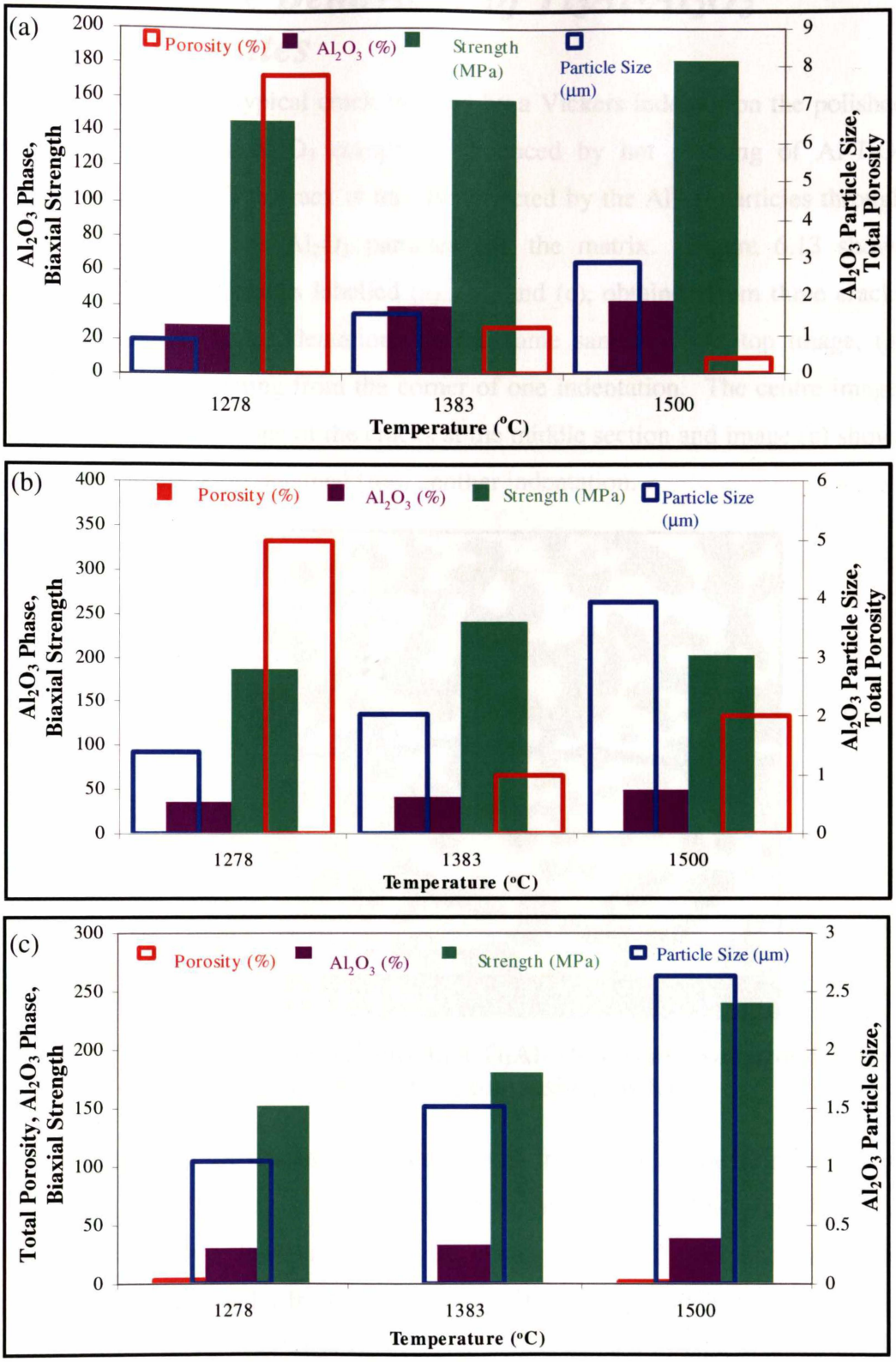

Figure 6.11: Phase-porosity-Al_2O_3 particle size-strength of Ti_3Al-Al_2O_3 composite produced by hot pressing (a) 2(Al-TiO_2)-24, (b) 4(Al-TiO_2)-24 and (c) 6(Al-TiO_2)-24 composite powders under vacuum as a function of temperature

6.4 Fracture Behaviour of Ti_3Al-Al_2O_3 Composites

Figure 6.12 shows a typical crack induced by a Vickers indentor on the polished surface of the Ti_3Al-Al_2O_3 composite produced by hot pressing of Al-TiO_2 composite powder. The crack is mostly deflected by the Al_2O_3 particles through debonding between the Al_2O_3 particles and the matrix. Figure 6.13 shows sections of different cracks labelled (a), (b), and (c), obtained from three cracks from different Vickers indentations on the same sample. The top image, (a) shows the crack initiating from the corner of one indentation. The centre image, (b) was obtained from one of the cracks at the middle section and image (c) shows the end of the crack tip obtained from another indentation.

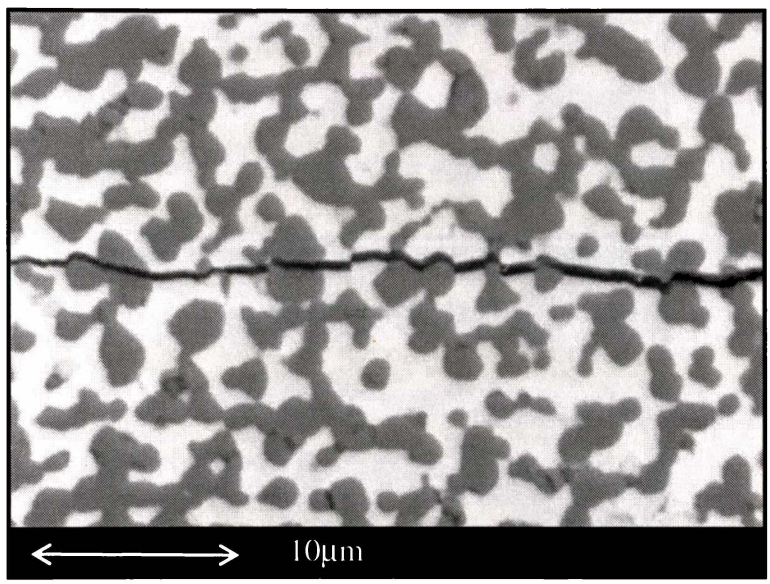

Figure 6.12: Indentation crack path in a Ti_3Al-Al_2O_3 composite produced by hot pressing Al-TiO_2 composite powder

It can be seen that the cracks propagate through transgranular fracturing of Al_2O_3 particles and Ti_3Al matrix and debonding or intergranular fracturing between Al_2O_3 particles and Ti_3Al matrix. The cracks circled in *pink* and *black* are examples of transgranular fracturing of the Al_2O_3 particles and Ti_3Al intermetallic phase, respectively. The 'zig-zag' crack segments circled in *blue* and *yellow* are examples of intergranular fracturing of the Al_2O_3 particles and the Ti_3Al matrix, respectively. The cracks circled in *green* are identified as debonding between Al_2O_3 particles and the Ti_3Al matrix.

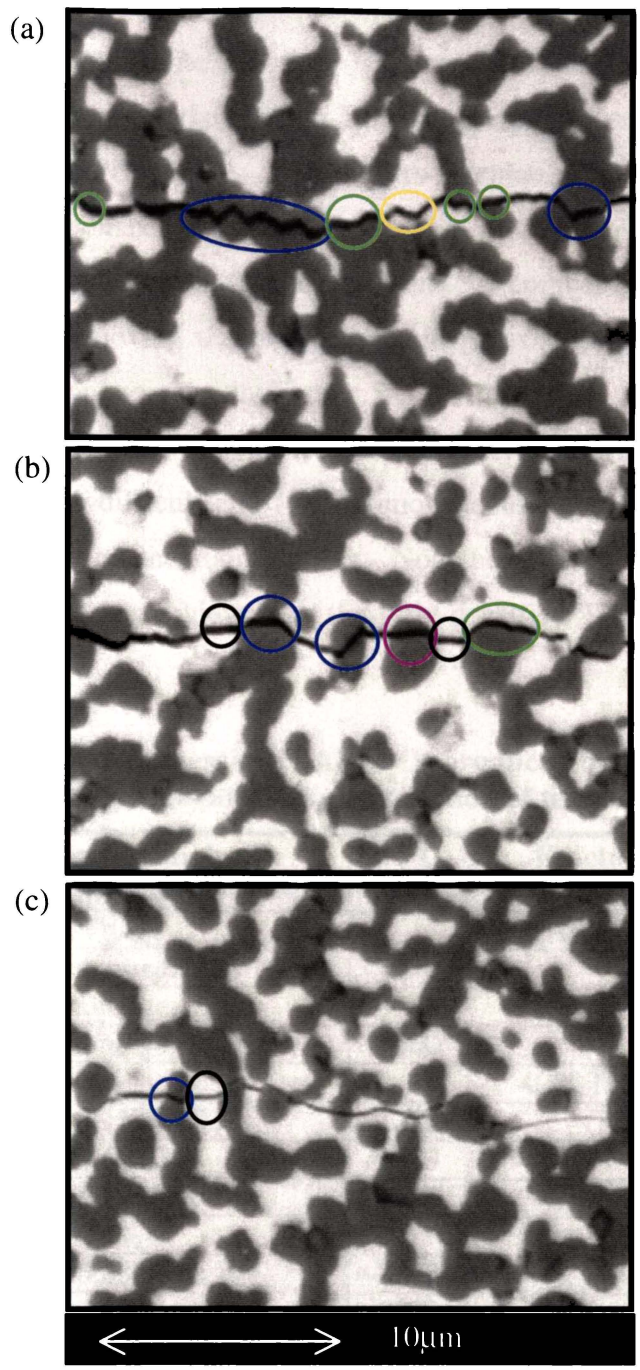

Figure 6.13: Different sections of indentation cracks of fully densified Ti_3Al-Al_2O_3 bodies

Debonding between alumina and aluminide phases is typical for this type of composite[3]. An outcome of alumina-aluminide interface debonding is enhanced energy dissipation of the propagating crack, which therefore contributes to the improvement of the fracture toughness of the composites. In addition, transgranular cracking by the more ductile Ti_3Al intermetallic phase may also control the fracture toughness of these composites.

The fracture toughness of the Ti_3Al-Al_2O_3 composites produced by hot pressing Al-TiO_2 (anatase) composite powders is shown in Table 6.1. The fracture toughness is obtained from the Vickers indentation measurements as described in Chapter Two and APPENDIX A. The Vickers indentation fracture toughness test was performed on polished surfaces. That means a fully dense material must be produced to achieve a meaningful measurement. A number of obstacles such as (1) difficulties in removing the residual closed pores; (2) particle pullout after polishing, which can be seen in Figure 5.11, Figure 5.12 and Figure 5.13 in Chapter Five; (3) two phase systems (Al_2O_3 and Ti_3Al) which make the estimation of the crack lengths difficult and (4) inhomogeneous microstructure, means an increased magnitude of uncertainty errors. Nonetheless fracture toughness up to 7.51±0.80 MPa.$m^{-1/2}$ was achieved for the fully densified Ti_3Al-Al_2O_3 composite hot pressed at 1383°C.

Table 6.1: Fracture toughness of Ti_3Al-Al_2O_3 produced by hot pressing of Al-TiO_2 composite powders as a function of temperature

T (°C)	Fracture Toughness (MPa.$m^{-1/2}$)	T (°C)	Fracture Toughness (MPa.$m^{-1/2}$)
2(Al-TiO_2)		2(Al-TiO_2)-24	
1278	inhomogeneous	1278	4.63±1.43
1383	inhomogeneous	1383	2.89±0.71
1500	inhomogeneous	1500	3.09±0.48
4(Al-TiO_2)		4(Al-TiO_2)-24	
1278	5.15±0.88	1278	4.75±1.37
1383	3.60±0.73	1383	6.30±0.80
1500	5.19±0.98	1500	4.89±0.53
6(Al-TiO_2)		6(Al-TiO_2)-24	
1278	5.83±1.12	1278	6.29±1.00
1383	7.51±0.80	1383	5.20±0.80
1500	5.55±1.00	1500	5.85±0.95

6.5 Discussion

6.5.1 Effect of Porosity Level

An increase in Vickers hardness was observed with the reduction of open porosity. This was especially noticeable for the hot pressing of 1.2μm Ti_3Al-Al_2O_3 composite powder at 31MPa where by increasing the hot pressing temperature from 1250°C to 1500°C, the Vickers hardness increased from 6 to 16GPa as seen in Figure 6.6. However, when the hot pressing temperature is

above 1500°C, the Vickers hardness reduced, which is attributed to the occurrence of pores due to segregation of Ti_3Al (Figure 3.26 and Figure 3.27) and increased TiO phase as seen in Figure 3.15(c) in Chapter Three.

In general, Vickers hardness was observed to increase linearly with the decrease of open porosity of the composites produced by pressureless sintering of Al-TiO_2, Al-TiO_2-3, 4(Al-TiO_2), 4(Al-TiO_2)-24, 6(Al-TiO_2), 6(Al-TiO_2)-24 composite powders in argon as shown in Figure 6.14. The lower Vickers hardness of the Ti_3Al-Al_2O_3 composites compared to Ti_3Al-TiO-Al_2O_3 composites produced from Al-TiO_2 composite powders is due to the higher level of Ti_3Al and the absence of TiO phase in the composites.

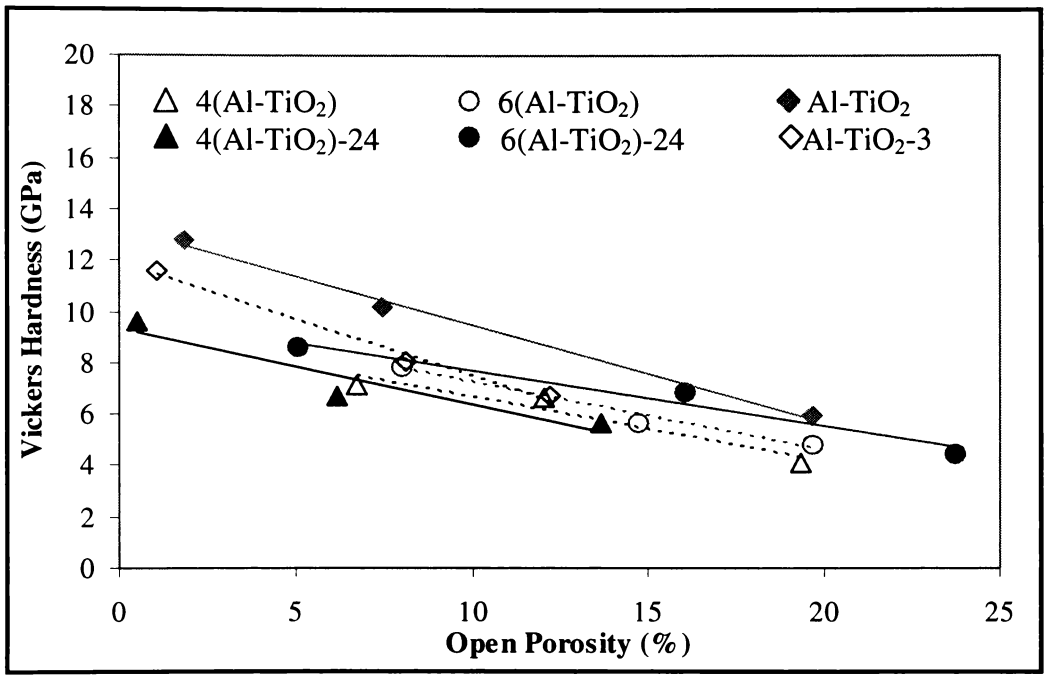

Figure 6.14: Vickers hardness of composites produced by pressureless sintering Al-TiO_2 composite powders in argon as a function of open porosity

Very fine-grained (<1μm) $NbAl_3$-Al_2O_3 composite (50vol.%$NbAl_3$) with 95% theoretical density produced by pressureless sintering Al and Nb_2O_5 composite powders at 1550°C shows a significant increase in Vickers hardness over the monolithic $NbAl_3$ from 7.50 ± 0.20 GPa to 14.60 ± 0.20 GPa[4]. Also, Vickers hardness of 5.65 ± 0.27GPa was achieved for the interpenetrating Al_2O_3-$TiAl_3$ (5μm Al_2O_3 grain size, 58.1vol.% Al_2O_3) alloys produced by reactive infiltration[5]. In this study, Vickers hardness of ≤16GPa was obtained for Ti_3Al-TiO-Al_2O_3 composites (~10% Ti_3Al of XRD peak intensity) with 1.9μm Al_2O_3

particle size produced by hot pressing 1.2μmTi_3Al-Al_2O_3 composite powder at 1471°C under vacuum.

Biaxial strength is influenced by the level of sample porosity such that higher porosity results in lower biaxial strength. For a Ti_3Al-Al_2O_3 composite, the biaxial strength of composites produced from Al-TiO_2 composite powders before and after 24 hours of ball milling is shown in Figure 6.10(c), Figure 6.11(a) and (b), which indicate that the increase of strength is controlled by the decrease of porosity level.

This is also seen in the Ti_3Al-TiO-Al_2O_3 composites produced by pressureless sintering Al-TiO_2 composite powders in argon where the biaxial strength decreased with increasing open porosity as shown in Figure 6.15. This trend is supported by fracture strength measured using a four-point bending technique, which shows that the strength decreases with increasing porosity level for the Al/Al_2O_3 composites produced by gas pressure metal infiltration[6].

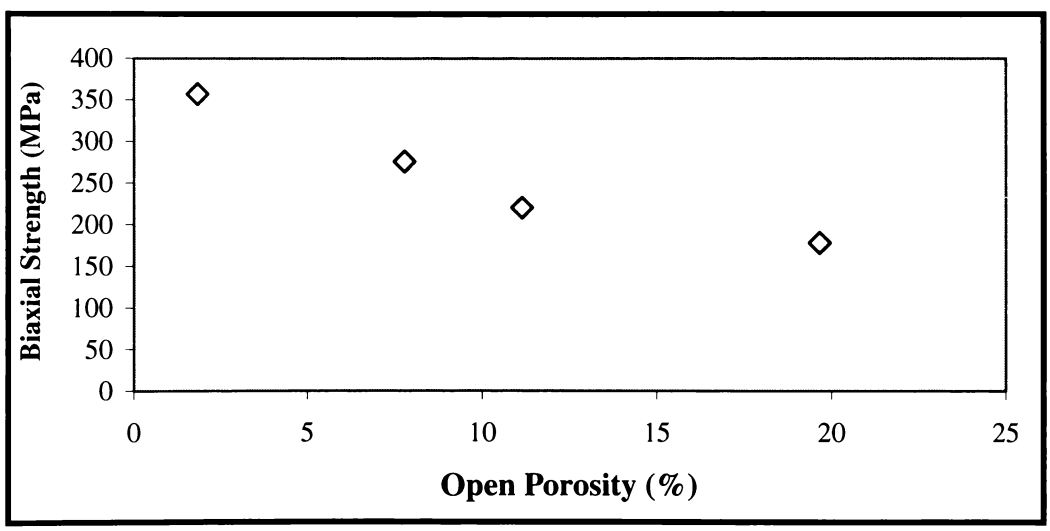

Figure 6.15: Biaxial strength of Ti_3Al-TiO-Al_2O_3 composites produced by pressureless sintering Al-TiO_2 composite powders in argon as a function of open porosity

6.5.2 Effect of Sintering Temperature

The Vickers hardness was increased for the Ti_3Al-TiO-Al_2O_3 composites produced by pressureless sintering Al-TiO_2 composite powder subjected to different ball milling times. The Vickers hardness was doubled by increasing the

ball milling time from 0 to 24 hours thereby reducing the starting particle size of the Al-TiO_2 composite powder as shown in Figure 6.3.

Vickers hardness measurements of the pressureless sintered Ti_3Al-Al_2O_3 composites produced from two, four and six hours discus milled Al-TiO_2 powders before and after 24 hours of ball milling showed Vickers hardness increased linearly with respect to the sintering temperatures as seen in Figure 6.5.

In general, Vickers hardness increased with increasing sintering temperature, which can be attributed to the decreased porosity of the composites produced by both pressureless sintering Al-TiO_2 composite powder and hot pressing Ti_3Al-Al_2O_3 composite powder as seen in Figure 6.16. In addition, the reduction of the starting particle size of the composite powders from 2.4μm to 1.2μm also contributes to the improved Vickers hardness.

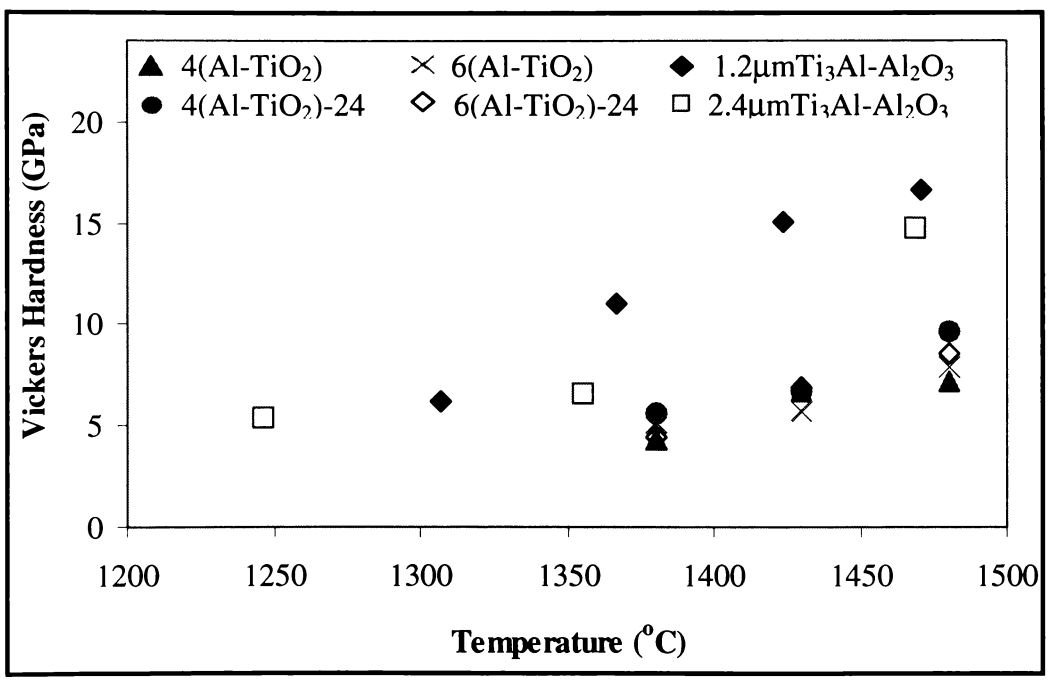

Figure 6.16: Vickers hardness of composites produced by pressureless sintering Al-TiO_2 composite powders in argon and hot pressing Ti_3Al-Al_2O_3 composite powder under vacuum as a function of temperature

6.5.3 Effect of Al_2O_3 Particle Size

Vickers hardness measurements of the Ti_3Al-Al_2O_3 composites produced by hot pressing Al-TiO_2 composite powders showed that the Vickers hardness maintained a constant level within 1-2GPa as shown in Figure 6.7. This is

understood by the increment of Al_2O_3 particle size from a minimum of 1μm to a maximum of 4μm as seen in Figure 5.14, which showed less particle coarsening compared to the hot pressing of Ti_3Al-Al_2O_3 composite powder discussed earlier in Chapter Three.

On the other hand, Ti_3Al-TiO-Al_2O_3 composites produced by pressureless sintering Al-TiO_2 composite powder after 16 and 24hours of ball milling showed increase of Vickers hardness from 8-15GPa and 14-18GPa, respectively, for Al_2O_3 particle size between 1.5-3.5μm, which levelled off towards approaching 3.5μm as shown in Figure 6.17. This is supported by the increasing hardness observed with the increase in Al_2O_3 particle size of the Ti_xAl_y-Al_2O_3 composites due to the larger contact areas of Al_2O_3 particles reported by Cai[7].

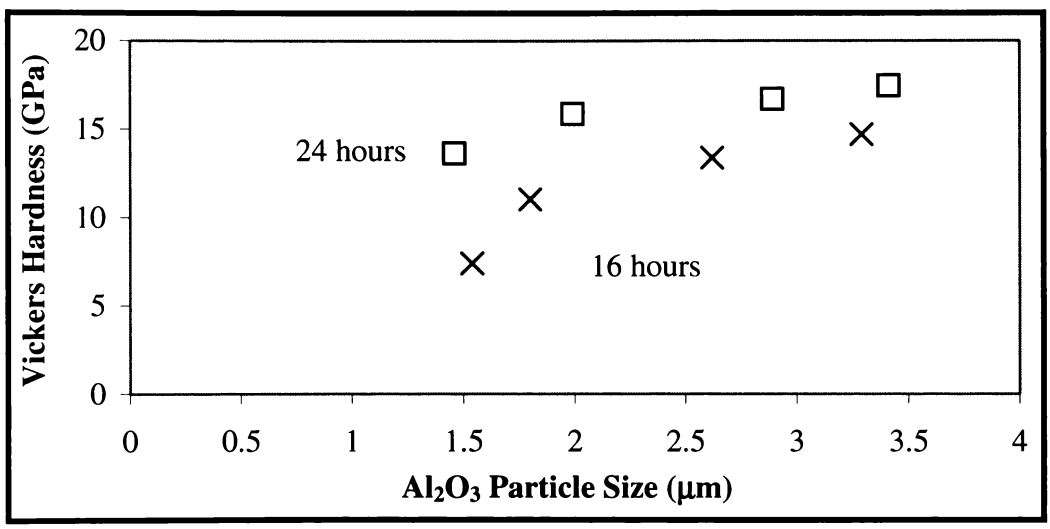

Figure 6.17: Vickers hardness of Ti_3Al-TiO-Al_2O_3 composites produced by pressureless sintering Al-TiO_2 composite powder (after 16 and 24 hours of ball milling) in argon versus Al_2O_3 particle size

Other mechanical properties such as biaxial strength are also influenced by the Al_2O_3 particle size of the composites. For a Ti_3Al-Al_2O_3 composite, biaxial strength is high when the microstructure is fine and homogeneous. For example, Figure 6.10(b) shows that the biaxial strength is controlled by the increase of particle size. As discussed previously, a maximum Al_2O_3 particle size of 4μm was obtained for these composites, which is close to the "fine grain size" category of 1-3μm[8]. This is supported by the Ti_3Al-TiO-Al_2O_3 composites produced by hot pressing Al-TiO_2 composite powder, which shows a decrease in biaxial strength with increasing Al_2O_3 particle size as seen in Figure 6.18. This is

supported by three-point bending strength reported by Cai, which decreased with increasing average Al_2O_3 particle size[7].

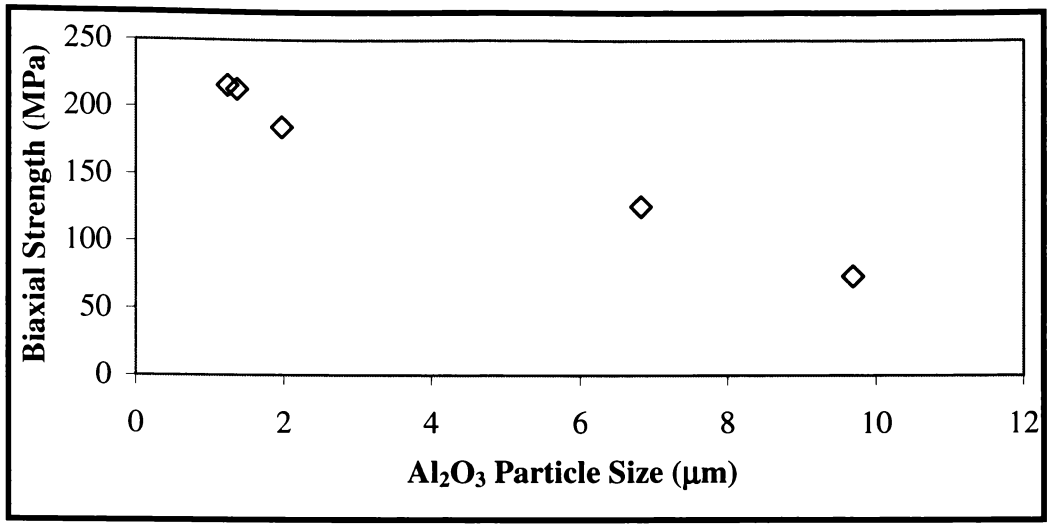

Figure 6.18: Biaxial strength of Ti_3Al-TiO-Al_2O_3 composites produced by hot pressing Al-TiO_2 composite powder under vacuum versus Al_2O_3 particle size

6.5.4 Effect of Ti_3Al Phase

The Vickers hardness of Ti_3Al-TiO-Al_2O_3 and Ti_3Al-Al_2O_3 composites decreased with increased Ti_3Al phase content. This is expected since Ti_3Al has lower Vickers hardness than Al_2O_3. Accepted literature values of Vickers hardness of Ti_3Al and Al_2O_3 are 5.9GPa and 14GPa, respectively[9, 10]. Cai et al. reported that microhardness values for Ti_3Al and Al_2O_3 in the Ti_3Al-Al_2O_3 composites are 7.2±0.6GPa and 15.2±1.0GPa[11]. As discussed earlier, Vickers hardness measurements were obtained for fully densified composites with Al_2O_3 particle size of 3-4μm after sintering produced by (1) hot pressing 1.2μm Ti_3Al-Al_2O_3 composite powder at 1474°C under vacuum at 4MPa, (2) pressureless sintering Al-TiO_2 composite powder in argon at 1480°C for 8 hours of holding period and (3) hot pressing 2(Al-TiO_2)-24 composite powder at 1500°C under vacuum. These data are plotted against the XRD peak intensity of Ti_3Al phase shown in Figure 6.19. It is clear that the Vickers Hardness decreased with increasing Ti_3Al phase as expected. Overall, Vickers hardness of ~15GPa was achieved for composite with around 50% XRD peak intensity of Ti_3Al phase.

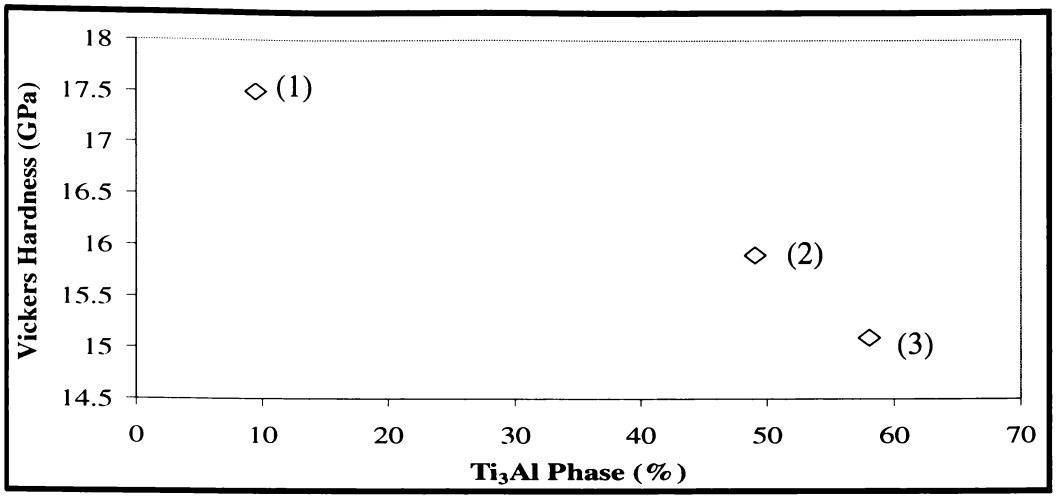

Figure 6.19: Vickers hardness of fully densified composites as a function of Ti_3Al phase obtained from XRD peak intensity

Biaxial strength should increase with increased densification. This is seen for the Ti_3Al-TiO-Al_2O_3 composites produced by pressureless sintering Al-TiO_2 composite powder in argon where the biaxial strength increased with decreasing porosity as seen in Figure 6.4. However this trend is not seen for the hot pressing of Al-TiO_2 composite powder under vacuum displayed earlier in Figure 6.2, where with the reduction of porosity, a decrease of biaxial strength was observed. This is due to the combination of increased Al_2O_3 particle size and the reduction of Ti_3Al intermetallic phase content from 60% XRD peak intensity to lower than 30% XRD peak intensity as seen in Figure 6.20. The Ti_3Al content controls the biaxial strength of the composite, which is supported by the increase in four-point bending fracture strength obtained with increasing metal content in the Al/Al_2O_3 composites (98% theoretical density) prepared by gas pressure metal infiltration, sintered at 1650°C[6].

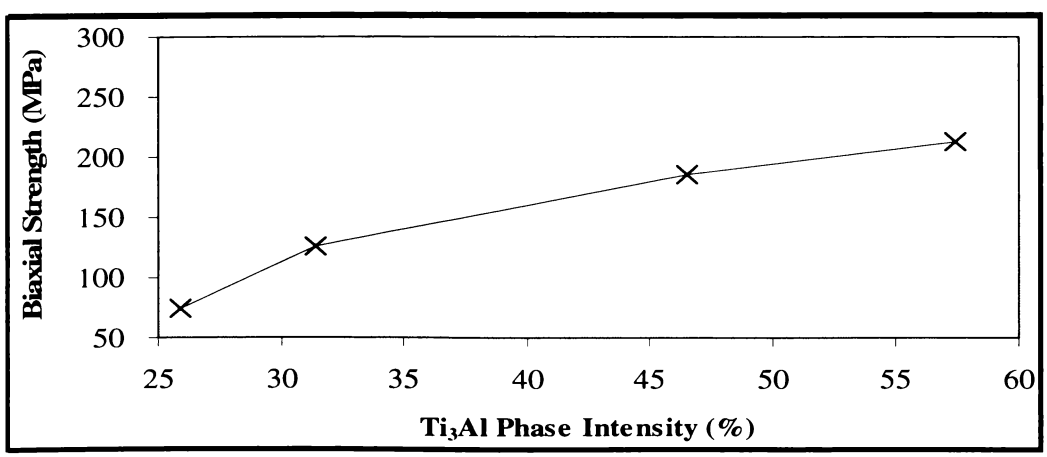

Figure 6.20: Biaxial strength of Ti_3Al-TiO-Al_2O_3 composites as a function of Ti_3Al phase obtained from XRD peak intensity

6.5.5 Fracture Toughness of Ti_3Al-Al_2O_3 Composite

Fully dense microstructures could be achieved by hot pressing at 1387°C under vacuum. A fully densified Ti_3Al-Al_2O_3 composite showed that both the phases are continuous and exhibit an interpenetrating network as seen in Figure 5.15 in Chapter Five. The average particle size of Al_2O_3 is approximately 2μm.

The crack induced by a Vickers indentor on the polished surface of the hot pressed composite shows that the crack is mostly deflected by the alumina particles. Debonding between alumina and aluminide is typical for this type of composite. As a result of both alumina-aluminide interface debonding and transgranular cracking by the more ductile Ti_3Al intermetallic phase, the enhanced energy dissipation of the propagating crack contributes to the composite toughness. Ultimately, a fracture toughness of 6.3±0.8 MPa $m^{1/2}$ was measured for the Ti_3Al-Al_2O_3 composite produced from 4(Al-TiO_2)-24 composite powder hot pressed at 1387°C under vacuum.

Typical fracture toughness values for alumina, monolithic TiAl and lamellar TiAl are 3.5-4, 7-8 and 12 MPa $m^{1/2}$, respectively[3]. For comparison, hot pressed Al_2O_3/TiC and Al_2O_3-10vol.%Ni_3Al show fracture toughness of 5.9MPa.$m^{1/2}$ and 7-8MPa.$m^{1/2}$, respectively[12, 13]. Cai reported fracture toughness in the range of 2-3.1MPa.$m^{1/2}$ for the Ti_xAl_y/Al_2O_3 composites fabricated by hot isostatic pressing of the pre-sintered composites. Interpenetrating Al_2O_3-$TiAl_3$ (5μm Al_2O_3 grain size, 58.1vol.% Al_2O_3) alloys produced by reactive infiltration exhibited fracture toughness of 8.6 ±0.4MPa.$m^{1/2}$[5]. In the present study, fracture toughness as high as 7.5±0.8MPa.$m^{1/2}$ was obtained when the phase structure exhibited a fine and homogeneous microstructure with 50% XRD peak intensity of Ti_3Al ductile phase in the matrix.

6.6 Summary

The results of mechanical property measurements of these composites, specifically Vickers hardness, biaxial strength and fracture toughness are discussed. These composites are formed from (1) hot pressing of Ti_3Al-Al_2O_3 composite powders and (2) pressureless sintering, hot pressing and sinter-HIP of Al-TiO_2 composite powders The composition-densification-mechanical properties

relationships of metal-ceramic composites with various compositions are discussed.

The level of porosity and Al_2O_3 particle size affect the mechanical properties of Ti_3Al-Al_2O_3 and Ti_3Al-TiO-Al_2O_3 composites. The volume fraction of the ductile intermetallic Ti_3Al phase is important in controlling the composite toughness. For fully densified Ti_3Al-TiO-Al_2O_3 composites, Vickers hardness of up to 17.5GPa was obtained depending on the composition and the Al_2O_3 particle size of the composites. For fully densified Ti_3Al-Al_2O_3 composites, optimum mechanical properties of Vickers hardness of 15.5GPa, biaxial strength of 278MPa and fracture toughness of $7.5\pm0.8MPa.m^{0.5}$ were obtained. For the fully densified Ti_3Al-Al_2O_3 composite produced by hot pressing, an *optimum* combination of 13.8GPa Vickers hardness, 260MPa biaxial strength and $7.5\pm0.8MPa.m^{0.5}$ fracture toughness was achieved. These values are comparable with some current high performance cutting tool materials such as nanocrystalline Al_2O_3-Fe, which has Vickers hardness of 14.9GPa and fracture toughness of $6.7MPa.m^{0.5}$[13].

REFERENCES

1. Fujikawa, T., *Hot isostatic pressing (HIP) of ceramics and HIP equipment for ceramics*, in *Fine Ceramics*, S. Saito, Editor. 1985, Elsevier Applied Science Publishers Ltd. p. 44-53.
2. Kingery, W.D., *Introduction of Ceramics*. 1960: Jonh Wiley & Sons, Inc. Canada. 374-383.
3. Travitzky, N., I. Gotman, E.Y. Gutmanas and N. Claussen, *Alumina-Ti aluminide interpenetrating composites: microstructure and mechanical properties.* Materials Letters, 2003. **57**: p. 3422-3426.
4. Garcia, D.E., S. Schicker, J. Bruhn, R. Janssen and N. Claussen, *Synthesis of novel niobium aluminide-based composites.* Journal of American Ceramic Society, 1997. **80**(9): p. 2248-2252.
5. Wagner, F., D.E. Garcia, A. Krupp and N. Claussen, *Interpenetrating Al_2O_3-$TiAl_3$ alloys produced by reactive infiltration.* Journal of the European Ceramic Society, 1999. **19**: p. 2449-2453.
6. Prielipp, H., M. MKnechtel, N. Claussen, S.K. Streiffer, H. Mullejans, M. Ruhle, and J. Rodel, *Strength and fracture toughness of aluminum/alumina composites with interpenetrating networks.* Materials Science and Engineering A, 1995. **197**: p. 19-30.
7. Cai, Z.H., *Processing, microstructure and mechanical properties of Ti_xAl_y/Al_2O_3 and $Al_2Ti_4C_2/Ti_xAl_y/Al_2O_3/TiC$ composites*, PhD Thesis 2003, The University of Waikato: Hamilton. p. 110.
8. Nakahigashi, J. and H. Yoshimura, *Ultra-fine grain refinement and tensile properties of titanium alloys obtained through protium treatment.* Journal of Alloys and Compounds, 2002. **330-332**: p. 384-388.
9. Kale, A., S. Seal, N. Sobczak, J. Morgiel and K.B. Sundaram, *Effect of deposition temperature on the morphology, structure, surface chemistry and mechanical properties of magnetron sputtered Ti70-Al30 thin films on steel substrate.* Surface and Coatings Technology, 2001. **141**(2-3): p. 252-261.
10. Brinson, H.F., T.J. Reinhart, S.J. Schneider and A.I.H. Committee, *Engineered Materials Handbook.* Vol. 4. 1987: Metals Park, Ohio.
11. Cai, Z.H. and D.L. Zhang, 2005.
12. Tiegs, T.N., K.B. Alexander, K.P. Plucknett, P.A. Menchhofer, P.F. Becher, and S.B. Waters, *Ceramic composites with a ductile Ni_3Al binder phase.* Materials Science and Engineering A, 1996. **209**: p. 243-247.
13. Mishra, R.S. and A.K. Mukherjee, *Processing of high hardness-high toughness alumina matrix nanocomposites.* Materials Science and Engineering A, 2001. **301**: p. 97-101.

CHAPTER SEVEN:

CONCLUSIONS AND RECOMMENDATIONS

7.1 CONCLUSIONS

7.1.1 Ti_3Al-TiO-Al_2O_3 Composites Produced by Pressureless Sintering/Hot Pressing Ti_3Al-Al_2O_3 Composite Powder

- The average particle size of the Ti_3Al-Al_2O_3 composite powder can be reduced from 12.6μm to 1.2μm by Si_3N_4 ball milling in chloroform for up to 72 hours.
- The porosity and bulk density decreased and increased respectively with increasing sintering/hot pressing temperature for both pressureless sintering and hot pressing. A pressureless sintering temperature of 1600°C is required to achieve >95% theoretical density of the Ti_3Al-TiO-Al_2O_3 composites. However, fully densified composites were fabricated by hot pressing 1.2μm Ti_3Al-Al_2O_3 composite powder at 1474°C under vacuum for a one hour of holding period.
- The Ti_3Al-TiO-Al_2O_3 composite microstructure shows that Al_2O_3 is embedded in a Ti_3Al/TiO matrix. Al_2O_3 particle coarsening and microcracking were observed at hot pressing temperatures above1500°C. The microcracking is due to the large difference in the thermal expansion coefficients between the Al_2O_3 particles and Ti_3Al/TiO matrix.
- Vickers hardness of 17.5GPa was achieved for the fully densified Ti_3Al-TiO-Al_2O_3 composite produced by hot pressing 1.2μm Ti_3Al-Al_2O_3 composite powder at 1474°C under vacuum at 4MPa.

7.1.2 Ti_3Al-TiO-Al_2O_3 and Ti_3Al-Al_2O_3 Composites Produced by Pressureless/Pressure-Assisted Sintering Al-TiO_2 Composite Powder

- Sintering and densification processes are accelerated by reducing the particle size of the starting discus milled Al-TiO_2 (anatase) composite powder from 19μm to 10μm median particle diameter. A minimum median particle diameter of 7μm was reached by ZrO_2 ball milling in chloroform for 24 hours.
- Near fully densified Ti_3Al-TiO-Al_2O_3 and Ti_3Al-Al_2O_3 composites of 96% of theoretical density with ≤4μm Al_2O_3 particle size in the composites

could be achieved for pressureless sintering Al-TiO_2 composite powder at 1480°C in argon for 4-5 hours of holding period.

- Hot pressing and sinter-HIP assist the sintering and densification processes allowing a reduction of temperature that leads to particle growth and pore suppression. The coarsening of the Al_2O_3 particles was suppressed after hot isostatic pressing at 1350°C in argon for two hours for Ti_3Al-TiO-Al_2O_3 composites prepared by pressureless sintering Al-TiO_2 composite powder at 1480°C.
- The volume fraction of the ductile intermetallic Ti_3Al phase in the Ti_3Al-Al_2O_3 composite is important in controlling the composite toughness. The composite microstructure demonstrates that both the Al_2O_3 and Ti_3Al phases are continuous and exhibit an interpenetrating network with fracture toughness as high as 7.5±0.8MPa.$m^{1/2}$.
- Vickers hardness of the composites increased with increasing densification and increased Al_2O_3 ceramic phase content. Vickers hardness's of ≤17.5GPa and ≤15GPa were achieved for the fully densified Ti_3Al-TiO-Al_2O_3 and Ti_3Al-Al_2O_3 composites, respectively. In the sinter-HIP experiments, the Vickers hardness increased by up to 2GPa due to the decreased total porosity after hot isostatic pressing of the pre-sintered Ti_3Al-TiO-Al_2O_3 composites with 96% theoretical density.
- Biaxial strengths of ≤350MPa and ≤278MPa were achieved for Ti_3Al-TiO-Al_2O_3 and Ti_3Al-Al_2O_3 composites, respectively.

7.2 RECOMMENDATIONS FOR FUTURE WORK

- Finer particle sizes of Al and TiO_2 raw materials could be used for discus milling to investigate the solid state sintering of these materials.
- Mechanical properties such as bending strength and fracture toughness of the pre-sintered composites with >95% of theoretical density subjected to hot isostatic pressing at temperature >1350°C could be investigated.
- TEM should be used to determine the Al_2O_3 grain size in order to study the grain growth kinetics of the Al_2O_3 in two-phase system.

APPENDIX A

A1.0 XRD Phase Intensity Measurement

The intensities of the phases were measured by using the peak height of the strongest peaks of a phase in the XRD pattern. This method produced a reasonable comparison of XRD phase intensity of different phases in the composites. As an example, the strongest Al_2O_3 peak is labelled (a) and the strongest Ti_3Al peak is labelled (b) in the Figure A1.1. This figure also shows two XRD patterns overlapping each other. The XRD pattern colour in red is the standard measurement achieved on a powdered composite. The XRD pattern coloured in blue is the same powdered composite with the addition of 10% alumina. The change in peak height corresponds to the 10% alumina addition. Repeat measurements on a number of powdered composites were undertaken to compare the reproducibility and reliability of this method as shown in Table A1.1 and Table A1.2. It was shown that the volume fraction of Al_2O_3 obtained from the XRD phase intensity without 10% alumina was comparable to the volume fraction of Al_2O_3 obtained from the XRD phase intensity with 10% alumina for randomly selected samples A, B, C, D and E. An example of how the extrapolation was measured is shown in Figure A1.2. The extrapolations were measured on four XRD peaks for each sample.

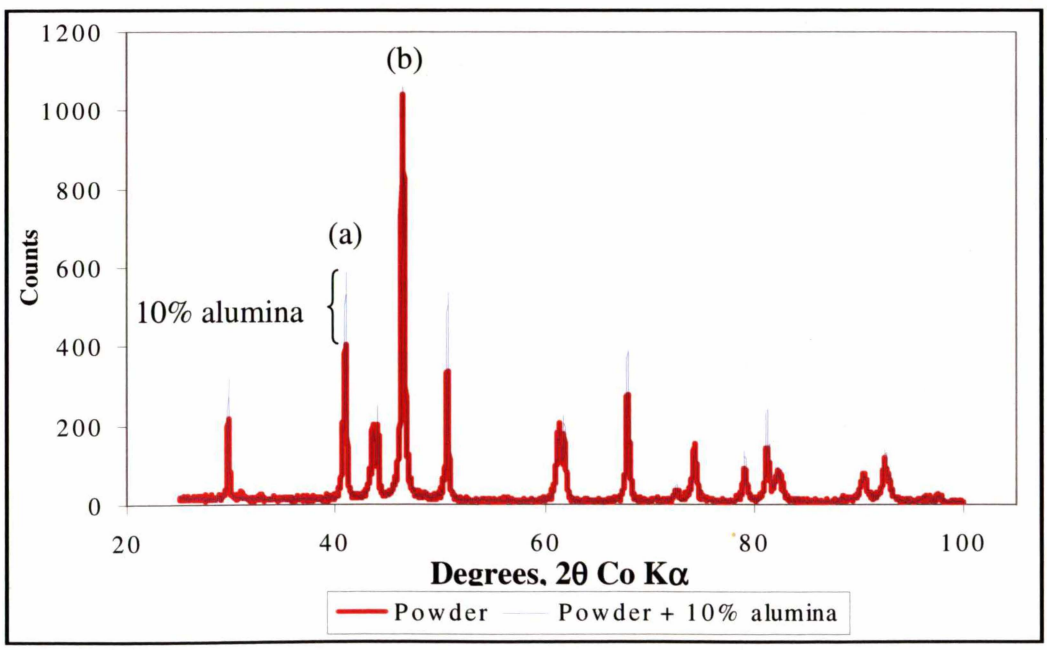

Figure A1.1: XRD pattern of the powdered sintered composite before and after 10% alumina addition

Table A1.1: Sample A, B, C and D

	Sample A	**0.35**		
Al_2O_3 in composite	% Al_2O_3 addition	Counts		
Peak I	0	280		
	0.1	372	0.3	
Peak II	0	260		
	0.1	318	0.32	
Peak III	0	469		
	0.1	566	0.45	
Peak IV	0	373		Average
	0.1	491	0.48	

	Sample B	**0.33**		
Al_2O_3 in composite	% Al_2O_3 addition	Counts		
Peak I	0	331		
	0.1	425	0.26	
Peak II	0	275		
	0.1	329	0.28	
Peak III	0	422		
	0.1	584	0.35	
Peak IV	0	205		Average
	0.1	277	0.5	

	Sample C	**0.27**		
Al_2O_3 in composite	% Al_2O_3 addition	Counts		
Peak I	0	279		
	0.1	388	0.17	
Peak II	0	220		
	0.1	323	0.21	
Peak III	0	406		
	0.1	589	0.22	
Peak IV	0	340		Average
	0.1	537	0.255	

	Sample D	**0.28**		
Al_2O_3 in composite	% Al_2O_3 addition	Counts		
Peak I	0	268		
	0.1	401	0.2	
Peak II	0	345		
	0.1	493	0.23	
Peak III	0	415		
	0.1	525	0.36	
Peak IV	0	237		Average
	0.1	302	0.38	

Table A1.2: Sample E

	Sample E	0.42		
Al_2O_3 in composite	% Al_2O_3 addition	Counts		
Peak I	0	257		
	0.1	364	0.25	
Peak II	0	346		
	0.1	432	0.32	
Peak III	0	126		
	0.1	175	0.4	
Peak IV	0	204		Average
	0.1	268	0.7	

Volume fraction of Al_2O_3 in the composite obtained from the strongest XRD peak without 10% alumina

Average volume fraction of Al_2O_3 in the composite obtained from Extrapolation of four XRD peaks with 10% alumina addition

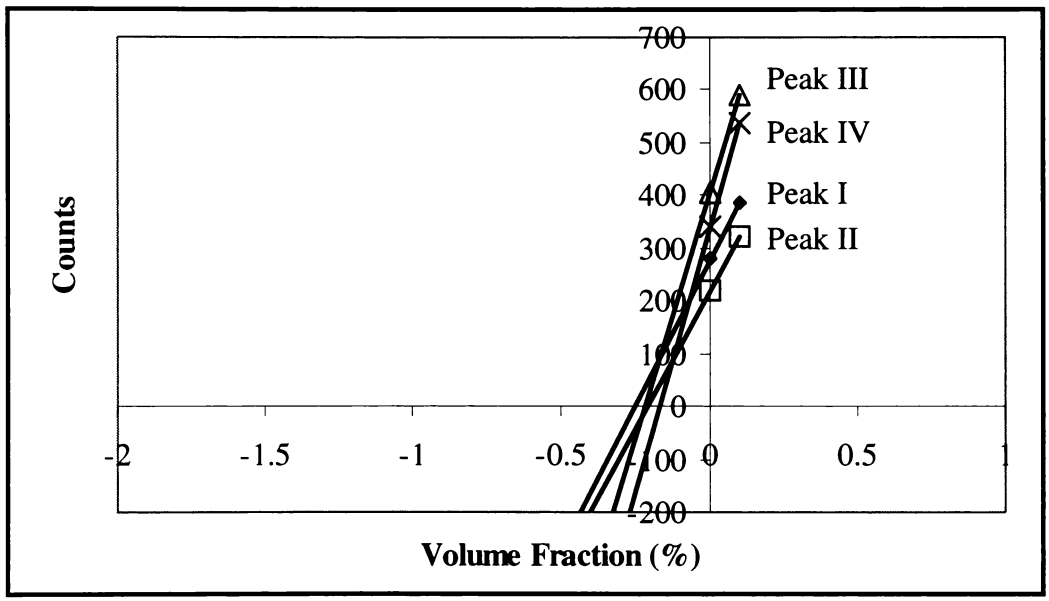

Figure A1.2: Extrapolation of four XRD peaks of sample C

A2.0 Image Analysis

The particle size of the Al_2O_3 in the composite as shown in Figure A2.1 was measured using Scion Image Software. The particles of the Al_2O_3 phase were schematically defined as shown in Figure A2.2. By clicking *Measure* on the software gives a range of results such as the *area*, *major* and *minor diameter* of the particles.

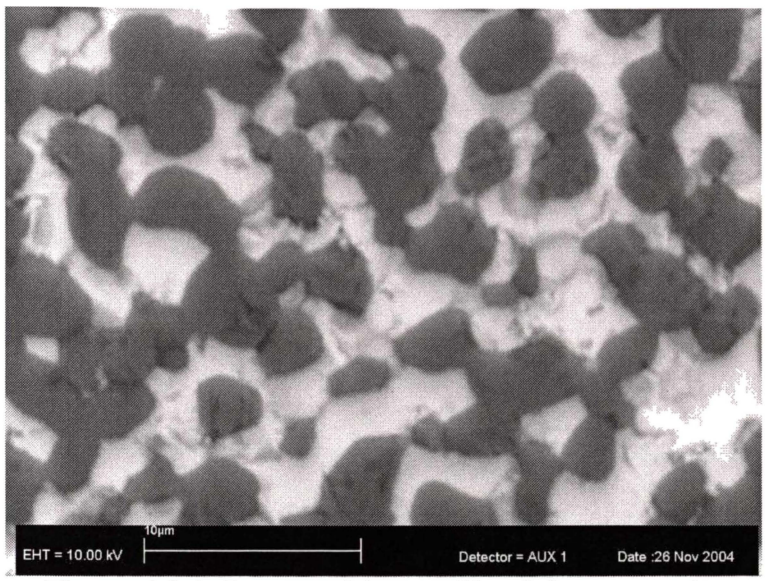

Figure A2.1: Imported image file of the composite

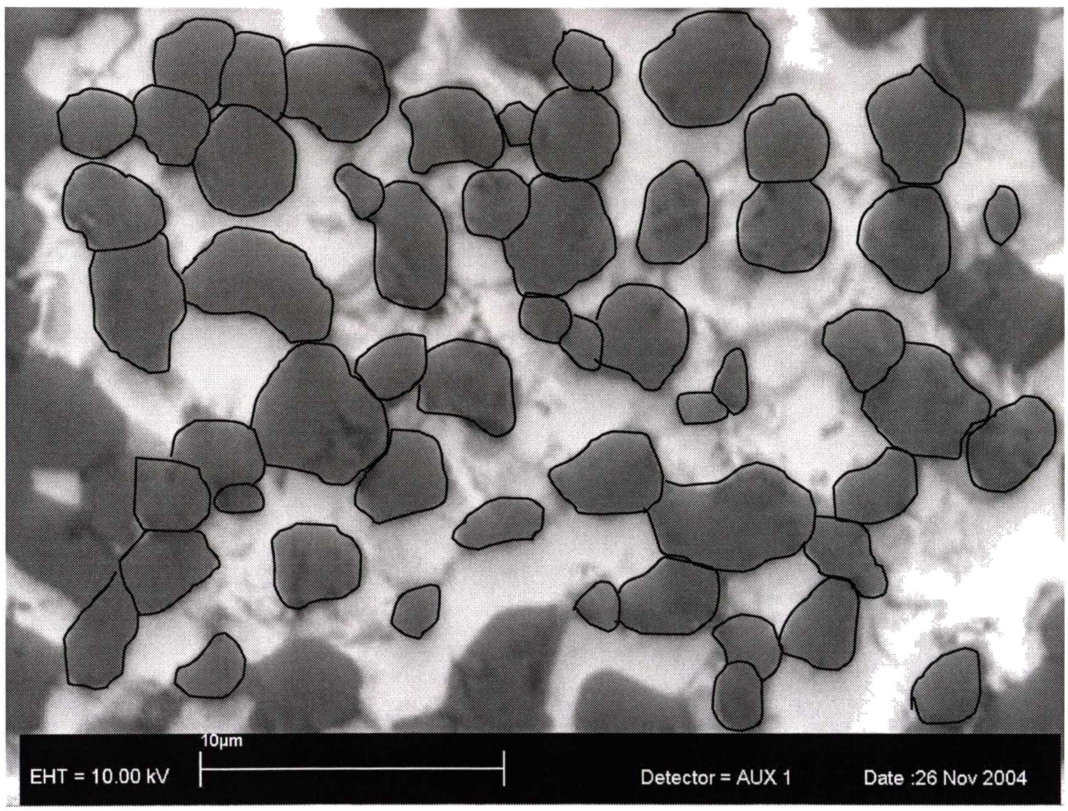

Figure A2.2: Approximate definition of the Al_2O_3 particles